GLOBAL RETRIEVALS OF UPPER-TROPOSPHERIC PHOSPHINE FROM THE CASSINI/CIRS JUPITER ENCOUNTER

A thesis submitted to the Faculty of Physical Sciences for the
degree of Doctor of Philosophy at the University of Oxford.
Michaelmas Term 2003

Paul David Parrish
Keble College

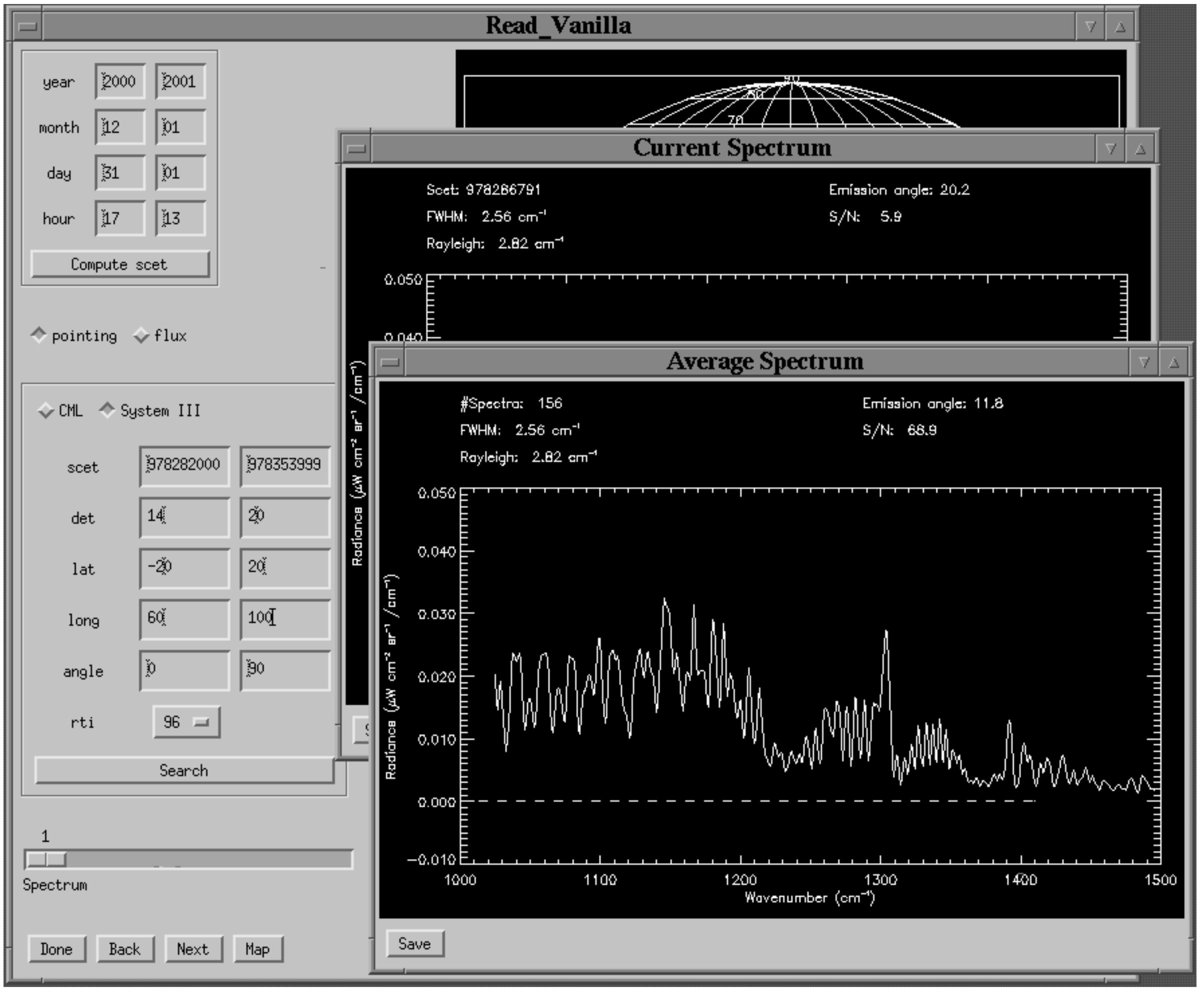

year	2000	2001
month	12	01
day	31	01
hour	17	13

scet	978282000	978353999
det	14	20
lat	-20	20
long	60	100
angle	0	90
rti	96	

Spectrum 1

Current Spectrum:

Scet: 978286791
FWHM: 2.56 cm^{-1}
Rayleigh: 2.82 cm^{-1}
Emission angle: 20.2
S/N: 5.9

Average Spectrum:

#Spectra: 156
FWHM: 2.56 cm^{-1}
Rayleigh: 2.82 cm^{-1}
Emission angle: 11.8
S/N: 68.9

Figure 1: The `Read_vanilla` graphical user interface.

Abstract

On December 30^{th} 2000, the Cassini-Huygens spacecraft reached the perijove milestone in its continuing journey to the Saturnian system. During an extended six-month encounter, the Composite Infrared Spectrometer (CIRS) returned spectra of the Jovian atmosphere, rings and satellites from 10 to 1400 cm^{-1} (1000 to 7 μm) at a programmable spectral resolution of 0.5 to 15 cm^{-1}. The improved spectral resolution of CIRS over previous infrared instrument-missions to Jupiter, the extended spectral range and higher signal-to-noise performance provide significant advantages over previous data-sets.

Both optimal-estimation retrieval and radiance-differencing are used to investigate the global variation of upper-tropospheric temperature, ammonia, phosphine and cloud opacity between ± 60° latitude. The analysis methods are shown to successfully reproduce Jovian conditions with results consistent with previous investigations. The composition results in particular are well characterised and suggest an important role played by mixing and transport within the upper-troposphere. Interpretation and validation of the retrieved results is conducted via the construction of a simple dynamic model incorporating transport, diffusion and (photo)chemistry.

Acknowledgements

I devote this thesis principally to my Father without whose encouragement, guidance and support none of this would have been possible. Also to my good friend David and my girlfriend Catherine who have played, and are likely to continue to play, significant roles in my personal development.

I am also greatly indebted to Universities UK (formerly The Committee of Vice-Chancellors and Principals of the Universities of the United Kingdom) for sponsoring my work via the Overseas Research Scholarship. Appreciation is extended to P.G.J. Irwin, S.B. Calcutt and F.W. Taylor for their supervision, C.A. Nixon and T. Fouchet for their assistance and C.L. Hepplewhite and M. Roos-Serote, my *viva voce* examiners. Other notables include R.G. Grainger, A. Dudhia and C.D. Rodgers for their Earth-observation perspectives and B.J. Conrath for keeping Dr. Irwin and I honest. Also to my officemate N.E. Bowles, who deserves an acknowledgement of his own, for his patient understanding.

And lest I forget, the acquisition of the data described in this report was accomplished through the coordinated effort of the Cassini-Huygens project staff, Deep Space Network personnel and the CIRS instrument team; their participation, though mostly anonymous, I am dutifully grateful.

Contents

List of Figures

List of Tables

Glossary

This glossary has been written to provide the reader with an explanatory list of the acronyms, notation and terminology used frequently throughout this document.

Acronyms: Below is a list of the acronyms used within the thesis.

ASI	Atmospheric Structure Instrument [Galileo probe]
AU	Astronomical unit (1 AU = 149.6×10^6 km)
CA	Closest approach
CIA	Collision induced absorption
CIRS	Composite Infrared Spectrometer [Cassini]
E99	Edgington *et al.* 1999: [54]
ESA	European Space Agency
ESO	European Southern Observatory [Cerro Paranal, Chile]
FOV	Field-of-view
FP1	CIRS focal plane 1 (thermopile detectors; 10-600 cm^{-1}, 16.7-100 μm)
FP3	CIRS focal plane 3 (PC detectors; 600-1100 cm^{-1}, 9.1-16.7 μm)
FP4	CIRS focal plane 4 (PV detectors; 1100-1400 cm^{-1}, 6.7-9.1 μm)
FSH	Fractional scale height

FT	Fourier transform
FWHM	Full-width-at-half-maximum
G92	Griffith *et al.* 1992: [78]
GEISA-97	Gestion et Etude des Informations Spectroscopiques Atmospheriques 1997
GPMS	Galileo probe Mass Spectrometer
GRS	Great Red Spot (22°S, 60°W)
HITRAN-2K	High Resolution Transmission Molecular Absorption Database 2000
HST	Hubble Space Telescope
ILS	Instrument line shape
IR	Infrared
IRIS	Infrared Interferometer Spectrometer [Voyagers 1 and 2]
IRTF	Infrared Telescope Facility [Mauna Kea, Hawai'i]
ISO	Infrared Space Observatory
ISS	Imaging Science System [Cassini]
IUE	International Ultraviolet Explorer
IUS	Inertial upper-stage
JPL	Jet Propulsion Laboratory
KAO	Kuiper Airborne Observatory
L98	Lara *et al.* 1998: [112]
NEB	Northern Equatorial Belt (7°N to 18°N)
NESR	Noise equivalent spectral radiance
NICMOS	Near-Infrared Camera and Multi-Object Spectrometer [HST]

NIMS	Near-Infrared Mapping Spectrometer [Galileo orbiter]
PC	Photoconductive
PV	Photovoltaic
QQO	Quasi-quadrennial oscillation
RTI	Real time interrupt
RWA	Reaction wheel assembly
SNR	Signal-to-noise ratio
SCET	Spacecraft event time
SEB	Southern Equatorial Belt (20°S to 7°S)
SL9	Comet Shoemaker-Levy 9
STrZ	South Tropical Zone (25°S to 24°S)
SWAS	Submillimeter Wave Astronomy Satellite
SWS	Short-Wave Spectrometer [ISO]
VMR	Volume mixing ratio
WFPC2	Wide-Field and Planetary Camera 2 [HST]
ZPD	Zero path-difference

Notation: In general, vectors and matrices are denoted by bold lower-case letters and bold upper-case letters (respectively) while superscripts $^{-1}$ and ^{T} are used to represent matrix inverse and transpose (respectively) and $\hat{}$ is used to signify the best estimate. In cases where the same variable is used to denote different quantities, the usage of the variable in the text should convey the difference in meaning. Below are the variables, grouped by association, used within the thesis. All of the optimal estimation equations are presented in “m-form” (*vice* n-form) in reference to the size of the matrix (*i.e.* the number of measurements *versus* the number of state parameters) to be inverted.

GAS SPECIES

He	Helium	HCN	Hydrogen cyanide	HD	Deuterated hydrogen
H_2	Molecular hydrogen	H_2O	Water	H_2S	Hydrogen sulphide
CH_3	Methyl	CH_3D	Monodeuteromethane	CH_4	Methane
C_2H_2	Acetylene	C_2H_4	Ethylene	C_2H_6	Ethane
C_3H_4	Methylacetylene	C_3H_8	Propane	C_4H_2	Diacetylene
C_6H_6	Benzene	CO	Carbon monoxide	CO_2	Carbon dioxide
AsH_3	Arsine	GH_4	Germane	PH_3	Phosphine
NH_3	Ammonia	NH_4SH	Ammonium hydrosulphide		

ATMOSPHERIC PHYSICAL PROPERTIES

T	Temperature [K]	P	Pressure [bar or mbars]
T_B	Brightness temperature [K]	ρ	Density [kg/m^3]
T_E	Radiative-equil. temperature [K]	q	VMR/Mole fraction
n	Number density [molecules/cm^3]	g	Gravitational acceleration [m/s^2]
t	Time [s]	z	Height [km]
t_R	Radiative-equilibrium time [s]	H	Scale height [km]

t_K	Diffusive-equilibrium time [s]	N	Brunt-Väisälä frequency [/s]
c_P	Specific heat capacity at constant pressure [J/(K kg)]	R_{gas}	Jovian gas constant [J/(K kg)]

GENERAL VARIABLES

$\tilde{\nu}$	Wavenumber [cm^{-1}]	$A(\tilde{\nu})$	Spectral distribution
$\varphi(\tilde{\nu})$	Phase spectrum	$R(\tilde{\nu})$	Responsivity
L	Path difference	$\mathcal{I}(L)$	Interferometric intensity
$\Psi(L)$	Symmetrising function	$I(\tilde{\nu})$	Irradiance [W/m^2]
$B(\tilde{\nu}, T)$	Planck function [W/(m^2 sr cm^{-1})]	$J(\tilde{\nu})$	Source function [W/(m^2 sr)]
u	Absorber amount [g/cm^2]	$k(\tilde{\nu})$	Mass-extinction coefficient [cm^2/g]
$\chi(\tilde{\nu})$	Optical depth/cloud opacity	$\tau(\tilde{\nu})$	Transmissivity
ϕ	Zenith angle [°]	θ	Scattering angle [°]
ϖ	Single-scattering albedo	$p(\theta)$	Scattering-phase function
w	Vertical wind speed [μm/s]	ψ	Flux [g/(cm^2 s)]
$\mathcal{K}$	Eddy-diffusion coefficient [cm^2/s]		

OPTIMAL ESTIMATION

n	Number of state parameters	m	Number of measurements
$\mathbf{x}$	State vector	$\mathbf{y}$	Measurement vector
$\mathbf{x}_a$	*A priori* state vector	$\mathbf{S}_a$	*A priori* covariance
$\mathbf{x}_i$	Current/i$^{\text{th}}$ iteration state vector	$\mathbf{S}_\varepsilon$	Measurement covariance

$\widehat{\mathbf{x}}$	Best estimate of $\mathbf{x}$	$\widehat{\mathbf{S}}$	Best estimate/Final covariance
$\mathbf{K}$	Sensitivity kernel function	$\mathbf{D}$	Retrieval gain matrix
λ	Levenberg-Marquardt-type braking parameter	ϕ	Cost function

Terminological Note: Throughout this thesis, the words "day" and "year" should be taken as referring to the 24-hour Earth day and the 365-day Earth year respectively. This convention is both for convenience and is in agreement with the official Cassini-Huygens tour-planning documentation. Unless otherwise stated, planetographic latitude and System III[1] west longitude coordinates are used.

The metric system is employed throughout. Accordingly, vertical levels are specified in kilometres (or in terms of mean pressure in units of bars or millibars where zero altitude occurs at one atmosphere or 1.01325 bars) and wavelengths in wavenumbers (cm^{-1}) or micrometers (μm, familiarly known as "microns"). The word "abundance" is used interchangeably with volume mixing ratio or mole fraction and is unitless.

---

[1] As there are no fixed features on Jupiter with which to assign longitudinal meridians, and because different latitudes rotate at different rates, several arbitrary systems are used to describe observations of Jovian longitude. These systems are defined as constant sidereal rotation periods of exactly 877.900°/day (System I), 870.270°/day (System II) and 870.536°/day (System III). Systems I and II are particularly useful as frames of reference during transit observations. For example, cloud features within ±10°and the jet at 25°N drift slowly in System I coordinates (period = $9^{\mathrm{h}}\ 50^{\mathrm{m}}\ 30.0^{\mathrm{s}}$). System II on the other hand (period = $9^{\mathrm{h}}\ 55^{\mathrm{m}}\ 40.6^{\mathrm{s}}$), is based on the mean rotation of the equatorial belts and is used for all other latitudes. Professional astromers use System III, with a period of $9^{\mathrm{h}}\ 55^{\mathrm{m}}\ 29.7^{\mathrm{s}}$, which represents the rotation period of the core/interior as deduced by radio observations. There have also been calls for a System IV longitude-coordinate system (to assist in the tracking of features within the plasma torus – sidereal rotation rate = 845.05°/day [162]), although the International Astronomical Union seems not to have taken notice.

Foreword

The Cassini/CIRS project is a large international collaboration between NASA Goddard Space Flight Center (GSFC), Oxford University (the Atmospheric, Oceanic and Planetary Physics – AOPP, sub-department) and other British, French and German groups. A large number of people have been (and remain) involved in the project, so my efforts have inevitably been intertwined with the work of other team members. Below, I outline the contents of the thesis which I have personally contributed to the CIRS project.

Instrument Construction: The CIRS instrument was designed, built and tested by the University of Oxford, Queen Mary and Westfield College of the University of London, Le Centre d'Etudes Nucléaires de Saclay, L'Observatoire de Paris-Meudon and Universität Karlsruhe. AOPP contributed the CIRS cooler in addition to integrating the low temperature focal-plane assembly to the mid-infrared detectors.

Sequence Planning and Spectral Calibration: The pre-flight calibration of the CIRS instrument was carried out by the team lead by V.G. Kunde and F.M. Flasar of GSFC. P.J. Schinder of the Jet Propulsion Laboratory (JPL) was responsible for developing the observational sequences and the associated CIRS pointing commands for the Jupiter encounter. The inflight radiometric calibration was completed at GSFC (principally C.A. Nixon and R.C. Carlson) with contributions from the AOPP team.

Data-processing: S.B. Calcutt was responsible maintaining a mirrored CIRS database at Oxford. The automated code used to download the calibrated spectra from the CIRS database (exemplified by the image on the inside cover) was primarily authored by T. Fouchet with several additions of my own. I contributed the subsequent processing programs to sequence the large number of files from database extraction, through retrieval calculation to graphical representation of results.

Analysis: The creation and management of the spectroscopic database and the associated absorption-coefficient reference tables used in conjunction with the correlated-k method (Chapter 3) was my own. Updated line-data for ammonia and methane were provided by G.S. Orton and L.R. Brown of JPL from the, at the time, unpublished HITRAN-2K spectroscopic database.

The radiative-transfer code highlighted in Chapters 3 and 4 was developed and written by P.G.J. Irwin and others within AOPP, with several necessary additions made by myself. The `FORTRAN` routines used to compute the collision-induced absorption are due to A. Borysow and collaborators, of the University of Michigan.

While the concepts employed in the inverse model validation and spectral differencing were of Dr. Fouchet's and Dr. Irwin's respectively, I authored the various analysis, modelling and plotting routines of Chapters 4 and 5. All the graphics presented in the thesis are of my design unless otherwise stated.

Results: The interpretation of the results and the recommendations are my own.

Chapter 1

The Jovian Atmosphere

Contents

The thesis begins with an introduction to the Jovian system. Particular emphasis is given to Jupiter's structure and atmospheric temperature and composition. An overview of previous missions to Jupiter is also given providing the reader with the overall context in which to consider the composition retrievals and modelling of Chapters 4 and 5.

1.1 Physical Characteristics

Jupiter, given the Roman name for lord of the sky, is the largest of the planets within the Solar System and has an impressive system of sixty-one[1] known satellites. The predictability of Jupiter's movement in the sky as seen from Earth (a twelve year cycle in tune with the circumnavigation of the zodiacal signs) and its brilliance with respect to the background stars (forth brightest after the Sun, Moon and Venus) suggest that it was aptly named. As one examines the physical characteristics of Jupiter, one is further convinced its name is appropriate (see Table 1.1). At 0.1% the mass of the Sun, Jupiter is more than three times as massive as Saturn, the next largest planet, and possesses four of the largest satellites in the Solar System. Similarly impressive is the fact that even though Jupiter is 318 times more massive than the Earth, its average density is less than one-fourth that of the Earth! This suggests that the amount of dense rock and metallic material that can be present within the planet's cloud-shrouded interior is likely to be severely limited and that, like the Sun, Jupiter must be composed mainly of light elements (see Table 1.2).

1.2 Observational History

The observational history of Jupiter will be described in this section. The section begins with a review of visible and infrared investigations, looking at each progressive advancement in turn, prior to speaking about ground-based observations and those conducted

---

[1] Just over half of Jupiter's moons are "irregular" satellites with eccentric orbits that can be highly inclined or retrograde relative to the equatorial plane [173]. While the majority of the irregular moons are less than 10 km in diameter and are thought to be captured asteroids, there are seventeen regular satellites that follow uninclined, nearly circular and prograde orbits.

Physical Properties	**Jupiter**	$\frac{Jupiter}{Earth}$	**Note**
Sidereal rotation period	$9^{\mathrm{h}}\ 55^{\mathrm{m}}\ 29^{\mathrm{s}}$	0.415	a
Equatorial radius at 1 bar	71,492 ± 4 km	11.21	
Polar radius at 1 bar	66,854 ± 10 km	10.52	
Oblateness	0.06487 ± 0.0002	191.2	b
Mass	1.898×10^{27} kg	317.7	
Equatorial gravity at 1 bar	23.12 ± 0.01 m/s^2	2.36	
Escape velocity	58.6 km/s	5.26	
Mean density	1.326×10^3 kg/m^3	0.24	
Scale height	24.35 km	3.5	
Bolometric temperature	124.4 ± 0.3 K	0.49	c
Temperature at 1 bar	165 ± 5 K	0.57	
Visible geometric albedo	0.51	1.82	d
Emitted/absorbed flux ratio	1.668 ± 0.085	1.67	
Orbital Properties			
Mean distance from Sun	778.3×10^6 km	5.203	
Eccentricity	0.048	2.82	
Obliquity	$3^\circ\ 4'\ 48''$	0.13	e
Sidereal revolution period	11.8623 years	11.8623	
Solar irradiance	51.0 W/m^2	0.04	

Table 1.1: Physical properties of Jupiter (compiled from [96, 124]). a: System III (bulk rotation) longitude coordinates; b: $\frac{R_{eq.} - R_{pole}}{R_{eq.}}$; c: the temperature of a blackbody sphere which would radiate heat to space at the same rate as that observed for the planet; d: the ratio of the object's brightness to that which diffusely reflects all incident light, under vertical illumination. Another measure of albedo, the Bond albedo (the fraction of incident radiation reflected isotropically without absorption), varies from 0.62 in the NEB to 0.76 in the STZ [144]. The corresponding infrared values, weighted by the solar spectrum, are 0.274 ± 0.013 (geometric) and 0.343 ± 0.032 (Bond) [83]. Under Lambertian conditions, the two albedos are identical; e: the inclination of the Equator to the orbit.

in orbit, finishing with the Pioneer, Voyager and Galileo missions to Jupiter. The review will include brief summaries of the most important observational results directly relevant to the thesis (principally meaning temperature, composition and cloud).

1.2.1 Ground-Based Observations

The history of the visual observation of Jupiter goes back to antiquity. Closer to the present, Galileo Galilei made the first recorded telescopic observations of Jupiter in 1610. Other discoveries soon followed: a description of the zone-belt structure was published in 1630 by Niccolo Zucchi. The shadows of the transiting moons were observed in 1643 by Giovanni Riccioli, while the rapid rotation of Jupiter was revealed via the observation of spots by Robert Hooke and Guiseppe Campani *circa* 1664. A year later, Giovanni Cassini[2] began his nearly three-decade series of continuous observations of a "permanent spot" on Jupiter which may be identical to the current Great Red Spot (GRS).

Such work resulted in a period of Jovian observation and investigation that has not diminished to the present day. The early observers, noting changes in the colour and texture of Jupiter's distinctive banded structure, paid special attention to the dark bands thinking they were breaks in the brighter clouds which would allow them to view down to the planetary surface. Although a futile effort because Jupiter lacks a solid surface akin to Earth's, it initiated a concerted effort of feature tracking by several different organizations around the world. Through the efforts of groups like the Observatoire de

---

[2] Later, in Chapter 2, Jean Dominique Cassini is referred to when describing the namesake of the Cassini-Huygens mission. To avoid confusion, Giovanni Dominico Cassini changed his name to Jean Dominique Cassini when he moved from the University of Bologna to become the head of the Observatoire de Paris – it is the same individual.

Paris, the British Astronomical Association, and the Lunar and Planetary Society, a valuable database of rotation periods and drawings was generated which now form the historical basis for the photographic and digital observations conducted today.

The tool that opened up investigation in the infrared (IR) was spectroscopy. A grating spectrometer for example, uses a large number of equally-spaced, parallel lines or slits ruled on a flat surface (grating) to disperse the incident radiation into its frequency components. Using the distinct spectral features attributed to both methane and ammonia, Rupert Wildt in the 1930s and Gerard Kuiper in the 1940s were able to determine the existence of these gases (respectively) within the Jovian atmosphere. But grating spectroscopy has its drawbacks since it is a time consuming process and, because of its nature, different parts of the spectrum are recorded at different times.

The spectroscopic technique that revolutionised planetary astronomy was interferometry. Interferometers use the principle of interference and the mathematical process of Fourier Transformation (FT) for converting periodic functions (the time domain) into the separate frequencies of a spectrum (the frequency domain). A FT spectrometer works by splitting the incident radiation into two beams and then recombining the beams after the introduction of a path difference. On recombination, interference between the two beams causes the energy reaching the detector to be modulated proportional to the path difference introduced. For a broad spectral source, the interference pattern is the superposition of many different source functions. Via Fourier Transformation, the various source function frequencies and amplitudes can then be obtained (see §2.3 for an extended discussion of interferometers, their workings and calibration).

The main advantage of an interferometer is its high throughput. This is in contrast to a dispersive spectrometer where the energy is restricted by the slits. As a result, and because the entire frequency range is sampled simultaneously, the scan time for a FT spectrometer is considerably less than that required to produce a dispersive spectrum of the same sensitivity and resolution. As there are no grating or filter changes, there are no discontinuities in the spectrum either. For these reasons and others, moderately-sized interferometers can be constructed with high spectral resolution, increased spectral coverage and short integration times which are of great use in planetary applications.

ESO, IRTF and Kuiper Airborne Observatory: Like their predecessors, today's ground-based astronomers have the unenviable task of observing the heavens with clouds, atmospheric absorption and light pollution working against them. Clouds present an obvious hazard, but it is actually atmospheric "seeing", the rapid fluctuation of the visible disk due to passing cells of thermal air along the line-of-sight (the phenomena that makes stars twinkle), which prevents telescopes yielding the spatial detail they are theoretically capable. Carbon dioxide and water vapour in the Earth's atmosphere also limit the observations of ground-based infrared astronomers as only a few attenuation-free atmospheric windows exist which allow unhindered viewing. And finally, stray light from populated areas diminishes the contrast in faint-object observations.

To avoid these complications, remote elevations in dry climates are often sought to conduct the observations. Examples of which include the European Southern Observatory's (ESO) Cerro Paranal Very Large Telescope in Chile's Atacama desert and the Infrared Telescope Facility (IRTF) sitting atop the Hawai'ian islands in the middle of the Pacific. The recently retired Kuiper Airborne Observatory (KAO), a retrofited cargo plane modified to carry an infrared telescope, is another, if slightly different, example.

Despite the inherent difficulties, sophisticated technology and observing methods such as active and adaptive optics, segmented mirrors, the use of cryogenics and aperture-synthesis interferometry have advanced observing to levels comparable or better than that achieved with the Hubble Space Telescope (HST).

1.2.2 Space-Based Observations

The minimal-atmosphere conditions exploited by ESO, IRTF and KAO are taken to the extreme in the case of the HST (and the other Earth-orbiting observatories discussed here). Exploiting successes in rocketry and space technology, observatories based in space have opened up large, previously-unavailable segments of the electromagnetic spectrum to observation.

At the short end of the spectrum, the **International Ultraviolet Explorer** (IUE) was a regular observer of Jupiter prior to its retirement in 1996. Equipped with a 45-centimetre telescope[3] and two ultraviolet spectrographs (spanning 0.115 μm to 0.32 μm), IUE's observations of stratospheric abundance are useful when considering vertical transport, eddy diffusion and/or photochemistry.

---

[3] Shorthand reference to the diameter of the telescope aperture.

The **Hubble Space Telescope** was the first, and flagship, mission of NASA's Great Observatories program. Designed to complement the wavelength capabilities of the other spacecraft in the program, HST utilised a 2.4-metre telescope located in low-Earth orbit to perform observations from the near-ultraviolet through the near-infrared. However, the mission was troubled soon after launch in 1990 by the discovery that the primary mirror was spherically aberrated. While still able to conduct scientific investigations, HST was refurbished in 1993 with a self-contained corrective optics package in addition to a second-generation Wide-Field and Planetary Camera (WFPC2) which restored most of the originally-expected imaging performance. WFPC2 has since been used to observe Jupiter on numerous occasions. However, because of its limited spectral range (0.115 μm to 1.1 μm), the observations are mainly of benefit to ultraviolet auroral studies or cloud-feature tracking in the visible (*e.g.* the evolution of the Comet Shoemaker-Levy 9 – SL9, impacts in 1995).

During the second servicing mission in February 1997, the Near-Infrared Camera and Multi-Object Spectrometer (NICMOS) was installed onboard HST. NICMOS extended the spectral range of HST out to 2.5 μm and has since been used to complement the observations of Jupiter's rings, moons, and high-altitude clouds.

The European Space Agency's **Infrared Space Observatory** (ISO) was an astronomical satellite which operated in a highly-elliptical Earth orbit from November 1995 to May 1998. Like its predecessor the Infrared Astronomical Satellite, ISO was primarily manufactured to observe deep space, but also had the ability to observe solar system objects like Mars, certain bright comets and the Jovian planets.

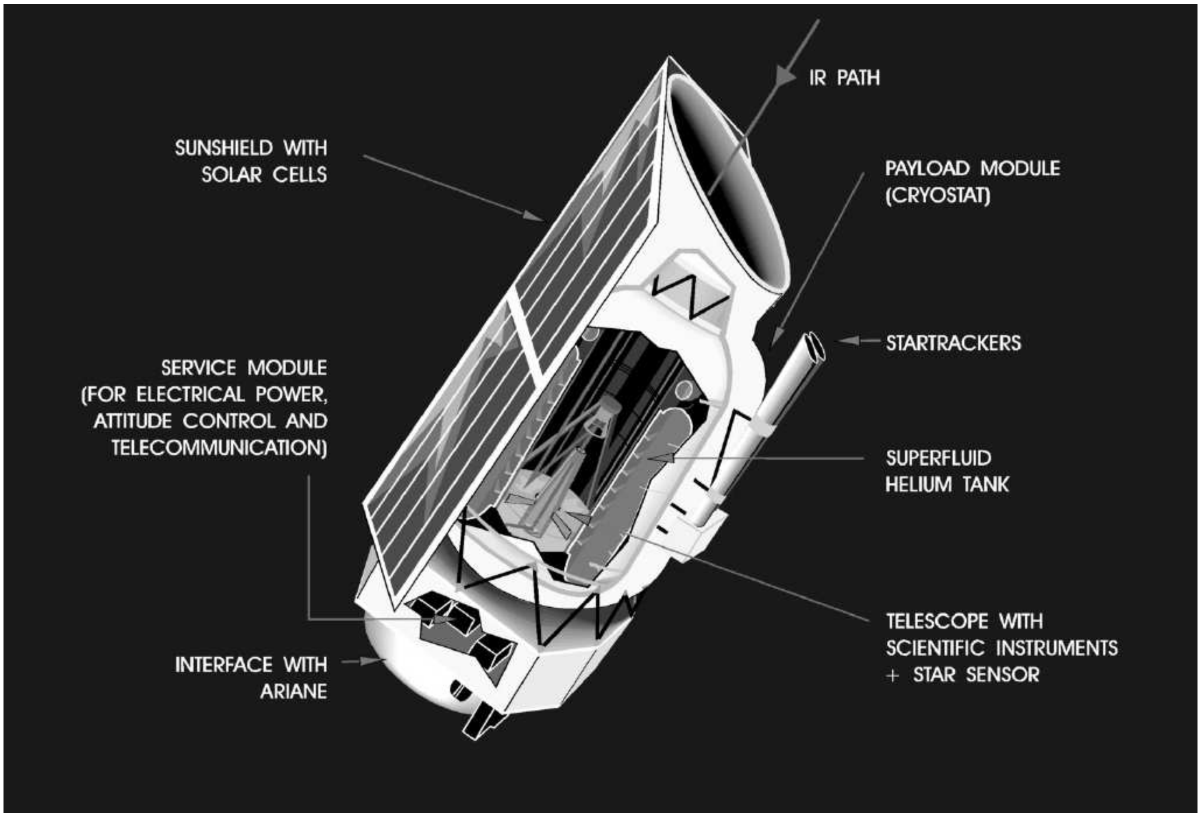

Figure 1.1: The ISO spacecraft. [ESA]

The ISO satellite ([101], Figure 1.1) consisted of a 60-cm helium-cooled telescope equipped with four focal-plane instruments: a camera, a photometer and both a short-wave and long-wave grating spectrometer. The two spectrometers covered the ranges 2.3-45 μm and 45-195 μm and had a mean resolving power approximately three times that, and equivalent to, the infrared spectrometer aboard Voyager, respectively.

In addition to discovering previously undetected hydrocarbons [65], ISO also made the unexpected detection of water in the Jovian upper-stratosphere where it was thought too cold to exist [56]. Water on Saturn might be expected due to possible sputtering of water from its ring system, but was not expected on the other giant planets. With the tropopause acting as a cold trap limiting transport from tropospheric levels, the observations suggest an external origin for the observed water [114].

Two major sources have been considered: an interplanetary source which could be either in the form of micrometeorite ice particles or larger objects like comets, or a local source which would include sputtering from rings and/or satellites. Considering the infrequency of SL9 impacts and the short lifetime of stratospheric water after such events, the interplanetary micrometeoritic source is favoured [58].

Submillimeter Wave Astronomy Satellite: The Submillimeter Wave Astronomy Satellite (SWAS), another Earth-orbiting observatory, was dedicated to the study of star and planet formation via the measurement of the chemical composition, energy balance and structure of interstellar clouds [132]. However, it was also used to observe both Jupiter and Saturn in September 1999.

SWAS consists of a 55 cm × 68 cm off-axis telescope with a pair of passively-cooled Schottky-diode receivers. During its three-year mission, SWAS observed the ground state or low-lying transitions of five astrophysically-important species. For the observations of Jupiter and Saturn, only the two bands centered at 489 GHz (O_2) and 553 GHz (H_2O) were used. Spectrally resolved water emission was detected for both planets, with the amount of water implied by the data up to 2.5 times larger than that inferred from ISO data [21]. For Jupiter, the data further showed that the water is not uniformly mixed, but increases with altitude above a second condensation level ($\sim$ 10 mbars) in the stratosphere [21, 58]. The authors were however unable to prove the large influx of water indicated real variability since the result could equally stem from an increase of small cometary impacts, as suggested by ISO investigations.

1.2.3 Interplanetary Spacecraft

Pioneers 10 and 11: The first spacecraft to reach (and subsequently fly-by) Jupiter were Pioneer 10 and 11 (in 1973 and 1974 respectively). These NASA spacecraft, though built to study the electromagnetic fields and charged particles of interstellar space, did have a small suite of imaging systems aboard. Both the Pioneer spacecraft were equipped with infrared radiometers (14 μm to 56 μm, 715-180 cm^{-1}), which, like the accompanying imaging photopolarimeter, were scanned across the planet by the spin of the spacecraft.

Radio occultation experiments and inversion of the measured radiance provided the first accurate determinations of temperature and composition at stratospheric levels. While the temperatures of the belts were found to be greater than those of the zones (at 0.3 bar) by as much as 3.5 K, the derived bolometric temperature (125 K) implied a value of 1.9 ± 0.2 for the ratio of thermal emission to solar energy absorbed [93].

Voyagers 1 and 2: The Voyager missions also comprised a pair of fly-bys (both in 1979) but were more advanced than the Pioneer spacecraft. The NASA-built twin Voyagers had a 3-axis stabilized orientation and contained sophisticated cameras, on-board computers and ten dedicated instruments including the Infrared Interferometer Spectrometer (IRIS, [84]). The IRIS instrument, operating in the near to mid-IR (2.5 to 50 μm, 4000 to 200 cm^{-1}) not only had much greater spatial resolution than the Pioneer instruments, but also had sufficiently-high spectral resolution (4.3 cm^{-1}, apodised) to detect many of the significant absorption features in the Jovian atmosphere.

Vertical temperature profiles were obtained via radio occultation measurements and inversion of the IRIS spectra. The lapse rate was determined to be approximately adiabatic at pressures greater than 0.3 bar, but substantial spatial variation in the temperature profiles was found within both the tropopause and in the stratosphere [83, 120]. Aside from the anticipated H_2, He, CH_4 and NH_3 composition, the Voyager spectra also showed clear evidence of C_2H_2, C_2H_4, C_2H_6, CH_3D, GH_4, H_2O and PH_3 [81, 82].

Galileo: The Pioneer and Voyager observations however initiated more questions than they were capable of answering and two more spacecraft devoted solely to the investigation of the Jovian system were sent: the Galileo orbiter and its atmospheric probe. The mission blueprint [205] called for the probe to parachute through Jupiter's atmosphere measuring temperature, pressure, cloud structure and composition, while the orbiter's nominal two-year mission allowed for time-integrated studies of the Jovian system. Although destroyed by the increasing temperatures and pressures, the probe mission was to prove extremely useful both because it was the first *in situ* sampling of a giant planet atmosphere and because it could sound depths unobservable to remote sensing.

The Galileo orbiter (Figure 1.2) was a "dual-spin" design combining the spinning-spacecraft features of the Pioneers necessary for fields and particles investigations and the three-axis stabilized spacecraft of the Voyagers optimal for remote sensing experiments. After long delays, Galileo was launched on the Space Shuttle Atlantis in October 1989.

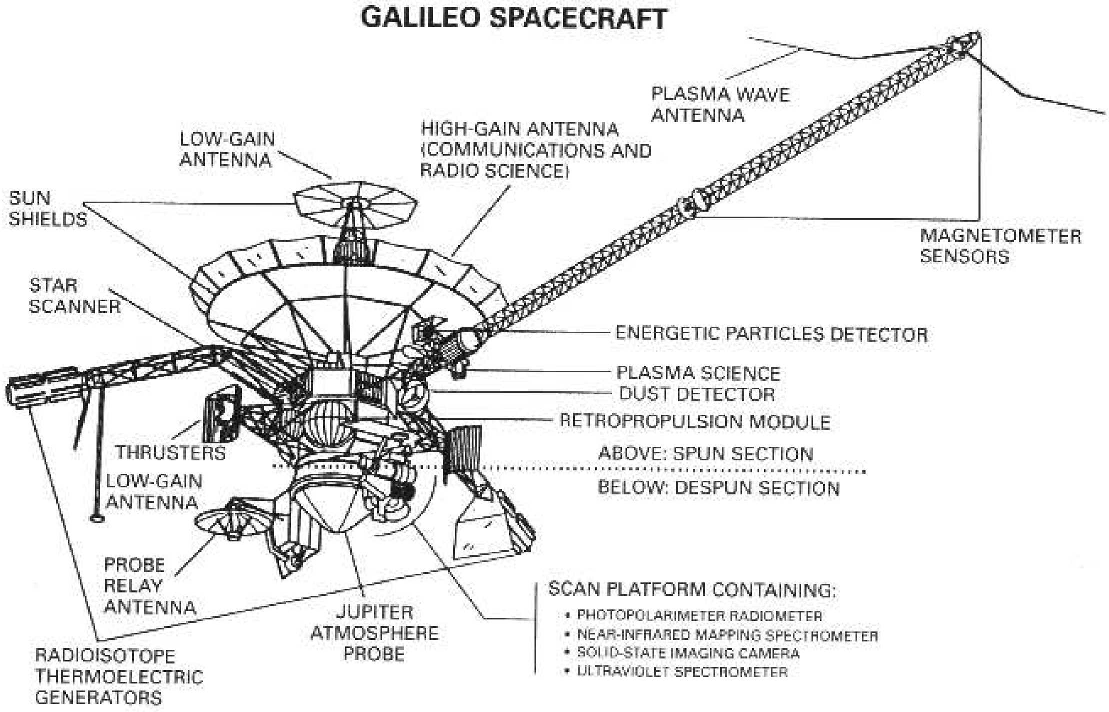

Figure 1.2: The Galileo spacecraft. [NASA]

Due to the Challenger Space Shuttle incident, a policy change[4] within NASA meant that Galileo was unable to launch directly to Jupiter and instead required gravitational boosts from both Venus and Earth. This in turn required modifications and additional heat shielding to be added to the spacecraft. The delay, coupled with the extra handling, has been suggested as the cause of the loss of lubricant that subsequently prevented the high-gain antenna from unfurling properly. The loss of the high-gain antenna threatened the ability of the orbiter to complete its mission. Mission managers were consequently forced to use the low-gain antenna only, drastically limiting the ability to return data

---

[4] The United States did not have a rocket that could launch Galileo and its probe directly to Jupiter after the retirement of the Saturn family of rockets. Hence, instead of opting to de-mate the orbiter and probe and have each launch separately, NASA elected to launch Galileo from the Space Shuttle with an upgraded Centaur Inertial Upper-Stage (IUS) booster. Four months prior to the launch of Galileo, the Space Shuttle Challenger exploded on takeoff. The resulting inquiry board deemed the Centaur IUS with its highly-explosive liquid-hydrogen fuel too risky for use on humanned space missions.

from Jupiter (10 bits/s instead of the anticipated 130,000+ bits/s). Innovative data compression techniques, improved sensitivity of the receiving stations and use of the onboard tape recorder have diminished the severity of the communications failure raising the bitrate to 100 bits/s. Despite the setback, the nominal orbiter mission was so successful that it has since been extended twice. The mission was still in operation, if slightly handicapped, when the Cassini-Huygens flew by the planet in December 2000.

The Galileo probe was released from the orbiter in July 1995 and entered the atmosphere five months later at 6.5° north latitude and 0.9° west longitude [147]. Both ground-based observations and the experiments aboard the probe showed that the entry site was a so-called 5-μm "hot-spot": an almost cloud-free region, characterised by enhanced thermal emission from the planet's interior, and assumed to be an area of atmospheric downwelling. The hot-spot's cloud-free nature was revealed by the probe's nephelometer experiment which detected evidence of clouds *circa* 0.5 and 1.5 bars only, omitting the proposed water cloud between 5 and 8 bars [158]. This result was further supported by the derived temperature structure which was shown to be approximately 3 K warmer than the dry adiabat at pressures less than 0.6 bar [172]. In terms of composition, the heavy elements (C, N, S, Ar, Kr and Xe) were determined by the Galileo probe mass spectrometer (GPMS) [136] to be two to four times the relative abundance, compared to hydrogen, found in the Sun. And while CH_4 was found to have a constant mixing ratio, the condensible volatiles (NH_3, H_2S, H_2O) were found to be depleted [135] – a likely consequence of the characteristic downwelling.

The Galileo orbiter [91] carried four instruments of relevance to atmospheric dynamics, which together span from the ultraviolet to the far-IR. Of the optical instruments, the Near-Infrared Mapping Spectrometer (NIMS) was responsible for determining the temperature and composition of the satellite surfaces, rings and atmosphere of Jupiter. The NIMS instrument [41] employed a dual-blazed diffraction grating which obtained infrared spectra from 0.7 to 5.2 μm at a resolution of 0.0125 μm below 1 μm, and 0.025 μm above. The NIMS instrument complemented the GPMS composition studies by examining the composition in the upper troposphere. The NIMS observations of the probe entry site confirmed the depletion of NH_3 and H_2O between 8 bars and 1 bar [40, 167] while separate observations of Jupiter suggest the existence of both ammonia ice [11] and deep water cloud in localised regions [13, 74, 141].

After fourteen years of service, including six years of interplanetary cruise, the Galileo orbiter was “retired” and sentenced to the same fate as its atmospheric probe. In light of sub-surface oceans on Europa and Callisto [102] and the possibility of life on Europa [171], the decision was made to insure that the Galileo orbiter was unable to bias/biologically-contaminate future-mission findings[5] by vapourizing it in Jupiter’s atmosphere. On 21 September 2003, Galileo entered the Jovian atmosphere at approximately 50 km/s a quarter of a degree south of the Equator on the nightside of the planet [69], ending a mission spanning a quarter-century.

---

[5] Since Galileo was never specifically designed to search for life, it was not subjected to the same, rigorous sterilization procedures mandated for planetary landers.

1.3 Atmospheric Structure

Jupiter is quite unlike the rocky, terrestrial worlds of the inner Solar System. Analogous to the Sun in construction and composition, Jupiter's structure can be divided into two distinct regions, one which is dependent upon modelling and indirect determinations and another which can observed directly. Using the observational clues available (*e.g.* Jupiter's thermal emission, its high oblateness and orbital anomalies in its moons), researchers have derived models for Jupiter's interior structure which all agree in the same macro-features (working from innermost layer outward):

- *A core made of rocks and metals:* A mere tenth of the planetary radius, the core is thought to be composed of rocks and metals that slowly sank towards the planet's centre over its evolutionary period [88]. Utilising available gravitational and magnetic field data, theoretical models estimate a 50 to 100 megabars, 15,000 to 23,000 K core environment. Jupiter's high oblateness (0.065) and low moment of inertia (0.264) suggest a significant concentration of mass at the center of the planet with the models indicating a wide range of core masses (five to fifteen $M_\oplus$ [127]). These studies also show that Jupiter's core is three times heavier than would be expected were the elements present in solar abundance [79].

- *A mantle of metallic hydrogen:* The mantle comprises the bulk of Jupiter, occupying approximately three-quarters of the planetary radius. While the lower boundary of the mantle is not well characterised, the nature of the upper boundary has been recently tested in the laboratory. Via the use of gas-guns, lasers and/or diamond-anvil-cell experiments, the upper boundary has been shown to involve the transition from molecular hydrogen to an electron-degenerate state of pressure-ionised protons and electrons called “metallic hydrogen”. Such a phase transition is thought [134] to be continuous and take place at megabar pressures ($\sim$ 7,000 km depth) where the temperatures are in excess of 3,000 K.

While helium is theorised to exist in a similar metallic state [90], it is the convective motion of electrically-conducting hydrogen within the mantle that is thought to play a major role in the planet’s strong magnetic field (approximately twelve times the terrestrial magnetic field strength) [189].

- *A deep atmosphere/ocean of molecular hydrogen:* This envelope extends from the mantle to the “surface” at one bar. Although the gross construction of this region is unknown (despite the Galileo probe sounding the first 24 bars), opacity studies predict the presence of a thin radiative region between 1.5 and 6.0 kbars. If true, that would place it immediately above the critical point ($\sim$ 10 kbars, 1,000 to 2,000 K) at which the hydrogen transitions from molecular to metallic [80]. Otherwise, the temperature structure is modelled to be adiabatic with convection the prevailing transport mechanism. Equally, the composition is thought to be akin to Jupiter’s visible atmosphere in that it is well mixed with condensation and chemical reactions playing an increased role in any vertical and horizontal variation [79].

- *Observable atmosphere:* Although very thin ($>$ 1% of the planetary radius) in comparison to the gross features below, knowledge about Jupiter’s observable atmosphere was greatly advanced by the determination of the temperature profile. Consequently, Jupiter’s observable atmosphere may be divided into distinct regions (analogous to the divisions given to Earth's atmosphere) described by the various characteristics therein – a stylised diagram of which can be found in Figure 1.3.

- *Sub-Tropopause/Troposphere:* The tropopause is defined as the atmospheric level at which the lapse rate falls to zero. For Jupiter, the tropopause is located *circa* 0.1 bar with an approximate temperature of 115 K.

  In the troposphere proper, at pressures greater than 0.6 bar, the temperature profile closely follows the dry adiabat, implying active convection. In the upper troposphere ($0.1 < p < 0.6$ bar), radiative processes start to become more important and the atmosphere appears to be stably stratified (although occasional convective events may penetrate from below). It is here that the cloud systems visible from Earth are located (see §1.3.3).
- *Stratosphere:* The temperature steadily rises within this region ($p < 0.1$ bar) due to the UV absorption by hydrocarbons [203]. The atmosphere is strongly stratified with typical temperatures ranging from 110 to 180 K.
- *Mesosphere:* The mesosphere (1 to 10^{-3} mbars) is notoriously difficult to observe directly and is consequently modelled to be approximately isothermal ($\sim$ 200 K) in nature. Much of the information about the mesosphere comes from stellar occultations with σ Arietis [16] and β Scorpii [89, 195, 198].

1.3.1 Temperature

The global heat balance of Jupiter is determined by the amount of heating (both internal and solar) and radiative cooling that takes place in its atmosphere. The tropopause

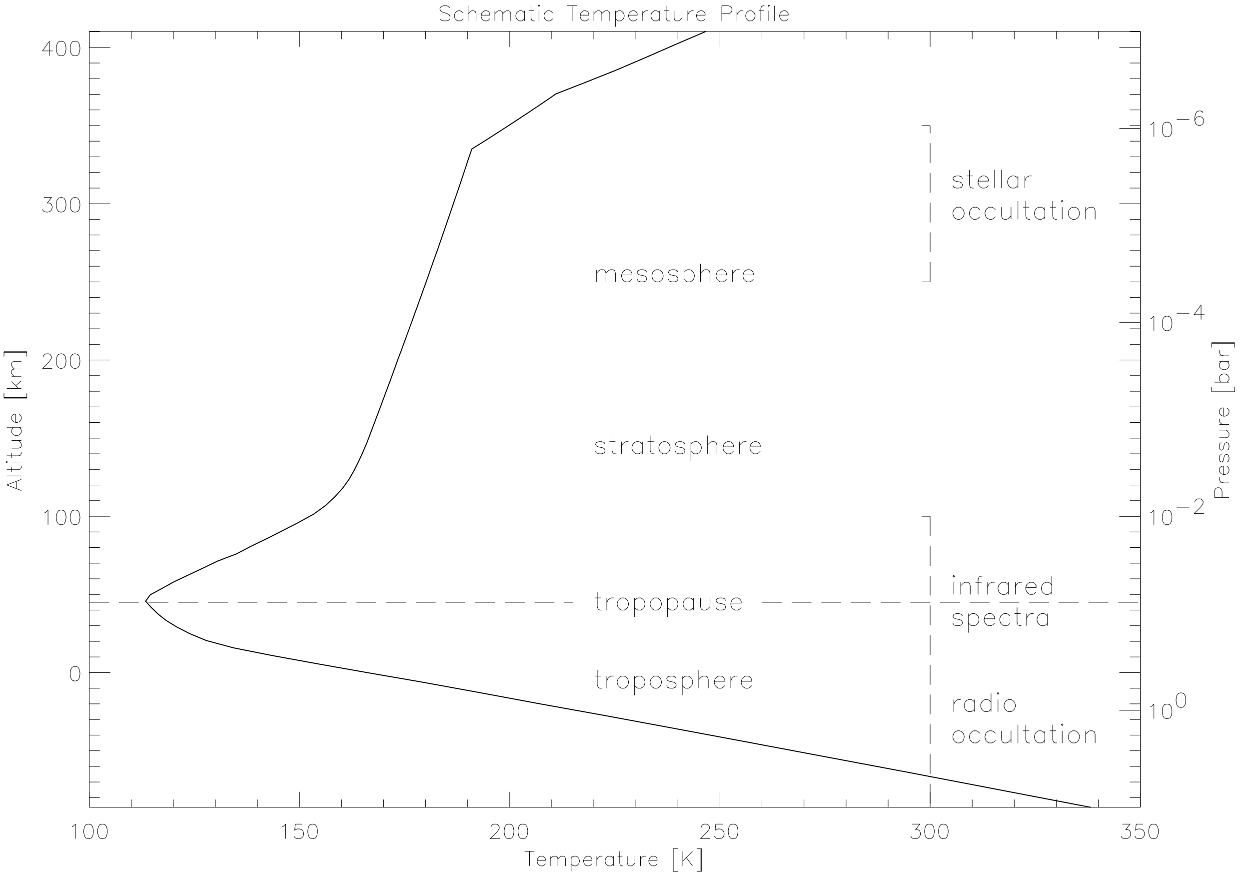

Figure 1.3: Jupiter's thermal structure: stylised representation of the upper-atmosphere from stellar and radio occultation experiments, inversion of Voyager/IRIS spectra and Galileo probe data.

roughly defines the division between these two influences. Below the tropopause, convection is the main means by which heat is vertically transported and the temperature profile is to all intents and purposes adiabatic. The deep interior of Jupiter is then barotropically stratified, where surfaces of constant temperature are co-incident with surfaces of constant pressure. Above the tropopause, the atmosphere ceases to be optically thick and radiation is responsible for energy transfer; the observed temperature depending on the altitude at which the radiation is absorbed.

The upper regions of Jupiter's atmosphere were first explored when observers realized that the manner in which light from a background star is refracted as it is occulted by a planet reveals characteristic properties about the atmosphere through which the light passed. At visible wavelengths and longer, the deviation of starlight is caused by differential refraction of the light by atmospheric molecules. Since the extent of refraction at any height depends on the local density, observers were able to measure the density of the gases along the line of sight by careful monitoring of the star's intensity as it is occulted. It was then possible to deduce the particle density as a function of altitude, and, by assuming a mean molecular density, the pressure and temperature profiles.

The same principle can be applied to the spacecraft's radio signal. Consequently, all of the Pioneer and Voyager fly-by trajectories were selected to take maximum advantage of the refraction effect. The radio-occultation experiment was carried out on all four spacecraft with the flight paths selected so that ingress and egress profiles were obtained for each spacecraft. The Voyager experiment [120] proved more advantageous than that of Pioneer [107] because Voyager could transmit at two different frequencies instead of just one. The atmospheric profiles from the two frequencies complemented each other since the degree of refraction is different for dissimilar frequencies, with the stronger of the two signals allowing a deeper sounding of the atmosphere.

The upper-tropospheric temperatures obtained via radio occultation were supplemented with stratospheric temperatures provided by infrared spectrometers aboard both Voyager spacecraft. The definitive temperature-pressure profile was obtained some years later by experiments aboard the Galileo probe. The Atmospheric Structure Instrument (ASI) established that the temperatures between 0.41 and 15 bars follow the dry adiabat and provided confirmation of the approximately isothermal nature of the stratosphere and mesosphere (160 ± 20 K and 200 ± 50 K, respectively).

While the temperature structure resembles that in Figure 1.3 (notably in the troposphere where the lapse rate is approximately adiabatic and zonally constant for pressures greater than 0.3 bar), substantial spatial variation in the measured profiles were observed by Voyager at stratospheric levels [83, 120]. For example, the temperature at the tropopause ($\sim$ 0.14 bar) was found to range from 100 to 115 K across the disc of the planet and is warmest and deepest at 15°S and cooler and higher at high latitudes.

The belt-zone spatial structure observed in visual imaging is also apparent in the infrared with relatively cold regions ($\sim$ 2 K at 0.5 bar) corresponding to the visually-bright zones and warmer temperatures in association with the visually-dark equatorial belts [83, 151]. The warmest tropospheric temperatures found by Voyager/IRIS were centred at 15°S and 15°N, regions associated with the equatorial belts. The coolest regions lie at the Equator and between 20°and 35°north and south, all of which are associated with the zones. Quite notably, the upper troposphere and the lower stratosphere above the Great Red Spot (GRS) are colder than any of the surrounding regions. Figure 1.4 presents example temperature profiles retrieved from Cassini/CIRS observations.

Ground-based observations have shown that the spatial organisation and time dependence of Jupiter's stratospheric temperatures exhibit seasonal forcing with a period of approximately four to five years [148]. Such behaviour is analogous to the Earth's

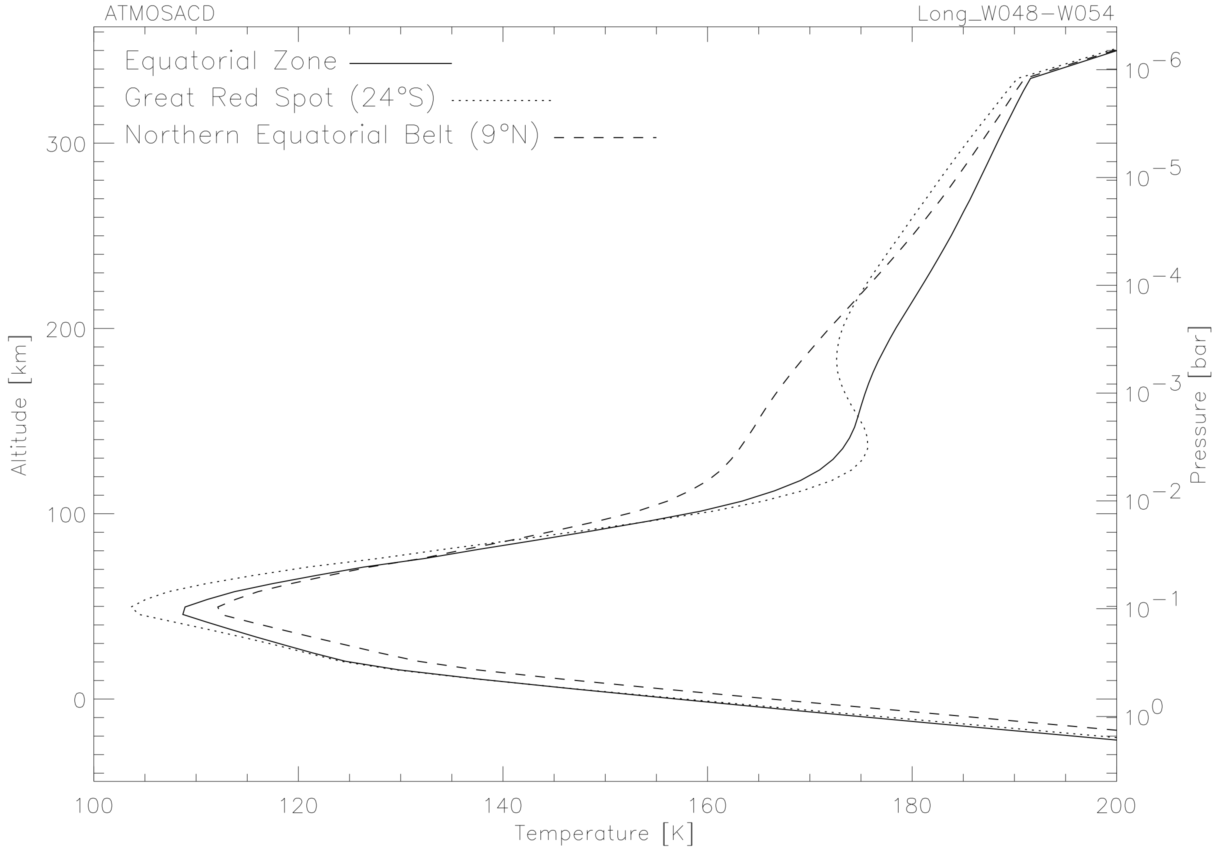

Figure 1.4: Mean temperature difference for the Equatorial Zone, GRS and NEB obtained by inversion of Cassini/CIRS infrared spectra. The local maximum at 3 to 10 mbars is likely the result of absorption of solar radiation by dust or aerosol [203]. ATMOSACD spectra – see §2.4; 48° - 54° west longitude.

quasi-biennial oscillation (except, in Jupiter's case, it is a quasi-quadrennial oscillation – QQO). In either oscillation, the meridional-mean temperature structure is modulated by the seasonal onset of vertically propagating waves. Detailed simulation of the QQO [67] has determined that the brightness-temperature patterns are driven by small-scale, short-period gravity waves. The amplitude of the QQO predicted by these simulations is large, suggesting that the QQO may have a significant effect on Jupiter's stratospheric thermal structure. Such an effect may be apparent in the vertical temperature profiles measured by the Galileo probe and/or Voyager radio-occultation experiments.

1.3.2 Composition

The Jovian planets occupy a unique place within the Solar System as regards composition. Had Jupiter been 50 to 100 times more massive, there would have been significant enough pressure within its core to fuse hydrogen together, thereby starting the internal thermonuclear process which supports the Sun [55]. However, because the interior of Jupiter did not ignite, it remains nearly primordial in composition.

Since the pioneering work of Wildt in the 1930s and Kuiper in the 1940s, the presence of methane and ammonia in Jupiter's atmosphere has been known. Hydrogen and helium were presumed to exist given Jupiter's surprisingly low bulk-density. With the technological improvements of spectroscopic instrumentation, the number of known species has greatly increased (see Table 1.2). The following molecules have been detected:

- Molecular hydrogen (H_2), was only detected in the mid-twentieth century [103] and makes up nearly ninety percent of all the planet's molecules. Hydrogen is assumed to be uniformly mixed throughout the atmosphere.

- Helium (He): Helium's abundance was successfully, if indirectly, determined via its collisionally-induced absorption with hydrogen by instruments aboard both Pioneer and Voyager [156]. Later, two Galileo probe instruments (the GPMS and the Helium Abundance Detector [199]) independently provided the first *in situ* measurements. He was found to be uniformly distributed throughout the atmosphere, if slightly depleted relative to solar abundances. The depletion is tentatively pegged to the fractionation of helium from metallic hydrogen at the 1 to 3 Mbars level, followed by "rain-out" of the helium droplets towards the core of the planet.

	Species	**Abundance (mixing ratio)**	**Note**
Major species	H_2	1.0	a
	He	0.157 ± 0.0036	
Condensible gases	CH_4	$(2.1 \pm 0.4) \times 10^{-3}$	
	NH_3	$(0.2 - 1) \times 10^{-5}$ (0.5 - 2 bar, hot-spot) $(3.3 \pm 1.5) \times 10^{-4}$ (4 bar, hot-spot) $(8.1 \pm 1.2) \times 10^{-4}$ (8 bar, hot-spot) $(7.1 \pm 3.2) \times 10^{-4}$ (9 - 12 bar, hot-spot)	
	H_2O	$(2 - 20) \times 10^{-9}$ (upper-stratosphere) $\leq 10^{-6}$ ($\leq$ 4 bar, hot-spot) $(5.6 \pm 2.5) \times 10^{-5}$ (12 bar, hot-spot) $(6.0^{+3.9}_{-2.8}) \times 10^{-4}$ (19 bar, hot-spot)	
	H_2S	$< 2 \times 10^{-8}$ ($<$ 0.7 bar) $< 1 \times 10^{-7}$ ($\leq$ 4 bar, hot-spot) 7.0×10^{-6} (8.7 bar, hot-spot) $(7.7 \pm 0.5) \times 10^{-5}$ (16 bar, hot-spot)	
Noble gases	Ne	$(1.2 \pm 0.1) \times 10^{-5}$	
	Ar	$(9 \pm 2) \times 10^{-6}$	
	Kr	$(4.3 \pm 0.8) \times 10^{-9}$	
	Xe	$(4.4 \pm 0.8) \times 10^{-10}$	
Photochemical species	CH_3	Detection (north polar region)	b
	CH_3D	$(1.3 - 2.3) \times 10^{-7}$	c
	$^{13}CH_4$	$(2.2 \pm 0.4) \times 10^{-5}$	d
	C_2H_2	$(3 - 10) \times 10^{-8}$ (stratosphere)	
	C_2H_4	$(7 \pm 3) \times 10^{-9}$ (north polar region)	
	C_2H_6	$(1 - 5) \times 10^{-6}$	
	CH_3C_2H	$(2.5^{+2}_{-1}) \times 10^{9}$ (north polar region) Detection (mid-latitudes)	
	C_3H_8	Detection	e
	C_4H_2	Detection (polar regions)	f
	C_6H_6	$(2^{+2}_{-1}) \times 10^{-9}$ (north polar region) Detection (mid-latitudes)	
Non-equilibrium species	PH_3	6×10^{-7} ($>$ 1 bar)	
	HCN	$(0.9 - 3.6) \times 10^{-9}$ (upper troposphere)	g
	GH_4	$(7 \pm 2) \times 10^{-10}$	
	AsH_3	$(2.2 \pm 1.1) \times 10^{-10}$	
	CO	1.6×10^{-9}	
	CO_2	3.0×10^{-10} ($<$ 10 mbars)	h

Table 1.2: Atmospheric composition of Jupiter (compiled from [9] and the references therein). a: the mixing ratios are given relative to H_2, where the mole fraction of H is 0.864 ± 0.006. b: [109]; c: [114]; d: based on the $^{13}C/^{12}C$ isotopic ratio 0.0108 ± 0.0005 [135]; e: [135]; f: [23]; g: reported by [193] but called into question by [24]; h: [56].

- Methane (CH_4) comprises just 0.2% of all molecules within Jupiter's atmosphere. As the Jovian temperatures are too warm for CH_4 to condense [202], it has a constant tropospheric mixing ratio [135]. In the stratosphere however, methane undergoes a series of photochemical reactions which produce intermediate hydrocarbons like acetylene and ethane [163]

- Ammonia (NH_3) is the next most abundant molecule, but only at one bar or deeper, as it is predicted [118] to condense out into the white clouds seen in the visible. Above the condensation level, gaseous ammonia is expected to be sub-saturated to various degrees depending on the upwelling/downwelling rates. As NH_3 has been observed in smaller quantities in the belts than the zones [48, 112], the observations are consistent with the canonical view that the belts are regions of sinking, desiccated air and the zones are regions of upwelling, regularly associated with convective clouds. The Galileo probe further confused the issue, reporting a subsolar NH_3 abundance [10] despite earlier studies [120, 129] which showed supersolar enrichment.

  The existence of ammonia clouds within Jupiter's visible atmosphere has been modelled using thermochemical considerations [202, 203] and it is thought to condense around 0.6 bar ($\sim$ 150 K). Yet, despite decades of observation, the spectral signature of ammonia ice was only recently reported [11, 34, 204]. For an extended discussion of ammonia ice clouds, see §1.3.3.

- Water (H_2O), although thought to be much more abundant at depth, is apparently less abundant than ammonia within the observable atmosphere and is only observed in a couple of atmospheric windows. These windows (especially at 5 μm) are important because hydrogen, methane, and ammonia are all very weak absorbers at this wavelength thereby allowing researchers to see unusually deep into the atmosphere. Like NH_3, water's low abundance is attributed to it condensing into clouds at the five bar level. Although undetected originally, re-analysis of both Voyager/IRIS [179] and Galileo/NIMS [13, 97, 141] data have inferred the presence of water ice on Jupiter – see §1.3.3 for details.

The GPMS found a lower H_2O mixing ratio than anticipated [135], but this was explained by the probe entering an atmospheric hot-spot where condensible volatiles such as H_2O are depleted. There was also no sign of a dense water cloud or corresponding vapour, which although expected, is in agreement with hot-spots being relatively cloud-free regions. Gaseous H_2O was however found by the Infrared Space Observatory; not where one would expect it in the upper troposphere but in the stratosphere [55]. The authors of the ISO study explained the surplus H_2O as the result of in-falling meteoritic material.

- Hydrogen sulphide (H_2S), yet to be detected via remote-sensing, is thought to be present below Jupiter's obscuring clouds. The lack of remote-detection is attributed to H_2S being a significant contributor to the formation of NH_4SH clouds at 1.5 bars. Unlike H_2O however, H_2S was essentially undetectable by the Galileo probe at pressures less than 8 bars [135]. At further depth, the mixing ratio gradually rose from 0.23 times solar to 2.5 times solar at 16 bars.

- The abundance of the noble gases (argon (Ar), krypton (Kr), neon (Ne) and xeon

(Xe)) were determined by the GPMS to be consistent with solar values within an order of magnitude [135]. While Ar, Kr and Xe are all enriched with respect to solar values, Ne is significantly subsolar which is believed to result from its removal by liquid helium (if Ne is dissolved within He as proposed, it is carried with the "raindrops" into the planetary interior [168]).

- Carbon monoxide (CO) and carbon dioxide (CO_2): The observations of CO and CO_2 are surprising as they are oxidized-compounds, inherently unstable in a reducing atmosphere. The presence of CO and CO_2 at observable levels is explained by either convective transport from the deep atmosphere [57] or external delivery of oxygen in the form of micrometeoroids, subkilometre-sized comets and/or material ejected from the icy satellites [58]. Although these two sources lead to very different vertical profiles, evidence has been found in support of both sources in the case of CO [25].

- Arsine (AsH_3), germane (GH_4) and phosphine (PH_3) have been detected in proportions similar to those which are predicted from cosmic abundances [9]. However, Jovian photochemistry suggest these species should not be present in the observable atmosphere. Their presence is thought [156] to be due to updrafts from much deeper levels, however there has not yet been a definite sign of variations in their abundances between the belts and zones.

- Hydrogen cyanide (HCN)'s existence on Jupiter is uncertain. Although detected by [193], a more recent study [24] has called this result into question. Despite being a non-equilibrium species, HCN is thought [156] to be one of the main products of hydrocarbon/ammonia photochemistry lending credence to its observation. Furthermore, models of the coupled photochemistry of NH_3 and hydrocarbons in the lower stratosphere find that HCN should be produced in abundances within detectable limits ($\sim 2 \times 10^{-9}$) [100].

- Although much of the analysis has concentrated on the polar regions [53, 104], acetylene (C_2H_2), ethylene (C_2H_4) and ethane (C_2H_6) have all been detected in the stratosphere at all latitudes [65, 170]. Recent research also suggests a substantial abundance of C_2H_2 in the upper-troposphere [22, 140]. Photolysis of methane leads to the formation of these hydrocarbon products. C_2H_2 and C_2H_6, with their long lifetimes due to no significant chemical losses [75, 133], are transported by eddy mixing down into the deep atmosphere where they undergo pyrolysis back to CH_4.

- Methyl (CH_3), methylacetylene (C_3H_4), propane (C_3H_8) and diacetylene (C_4H_2) are all formed by methane photodissociation near the homopause [75] and are involved in the photochemical recycling of methane via C_2H_2 and C_2H_6. Methylacetylene has also been detected at mid-latitudes [65] and is assumed to be in photochemical equilibrium. CH_3, in contrast, is a short-lived species with a rapidly-decreasing abundance downwards due to chemical losses [23]. While C_4H_2 has been previously detected on Saturn [47] and is an important sink for C_2H_2, the detection on Jupiter [109] revealed little more than its existence. Similarly, the detection of propane [135] is marginal having been somewhat discredited by the outgassing of terrestrial CO_2 from the Galileo probe mass spectrometer.

- Benzene (C_6H_6) is the heaviest hydrocarbon ever identified in the giant planets [23, 104] and may prove to be an important component or precursor of the stratospheric hazes present. However, many of the chemical pathways leading to benzene at low temperatures and pressures are poorly constrained and have yet to be fully integrated into the detailed photochemical models.

Non-equilibrium Species: a non-equilibrium species is one in which the assumption of a thermochemical and dynamic steady state is invalid. Non-equilibrium occurs when there is a change of state, a gradient in the thermodynamic variables and/or a significant dependence of the system on its history. In the Jovian atmosphere, non-equilibrium may occur as the result of advection (the net exchange of material of the system with its surroundings), an irreversible chemical reaction and/or advection. Species may either be depleted or enriched because of non-equilibrium processes.

For example, the abundances of AsH_3, CO, GH_4, HCN and PH_3 are higher than would be expected within the upper-troposphere if the atmosphere was in thermochemical equilibrium. Thus, their detection is indicative of advection and their measurement an important diagnostic tool in understanding the circulation of giant-planet atmospheres.

1.3.3 Clouds and Haze

From the ultraviolet to the infrared, Jupiter's appearance is dominated by contrasts produced by the clouds and haze. Early investigators used thermochemical considerations to infer the existence of molecular ices in Jupiter's atmosphere. These investigations, aided by the new information gained from the Pioneer and Voyager fly-bys [203], predicted a multilayer cloud system (Figure 1.5). The uppermost layer (0.6 bar, 150 K), that of the

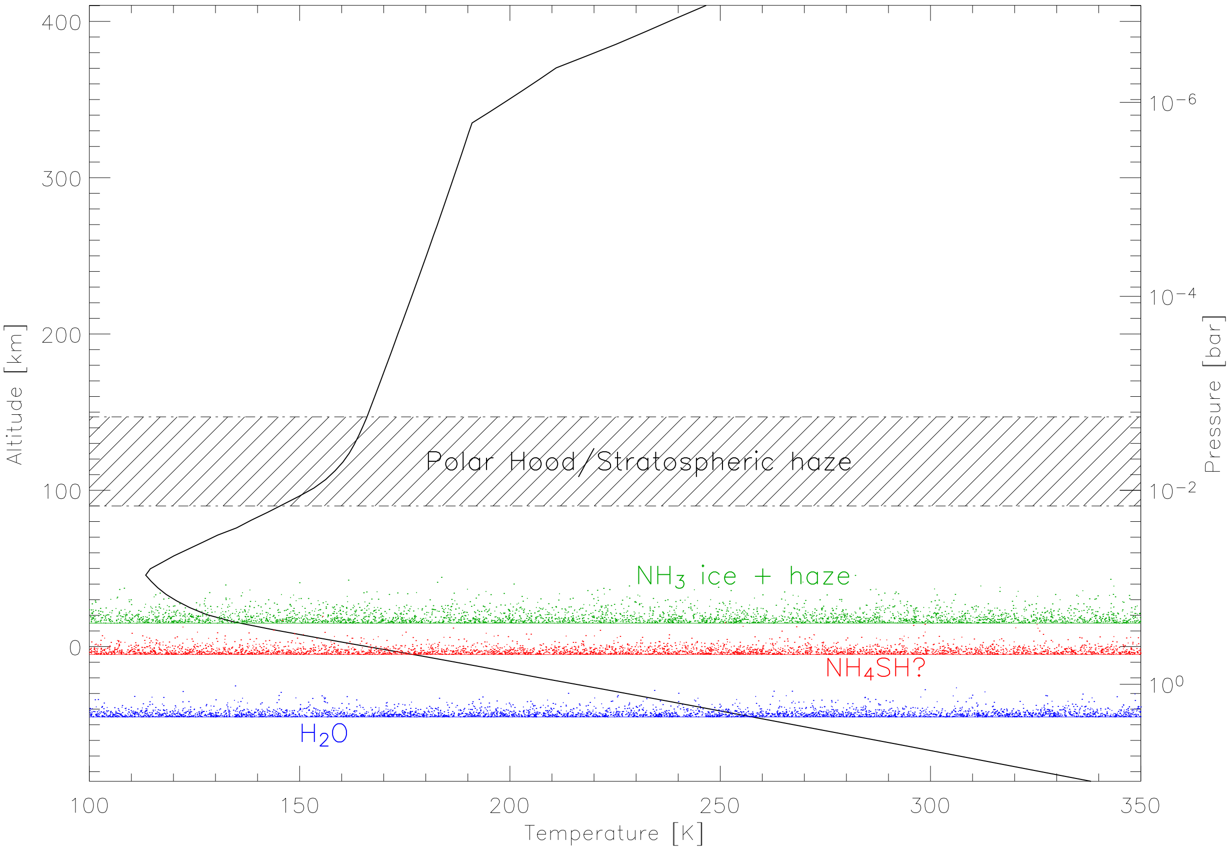

Figure 1.5: Conjectured Jovian cloud structure: cloud layers *versus* height (the temperature profile is the same stylised representation presented in Figure 1.3). Jupiter's visible cloud structure is dominated by hazes within the upper troposphere/lower stratosphere and by condensate clouds of ammonia, ammonium hydrosulfide and water at deeper levels [178]. The stratospheric aerosols are almost uniformly distributed in latitude except for increased concentration in the polar regions between 1 and 20 millibars. In addition to increased optical thickness at high latitudes, the polar aerosols have been determined to be significantly different from those found at other latitudes and are thought [159] to result from a different haze-production mechanism, possibly linked to the aurora. (After Irwin 2003: [96])

visible clouds, is thought to be ammonia ice and haze [118]. Ammonium-hydrosulphide (NH_4SH – the result of the reaction between NH_3 and H_2S) is then thought to exist at a level of approximately two bars (210 K) [118]. Water ice is anticipated still deeper, at a pressure of nearly five bars (270 K) [202].

As the spectral features of ices can be difficult to distinguish from their gaseous counterparts, detection of the three proposed cloud layers remained elusive until the

Galileo probe provided the first *in situ* measurements. The Nephelometer Experiment detected evidence of clouds between 0.46-0.55 bar and 0.76-1.34 bar only [158]. A third, weak structure was observed between 1.9 and 4.5 bar which may have been the water cloud, but it remains to be identified. While providing no indication of either NH_4SH or H_2O ice, small (no bigger than 0.75 μm radius) NH_3 particulates of 1 to 2 optical depths (at 0.5 μm) were observed above 0.5 bar by the Net Flux Radiometer [187]. Although in general agreement with the proposed cloud structure, the clouds observed were found to be lower in altitude than expected and very tenuous. Due to the uncharacteristically low abundance of volatiles, it is presumed the unrepresentative 5-μm hot-spot into which the probe descended played a significant role in the absence of observed clouds.

The disagreement doesn't stop there however, as results from Galileo/NIMS also reveal a cloud structure seemingly inconsistent with expectations. While three main reflecting cloud layers (NH_3 haze, NH_4SH and H_2O) were required to simultaneously fit all parts of the IR spectrum [98], the main cloud deck was found to be deeper (1 to 2 bars *versus* 0.7 bar) and more vertically extended than originally thought [13, 99, 165]. Given that it is too warm for pure ammonia ice at one bar, either NH_4SH or NH_3 contaminated with photochemically-produced haze is thought responsible for the albedo contrast observed at these wavelengths [141, 188].

An intercomparison of the cloud structures determined by Voyager/IRIS, Galileo/NIMS and ISO/Short-Wave Spectrometer (SWS) via an analysis of 5-μm spectra revealed a small but significant slope in the IRIS measurements in comparison to the other two [166]. The slope suggests either Jupiter had changed significantly in the intervening years, or a calibration problem exists in the IRIS data-set. Given that instrumental differences were noted between Voyager 1 and 2 data [81], the latter interpretation has been favoured. Since the Galileo and ISO fits are slope-free, there is no requirement for a grey cloud in the 3.5 to 7 bar region to be present. This is an important point because it suggests that, at least in the hot spot regions, the atmosphere has very little cloud opacity between two and eight bars [165, 167].

Stratospheric Haze: Above the convective clouds (at low and middle latitudes) lies a thin, upper-tropospheric haze layer with modelled mean radius of 0.5 μm [188]. Galileo images at high phase angle were used to determine that the aerosol is mainly concentrated over the Great Red Spot, the northern edge of the Equatorial Zone (9°N) and at the southern edge of the north polar region (60°N) [159]. The haze layer is more zonally homogeneous than the tropospheric clouds and is thought to be produced by the photolysis of ammonia and phosphine near the tropopause in addition to the settling of photochemical hydrocarbons from the stratosphere [203].

The haze becomes optically thick at mid-latitudes becoming the “polar hood” *circa* 35°N. Such polar haze is thought to result from a different haze-production mechanism than that found at temperate latitudes [159] and has been linked with auroral precipitation [157]. The observation of a “dark” polar oval the size of the GRS aligned with the northern auroral oval [153] suggests that auroral processes *are* contributing to the formation of material found at these latitudes.

Ammonia Cloud: Cloud opacity has been shown to be strongly correlated with ammonia abundance [73]. The first spectroscopic identification of ammonia ice [34] was obtained from a single ISO/SWS spectrum. The authors found that a cloud containing approximately unit optical depth of bimodal 1-μm and 10-μm ammonia-ice spheres gave the best fit to the spectrum (*circa* 3 μm). However, the single spectrum used was disc-averaged, spanning some 60° latitude and 40° longitude. Furthermore, the inclusion of ammonia-ice particles introduced erroneous features in other parts of the spectrum [99] casting suspicion on the microphysical properties and vertical structure derived.

In contrast, spectral detection of ammonia ice in discrete, high-altitude clouds was obtained using high-spatial resolution Galileo/NIMS spectra of the region to the northwest of the Great Red Spot. The study revealed that the spectrally-identifiable ammonia-ice clouds cover less than 1% of the planet's surface and are correlated with regions of dramatic uplift (*e.g.* in the wake of the GRS near 10°S and to the east of 5-μm hot-spots in the NEB at 2°to 7°N) [11].

The most recent detection, in the mid-infrared by the Cassini/CIRS instrument, reports a wider distribution of ammonia-ice absorption. Using brightness-temperature difference as an indicator of spectrally-identifiable NH_3 ice, Wong *et al.* 2003: [204] retrieved at least two clouds exhibiting latitudinal inhomogeneity with local maximums at the Equator and near 23°N. The first cloud, essentially a grey cloud of unidentifiable composition (interpreted to be 10-μm NH_3 ice spheres), contrasts with the second which was modelled as 0.79-μm 4:1 prolate NH_3-ice spheroids. Despite the multiple detections, many questions remain regarding spatial (*e.g.* longitudinal) and temporal variation of ammonia ice clouds.

Water Cloud: Although undetected originally, there is increasing evidence for a deep water cloud *circa* 5 bars. For example, comparisons between infrared and visible spectra have linked lightning to vertically-extended water-ice clouds[6] [74, 167]. In this, and other supportive findings [13, 141], the clouds were found to be clustered in spatially-limited, localised areas associated with strong convection (*e.g.* west of the Great Red Spot – vigorous convection being required to lift the water ice from the condensation level to 0.4 bar where it could be seen above the NH_3 clouds and haze). In contrast with the ammonia-ice detection however, water-ice clouds have shown a wide latitudinal range with the majority of detections occurring between 50°S and 20°N latitude [179].

1.3.4 Large Scale Features

A remarkable feature of Jupiter is the stability of its large scale (on the order of 10,000 km) features. Whether in terms of the dominant weather patterns (the zonal jets and long-lived ovals) or in terms of the contrast between the visually-dark belts and visually-bright zones, Jupiter's bulk features have survived despite the turbulent and inhomogeneous nature of the atmosphere.

---

[6] The intercomparisons revealed a storm, on the day side of the planet, at the same location and within a couple hours of a lightning detection on the night side. If the observed storms are analogous to mesoscale convective complexes (familiarly known as thunderstorm cells) on Earth, then the linkage between convection and lightning is not unreasonable. According to Dwyer 2003: [52], lightning is thought to occur when updrafts and downdrafts push water molecules past each other causing them to shed electrons. If the shear is great enough, the electrons can eventually overcome the drag associated with travelling through air and speed up. The high-speed electrons then bump into other particles knocking off further electrons until a lightning bolt releases the energy from the established electric field.

Figure 1.6: Traditional nomenclature of the Jupiter's banded structure [17].

Zones and Belts: Jupiter's banded structure (Figure 1.6) may be broken down into a series of domains. Aside from the Equatorial Zone and the polar regions, each domain consists of a belt and a zone where a prograde (eastward) jet stream marks the boundary between domains. The stability of the belts and zones has its origin in the high rotational velocity of the planet. It is generally accepted that the "zones" are regions of dense cloud and thus high reflectivity and low thermal emission, while the "belts" are relatively cloud-free regions of low reflectivity characterised by high thermal emission.

Volatile molecules are thought to rise in the zones forming clouds along the way. The gases, then reduced in their condensible vapours, descend along the belts. The similarity between anticyclonic and cyclonic ovals to zones and belts (respectively) was used to show that regions of upwelling all have high, thick white clouds and that regions of subsidence have deeper, usually thinner, white clouds [105]. Although the belt cloud-tops are only marginally (~ 2 K) warmer than the zone cloud-tops [83, 151], because the belts are relatively cloud-free, the radiation comes from deeper layers of the atmosphere and appear roughly 80 K warmer in brightness temperature (near 5 μm). The colour in the subsidence regions is partly caused by blue absorption in the stratospheric haze [178] either because it is denser over the belts or because the belt cloud-tops lie deeper.

Winds: Jupiter has an impressive assembly of winds; a fact that did not escape late nineteenth-century observers who, via the observation of specific cloud features, determined that not only do equatorial markings move faster than their higher latitude counterparts, but also that, in extreme cases, these same winds blow at nearly 100 m/s. Seen at visible wavelengths, Jupiter is characterised by alternative bright zones and dark belts whose albedo variations are strongly correlated with mean zonal flow. The wind pattern is one of alternating easterly and westerly zonal jets (see Figure 1.7) whose speed (at the cloud-tops) can be determined by tracking atmospheric features [119].

Improved measurements of the horizontal wind speed were obtained from Voyager [197], Galileo [177], HST [71] and Cassini [153] photographs. Surprisingly, despite the data from Voyager and Cassini being obtained twelve years apart, there is little variation in the magnitude or latitudinal position of the zonal winds. Specifically, the tropospheric zonal winds have been remarkably steady, with temporal variations at low latitudes amounting to less than 20 m/s [153]. After an initial decay in the upper troposphere, the low-latitude zonal winds build back up in the stratosphere to form several strong (> 100

m/s) high-altitude (4 mbars) jets at 7°N and 23°N [61]. Analysis of the Voyager/IRIS data also allowed the determination of north-south/meridional winds which were found to be significantly weaker than their east-west counterparts [197].

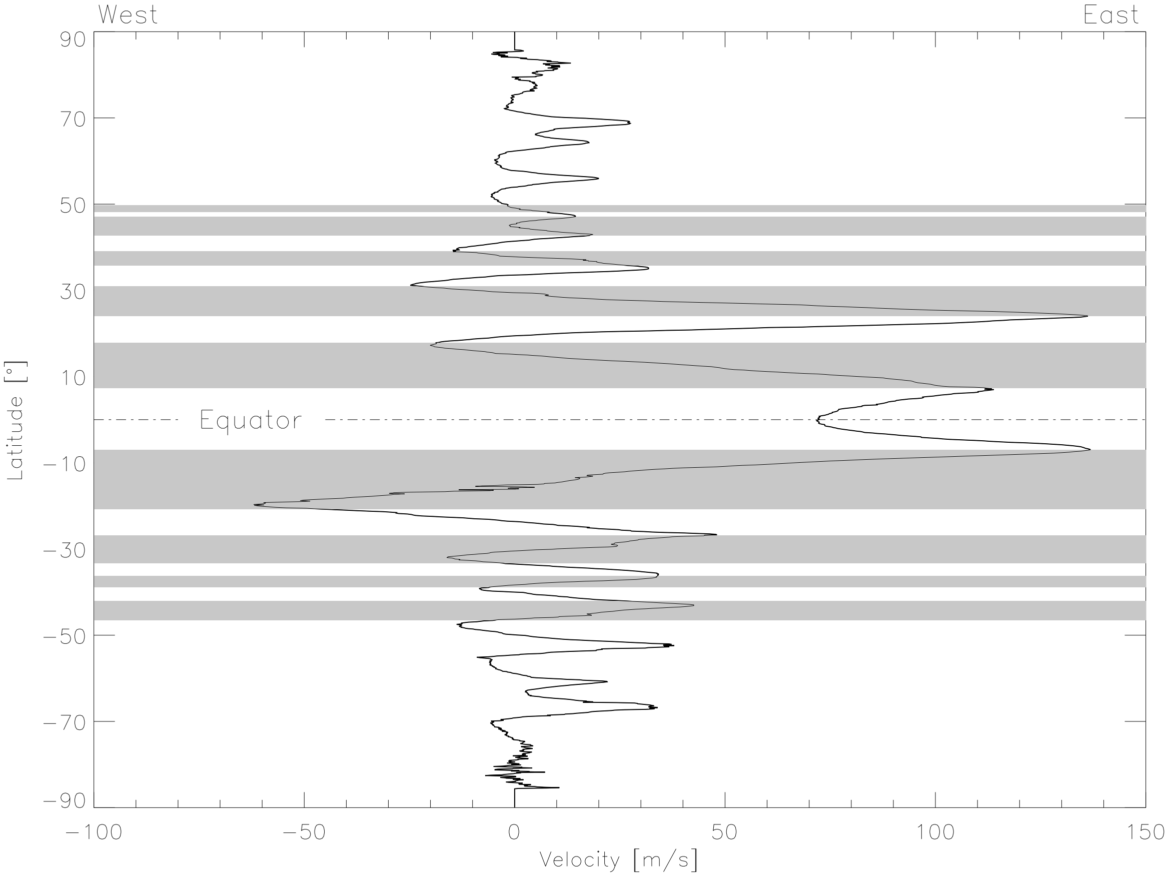

Figure 1.7: Zonal wind speeds from the Cassini-Huygens Jupiter encounter [153, 196]. Average west-east wind speed (measured at the cloud tops) *versus* latitude where positive wind speed values imply the clouds are rotating eastward faster than the planet's core. The grey regions are belts while the white regions are zones (from Rogers 1995: [162]).

Revised results of the Doppler Wind Experiment aboard the Galileo probe showed that the zonal wind speed increased with depth, from 90 m/s at 0.7 bar to 170 m/s at five bars (below this level, the winds were approximately constant) [6]. This was a surprise because it is inconsistent with the proposal that hot-spots are localised regions of intense downwelling. While further detailed studies are required to resolve this problem, analysis of hot-spot regions [167, 176] has shown that they are dynamic regions of complex meteorology which are likely anomalous to other parts of the planet.

The Great Red Spot: The bands of Jupiter are often studded with giant oval eddies, some of which are long-lived – the Great Red Spot being the most famous example. The GRS is approximately twice the size of Earth, measuring roughly 21° longitude (22,000 km) by 10° latitude (11,000 km) [162]. The GRS is centred at 22°S in the shear region between two jets, one of which is the strongest westward wind on the planet. These driving winds are deflected around the eddy which itself has high winds (70 to 140 m/s) concentrated in a narrow "collar" around a quiescent (5 m/s) interior [169]. Studies of the interior show that it may have some coherent structure (possibly even including cyclonic counter-rotating regions) as it rotates about its centre in approximately seven days. The GRS also drifts erratically in longitude, with no clear explanation.

The way the GRS is driven and sustained is the source of much debate, as is the source of its red colouration. What is known however, from vertical structure analyses about Galileo and Voyager, is that the GRS has a tilt from north to south [180] and that it is shrinking in longitudinal extent at a rate of 0.1° - 0.2° per year [19, 162, 169]. This has important dynamical ramifications and implications as to whether or not this is the same weather system observed by Cassini in 1665. Both visible and infrared data suggest that the GRS has a thick, white cloud deck with a top near 0.8 (± 0.1) bar and an extended (that is, higher and colder), blue absorbing, optically-thick haze up to about 0.2 bar with a thin stratospheric haze above that [59, 180]. Colour studies also indicate a difference in the GRS colour from other red regions [178, 203].

1.4 Scope of the Thesis

Although many of the original questions regarding the Jovian system have been answered, several remain concerning Jupiter's construction and dynamics. A major scientific endeavour meant to shed light on these queries is the Cassini-Huygens mission which passed by Jupiter on the way to Saturn. Amongst other instruments, Cassini-Huygens carries the Composite Infrared Spectrometer whose spectra constitute the subject of this thesis.

Chapter 2 describes the Cassini/CIRS Jupiter encounter and the calibration of the spectra which complement and extend previous investigations of the Jovian atmosphere. Chapter 3 summarises the radiative-transfer theory and methods that were used in the analysis presented in Chapter 4. The analysis concerns the retrieval of tropospheric temperature and composition via the application of a correlated-k radiative-transfer model. To round out the study, a simple dynamic model of Jupiter is constructed for comparison with the CIRS results. The final chapter has a summary of the findings with suggestions for the conduct of future investigations.

Chapter 2

The Cassini-Huygens Jupiter Fly-by

Contents

This chapter provides a summarising overview of the Cassini-Huygens mission, the CIRS instrument and the spectra returned from the Jupiter Millennium Fly-by. The concepts and techniques of Fourier analysis are also covered in a discussion regarding the calibration of the CIRS spectra.

2.1 The Cassini-Huygens Mission

Cassini-Huygens[1], a cooperative project between NASA, ESA and the Agenzia Spaziale Italiana [131], was launched to Saturn in 1997 on a circuitous path utilizing gravity-assists from Venus (twice), Earth, and Jupiter (see Figure 2.1). The conjoined spacecraft (making it one of the largest, heaviest and most complex interplanetary spacecraft ever built) are due to arrive in the Saturnian system in 2004. The complexity of the spacecraft is necessitated both by its trajectory to Saturn and by the ambitious program of scientific observations to be undertaken once Cassini-Huygens reaches the Saturnian system.

The mission consists of two spacecraft: the Cassini orbiter and the Huygens descent probe (see Figure 2.2). During the orbiter's nominal 4-year lifetime, Cassini will pay nearly 40 visits to Saturn's largest moon, Titan. The large number of Titan fly-bys will facilitate two mission objectives. First, the fly-bys will allow numerous observations of Titan over the course of the mission's duration. Second, the visits will allow the spacecraft to make the necessary gravity-assist manoeuvres that will keep it in orbit. After a couple initial orbits of Saturn, the Huygens probe will separate from the orbiter on a trajectory directed at Titan. Upon arrival, the probe will descend via parachute through Titan's atmosphere and land on its surface.

---

[1] The Cassini-Huygens mission was named after two seventeenth-century astronomers, Jean Dominique Cassini (1625-1712) and Christian Huygens (1629-1695).

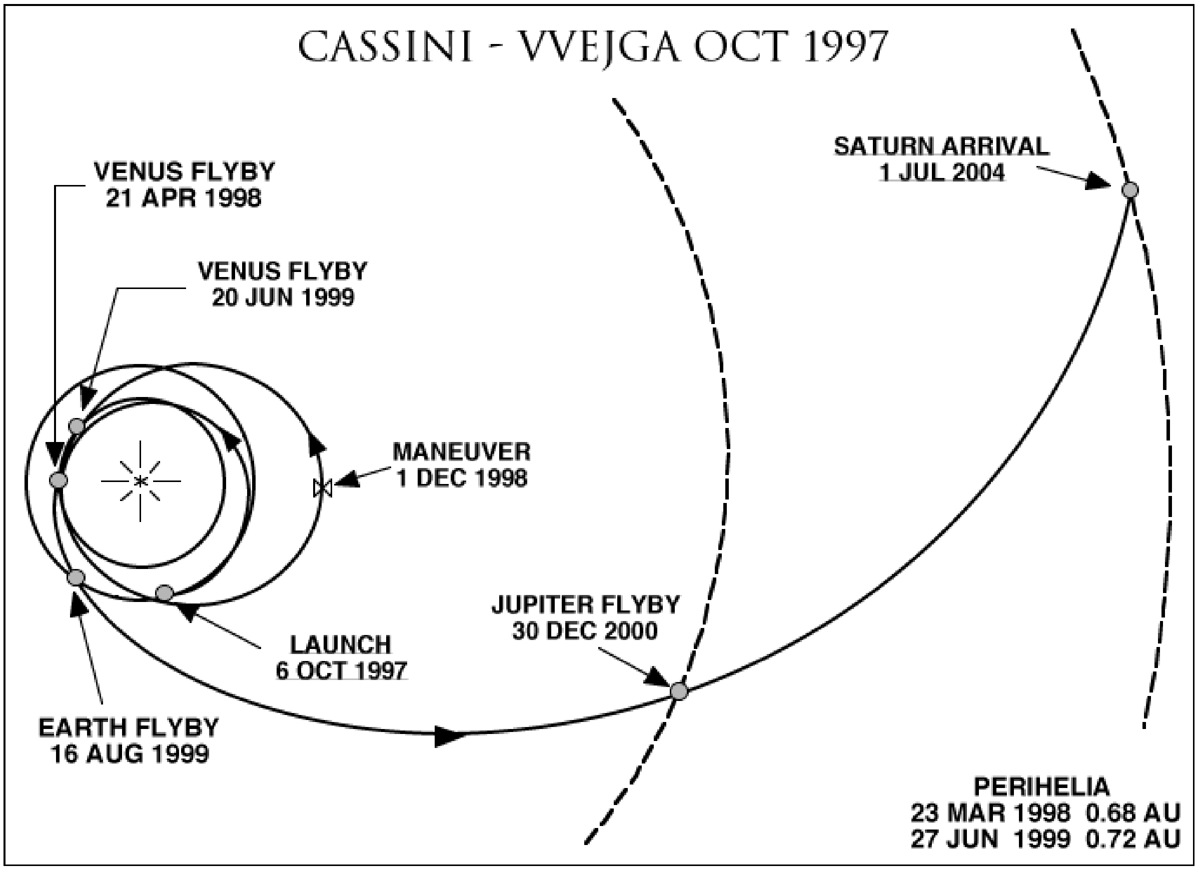

Figure 2.1: The Cassini-Huygens cruise trajectory to Saturn (VVEJGA = Venus, Venus, Earth, Jupiter Gravity Assist). Cassini-Huygens also flew within 2 million kilometres of the asteroid Masursky in early February 2000. [NASA]

2.1.1 The Cassini Orbiter

The orbiter stands 6.8 metres high and is 4 metres (at its widest) in diameter. The functions of the orbiter are to carry the Huygens probe and the on-board science instruments to the Saturnian system, to serve as the platform from which the probe is launched and the scientific observations are made, and to store information and relay it back to Earth. Because of Saturn's distance from the Sun, solar panels are not feasible power sources for the spacecraft and all its instruments. Thus, the Cassini orbiter gets its power from three radioisotope thermoelectric generators which use heat from the

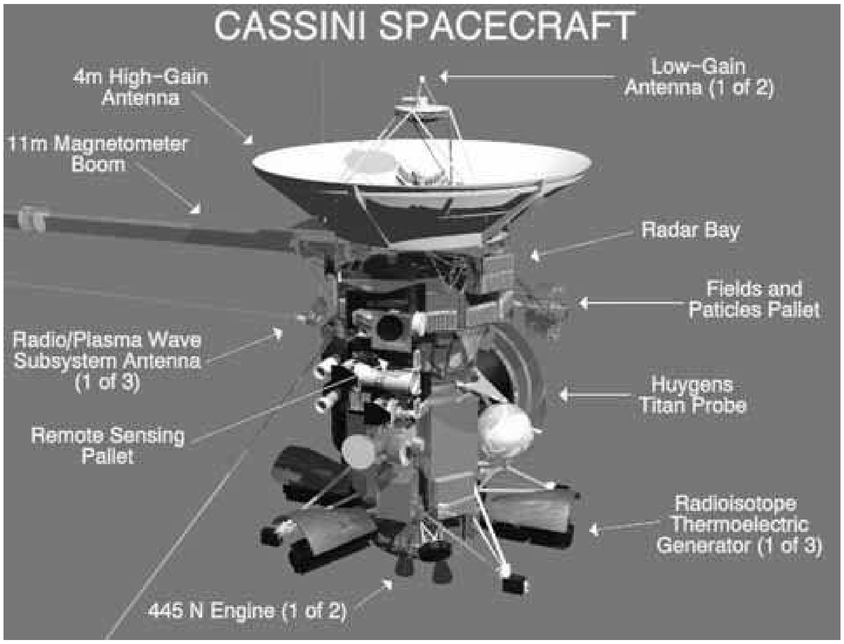

Figure 2.2: The Cassini-Huygens spacecraft – the CIRS instrument is located on the Remote Sensing Pallet at the lower center of the vehicle. [NASA]

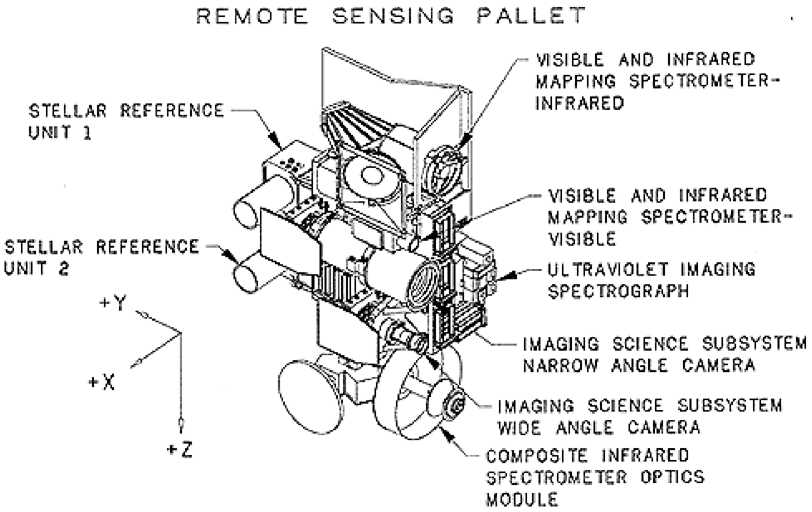

Figure 2.3: The Cassini-Huygens Remote-Sensing Pallet. Note the telescope and cooler assembly of the CIRS instrument at the bottom of the pallet. [NASA]

natural decay of plutonium to generate direct current electricity. The orbiter's scientific emphasis is the investigation of Saturn's atmosphere, rings, icy satellites, radiation belts and magnetosphere.

The orbiter's science instruments are concentrated onto two separate platforms: the Remote Sensing Pallet and the Fields and Particles Pallet. The Composite Infrared Spectrometer (CIRS), along with the other optical instruments, are housed on the Remote Sensing Pallet (see Figure 2.3). The other instruments aboard the Remote Sensing Pallet include a joint wide-angle and narrow-angle camera, a visible and infrared spectrometer and an ultraviolet spectrometer. The Fields and Particles pallet houses an Ion and Neutral Mass Spectrometer, a Cosmic Dust Analyzer, a magnetometer, and two other instruments investigating the particle and wave properties of Saturn's magnetosphere. The orbiter will also use the spacecraft's large high-gain antenna to investigate the geologic features and topography of the icy satellites and Titan via radar. Radio occultations of the atmosphere and rings will also be conducted using Cassini's communications link.

2.1.2 The Huygens Probe

The Huygens probe, supplied by the European Space Agency (ESA), will scrutinize the clouds, atmosphere, and surface of Titan, with the emphasis on determining the source and composition of the complex organic molecules that make up Titan's obscuring atmospheric haze. The probe system consists of the probe itself, which will descend to Titan, and the probe support equipment which will remain attached to the orbiting spacecraft. The Huygens payload consists of a complement of six scientific instruments including a gas chromatograph mass spectrometer, several descent imagers/radiometers and a number of sensors designed to determine the physical properties of Titan's surface at the point of impact. Due to mission constraints, the probe's lifetime is predicted to last little more than two hours which is thought to be just enough to allow Huygens to land on Titan's surface.

2.2 The Composite Infrared Spectrometer

CIRS [108] is a direct descendant of the Infrared Interferometer Spectrometer (IRIS) instruments which were originally flown on the Nimbus satellites to investigate the Earth's atmosphere but were also sent to Mars on Mariner 9, and to the outer planets on Voyagers 1 and 2. CIRS' main conceptual difference from the IRIS device is the use of both ends of the mirror carriage mechanism (see Figure 2.4) so as to allow the inclusion of two separate interferometers to cover a wider spectral range. Additional improvements include the use of cryogenics, advanced electronics and arrays of detectors with a small field-of-view (FOV).

2.2.1 Scientific Objectives

The circuitous route needed for the planetary gravity assists presented mission planners with the opportunity to test the orbiter's instruments prior to arriving in the Saturnian system. The tests, termed "cruise science", allowed as many of the broad scientific mission-objectives outlined below to be attempted during the Jupiter encounter balancing the power constraints, observing times, and viewing geometries of the other instruments aboard the spacecraft. The CIRS science objectives are:

- To determine the global, three-dimensional and temporal variation of atmospheric:
  - Temperature,
  - Gas composition,
  - Aerosols, hazes and clouds.
- To improve upon and extend the scientific advances made by Voyager/IRIS via:
  - Improved and programmable spectral resolution,
  - Extension of spectral sensitivity to submillimetre wavelengths.
- And to map the composition and thermal characteristics of the planet's rings and icy satellites.

The improved and programmable spectral resolution should help to find new trace constituents, higher order hydrocarbons and cloud condensates like NH_3 and NH_4SH. The far-IR coverage is important because molecular species such as CO, HD, HCN, H_2O, H_2S, NH_3, and PH_3 have rotational bands in this region.

2.2.2 Instrument Description

The Composite Infrared Spectrometer is a coordinated pair of interferometers (*cf.* Table 2.1) designed to measure infrared radiation from 10 cm^{-1} to 1400 cm^{-1} (1000 μm to 7 μm) with a variable spectral resolution that can be set from 0.5 cm^{-1} to 20 cm^{-1} [35]. The two interferometers are situated opposite each other, across the central axis of the

	Far-IR	Mid-IR	
Interferometer Type:	Polarising	Michelson	
Focal Plane[†]:	**FP1**	**FP3**	**FP4**
Spectral Range [cm^{-1}]:	10-600	600-1100	1100-1400
Spectral Resolution [cm^{-1}][‡]:	0.5-20	0.5-20	0.5-20
Detector Type:	Thermopile	Photoconductive	Photovoltaic
Number of Pixels:	1	1 ×10 array	1 ×10 array
Pixel FOV [milliradians]:	3.9	0.27	0.27
Temperature [K]:	170	70-85	70-85

Table 2.1: CIRS instrument specification. †: In the original proposal, the far-IR was to be monitored via two focal planes (FP1: 10-300 cm^{-1} and FP2: 300-600 cm^{-1}) which were later combined [137]. ‡: For both interferometers, the scan length controls the spectral resolution; see Table 2.2.

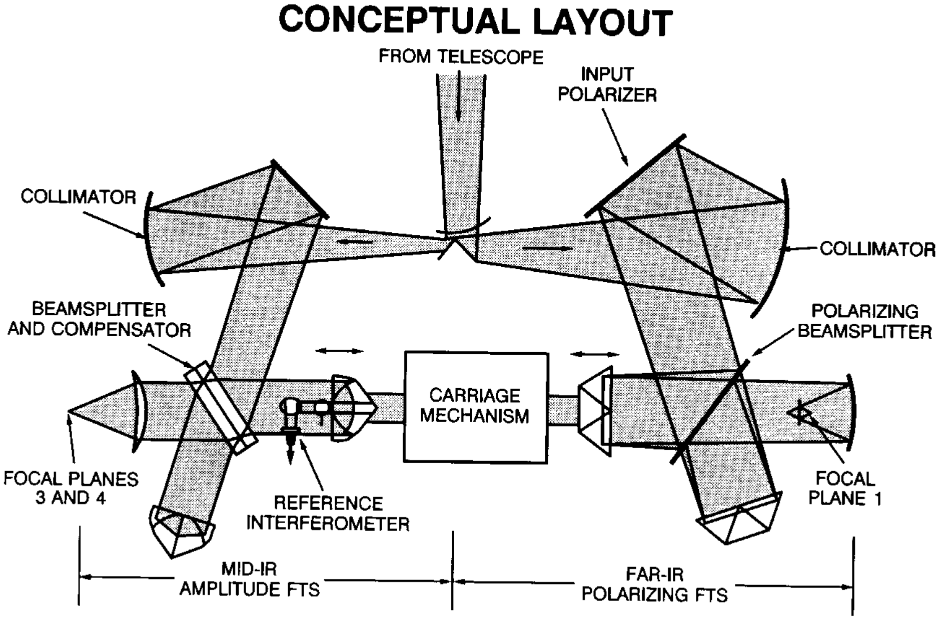

Figure 2.4: The conceptual layout of the CIRS instrument. [NASA]

instrument, and share the photons received from the 50-cm telescope situated outside, and in front of, the instrument housing (see Figure 2.4). The "coordination" arises from the interferometers' use of both ends of the moving-mirror/carriage mechanism.

The mid-infrared interferometer is a classic Michelson design and has two different focal planes (FP3: 600-1100 cm^{-1} and FP4: 1100-1400 cm^{-1}), each consisting of 1x10 arrays of 0.27 milliradian (mrad) square detectors. The small FOV and higher spectral resolution of the mid-infrared channels require better noise performance than Voyager/IRIS which received 4000 times more power per wavelength interval than CIRS will [35]. This improved performance is achieved by cooling the detectors via an external radiator.

The second interferometer (FP1) operates in the far-infrared (out to 10 cm^{-1} / 1000 μm) with a circular FOV of 3.9 mrad (Figure 2.5 presents a schematic of the joint FOVs). FP1 uses polarisation to separate and recombine the incoming signal (see Appendix A) in order to increase the interferometer's measurement precision.

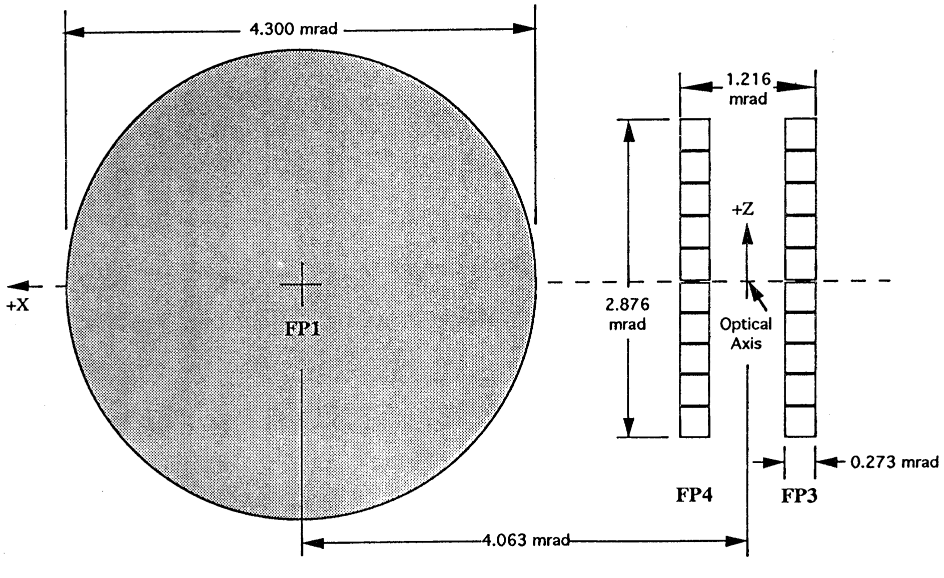

Figure 2.5: The fields-of-view of the CIRS instrument. FP1 is in fact elliptical having a long-axis diameter of 4.2 mrad and a short-axis diameter of 3.6 mrad [183]. The median between these two values is that reported in Table 2.1. Also note how FP1 is located 4 mrad off the optical boresight of the instrument. [NASA]

2.3 CIRS Calibration

The output of CIRS is not a true representation of the radiation entering the instrument; rather, the radiation has been modified by the instrument. The true spectrum needs to be faithfully reconstructed from the measured signal with any instrumental effects removed as best as possible. To this end, Fourier Transform spectroscopy is used to convert the individual interferograms into spectral distributions. [Note that it was not the author's responsibility to calibrate the CIRS spectra. Nevertheless, a brief description of the calibration process is given here.]

2.3.1 Recovery of the Spectral Distribution

For an input beam of monochromatic light of wavenumber $\tilde{\nu}_0$ and intensity A, the intensity of the interferogram as a function of optical path difference, L, between the two beams is given by the two-beam interference relation (Equation A.14):

$$\mathcal{I} \;=\; A\,[1 \;+\; \cos(2\pi\tilde{\nu}_0 L)]. \tag{2.1}$$

When the source contains more than one frequency, an ideal detector sees a superposition of such cosines:

$$\mathcal{I}(L) \;=\; \int_0^\infty A(\tilde{\nu})\;[1 \;+\; \cos(2\pi\tilde{\nu}L)]\;d\tilde{\nu}, \tag{2.2}$$

so that, with the subtraction of the mean, an expression for the intensity as a function of path difference can be formed:

$$\mathcal{I}(L) \;=\; \int_0^\infty A(\tilde{\nu})\;\cos(2\pi\tilde{\nu}L)\,d\tilde{\nu}. \tag{2.3}$$

The right-hand-side of Equation 2.3 is the cosine FT of the spectral distribution, $A(\tilde{\nu})$. The corresponding interferogram is symmetric, consisting of a strong signal at the point where the path difference is zero (ZPD). It can be shown that the spectral distribution can be recovered from the interferogram by the inverse FT:

$$A(\tilde{\nu}) \;=\; \int_0^\infty \mathcal{I}(L)\;\cos(2\pi\tilde{\nu}L)\,dL. \tag{2.4}$$

However, this solution is not unique as $\cos(2\pi\tilde{\nu}L)$ equals $\cos(-2\pi\tilde{\nu}L)$ and consequently $A(\tilde{\nu})$ and $A(-\tilde{\nu})$ produce identical interferograms symmetric about ZPD. Although the negative frequencies are physically unreal and contain no extra information, the mirrored, or "phase", spectrum plays an important role in transforming back and forth between the interferogram and spectral domains.

2.3.2 Phase Correction

While non-uniqueness does not invalidate the solution, the assumption that the true spectrum can be represented by a symmetric function is flawed, as experimental, instrumental, observational and computational limitations introduce asymmetries into the interferogram. The introduction of asymmetry effectively produces a frequency-dependent phase, $\varphi(\tilde{\nu})$, such that the cosine in Equation 2.4 does not equal one at ZPD. As the interferograms are no longer symmetric, the features formed for each frequency cannot be recovered by a simple cosine transform. Instead, an appropriate combination of even (cosine) and odd (sine) functions can be used to reproduce the asymmetric $\mathcal{I}(L)$:

$$\mathcal{I}(L) \;=\; \int_{-\infty}^{\infty} A(\tilde{\nu}) \;\exp(i[2\pi\tilde{\nu}L \;+\; \varphi(\tilde{\nu})])\, d\tilde{\nu}, \tag{2.5}$$

where

$$\begin{aligned} A(\tilde{\nu}) \;&=\; A(\tilde{\nu})^{\text{even}} \;+\; iA(\tilde{\nu})^{\text{odd}}, && (2.6) \\ &=\; |A(\tilde{\nu})| \;\exp(-i\varphi(\tilde{\nu})). && (2.7) \end{aligned}$$

Despite the true spectrum being real and positive, the measurement process produces a less-than-ideal interferogram with an imaginary component necessitating a complex transform. As measuring the phase is equivalent to measuring the asymmetry in the interferogram, if $\varphi(\tilde{\nu})$ can been determined and corrected, then symmetry can be restored and the cosine transform used to recover the real spectrum, $A(\tilde{\nu})^{\text{even}}$.

The phase spectrum represents the phase for each frequency component and is the angle between the imaginary and real components of the complex spectrum:

$$\varphi(\tilde{\nu}) \;=\; \tan^{-1}\left(\frac{A(\tilde{\nu})^{\text{odd}}}{A(\tilde{\nu})^{\text{even}}}\right). \tag{2.8}$$

Phase correction concerns the assignment of unique φ at each $\tilde{\nu}$ so that the cosines can be shifted to the appropriate origin. As no single origin exists for all frequencies, such a phase correction must be done for each interferogram and must be deduced from the data contained within the interferogram itself.

The process of phase correction turns the complex spectrum, $A(\tilde{\nu})$, into a real function by multiplying it by a rotation function, $\exp(i\varphi(\tilde{\nu}))$. Consider $\mathcal{I}(L)$ in Equation 2.5. As integrals of odd integrands over all space vanish, $\mathcal{I}(L)$ can be rewritten:

$$\begin{aligned}
\mathcal{I}(L)^{\text{even}} &= \int_{-\infty}^{\infty} A(\tilde{\nu})^{\text{even}} \exp(i2\pi\tilde{\nu}L) \exp(-i\varphi(\tilde{\nu}))\, d\tilde{\nu}, && (2.9)\\
&= \text{FT}[A(\tilde{\nu})^{\text{even}} \exp(-i\varphi(\tilde{\nu})], && (2.10)\\
&= \text{FT}[A(\tilde{\nu})] \exp(i\varphi(\tilde{\nu})), && (2.11)
\end{aligned}$$

which, if multiplied by the phase-correction function results in:

$$\mathcal{I}(L)^{\text{even}} = \text{FT}[A(\tilde{\nu}) \exp(-i\varphi(\tilde{\nu}))]. \tag{2.12}$$

While this cannot be applied directly as $A(\tilde{\nu})$ can only be determined via a two-sided transform, it can be shown that the asymmetric (measured) interferogram can be transformed into the ideal (symmetric) interferogram by convolution with a symmetrising function, $\Psi(L)$:

$$\mathcal{I}(L)^{\text{even}} = \mathcal{I}(L)\, \Psi(L) \qquad \text{where } \Psi(L) = \text{FT}[\exp(-i\varphi(\tilde{\nu}))]. \tag{2.13}$$

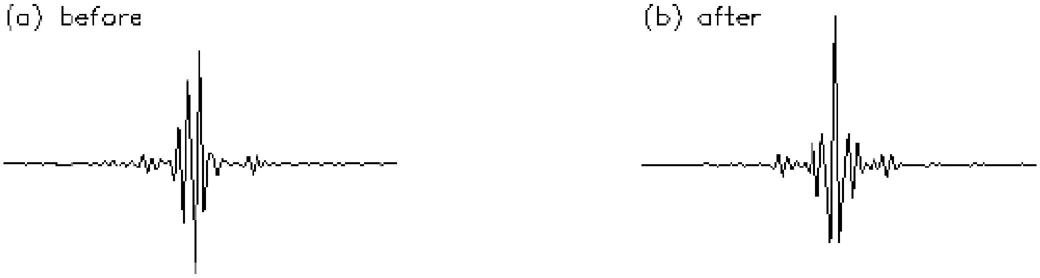

Figure 2.6: Example phase-correction by the Forman method. The ZPD of an example CIRS interferogram (a) before and (b) after phase correction. [137]

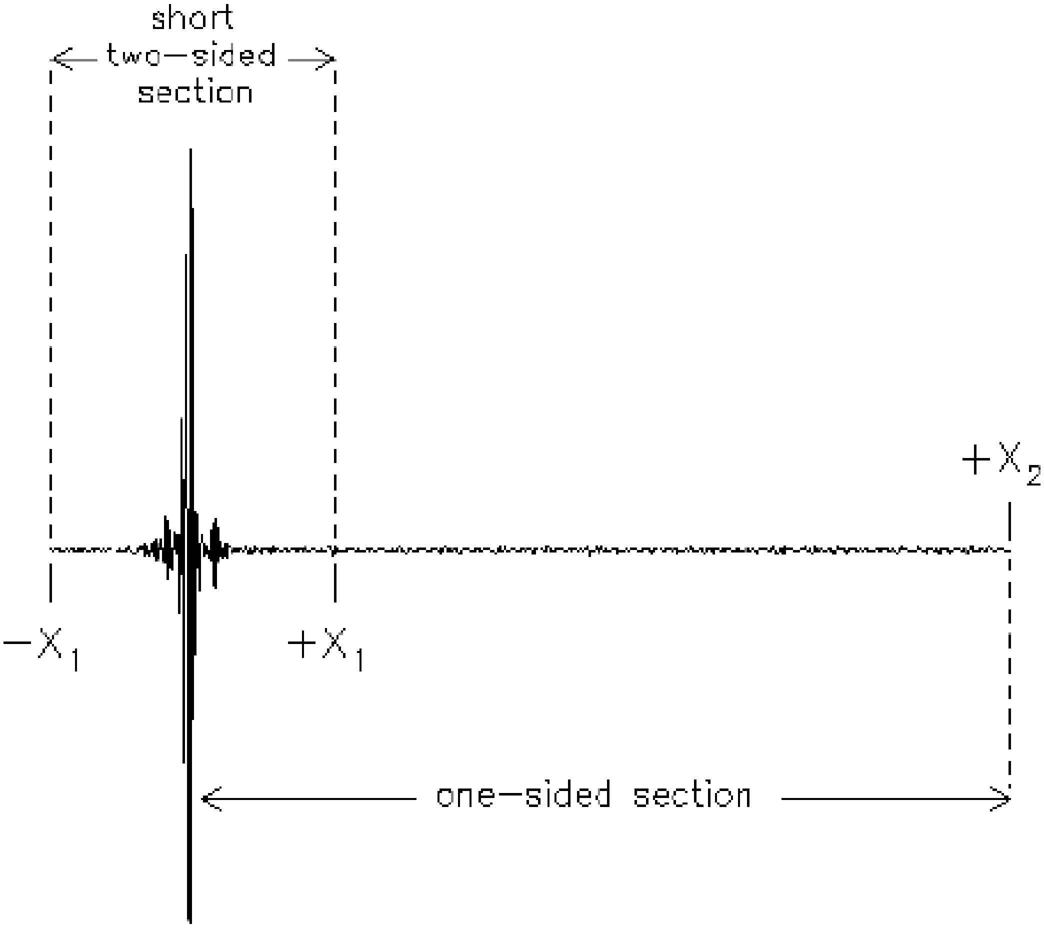

Figure 2.7: Example two-sided interferogram before phase-correction (*N.b.* the asymmetry of peaks on either side of ZPD). [137]

This is known as the *Forman method* of phase-error correction [62] – see Figure 2.6 for an illustration. In this way, a symmetric interferogram from the original asymmetric record is produced, allowing the spectral distribution to now be computed using the cosine transform (Equation 2.4).

Phase Correction within CIRS Spectra: Although the two-sided interferogram is clearly needed to calculate the phase spectrum, the factor of two increase (for $\pm\ \tilde{\nu}$) in terms of data storage and measurement and downlink times is a great inefficiency. This overhead can be reduced in practical terms by making use of the fact that $\varphi(\tilde{\nu})$ for calibrated interferometers are generally smooth functions that do not rapidly vary with $\tilde{\nu}$ [62]. Therefore, $\varphi(\tilde{\nu})$ can be derived from an interferogram that covers only a small range of negative frequencies beyond ZPD. This process is called *ameritization* and is designed to accurately account for the artefacts introduced in the transform as a result of the lost information.

The steps to calculating the spectral distribution are then as follows (*cf.* Figure 2.7):

1. A large, two-sided interferogram, asymmetric in length with a short negative path-difference and a much longer positive path-difference, is measured and returned by the CIRS instrument.

2. The central portion (-X_1 to +X_1) of the interferogram, symmetric about ZPD, is extracted from the large interferogram to allow for a low-resolution estimation of the phase spectrum.

3. The short interferogram is transformed and $\Psi(L)$ calculated.

4. $\Psi(L)$ is then convolved with the entire original spectrum (-X_1 to $+X_2$).

5. The negative path-difference is then discarded leaving the corrected, symmetric, one-sided (0 to $+X_2$) interferogram $\mathcal{I}(L)^{\text{even}}$.

6. $\mathcal{I}(L)^{\text{even}}$ is then apodised (see §2.3.3) and cosine-transformed to produce $A(\tilde{\nu})^{\text{even}}$.

It is important to note that, in the thermal infrared where the instrument radiance mingles with the source function, the phase cannot always be assumed to vary smoothly.

2.3.3 Apodisation

A continuous, infinitely-long interferogram, Fourier transformed, reproduces the spectrum exactly [46]. In practice however, it is impossible to measure an infinite function such as $\mathcal{I}(L)$. When an interferogram is terminated at some finite length, the interferogram is effectively convolved with a rectangular ("boxcar") function:

$$W\left(\frac{L}{X}\right) = \begin{cases} 1 & 0 \leq L \leq X \\ 0 & L < 0,\ L > X \end{cases}$$

that is unity during the sampling window, and zero otherwise. This process is known as *windowing*. The effect of windowing results in the convolution of the sinc function[2] on the calculated spectrum and a reduction in resolution (due to the loss of information). The sinc function also leads to aliasing, an undesired "ringing" effect on the final spectrum. The ringing can be reduced by changing the form of the windowing function to one

---

[2] $$\text{sinc}(2\pi\tilde{\nu}L) = \frac{\sin(2\pi\tilde{\nu}L)}{2\pi\tilde{\nu}L}$$

that smoothly reduces its amplitude to a small value or zero at $L = X$. This process of "cutting the feet off" is known as *apodisation.* For the CIRS project, a "Hamming" apodisation was chosen. The Hamming window function:

$$W(L) = \begin{cases} 0.54 - 0.46\cos\left[\frac{2\pi L}{L_{max}}\right] & |L| \leq L_{max} \\ 0 & |L| > L_{max} \end{cases}$$

is a special case of the cosine-squared window with carefully selected coefficients to ensure smaller side-lobes at the cost of a widened central peak (and hence further degraded resolution). The apodising function is applied in the measurement domain, prior to the application of the FT.

2.3.4 Spectral Calibration

Having formalised a means of recovering the original spectrum minus measurement effects, the spectral characteristics of the recovered distribution need now be determined. Spectral calibration is achieved using a tiny reference interferometer located within the mid-IR segment of the CIRS instrument. The reference interferometer uses a monochromatic laser at 784 nm to log the number of interferometric-nulls caused by mirror displacement during scans. The length of the scan, specified in multiples of Real Time Interrupts (RTI, = 1/8 second), determines the number of samples in the interferogram which in turn translates into unique spectral resolutions (see §2.3.5).

As none of the CIRS detectors are actually centred on the optical axis of the instrument, three "effective" laser wavelengths were chosen for use in calibrating each of the respective focal planes. After the experience of the Jupiter encounter however, the three effective laser wavelengths were modified to be 31 effective laser wavelengths – one per detector (including pair modes[3]). In this way, the accuracy of the wavelength calibration was further improved (as the light path-lengths varied from detector to detector on FP3 and FP4) and allowed spectra of the same scan-length to be interpolated onto a uniform resolution grid. The use of a uniform resolution also facilitated the co-adding of spectra from different detectors on the same array and from the different focal planes.

2.3.5 Resolution

There are several different possible definitions for the resolving power, or resolution, of an instrument. The distance between statistically independent samples in the spectrum, $\delta\tilde{\nu}$, is one method. $\delta\tilde{\nu}$ is effectively the spacing of the output and is the reciprocal of the optical path-difference:

$$\delta\tilde{\nu} = \frac{1}{\text{optical path-difference}}. \tag{2.14}$$

The optical path-difference is simply twice the physical path difference which is determined by the mirror velocity and duration of the observation. For the CIRS instrument, a maximum path-difference of 2 cm can be introduced, resulting in a minimum output spacing of 0.25 cm^{-1}. Actual resolutions however fluctuate from scan to scan depending on the number of samples measured. Mirror acceleration and speed, the length of the previous scan (including mirror fly-back time), mirror-motor voltages and the temperature

---

[3] Due to mass constraints on the instrument electronics, only five of the ten detectors may be used simultaneously, in one of four modes: odd detectors, even detectors, centre detectors for a reduced FOV, or reduced resolution mode where adjacent pairs of pixels act as one (pairs mode).

dependence of the reference laser frequency all contribute to uncertainty in the derived output spacing. As the exact duration of the observation is not independently verified, it is more useful to determine the resolution (via optical path-difference) according to the number of samples within the interferogram.

Sampling: Depending upon the observing mode, each detector is sampled in turn where only five of the ten detectors on FP3,4 are used at any one time. All the focal planes are then re-sampled electronically, prior to outputting the interferogram. The purpose of re-sampling, or *decimation* as it is also known, is data compression; to reduce the number of points within the interferogram without loss of information. Re-sampling factors of 18, 22.5 and 25 were used for FP1, FP3 and FP4 respectively.

The number of samples within an interferogram is directly proportional to the distance travelled by the scan mirror and inversely proportional to the reference laser frequency and/or any re-sampling factor used:

$$\text{number of sample points} \;\propto\; \frac{\text{optical path-difference}}{0.5\,\tilde{\nu}_{\text{laser}}}\,\frac{1}{\text{re-sample factor}}, \tag{2.15}$$

where the laser frequency has been halved because only the nulls are logged. For example, for the Jupiter encounter where the mirror velocity equalled 0.02092 cm/s [39], a FP4 integration with RTI = 92 would have an 11.5 s observation time and 491 samples. In practice, to enable the use of fast numerical calculation of the transforms (*e.g.* Fast Fourier Transform algorithm), the interferograms are additionally “zero-padded” until the number of samples within the interferogram is equal to a power of two. Assuming no

	Apodised		**Unapodised**	
RTI	**FWHM**	L_0	**FWHM**	L_0
36	14.10	15.50	9.30	8.00
40	12.50	13.80	8.30	6.90
92	2.70	2.98	1.80	1.48
96	2.56	2.82	1.70	1.40
224	0.91	1.00	0.60	0.50
400	0.48	0.53	0.32	0.26
401	0.48	0.53	0.32	0.26

Table 2.2: CIRS spectral resolutions [cm^{-1}]. There are two different means of representing the spectral resolution (both in terms of RTI): the full-width-at-half-maximum (FWHM) of a well-separated line, or the distance from line peak to the first null (not the first minimum) of the line shape (L_0). Because of L_0's similarity to the definition for a line-pair to be resolved, it is sometimes wrongly referred to as the Rayleigh criterion. However, the definitions are not identical as L_0 refers to an individual line.

zero-padding, the resulting spectral distribution of the 491 data samples would have an output spacing of 1.04 cm^{-1}. With zero-padding, the resulting spectra would be spaced $1.04 \times (491/512) = 1.0$ cm^{-1} apart.

The exact relationship for resolution however, depends on the instrument line shape (ILS) – the instrument response to a purely monochromatic input. As the observed spectrum is the convolution of the ideal spectrum with the ILS, all the spectral features are broadened to some extent. If the ILS is much narrower than a given line, the shape of the line will be almost unchanged. If however, the ILS is broader than the line, then the ILS width will dominate. In general, a variable numeric factor (according to apodisation type) is used to describe the full-width-at-half-maximum (FWHM) of the ILS in determining the instrument's resolving power. The unapodised and apodised CIRS spectral resolutions as a result of these considerations can be found in Table 2.2.

Month	**RTI**							**All RTI**
	36	**40**	**92**	**96**	**224**	**400**	**401**	
Oct-2000	0	60,309	0	12,867	0	28,945	0	102,121
Nov-2000	0	6,580	0	0	0	45,985	0	52,565
Dec-2000	9,654	0	2,643	23,561	0	47,185	0	83,043
Jan-2001	52,680	6,527	6,178	70,264	0	65,159	0	200,808
Feb-2001	0	0	0	0	0	86,006	0	86,006
Mar-2001	0	0	0	0	0	36,628	25,088	61,716
All Months	62,334	73,416	8,821	106,692	0	309,908	25,088	586,259

Table 2.3: Calibrated (version 0.72) CIRS spectra summary – a full listing of the CIRS observations planned at Jupiter and a mission update can be found in Appendix B.

2.4 CIRS Observations

On 30 December 2000, the Cassini-Huygens spacecraft reached the perijove milestone in its continuing journey to the Saturnian system. During an extended *Millennium Fly-by* from 1 October 2000 to 22 March 2001, Jupiter was routinely mapped pole-to-pole from the ultraviolet wavelengths to the far-IR. During this period, CIRS registered several million interferograms resulting in a total of 567,000 calibrated infrared spectra of the Jovian atmosphere, satellites and rings – see Table 2.3.

As the optical instruments aboard Cassini-Huygens possess limited pointing capability, a large number of the CIRS spectra were taken during "ride-along" opportunities when another experiment was the lead instrument. Of particular value are the ATMOS observations, of which there are four in total: A, B, C and D, which were recorded during and immediately after closest approach – see Table 2.4. In these nadir observations, the FP3 and FP4 detector arrays were aligned parallel to the Equator of Jupiter and cyclically scanned from north to south pole at medium spectral resolution (2.5 cm^{-1}, apodised). Each scan was approximately 90 minutes in duration with a longitude separation of 45° between scans. Full global coverage of the ATMOS maps was however, not achieved as the mapping was cut short leaving large pole-to-pole swathes of no data.

Map Designation	**Start Time**	**Duration [hours]**	**FOV**[†] **FP3, FP4**	**Number of Spectra**[‡] **FP3**	**FP4**
ATMOSA	17:00 31-Dec-2000	20.0	2.17° (2700 km)	7295	7389
ATMOSB	15:00 04-Jan-2001	20.0	2.44° (3040 km)	7040	7205
ATMOSC	18:00 09-Jan-2001	15.0	3.08° (3840 km)	4758	4727
ATMOSD	23:00 10-Jan-2001	16.0	3.26° (4060 km)	4480	4445

Table 2.4: Calibrated (version 0.72) ATMOS map summary – all the observations were measured with 96 RTI. Closest approach took place at 10:05 on 30 December 2000 at a distance of 9.72 million km (136 R_J). †: the field-of-view at the Equator. ‡: spectra with emission angle ≤ 60°.

A spatial resolution of 2.1° to 3.2° at the sub-spacecraft point is achieved by the 0.27 mid-IR detectors during the ATMOS observations (see Table 2.4). This is more than adequate for resolving the Jovian belts and zones and the GRS, but not enough to observe small features like the white ovals of South South Temperate Belt. Note that while the mid-IR pixels have square projections at the sub-spacecraft point, the footprint becomes progressively more stretched at latitudes towards the poles. There are also more spectra at lower latitudes due to the viewing angle effect coupled with a steady scan rate.

Analysis and interpretation of the ATMOS data forms the core of the work presented in this thesis. The calibrated CIRS spectra were drawn from version 0.72 of the CIRS database with the selection criteria as follows: all available spectra for Jupiter and its rings were extracted from the CIRS database (due to the way the pointing information was configured, the inclusion of Jupiter's rings[4] was necessary for the extraction of near-

---

[4] The Jovian rings, unlike their Saturnian counterparts, are very dark and possibly even invisible to CIRS. Although the rings are essentially transparent, the available measurements suggest they are

equatorial spectra). The spectra were averaged into bins of 6° spatial resolution in both latitude and longitude and stepped every 3° (there were insufficient spectra to create useful averages at latitudes greater than ± 60°). Spectra with FOVs that contained any of the Galilean satellites and/or had emission angles greater than 60° were excluded (beyond 60° the emission falls off due to limb darkening).

Limited processing of the collected data was required. While previous versions of the CIRS database required the addition of wavelength offsets for the respective focal planes, version 0.72 did not. Weighted interpolation of the radiances between 1070 and 1130 cm^{-1} was carried out to concatenate FP3 and FP4 spectra; for bins without representative focal plane spectra, no processing was completed. Spectral subranges between 600 to 700 cm^{-1} and 1000 to 1200 cm^{-1} were then systematically extracted from the binned spectra for retrieval purposes.

2.4.1 Radiometric Calibration and Noise

The success of the CIRS investigations will, in no small part, be dependent on the radiometric accuracy and precision of the final calibrated radiances. As previously discussed, the shape of the measured spectrum is determined by the characteristics of both the instrument and the target source:

$$A(\tilde{\nu}) \;=\; R(\tilde{\nu})\,\mathrm{FT}[\mathcal{I}(L)^{\mathrm{instru}} \;-\; \mathcal{I}(L)^{\mathrm{target}}]. \tag{2.16}$$

where $R(\tilde{\nu})$ is the spectral responsivity of the instrument. Both $R(\tilde{\nu})$ and $\mathcal{I}(L)^{\mathrm{instru}}$ are

---

composed of grains of rocky material and contain little or no ice [174].

important radiometric unknowns, central to the inflight calibration of the CIRS spectra. Accurate knowledge of these two quantities allows for the determination of $\mathcal{I}(L)^{\text{target}}$ which, when transformed, results in the true spectrum with instrumental effects removed as far as possible.

For FP1, as both the instrument and the focal-plane detectors are reliably thermostated to be the same, the instrument radiance is just the Planck function for blackbody emission, $B(\tilde{\nu}, T)$, at 170 K. The instrument radiance for the mid-IR focal planes is somewhat more complicated as it is composed of contributions from both the 170 K optics and the 80 K focal-plane cooler:

$$\text{FT}[\mathcal{I}(L)^{\text{instru}}] \;=\; \beta\, B(\tilde{\nu}, 170\,K) \;+\; (1 \;-\; \beta)\, B(\tilde{\nu}, 80\,K), \tag{2.17}$$

where β is a fraction between 0 and 1. Equation 2.17 implies that there is a target temperature, 80 K $< T^{\text{critical}} <$ 170 K, for which $\mathcal{I}(L)^{\text{instru}}$ - $\mathcal{I}(L)^{\text{target}} \simeq 0$ and the net counts falls to zero. This presents a problem for the Millennium Fly-by data as the focal-plane critical temperatures ($T^{\text{critical}}_{\text{FP1}} =$ 170 K, 130 K $< T^{\text{critical}}_{\text{FP3,4}} <$ 150 K [137]) are approximately those observed on Jupiter. For targets either warmer or colder than T^{critical}, the instrument outputs a negative and positive signal respectively; the signal remains positive as long as the instrument radiates more than it absorbs.

Having established the instrument radiance, it may then be used to calculate the spectral responsivity which, from extensive ground testing, is known to be linear:

$$R(\tilde{\nu}) \;=\; \left| \frac{\text{FT}[\mathcal{I}(L)^{\text{instru}} \;-\; \mathcal{I}(L)^{\text{target}}]}{B(\tilde{\nu}, T)^{\text{instru}} \;-\; B(\tilde{\nu}, T_0)^{\text{target}}} \right| \tag{2.18}$$

[137]. Due to its linearity, two temperature-calibration targets are required to establish the responsivity relationship. For the CIRS project, a shutter reflecting the interior of the instrument and observations of deep space (approximately 2.7 K) were chosen for T and T_0 respectively.

In order to carry out the radiometric calibration, each measured interferogram requires a reference interferogram measured under similar spectral conditions. A number of deep-space calibrations, at multiple spectral resolutions, were conducted during each Subphase of the Jupiter encounter to facilitate the radiometric calibration of the CIRS spectra. To minimise contamination from planetary emission, deep-space was defined as 2 mrad off the limb (the 1 bar level) of the planet; 4.3 mrad in the case of FP1.

Within the CIRS calibration pipeline, an algorithm was used to locate both deep-space and shutter scans for use in the calibration. However, the algorithm was relatively unsophisticated and rarely chose the best set of scans – trade-offs in terms of thermal stability, number of scans and scan resolution hampered selection. Thus, ATMOSA through C have been optimised in their calibration through the hand-picking of deep-space and shutter scans (ATMOSD was not hand-pick calibrated because of time constraints). This comes at a cost however, as the largest set of homogeneous deep-space scans were recorded at a slightly lower spectral resolution (92 *versus* 96 RTI). Hence, the calibration slightly degrades the resolution (to 2.97 cm^{-1}) at the cost of improving the quality.

2.4.2 Noise Equivalent Spectral Radiance

The Noise Equivalent Spectral Radiance (NESR) is another calibration diagnostic determined during ground testing. The NESR is the radiance corresponding to a signal-to-noise-ratio:

$$\mathrm{SNR}(\tilde{\nu}) = \frac{A(\tilde{\nu})}{\mathrm{NESR}(\tilde{\nu})}. \tag{2.19}$$

of unity, and represents the one-sigma uncertainty in an individual spectrum. The NESR gives the noise on an observation as a function of frequency. This is important because, following the radiometric correction, the SNR is no longer independent of wavenumber.

2.4.3 Systematic Errors

The data returned by the CIRS instrument suffers from a several systematic errors, each of which shape the results of the thesis in their own way.

Interference: CIRS suffers from at least three systematic interferences: a 0.5 Hz, an 8 Hz and a wandering sine wave. The 0.5 Hz signal is thought to be caused by the querying of the CIRS Bus Interrupt Unit by the Cassini data system, the act of which affects a transfer of cached data [139]. The 0.5 Hz equates to a repeat cycle every two seconds (every 16 RTI) so that any observations with a duration which is an even whole number will have the same spikes in the same place on every scan.

The 8 Hz interference is due to the RTI counter and appears clearly in the spectrum at 8 Hz, 16 Hz, 24 Hz on FP1 and also at 32 Hz and 40 Hz on FP3 [139]. A surprising silver lining to the RTI interference is the observation that, due to its synchronised nature at every RTI, the spikes are expected to cancel out (or at least reduce in size) when the interferograms are subtracted during the calibration procedure.

The interferogram sine wave on the other hand is not nearly as predictable and is suspected to have a thermal source. The frequency and amplitude of the sine wave changes with time with a weaker beat frequency for frequencies greater than 8 Hz [139]. Although a range of solutions exist for removing these interferences, none have been seriously attempted with the Jupiter encounter data. One reason for this is that the Jupiter spectrum may show spectral features of interest at similar positions to the interference spikes. As the interference amplitudes vary, should the spikes be removed, it could make interpretation problematic.

Pointing: The CIRS FOV has been found to be displaced +1.70 ± 0.02 mrad X and -0.04 ± 0.07 mrad Z (in spacecraft coordinates) with respect to the narrow angle camera [183]. This is of interest as the narrow angle camera boresight is used for targeting by the instruments aboard the Remote Sensing Pallet. Yet despite the displacement, spectra of both Callisto and Io have successfully been obtained during the satellite searches. In addition, FP4 detector 10 appears to be somewhat out of position (+0.05 mrad X, -0.02 mrad Z) relative to the other 19 detectors [183].

Detector Response: Detector 1 of FP3 was determined [137] to have an anomalous response compared to the other detectors during ground-truthing. Although both FP3 (photoconductive – PC) and FP4 (photovoltaic – PV) consist of an array of ten detectors,

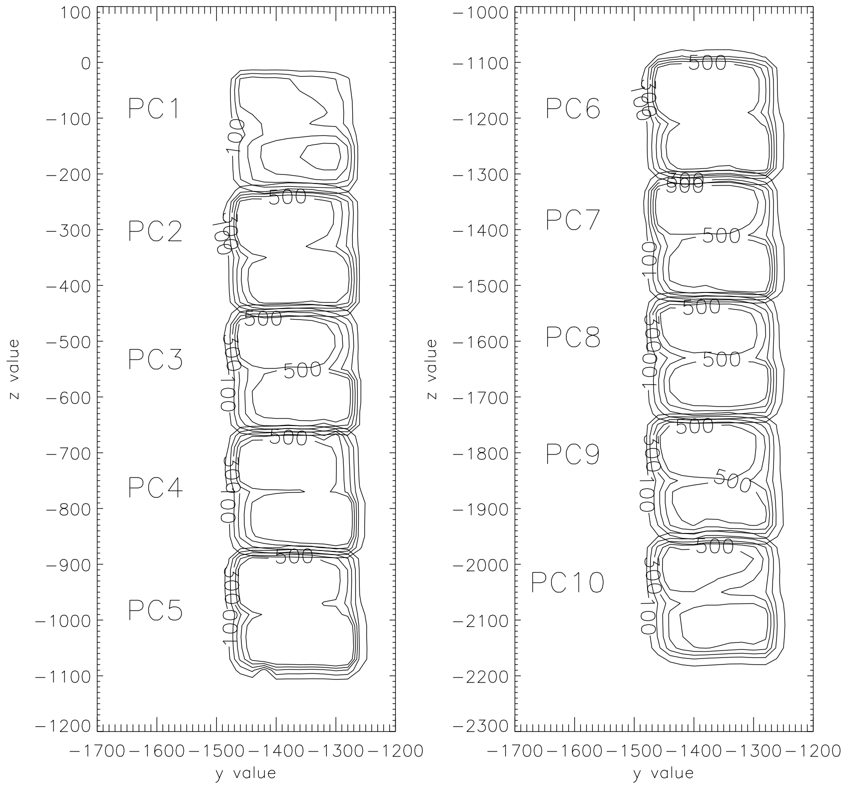

Figure 2.8: Focal Plane 3 detector response: the contour levels are in 100, 200, 300, 400 and 500 "counts" while Y and Z have units of μm. Note the weak, asymmetric nature of detector PC1. [137]

FP4 is more sensitive than FP3 due to the nature of the detectors. The response is also quite different. Whereas the PV detectors have a nearly uniform "top-hat" response, the PC detectors have a twin-lobed profile – see Figure 2.8. Detector 1 of FP3 was determined to both have a weaker response than the other PC detectors and also be asymmetric with one lobe significantly stronger than the other.

The bifurcated response of PC1 will likely only be a problem for limb observations (of which there were none during the Millennium Fly-by). This is because the asymmetrical response could conceivably weight the measurement towards higher or lower altitudes (depending on the relative orientation of the detector to the vertical). Although symptomatic of all the PC detectors in general (where one lobe is potentially, if only marginally, stronger than the other), it is particularly exacerbated in the case of PC1.

Radiometric calibration: Some subtle north-south banding, equivalent to a brightness temperature of 1 to 2 K [138], can be seen in ATMOSB (Figures 4.13, 4.14 and 4.16). The radiometric striping is due to a thermal drift within the instrument when it unexpectedly changed calibration-modes [94]. Essentially, the actively-controlled cooler temperature changed from one temperature setting to another halfway through the scan. This may potentially be related to an instrument temperature fluctuation of approximately 0.4 K reported elsewhere [39]. Only spectra from focal-planes 3 and 4 were affected.

Unrelated, but similarly affecting the radiometric calibration is the inability of the reference laser to maintain the same wavelength between observations. The laser appears to initialise at a slightly different wavelength (round or about the reference wavelength at 0.784 μm) each time it is turned on. Consequently, the number of measured samples is "mildly ambiguous" [95], resulting in different output-spacing between observations of the same resolution.

Chapter 3

Radiative-Transfer Modelling

Contents

This chapter will summarize the radiative-transfer modelling methods used in the thesis.

The theory of how atmospheric parameters such as temperature and composition relate to the radiation field and how they can be efficiently modelled and retrieved, is also discussed. Using the atmospheric information outlined in Chapter 1, this chapter forms the basis for the retrieval validation and composition results of Chapters 4 and 5.

3.1 Molecular Absorption

Polyatomic molecules like PH_3 absorb and radiate in the infrared by the excitation of the bonds between their constituent atoms. Since each molecule has its own unique set of energy states, absorption/emission spectra can be used to identify the characteristics of particular species.

The energy state of a molecule can be conveniently separated into four parts: electronic, due to electron excitation; vibrational, the periodic displacement of the atoms from their equilibrium position; rotational, by virtue of rotation about the molecule's centre of mass; and translational, the motion of the molecules relative to each other. The energy states are quantized and a molecule can exist in any (or all) of the excited states at any given time. The magnitudes of the energy states are however, significantly different such that they can be treated separately. Only transitions between vibrational and rotational energy states influence the radiance within the CIRS spectral range, so only they are addressed here.

The quantum-mechanical theory of molecular band spectra has been set out clearly in many textbooks (*e.g.* Herzberg 1945: [87], Banwell and McCash 1994: [14]) and so is not discussed here. However, it is important to note that the presence of simultaneous vibration and rotation causes the spectrum to show a series of lines grouped around the central vibration frequency. While the central frequency is indicative of the composition of the gas (atomic and/or molecular) producing the line, the strength and shape of the line contains information on the abundance of the gas, as well as the temperature and pressure of the environment. This knowledge was used in the selection of spectral windows for the retrieval of temperature and composition discussed later.

3.2 Radiative-Transfer Equation

The basis for all radiative-transfer modelling is the radiative-transfer equation. This is developed here from first principles, along with the process by which it was evaluated within this thesis, the correlated-k method. Correlated-k has several useful applications, some of which like multiple-scattering and overlapping absorption are also summarized. This discussion is complementary to that of §3.3 in outlining how temperature and composition relate to the radiation field.

Radiative-transfer modelling is the development and application of algorithms to simulate the interaction of radiation with a chosen medium, in the case of this thesis, the atmosphere of Jupiter. It is a complex physical process involving the consideration of such diverse influences as particle sizes, shapes and distributions, spectral absorption coefficients, line positions and strengths, and the laws of physics governing the interaction of light and materials.

Provided the physics involved are well understood, models can be constructed which accurately simulate how energy is deposited in an atmosphere. For example, in the

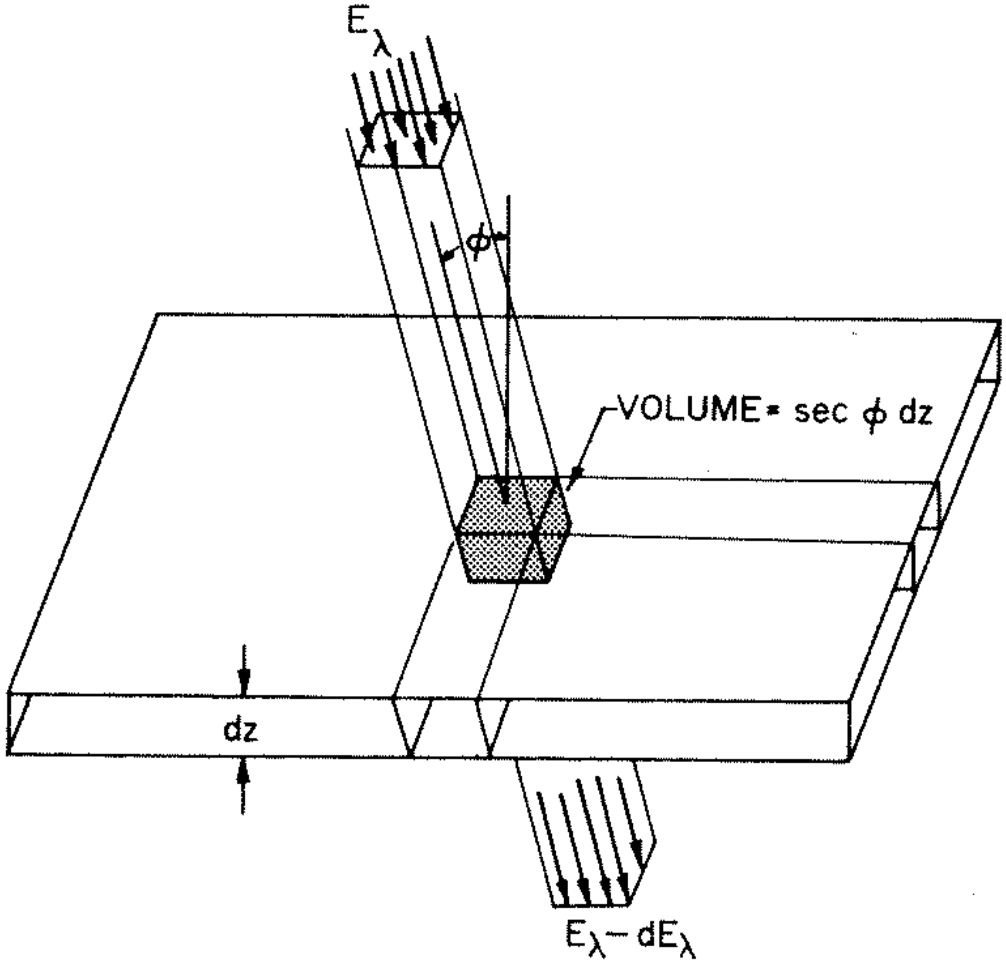

Figure 3.1: Atmospheric absorption of radiation: the depletion of an incident beam (of unit cross section) while passing through an absorbing layer of infinitesimal thickness. [201]

absence of scattering, the absorption of a parallel beam of radiation as it passes downward through a horizontal layer of infinitesimal thickness, dz, is proportional to the number of absorbing molecules per unit area along the path (Figure 3.1). This relationship can be described in the form:

$$dI(\tilde{\nu})^{\text{absorption}} = -\, k_{\tilde{\nu}}\, \rho\, \sec\phi\, I(\tilde{\nu})\, dz, \tag{3.1}$$

where $k_{\tilde{\nu}}$ is the mass absorption cross-section (hereafter referred to as the absorption coefficient) at wavenumber $\tilde{\nu}$, ρ is the density of the gas, ϕ is the zenith angle, $I(\tilde{\nu})$ is the radiance[1] and z is height. By Kirchhoff's Law, radiation is also emitted by the absorbing gas and can be similarly described by:

$$dI(\tilde{\nu})^{\text{emission}} = +\, k_{\tilde{\nu}}\, \rho\, \sec\phi\, J(\tilde{\nu})\, dz, \tag{3.2}$$

where $k_{\tilde{\nu}}$, ρ and ϕ are the same as before and $J(\tilde{\nu})$ is the source function in the absence of scattering. Under conditions of local thermodynamic equilibrium (LTE – where the population density is governed by Boltzmann statistics), $J(\tilde{\nu})$ is equal to $B(\tilde{\nu}, T)$, the Planck function for blackbody emission at temperature T. Thus, any change in the intensity resulting from the interaction of matter and radiation is the sum of Equations 3.1 and 3.2:

$$dI(\tilde{\nu}) = dI(\tilde{\nu})^{\text{absorption}} + dI(\tilde{\nu})^{\text{emission}} = k_{\tilde{\nu}}\, \rho\, \sec\phi\, dz\, [B(\tilde{\nu}, T) - I(\tilde{\nu})]. \tag{3.3}$$

The right-hand side of this expression, known as *Schwarzchild's equation*, is the basis for all radiative-transfer calculations. Schwarzchild's equation is useful as it describes how radiation interacts with an infinitesimally-thin slice of atmosphere. However, in order to determine the measured radiance from a layer of finite-thickness, Equation 3.3 must be

---

[1] Much of the early work on radiative transfer comes from astrophysical research which predated the adoption of Systéme International d'Unités (SI). In these early works, the energy per second per solid angle per unit area is commonly referred to as *intensity* and consequently denoted I. In this work, I is maintained, however SI units and nomenclature (*i.e.* the "radiance" cited here) are used.

developed further. To this end,

$$\text{optical thickness} \;\equiv\; \chi(\tilde{\nu}) \;=\; \sec\phi \int_{z_1}^{z_2} k_{\tilde{\nu}}\, \rho\, dz \tag{3.4}$$

and

$$\text{transmissivity} \;\equiv\; \tau_{\tilde{\nu}} \;=\; \exp(-\chi(\tilde{\nu})) \tag{3.5}$$

need to be introduced[2]. In this way, the dimensionless $\chi(\tilde{\nu})$ may be used to represent the cumulative depletion to a beam of radiation passing through an atmospheric layer. The formal solution to Schwarzchild's equation can be formulated with the aid of an integrating factor; multiplying each side of Equation 3.3 by the transmissivity allows the expression to be rewritten:

$$\frac{d}{d\chi(\tilde{\nu})}\left[\exp(-\chi(\tilde{\nu}))\, I(\tilde{\nu})\right] \;=\; \exp(-\chi(\tilde{\nu}))\, B(\tilde{\nu}, T). \tag{3.6}$$

Integrating Equation 3.6 from the surface to the "top" of the atmosphere (considered to be at infinity), results in:

$$\begin{aligned} I(\tilde{\nu}) \;&=\; B(\tilde{\nu}, T_0)\, \exp(-\chi(\tilde{\nu}, 0)) \;+\; \int_0^{\chi(\tilde{\nu},0)} B(\tilde{\nu}, T)\, \exp(-\chi(\tilde{\nu}, z))\, d\chi(\tilde{\nu}, z), & (3.7) \\ &=\; B(\tilde{\nu}, T_0)\, \tau(\tilde{\nu}, 0) \;+\; \int_{\tau(\tilde{\nu},0)}^{1} B(\tilde{\nu}, T)\, d\tau(\tilde{\nu}, z), & (3.8) \end{aligned}$$

where $B(\tilde{\nu}, T_0)$ is the Planck function representing the "surface" emission at T_0 and $\tau(\tilde{\nu}, 0)$ is the transmission of the whole atmosphere. Equation 3.8, known as the *radiative-*

---

[2] When the optical thickness is measured downwards from the top of the atmosphere it is known as the optical depth.

transfer equation, comprises two parts: the first term describes the exponential decrease with optical path-length of the radiation from the surface. The second term describes the cumulative emission and absorption between some level and the top of the atmosphere. The location of this level is accurately described by either the *transmission-weighting function*, $d\tau/dz$, or the *contribution function*, $B(\tilde{\nu}, T)\ d\tau/dz$. These functions describe the variation of thermal emission with height and are useful in determining the pressure-level that contributes most to the outgoing intensity.

If T and ρ are known as a function of height, and assuming a known wavenumber dependence of $k(\tilde{\nu})$ and $B(\tilde{\nu}, T)$, then Equation 3.8 can be used to numerically evaluate the radiance at a single wavenumber. However, this represents the monochromatic radiance as viewed at angle ϕ. A real atmosphere is composed of spectrally-extended sources with contributions from an infinite number of directions. In order to faithfully reproduce the radiance that would be observed by an instrument attached to a telescope or spacecraft, several further integrations are required; these are the angular integration, the integration over frequency and the vertical integral (Equation 3.8). In other words,

$$\text{Observed Flux} \equiv F = \int_{\text{angular}} \int_{\text{wavenumber}} \int_{\text{path}} B_0\, \tau_0 \;+\; \int_{z_0}^{\infty} B\, \frac{d\tau}{dz}\, dz\, d\tilde{\nu}\, d\Omega. \qquad (3.9)$$

Thus, a complete calculation is very complex. The method is usually carried out by a computer where a premium is placed on computational economy as the radiative calculations involved can create an unacceptable burden unless approximated. Fortuitously, as Jupiter lacks a solid surface, τ_0 equals zero and the problem is somewhat simplifies.

The angular integration involves both the integration over the field-of-view and the scattering solid-angle. By considering the restricted example where the radiance is measured at a distance (well outside the atmosphere), using a collimated, nadir-viewing spectrometer, the integration over the FOV can be eliminated. The scattering integration however cannot be eliminated and is usually normalized over the solid-angle to account for all possible angles between the incident and scattered radiation.

The frequency integral is evaluated by summing over a range suitable to the spectral resolution of the instrument. This is usually narrow enough to neglect changes in the source function, but wide enough to contain many lines. The calculation of the frequency integral is, in principle, achievable given adequate information about the intensities, positions, widths and shapes of the spectral lines in any given spectral region. However in practice, simplified methods are employed to minimise the computational burden.

The vertical integral is important in determining the transmission terms in Equation 3.8. The traditional, and most accurate, method of calculating the transmission is the line-by-line (LBL) method. The LBL method calculates the transmission for a selected band by integrating relatively narrow spectral intervals. Such individual calculations are required to adequately resolve the rapidly varying effects of the absorption lines. An alternative to the LBL method of radiative-transfer modelling is the *correlated-k* method.

3.2.1 Correlated-k

The correlated-k method replaces the rapidly varying absorption-coefficient function of the LBL method with an equivalent and much smoother function that is more amenable to numerical integration over wider intervals. In essence, correlated-k utilises the observation that, over a narrow spectral range, the rapidly oscillating absorption coefficient, k, attains the same value many times (at slightly different wavenumbers); each time resulting in the same intensity and radiative flux. Limited tests [42, 68] have shown that the correlated-k method can be potentially as accurate as LBL calculations, provided exact *k-distributions* can be found.

For the purposes of discussion, consider a "homogeneous" atmosphere, that is, one of constant pressure and temperature. Within such an atmosphere, the monochromatic absorption coefficient, $k_{\tilde{\nu}}$, is constant along all atmospheric paths and the spectrally-integrated transmission is:

$$\bar{\tau}(u) = \frac{1}{\Delta\tilde{\nu}} \int_{\Delta\tilde{\nu}} \exp(-k_{\tilde{\nu}}\, u)\, d\tilde{\nu}, \tag{3.10}$$

where, as $k_{\tilde{\nu}}$ is constant, the integral over the absorber concentration simplifies to just the absorber amount, $u = \int \rho(z)\, dz$. Thus, unlike the LBL approach, it is of no importance where in a frequency interval a particular absorption coefficient occurs; it is sufficient to know what fraction of the frequency domain, $f(k)dk$, is occupied by the absorption coefficients [77]. Thus, the transmittance is independent of the ordering of the absorption coefficients within a given spectral interval. The computational efficiency can thereby be improved by replacing the integration over wavenumber of Equation 3.10 with an integration of the frequency distribution, $f(k)$. Following the change in variable, the spectral transmission can be re-written:

$$\bar{\tau}(u) \;=\; \int_0^\infty \exp(-k\,u)\,f(k)\,dk. \tag{3.11}$$

Thus, the correlated-k method is potentially as accurate, yet more efficient, than the line-by-line method.

The frequency distribution is also sometimes referred to as *k-spectra* or the probability distribution due to its normalization over the spectral interval. Since Equation 3.11 is in the form of the standard Laplace transform, and because the spectral transmittance can be expressed in terms of an exponential function (Equation 3.5), the probability distribution function is the inverse Laplace transform of the spectral transmittance:

$$f(k) \;=\; \mathcal{L}^{-1}\,[\bar{\tau}(u)]. \tag{3.12}$$

Assuming $f(k)$ can be determined, Equation 3.12 provides a computationally-efficient way for solving the transmissivity. Taking advantage of k's highly repetitive nature, the reordering of the absorption coefficients into a *cumulative frequency distribution*:

$$g(k) \;=\; \int_0^k f(k)\,dk, \tag{3.13}$$

replaces the tedious wavelength integration of Equation 3.10 with a physically equivalent function that is easier to integrate. Since $f(k)\;dk$ represents the fraction of the frequency domain occupied by absorption coefficients between k and $k\,+\,dk$, the limit of the integral as k tends to infinity is unity. As $g(k)$ is monotonic, it is possible to invert it unambiguously to define the k-distribution:

$$k(g) = g^{-1}(k). \tag{3.14}$$

The k-distribution profile (as exemplified in Figure 3.2) is simply the result of the absorption coefficients being regrouped and ranked according to strength [76]. By using the g function, the spectral transmittance may again be re-written:

$$\bar{\tau}(u) = \int_0^1 \exp(-k(g)\, u)\, dg. \tag{3.15}$$

For a homogeneous path, the transmission can be calculated using Equation 3.10 via LBL spectral integration, by integrating over the frequency distribution as defined in Equation 3.11, or by integrating over the k-distribution of Equation 3.15. While all three approaches produce the same transmission for a given absorber amount, performing the integration over the k-distribution is clearly the simplest.

Dividing $g(k)$ into N intervals such that the variation of k with g is sufficiently well sampled, the mean transmission of a path may be calculated:

$$\bar{\tau}(u) = \sum_i^N \exp(-\bar{k}_i\, u)\, \Delta g_i, \tag{3.16}$$

where $\bar{k}_i$ is the mean absorption coefficient in the g-interval.

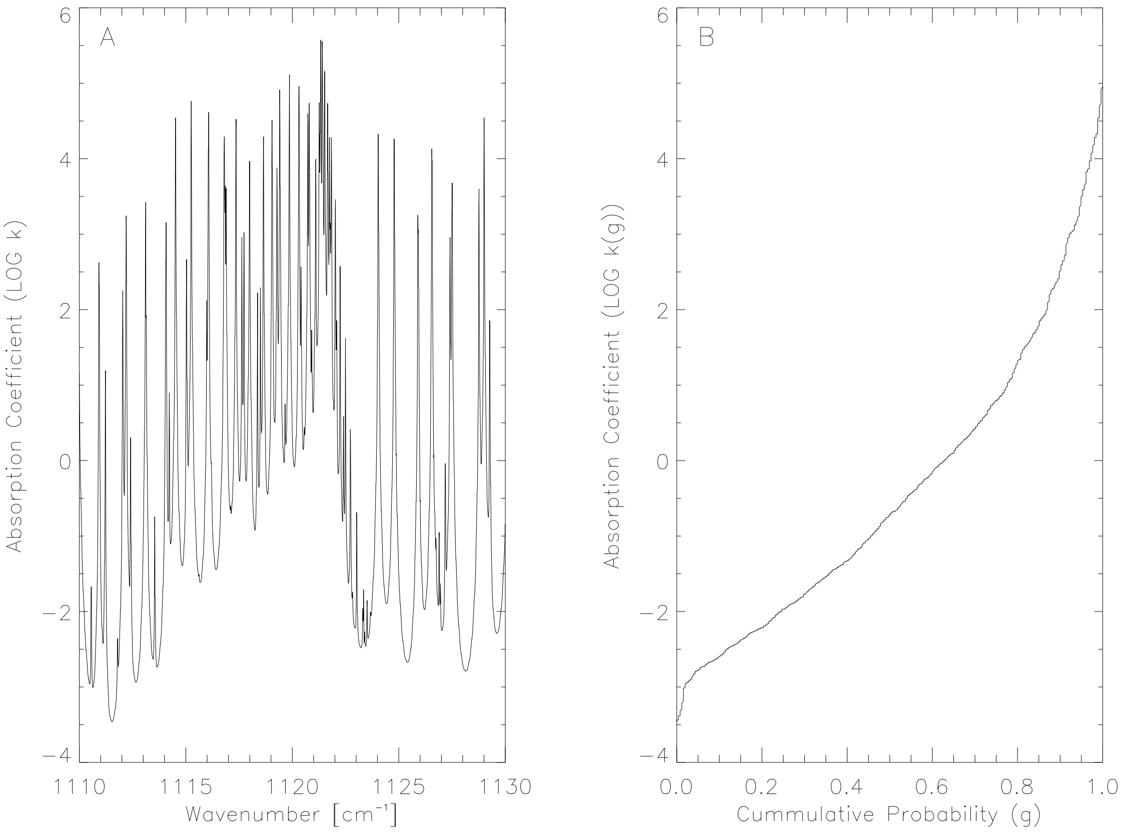

Figure 3.2: Example absorption-coefficients and corresponding k-distribution. A: PH_3 absorption spectrum at 0.1 bar, 115 K. B: The absorption coefficients ranked as a function of cumulative probability function (the k-distribution). (After Lacis and Oinas 1991: [111])

Vertical inhomogeneity: In a real atmosphere however, pressure and temperature gradients produce vertically-inhomogeneous absorber paths. Despite the inhomogeneity, the atmosphere can be approximated by a series of homogeneous layers. It can be shown that the monotonic ordering of the absorption coefficient strengths in the k-distributions implicitly preserves the monochromatic structure of the atmosphere at different pressure levels [111]. That is, for any given spectral interval, k-distributions at all locations along an inhomogeneous path are simply correlated in frequency space. Thus, the combined transmission of M layers can simply be written:

$$\bar{\tau}(u) \;=\; \sum_{i}^{N} \exp\left(-\sum_{j}^{M} \bar{k}_{ij}\, \Delta u_j\right)\, \Delta g_i. \tag{3.17}$$

It is from this relational-property that correlated-k gets it name; the fact that the transmissions can be correlated between atmospheric levels.

Since $g(k)$ is a smooth function, a relatively small number of computational points are required to achieve a high degree of accuracy. Consequently, the correlated-k method offers a speed advantage over LBL calculations. Aside from the principal advantage of computational-efficiency, correlated-k may also incorporate multiple scattering and the absorption of overlapping species.

Overlapping absorption: In determining the overlapping absorption, $k_{\tilde{\nu}}$ can be expressed in terms of the contributions by individual lines, j, of a number of different (assuming uncorrelated) gases, l, via:

$$k_{\tilde{\nu}} \;=\; \sum_{j,l} S_j^l\, f_j^l\,(\tilde{\nu} \,-\, \tilde{\nu}_{0,j}^l) \,+\, k_{\tilde{\nu}}^c, \tag{3.18}$$

where S and $\tilde{\nu}_0$ are the central-line strength and frequency respectively, f is the normalized line profile and $k_{\tilde{\nu}}^c$ is the continuum coefficient. This is however only valid for a single homogeneous path. For a vertically-inhomogeneous atmosphere, the k-distributions for each respective species are determined and then ranked in order of strength and resampled as if due to one absorber alone.

Multiple scattering: The correlated-k method may also be used for scattering calculations. In optically-thick atmospheres, aerosols are more likely to scatter previously-scattered photons than the incident radiation. Therefore, the source function of Equation 3.2 is no longer due to the thermal emission alone, but is now the sum:

$$J(\tilde{\nu}) \;=\; \varpi_{\tilde{\nu}}\, J(\tilde{\nu})^{\text{scattering}} \;+\; (1 \;-\; \varpi_{\tilde{\nu}})\, J(\tilde{\nu})^{\text{thermal}}, \tag{3.19}$$

where $\varpi_{\tilde{\nu}}$ is the single-scattering albedo:

$$\varpi_{\tilde{\nu}} \;=\; \frac{k_{\tilde{\nu}}^{\text{scattering}}}{k_{\tilde{\nu}}^{\text{scattering}} \;+\; k_{\tilde{\nu}}^{\text{absorption}}}. \tag{3.20}$$

The single-scattering albedo represents the fraction of incident radiation that undergoes a single scattering event. As the scattering field due to multiple scattering is significantly complex, the approximation of single-scattering for multiple-scattering is sometimes applied for computational efficiently.

Although the thermal source function may be considered constant over small spectral intervals, the scattering source function cannot as it is proportional to the intensity, which itself is a function of $k_{\tilde{\nu}}$ [122]. However, if $g(k)$ is any function of the radiation field, including the scattering intensity, that can be calculated for a single value of k [77], then it can also be used to give the spectrally integrated transmission:

$$\bar{\tau} = \sum_i^N \tau(\chi_i, \varpi_i)\, \Delta g_i \tag{3.21}$$

due to both scattering and absorption/emission. In this case, χ_i is the total optical thickness and ϖ_i is the bulk-atmospheric albedo:

$$\varpi_i = \frac{\chi^{\text{scattering}}}{\chi^{\text{extinction}} + k_{\tilde{\nu}}^{\text{absorption}}\, u}, \tag{3.22}$$

where the absorption coefficient takes into account absorption both by the aerosol particles and by the gas in between them.

3.3 The Inverse Problem

Inverse modelling, otherwise known as “retrieval” or “the inverse problem”, is described here. Inverse modelling is later used in Chapter 4 to retrieve temperature, composition and cloud properties from the Cassini/CIRS Jupiter-encounter data.

The general retrieval method has two main components: a forward model which uses an initial guess to calculate synthetic radiances and an iterative routine which systematically searches for the best estimate consistent with the available information. The terminology is explained and the solutions for both the linear and non-linear case are shown along with the related error analysis. The theory and definitions largely follow Rodgers 2000: [161].

3.3.1 Forward Model

Consider a set of m measurements, determined from a set of n input parameters (the "state vector"). The measurements, $\mathbf{y}$, known within the accuracy of the experimental error, ε, are related to the state vector by means of a forward model, $\mathbf{F}(\mathbf{x})$. Thus, the measurement process may be shown to be:

$$\mathbf{y} = \mathbf{F}(\mathbf{x}) + \varepsilon. \tag{3.23}$$

For example, consider the radiative-transfer equation (Equation 3.8). For an optically thick atmosphere (such as Jupiter's), the atmospheric transmission can be neglected so that $\mathbf{y}$ may represent the measured spectral radiances, $\mathbf{F}(\mathbf{x})$ the physics of the measurement (*i.e.* the radiative-transfer theory required to related the state to the measured signal as well as a full description of the measuring instrument) and $\mathbf{x}$ the atmospheric temperature, composition and/or cloud opacities. For a given atmospheric state, the forward model simulates the radiance within the accuracy of the experimental error.

3.3.2 Inverse Model

The inverse model performs the opposite task to the forward model; to learn as much as possible about $\mathbf{x}$ given $\mathbf{y}$ within ε. Or, continuing the example above, to infer the atmospheric state from the measured radiation field.

The solution to Equation 3.23 would appear to be $\mathbf{x} = \mathbf{K}^{-1}\mathbf{y}$, where $\mathbf{K}$ is some function which serves as a conversion matrix between the measurement and state vectors. In which case, **K** would be of dimensions $m \times n$. However, this represents an ill-conditioned retrieval as the number of measurements can be greater, equal, or even less than, the number of unknowns. Such ambiguity of retrieval can lead to an unstable solution and/or unacceptable amplification of errors. Given these considerations, the best estimate solution to the forward model is expressed:

$$\hat{\mathbf{x}} = \mathbf{D}\mathbf{y}, \tag{3.24}$$

where **D** is the retrieval *gain matrix*. In general, the retrieval problem does not have a unique solution; the best estimate of the solution being selected from a number of possible solutions.

3.3.3 Error Analysis

The extent to which $\hat{\mathbf{x}}$ is a good approximation of $\mathbf{x}$ depends on the accuracy of $\mathbf{F}(\mathbf{x})$ in representing the physical processes in the atmosphere and the noise level on the spectrum ε. In general, the forward model depends not only on the state vector $\mathbf{x}$, but also on a number of other parameters, $\mathbf{b}$:

$$\mathbf{y} = \mathbf{F}(\mathbf{x}, \mathbf{b}) + \varepsilon \tag{3.25}$$

which are not included in the state vector. Such parameters (for example the abundance profiles of additional species) contribute to the radiance, and so are required for the forward model, but are not themselves retrieved. The inclusion of **b** also contributes to the uncertainty of the model such that ε can be said to contain random measurement noise and a series of systematic errors:

$$\varepsilon = \varepsilon^{\text{random}} + \sum \varepsilon^{\text{systematic}}. \tag{3.26}$$

An example systematic error (the error that is constant between repeated measurements) is the forward-modelling error due to both approximations in the model and incorrect assumptions about $\mathbf{b}$. The systematic error provides the lower limit below which errors cannot be reduced by averaging.

Covariance: As every measurement or retrieval is made to finite accuracy, matrices of covariance are used to represent the uncertainty with respect to each variable. For example, element i, j of the measurement covariance matrix, S_ε, is given by:

$$S_{ij} = \mathcal{E}\{\varepsilon_i \varepsilon_j\}, \tag{3.27}$$

where $\mathcal{E}$ is the expectation value and ε is the measurement error. Usually, only the diagonal elements of the covariance are non-zero and contain the associated variance of the individual elements (*e.g.* S_{ii}). However, the off-diagonal elements can also be used to represent the correlation $\left(S_{ij}/\sqrt{S_{ii} \times S_{jj}}\right)$ between errors.

3.3.4 Linear Optimal Estimation

The linear solution to the inverse problem starts with a linear forward model. Forcing Equation 3.23 to be linear is accomplished by taking the first-order Taylor expansion about a reference state, $\mathbf{x_0}$:

$$\mathbf{y} - \mathbf{F}(\mathbf{x}_0) = \frac{\partial \mathbf{F}}{\partial \mathbf{x}}(\mathbf{x} - \mathbf{x}_0) + \varepsilon, \tag{3.28}$$

known to be close to the solution $\hat{\mathbf{x}}$. The matrix of derivatives, $\partial \mathbf{F}/\partial \mathbf{x}$, of Equation 3.28 represents the sensitivity of the measurement to a change in the state vector. Such a Jacobian transformation is commonly referred to as the *kernel function* $\mathbf{K}$, whose elements may be defined as:

$$K_{ij} = \left(\frac{\partial y_i}{\partial x_j} \right)_{x_0} . \tag{3.29}$$

Assuming Gaussian statistics[3], Equation 3.28 can be simplified by setting the origins to $\mathbf{x}_0$ and $\mathbf{F}(\mathbf{x}_0)$ resulting in

$$\mathbf{y} = \mathbf{K}\mathbf{x} + \varepsilon. \tag{3.30}$$

where $\mathbf{K}$ satisfies $\mathbf{DK} \equiv \mathbf{I}$ (a unit matrix).

The standard technique of solution for the inverse model (Equation 3.24) is the least squares fit. The least squares method minimises the sum-square difference between the measured and forward-modelled spectra, subject to minimum departure from the *a priori*

---

[3] Gaussian statistics are usually a good approximation for the random noise component in real measurements. For a linear forward model governed by Gaussian statistics, the most probable state is the same as the expected state since the probability density function is symmetric about its maximum.

values, $\mathbf{x}_a$:

$$\phi = [\mathbf{y} - \mathbf{F}(\widehat{\mathbf{x}})]^T \mathbf{S}_\varepsilon^{-1} [\mathbf{y} - \mathbf{F}(\widehat{\mathbf{x}})] + (\widehat{\mathbf{x}} - \mathbf{x}_a)^T \mathbf{S}_a^{-1} (\widehat{\mathbf{x}} - \mathbf{x}_a). \tag{3.31}$$

Any solution which minimises Equation 3.31, the *cost function*, is known as an *optimal estimation* retrieval. Note that the smaller the variance, the larger the contribution of a given variable to the cost function. Thus, the degree to which $\widehat{\mathbf{x}}$ will depart from $\mathbf{x}$ will depend upon the relative size of the errors contained within $\mathbf{S}_\varepsilon$ and $\mathbf{S}_a$.

Model constraints: If the ensemble of potential solutions can be described in terms of measurement and *ad hoc* constraints, the problem can be constrained to a point at which it is well-conditioned. An example measurement constraint is the assumption that the continuous properties of the atmosphere (*e.g.* temperature) are smoothly varying and can be represented by a finite set of parameters. Such an assumption allows the number of unknowns to be reduced to a value less than the number of measurements.

Example *ad hoc* constraints include smoothing, independent measurement and/or modelling. Such *ad hoc* constraints are called *a priori* information due to their knowledge prior to the measurement and have an associated *a priori* covariance matrix, $\mathbf{S}_a$.

Assuming a linear forward model, Gaussian error distribution and *a priori* knowledge of the state, the optimal estimation solution may be shown to be:

$$\widehat{\mathbf{x}} = \mathbf{x}_a + \mathbf{S}_a \mathbf{K}^T (\mathbf{K} \mathbf{S}_a \mathbf{K}^T + \mathbf{S}_\varepsilon)^{-1} (\mathbf{y} - \mathbf{K} \mathbf{x}_a). \tag{3.32}$$

Note that, the errors associated with linearizing the forward model in this way must be smaller than the measurement errors or the required accuracy of the solution.

3.3.5 Non-linear Optimal Estimation

In practice however, the forward model is rarely linear. While the measured radiance of the previous example may be considered linearly-related to temperature and concentration in cases of weak absorption, it is not true in cases of strong absorption. Small changes in the composition strongly affect the atmospheric transmission, and thus **K**. If the problem is non-linear, it is necessary to iteratively find a solution which fits the measurements. Extending the principles of optimal estimation to the non-linear case, the i^{th} estimate of the atmospheric state is:

$$\mathbf{x_{i+1}} = \mathbf{x_a} + \mathbf{S}_a\mathbf{K}_i^T(\mathbf{K}_i\mathbf{S}_a\mathbf{K}_i^T + \mathbf{S}_\varepsilon)^{-1}[\mathbf{y} - \mathbf{F}(\mathbf{x}_i) + \mathbf{K}_i(\mathbf{x_i} - \mathbf{x_a})], \tag{3.33}$$

where $\mathbf{K}_i$ is the kernel function calculated for the i^{th} state vector, $\mathbf{x}_i$. After every iteration, the cost function is re-evaluated.

If the problem is not too non-linear, a modified form of Newton's Method of iteration:

$$\mathbf{x'_{i+1}} = \mathbf{x_i} + \frac{\mathbf{x_{i+1}} - \mathbf{x_i}}{1 + \lambda}, \tag{3.34}$$

may be used to find $\hat{\mathbf{x}}$ where $\mathbf{x'_{i+1}}$ is the value used in evaluating ϕ. A Levenberg-Marquardt-type braking parameter, λ [115, 128], is used to moderate the step between iterative estimates of the state vector in an effort to prevent the model becoming unsta-

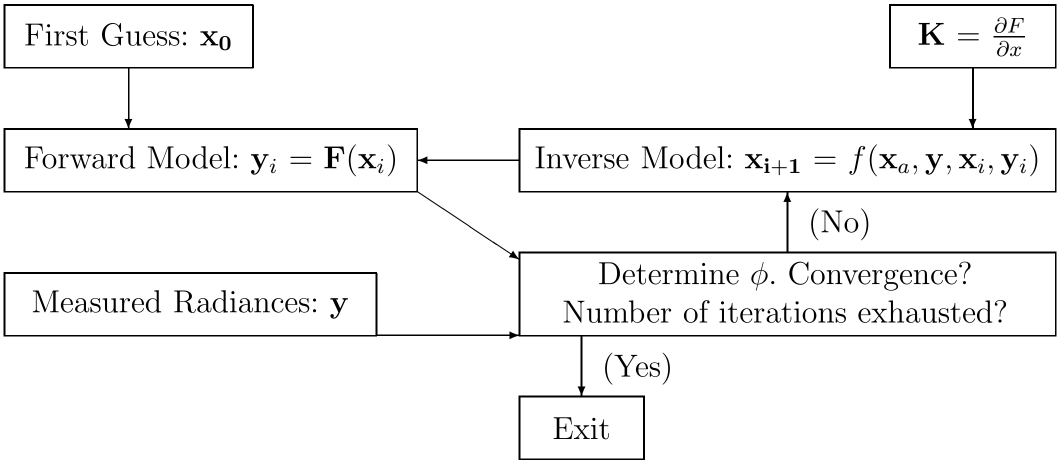

Figure 3.3: Diagrammatic methodology of the inverse problem. The forward model calculates a first guess based on the *a priori* information. This computed radiance is then compared to the measured radiance and the cost function evaluated. If the convergence criteria are not met, an inverse algorithm is applied to the synthetic radiances utilising the kernel function's contribution. This results in the state vector being slightly modified. The state vector is then passed back into the forward model for re-computation. This cyclic routine is continued until either the convergence criteria are met or the number of iterations has been exhausted. At this point, the state vector has been "retrieved".

ble. Values of λ are chosen to given the "steepest descent" qualities of the Levenberg-Marquardt method far from the solution and Newtonian iteration near the solution. The iterations are stopped once a suitable convergence criterion (*e.g.* a reduction in the cost function, number of iterations) has been reached. A schematic of the retrieval methodology is presented in Figure 3.3.

3.4 Jovian Atmospheric State

The atmosphere of Jupiter has been qualitatively described in Chapter 1. In this section, the creation of a quantitative description of the atmosphere is discussed. Also discussed are the CIRS forward model and retrieval scheme, which are used to convert back and forth between the measured radiance and the parameterized atmospheric state in anticipation of the temperature, composition and cloud retrievals of Chapter 4.

3.4.1 Temperature Profile

Central to the description of the atmospheric state is the temperature-pressure-height profile. The assumed equatorial and equinoctial profiles (Figure 1.3) are based on the findings of the Galileo probe Atmospheric Structure Instrument with smoothing in the stratosphere to avoid local wave phenomena characterising global properties. The effective pressures and temperatures for each layer (of which there were 80 in total) were calculated as the mass-weighted means using a Simpson's Rule integration:

$$\bar{u} = \int \frac{du}{dz}\, dz, \qquad \bar{P} = \frac{1}{\bar{u}} \int P(z)\, \frac{du}{dz}\, dz, \qquad \bar{T} = \frac{1}{\bar{u}} \int T(z)\, \frac{du}{dz}\, dz. \tag{3.35}$$

Several constraints were applied to the temperature profile to maintain a physically-realistic solution. Below the tropopause (0.1 bar), the temperature was constrained not to decrease more rapidly with height than the dry, adiabatic lapse rate (approximately -2 K/km [120, 172, 190]). This reflected the observed hydrostatic stability of Jupiter's upper-troposphere. In addition, the temperature uncertainty was set such that it increased with altitude (from ± 5 K at four bars to ± 20 K at 0.4 μbar), forcing barotropic conditions at higher temperatures.

3.4.2 Composition Profiles

Profiles of the composition volume mixing ratios (VMRs, Figure 3.4) are also used to describe the atmospheric state. The VMRs come from a variety of sources, where "deep" abundance refers to the concentrations below the cloud layer.

Although photolysed in the stratosphere to produce C_2H_2 and C_2H_6, methane is for all intents and purposes uniformly distributed from the troposphere up to 10 μbar due to the recycling of these hydrocarbons in the lower atmosphere. Both C_2H_2 and C_2H_6 are produced throughout the stratosphere from photolysis as loss processes lag behind production. C_2H_4 and C_4H_2 on the other hand are non-equilibrium, intermediary species in the conversion from CH_4 to C_2H_2 and C_2H_6 and because of their short-lifetimes do not have extended profiles.

In accordance with the other CIRS teams, methane was divided into three separate VMRs, one for each isotope: CH_4, $^{13}CH_4$ and CH_3D. This was done to reflect the approximate D/H abundance of Jupiter (2×10^{-5} assuming no fractionisation) where $^{13}CH_4/CH_4$ was scaled to the terrestrial relative-abundance (1×10^{-3}). The remaining hydrocarbon profiles [164] were calculated using a one-dimensional photochemical model. The photochemical model [163], since updated to incorporate new rate-reaction data and CH_4-branching ratios, is based on the Galileo probe temperature-profile [172] with the deep abundance of CH_4 shifted ($\sim 5\%$) upwards to match the results of the GPMS experiment.

The ammonia profile was constructed from two variable parameters. The first parameter, the deep abundance (q_0), is assumed constant from the base of the profile to some level, P_0. In the case of the ammonia, P_0 was chosen to coincide with the NH_3 condensation level *circa* 0.7 bar. Above P_0, the ammonia abundance decreases with a

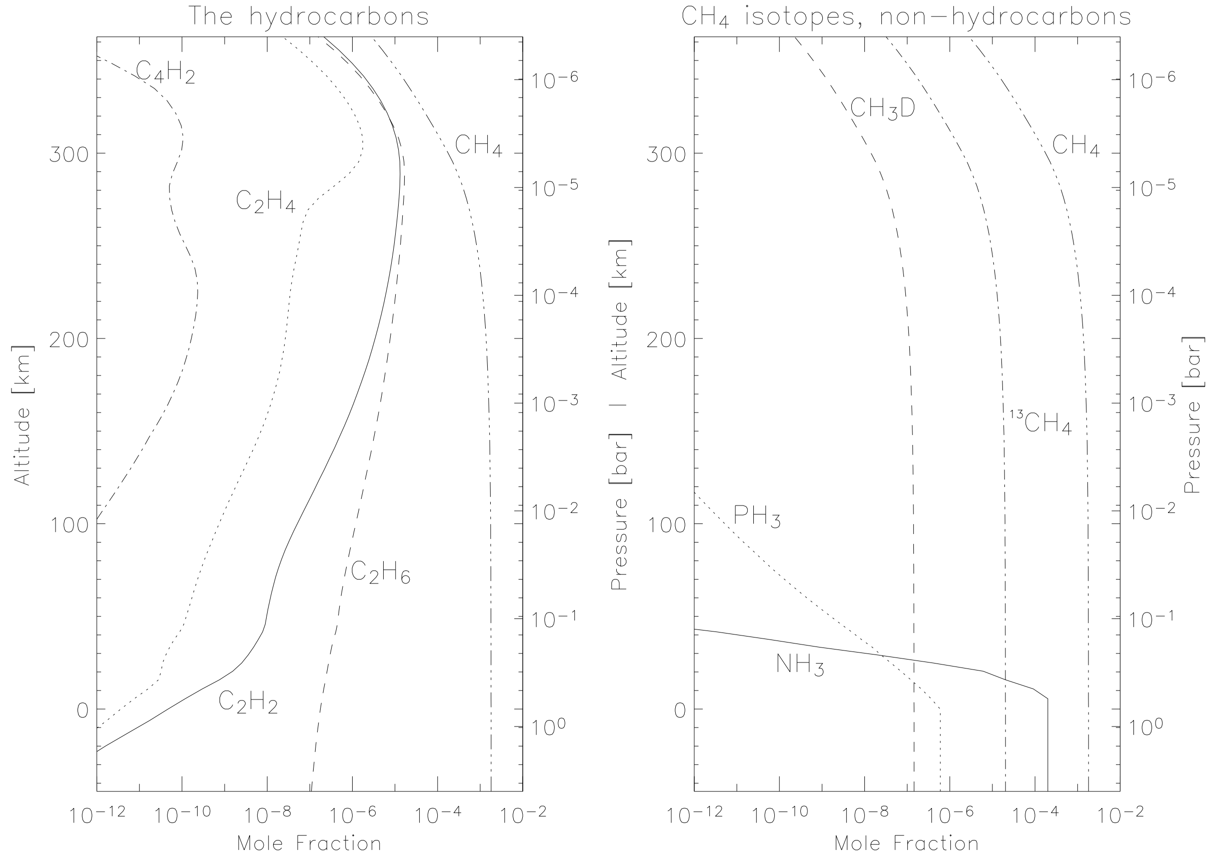

Figure 3.4: Model-atmosphere composition profiles. Molecular hydrogen and helium, which are not shown, were assumed to be uniformly mixed with VMRs of 0.863 and 0.134 respectively. As H_2O is assumed to be 1.85×10^{-3} at deep pressures and believed to condense at pressures greater than 5 bars, it is also not shown.

fractional scale height[4] (FSH) according to:

$$q \;=\; q_0 \left(\frac{P}{P_0}\right)^{(1\,-\,\mathrm{FSH})/\mathrm{FSH}} . \tag{3.36}$$

The phosphine profile was also constructed in this manner with P_0 set to 1.0 bar. The two-parameter approach is meant to mimic the rapid reduction in NH_3 and PH_3 mole fractions with altitude (due to photolysis and condensation in the case of NH_3 and

---

[4] The ratio of partial-pressure scale-height to total-pressure scale-height or, put another way, the fraction of a scale height at which a species falls off by a factor of e.

photolysis and thermochemical destruction in the case of PH_3). NH_3, PH_3 and CH_4 were also constrained to be less than the respective local saturation-vapour pressure (although PH_3 and CH_4 never come close to condensing under Jovian conditions).

3.4.3 Haze Opacity

A single aerosol cloud (used interchangeably in this context with "haze") based at one bar with fractional scale height and variable opacity of 0.5 was used in the model atmosphere. The opacity value is in approximate agreement with that determined by Galileo [13, 99, 178]. The cloud opacity was assumed to be spectrally "grey" (*i.e.* constant with wavelength). The grey approximation is accurate as long as heating is small and collisions dominate. Unfortunately, the opacity due to aerosols and its wavenumber-dependence are not well-known. Although assumed to have broad absorption features, the smaller the spectral interval, the better the approximation.

3.4.4 CIRS Forward Model

Collectively, the temperature, composition and aerosol profiles form a one-dimensional description of the atmospheric state at any location. For a given atmospheric state, the forward model can then be used to simulate the radiance within the limits of the experimental error. The forward model utilised in this study is a development previously used to analyse Galileo/NIMS observations of Jupiter [98, 99, 141]. The code has been validated against a number of LBL models [26] and is found to produce similar results, but is much faster. The small differences between the correlated-k and LBL spectra were

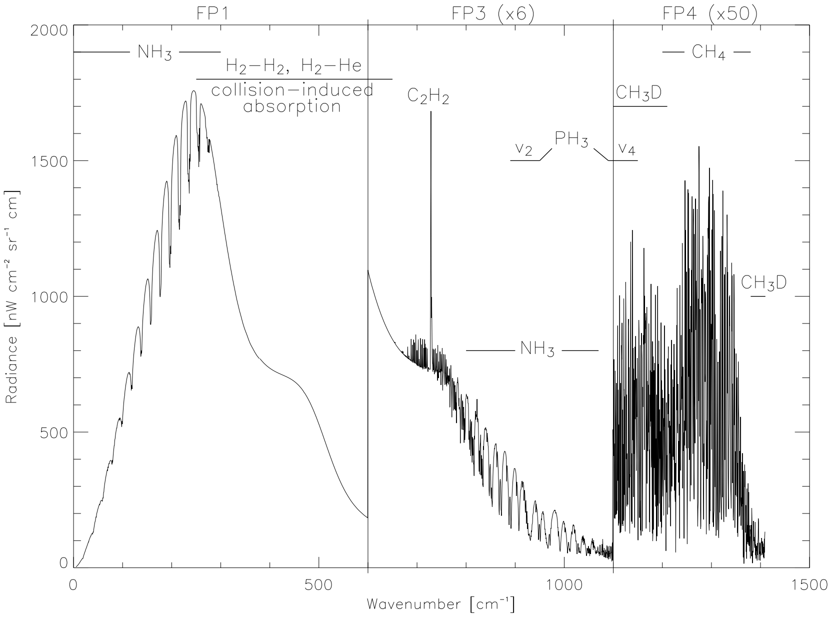

Figure 3.5: Forward model-synthesised radiances for the CIRS spectral range. Note that the focal planes are on separate radiance scales. Calculated at 0.5 cm^{-1} resolution assuming equatorial and equinoctial conditions.

included in the error budget of the retrieval model (presented in Chapter 4).

3.4.5 Spectral Data

The forward model references tables of pre-tabulated *k*-distributions when synthesizing the CIRS spectra. The *k*-distributions were computed on a grid of fifteen equally-spaced temperatures between 100 and 350 K and fifteen equally-spaced pressures from $-11 \leq \log P \leq +2$ (1.7×10^{-5} and 7.5 bar respectively). The resulting *k-tables* – a complete summary of which can be found in Appendix C, were produced at quarter-wavenumber resolution for CH_4 (its isotopes CH_3D, $^{13}CH_4$), C_2H_2, C_2H_4, C_2H_6, C_4H_2, NH_3 and PH_3. Example, synthetic radiances and brightness temperatures for the CIRS spectral range are presented in Figures 3.5 and 3.6.

Scattering: The single-scattering albedo can be useful in determining whether scattering needs to be taken into account within the forward model. From Equation 3.20 it can be seen that if ϖ is approximately one, then scattering is important.

Of the various types of scattering, within the CIRS spectral range only Mie scattering need be considered[5]. This is because, of the various cloud-particle sizes proposed for Jupiter (0.5-1.0 μm [158, 188, 204], 3.0-5.0 μm [146, 147, 185], 10 μm [34, 204], 45 μm [73], even 100 μm [203]) only 10 microns is of a size commensurate with the mid-infrared wavelengths studied here. Particles of larger size are likely to be sparse and to have settled to unobservable levels while particles of smaller radii are not a major influence within the CIRS spectral range because the molecular/dipole/Rayleigh scattering coefficient is

---

[5] Mie theory is the complete formalism for calculating the scattering properties due to the interaction of radiation and spherical aerosols and/or cloud droplets. Mie theory involves the analytical solution to Maxwell's equations for electromagnetic waves and is outlined in Hansen and Travis 1974: [85] and Goody and Yung 1989: [77].

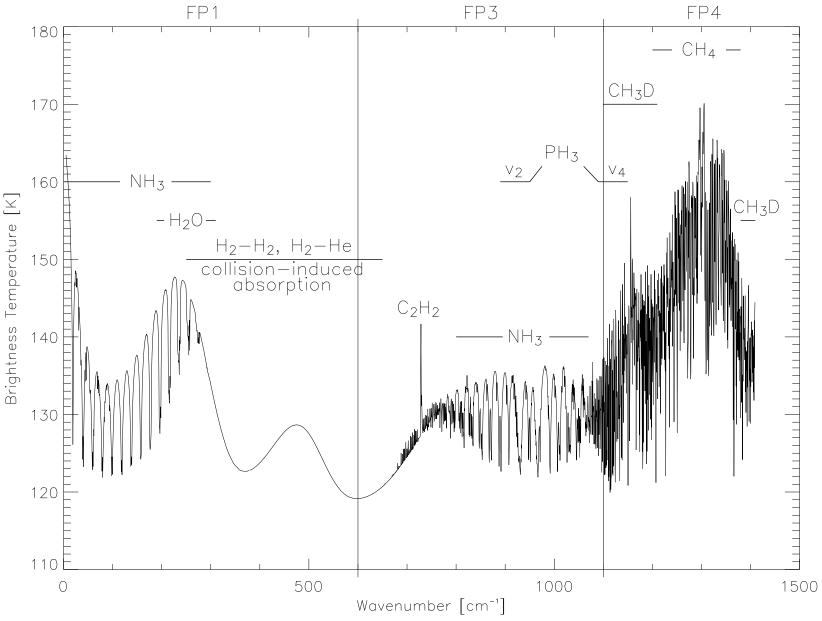

Figure 3.6: Forward model-synthesised brightness temperatures for the CIRS spectral range (the brightness temperature is the temperature a blackbody would have to emit the same radiance). Calculated at 0.5 cm^{-1} resolution assuming equatorial and equinoctial conditions.

proportional to $\tilde{\nu}^{-4}$.

As the Mie-scattered phase function is difficult to represent, it is usually approximated. The simplest, quasi-realistic approximation of the Mie phase function is the Henyey-Greenstein phase function:

$$p(\theta) = \frac{1}{4\pi}\left[f\,\frac{1 - a_1^2}{(1 + a_1^2 - 2\,a_1^2\,\cos\theta)^{3/2}} + (1 - f)\frac{1 - a_2^2}{(1 + a_2^2 - 2\,a_2^2\,\cos\theta)^{3/2}}\right], \quad (3.37)$$

where θ is the scattering angle, f is a positive fraction between 0 and 1 and a_1 and a_2 are asymmetry factors which model forward- and backward-scattering (respectively). This combined or "double" function can reproduce most phase functions.

Both the single-scattering albedos and the forward-modelled spectra with and without scattering are presented in Figure 3.7. Note that, despite aerosols being significant scatters, the effect of scattering is shown to have a negligible influence within the CIRS spectral range.

3.4.6 CIRS Retrieval Scheme

The CIRS retrieval scheme is based upon the method of non-linear optimal estimation, constrained to be consistent with both measurements and *a priori* knowledge (non-linear optimisation was chosen because of its heritage within the Planetary Physics group and, although other methods of constraint exist, is commonly applied to problems where linearisation of the forward model is inadequate in accurately determining the solution). λ, the Levenberg-Marquardt-type braking parameter, is initially set to 1.0 and is changed according to the size of the cost function:

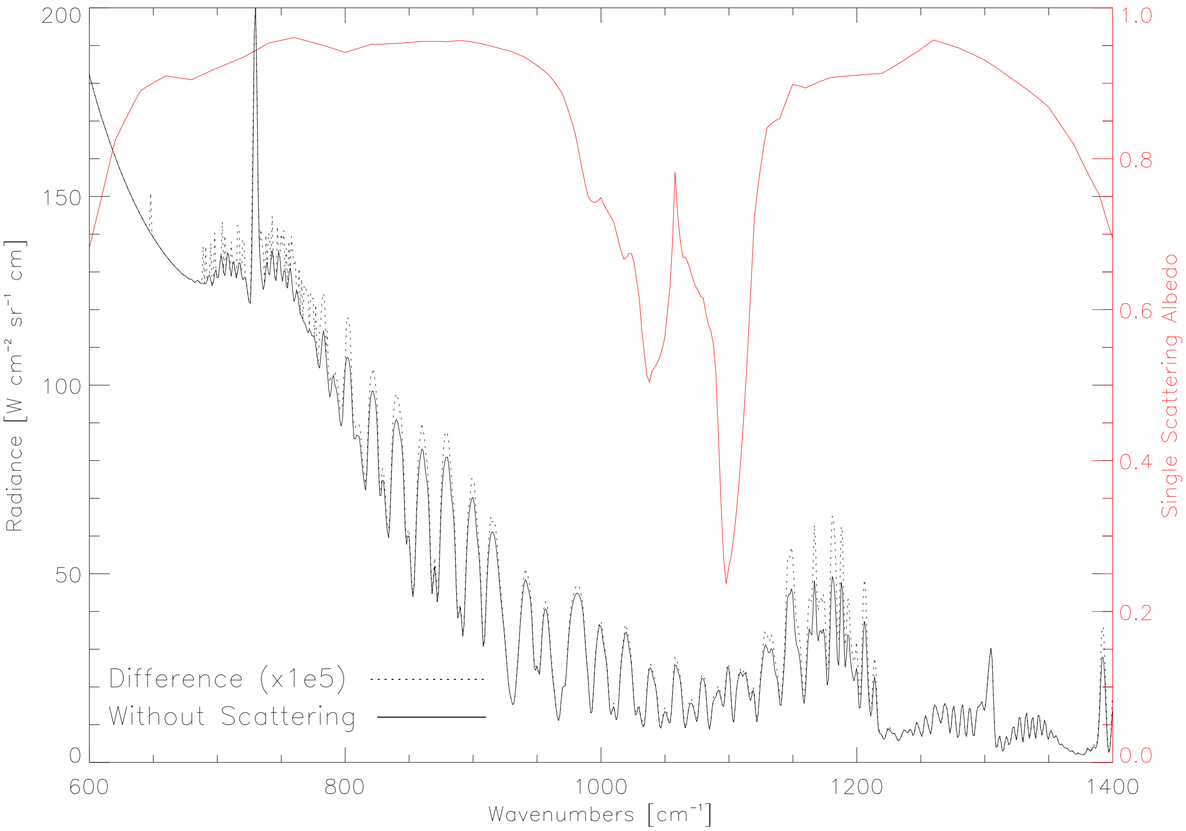

Figure 3.7: Forward-modelled scattering properties. To the left are the forward model-synthesised radiances with and without scattering. To the right are the ammonia-ice single-scattering albedos. The albedos were calculated by the Henyey-Greenstein phase functions (Equation 3.37) as Mie-scattered spheres of 10-μm radius.

- if the cost function decreases as the result of a step, then $\mathbf{x_i}$ is updated to $\mathbf{x'_{i+1}}$ and λ is multiplied by a factor of 0.3.

- if the cost function increases as the result of a step, then $\mathbf{x_i}$ is left unchanged and λ is increased by a factor of 10.

The choice of multiplicative factors is a matter of experiment; the successful iteration value (0.3) was chosen to be greater than the reciprocal of the unsuccessful iteration value so that λ did not decrease too quickly. The model was iterated for a maximum of ten iterations or until convergence ($\Delta\phi < 0.5\%$).

The spectral region most useful in deriving upper-tropospheric temperatures are the collision-induced, translation-rotation energy levels of H_2 between 300 and 700 cm^{-1}. However, due to the significant disparity in spatial resolution between FP1 and FP3, the spectral window selected for retrieving temperature was limited to just the 600-700 cm^{-1} span of FP3. Similarly, the spectral window most useful in deriving upper-tropospheric composition, particularly that of phosphine, is 1000 to 1200 cm^{-1}. Both ammonia and phosphine have strong vibrational features within this region, yet it is narrow enough to support the grey approximation.

Using the selected retrieval windows, four "composition" elements (deep NH_3 abundance, NH_3 fractional scale height, deep PH_3 abundance and haze opacity) and a 71-layer temperature profile were simultaneously retrieved. No vertical information was obtainable from the four non-temperature parameters because of the limited spectral ranges used. The assumed equatorial, *a priori* atmospheric state is summarised in Table 3.1.

The *a priori* range is set so that the final state vector is determined by the measurement vector. The measurement covariance matrix, $\mathbf{S}_\varepsilon$, is diagonal with each element set to the square of either the measurement variance or the appropriate NESR (as explained in §2.4.2). The diagonal elements of the *a priori* covariance matrix were set to the square of the estimated *a priori* error. The off-diagonal elements of the *a priori* covariance matrix were set to zero except for the temperature parameters where a correlation length

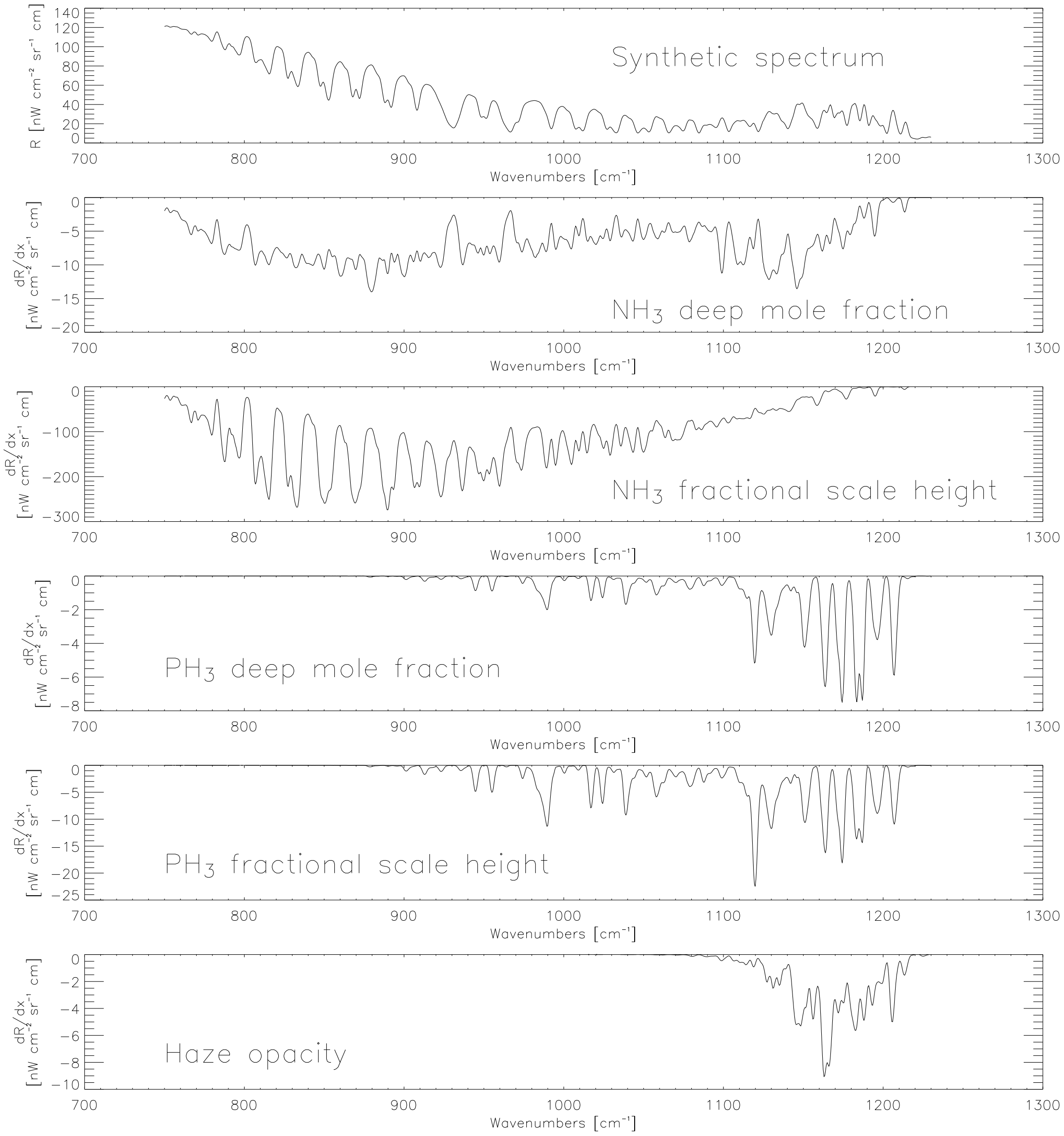

Figure 3.8: Forward model-synthesised, and rate-of-change of, radiances for Jupiter highlighting the active species within the CIRS mid-IR spectral range: ammonia, phosphine and haze opacity. Computed as if nadir viewing, using the assumed equatorial, *a priori* temperature and composition profiles.

Physical Quantity	**Parameter**	***A Priori* Value**	***A Priori* Error**	**Maximum Departure Allowed**
Ammonia	VMR	1.0	± 0.5	± 2.0
	FSH	0.15	± 0.1	± 0.2
Phosphine	VMR	1.0	± 0.5	± 5.0
Haze	opacity	0.5	± 0.3	± 2.0
Temperature†	profile	T_1 to T_{71}	± 5 K at 4 bars to ± 20 K at 0.4 μbar	± 20 K at 4 bars to ± 80 K at 0.4 μbar

Table 3.1: Parameterization of the atmospheric state. For ease, variable scale factors were utilised for NH_3 and PH_3 based on their deep abundances (respectively): 2.2×10^{-4} (Lindal *et al.* 1981: [120]) and 6.0×10^{-7} (Kunde *et al.* 1982: [110]). Supersaturation was not allowed for either NH_3 or PH_3. The maximum-departure limits were set to eliminate non-physical solutions. †: A correlation length of half a scale height was applied to the temperature profile to maintain smooth-variation between levels.

of half a scale height was assumed to maintain smooth-variation between levels.

The synthetic, and the rate-of-change of, radiances for selected species is presented in Figure 3.8. As can be seen, most of the gradient curves are notably different from each other, implying that they may each be independently retrieved. The main exception being phosphine, for which the dependence of deep abundance and fraction scale height is found to be very similar.

To quantify the ability to retrieve each of the *a priori* species "cleanly" (that is, independent of association with other variables), a linear cross-correlation analysis was conducted with selected correlations presented in Table 3.2. As anticipated, "significant" correlation (values > ± 0.8) was found between PH_3 and NH_3 and their respective FSHs. The PH_3 cross-correlation was so significant that the FSH was fixed to be constant (at 0.3) in the retrievals. Significant correlation was also found between temperature and haze opacity at the cloud-base (1 bar) and between temperature and NH_3 both at

Correlation Matrix	**NH_3**	**NH_3 FSH**	**PH_3**	**PH_3 FSH**	**Haze opacity**
NH_3	**1.0**				
NH_3 FSH	**0.82**	**1.0**			
PH_3	0.27	-0.01	**1.0**		
PH_3 FSH	0.38	0.13	**0.96**	**1.0**	
Haze opacity	0.42	-0.01	0.63	0.52	**1.0**
T(1.27 bars)	0.04	0.30	-0.46	-0.28	**0.82**
T(1.01 bars)	-0.05	0.34	-0.57	-0.40	**0.89**
T(0.80 bar)	-0.41	0.13	-0.63	-0.55	**0.88**
T(0.63 bar)	**0.88**	-0.58	-0.39	-0.49	-0.49
T(0.50 bar)	-0.77	**0.84**	-0.05	-0.19	-0.08
T(6.34 mbars)	**0.82**	0.74	0.40	0.46	0.51
T(5.04 mbars)	**0.84**	0.79	0.36	0.43	0.43
T(4.00 mbars)	**0.84**	**0.83**	0.29	0.38	0.31
T(3.18 mbars)	0.79	**0.81**	0.20	0.30	0.17

Table 3.2: Linear-correlation matrix for retrieved composition and temperature. Values near ± 1 indicate strong linear correlation and anti-correlation (respectively), whereas values near 0 indicate little or no correlation. The values highlighted in bold type are those greater than ± 0.8 and are deemed "significant" in this study.

cloud level (0.4 bar) and at stratospheric temperatures. These correlations result from the grey-absorbing NH_3 aerosols being indistinguishable from a cloud-free atmosphere with suitably adjusted temperature profile. While the latter correlation results from the influence of hazes at stratospheric levels (like that observed for the GRS in Figure 1.4), the tropospheric correlation occurs near the artificially-defined NH_3 cloud-base.

Chapter 4

Retrieval and Validation

Contents

The Cassini-Huygens Millennium Fly-by of Jupiter offered the opportunity to globally map the planet at unprecedented spectral resolution. The CIRS investigation in particular significantly complements and extends previous Jovian investigations.

The application of the inverse methods outlined in Chapter 3 to the CIRS spectra are described here. The method of spectral-differencing is also employed as a means of extracting qualitative information directly from the spectra. Both retrieval and spectral-differencing methods seek to determine the spatial variation of phosphine and (in the case of the retrievals) include the simultaneous determination of temperature, ammonia and haze opacity. The existence of phosphine is important in the understanding of non-equilibrium species and the transport mechanisms that allow such species to be seen in the upper-troposphere; transport mechanisms are discussed further in Chapter 5.

4.1 Inverse Model Validation

To demonstrate the validity of the retrieval method, a set of test spectra were calculated. The test spectra consisted of 23 retrieved temperature profiles from the ATMOSA dataset equally-spaced in latitude between 55°S to 55°N. The profiles were retrieved from medium spectral resolution (2.5 cm^{-1}, apodised) spectra over the spectral ranges 600 to 950 cm^{-1} and 1225 to 1310 cm^{-1} – regions sounding tropospheric and stratospheric temperatures respectively. For each of the 23 assumed temperature profiles and observing geometries, the following compositional parameters:

- NH_3 deep mole fraction (relative to 2.2×10^{-4}): set to 1.0 + 0.5x,

- NH_3 fractional scale height: set to 0.15 + 0.2x (limited not to go below 0.01),
- PH_3 deep mole fraction (relative to 6.0×10^{-7}): set to 1.0 + 0.5x. Fractional scale height fixed at 0.3,
- Haze opacity: set to 0.5 + 0.5x (limited not to go below 0.0). Haze cloud-base set to 1 bar, with fractional scale height 0.5,

were then randomly varied (where x is a random number between ± 1, recalculated for each element) and synthetic spectra calculated. For each temperature profile, four random sets of the parameters were generated and used to create 92 synthetic spectra. The spectral resolution of the forward model was 2.5 cm^{-1} FWHM with a triangular line-shape. The radiance error was set to the NESR reduced by a factor of $\sqrt{512}$ and $\sqrt{290}$ for FP3 and FP4 respectively, roughly equivalent to the number of spectra averaged in each latitude bin[1]. No forward modelling error was incorporated.

To test the model's ability to retrieve the original tropospheric ammonia, phosphine, haze and temperature input, the synthetic spectra were first reduced to the 600 to 700 cm^{-1} and 1000 to 1200 cm^{-1} spectral subranges. The model was run for each case for a maximum of 10 iterations or until the cost function ϕ had converged to within 0.5%. The results of the model validation can be seen in Figures 4.1, 4.2, 4.3 and 4.4 where the fitted values are indicated by + symbols and the vertical extent is set to the square root of the diagonal elements of the model covariance [161]:

$$\widehat{\mathbf{S}} = \mathbf{S}_a - \mathbf{S}_a\mathbf{K}^T(\mathbf{K}\mathbf{S}_a\mathbf{K}^T + \mathbf{S}_\varepsilon)^{-1}\mathbf{K}\mathbf{S}_a. \tag{4.1}$$

---

[1] At the time of the test, detectors 11, 12 and 13 of FP4 were thought to have radiometric calibration issues so that spectra from these detectors were ignored, hence the differing factors.

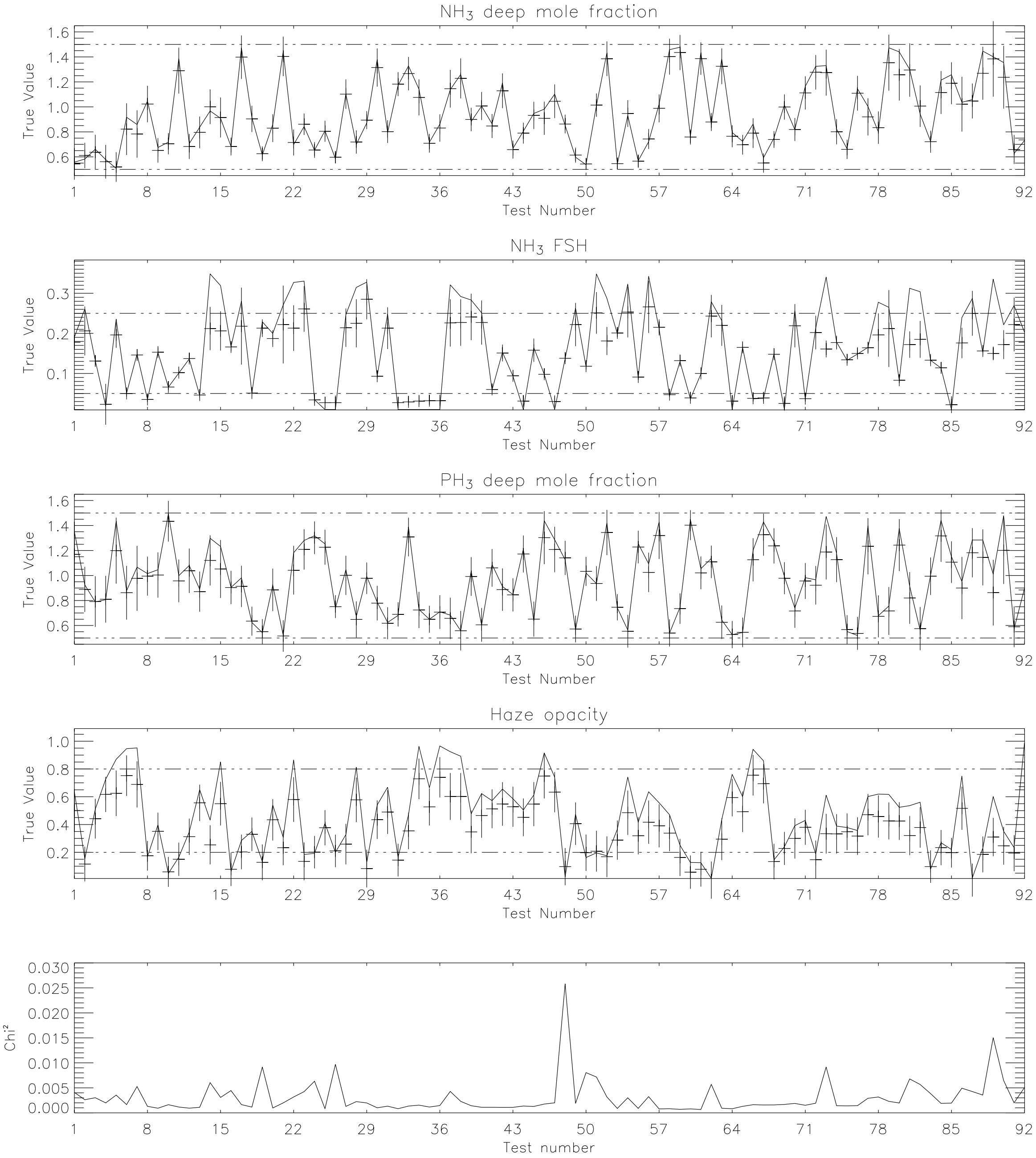

Figure 4.1: Retrieval validation: ammonia, phosphine and haze opacity. The solid line is the original value used to generate the synthetic spectrum and the dotted lines show the *a priori* estimates ± the *a priori* error. The fitted values are indicated by the + symbols, where the vertical extent is set to the model variance.

The inability of the retrieval model to reproduce high values of NH_3 FSH and haze opacity are discussed here and in the caption for Figure 4.2 (respectively). For NH_3 FSH, random combinations of NH_3 deep mole fraction and NH_3 FSH leads to the saturation of NH_3 at pressures less than 0.7 bar. Since the NH_3 VMR is constrained not to exceed the saturated VMR, the NH_3 profiles used to generate the synthetic spectra have lower NH_3 concentrations than the two parameters alone. Hence the lower values.

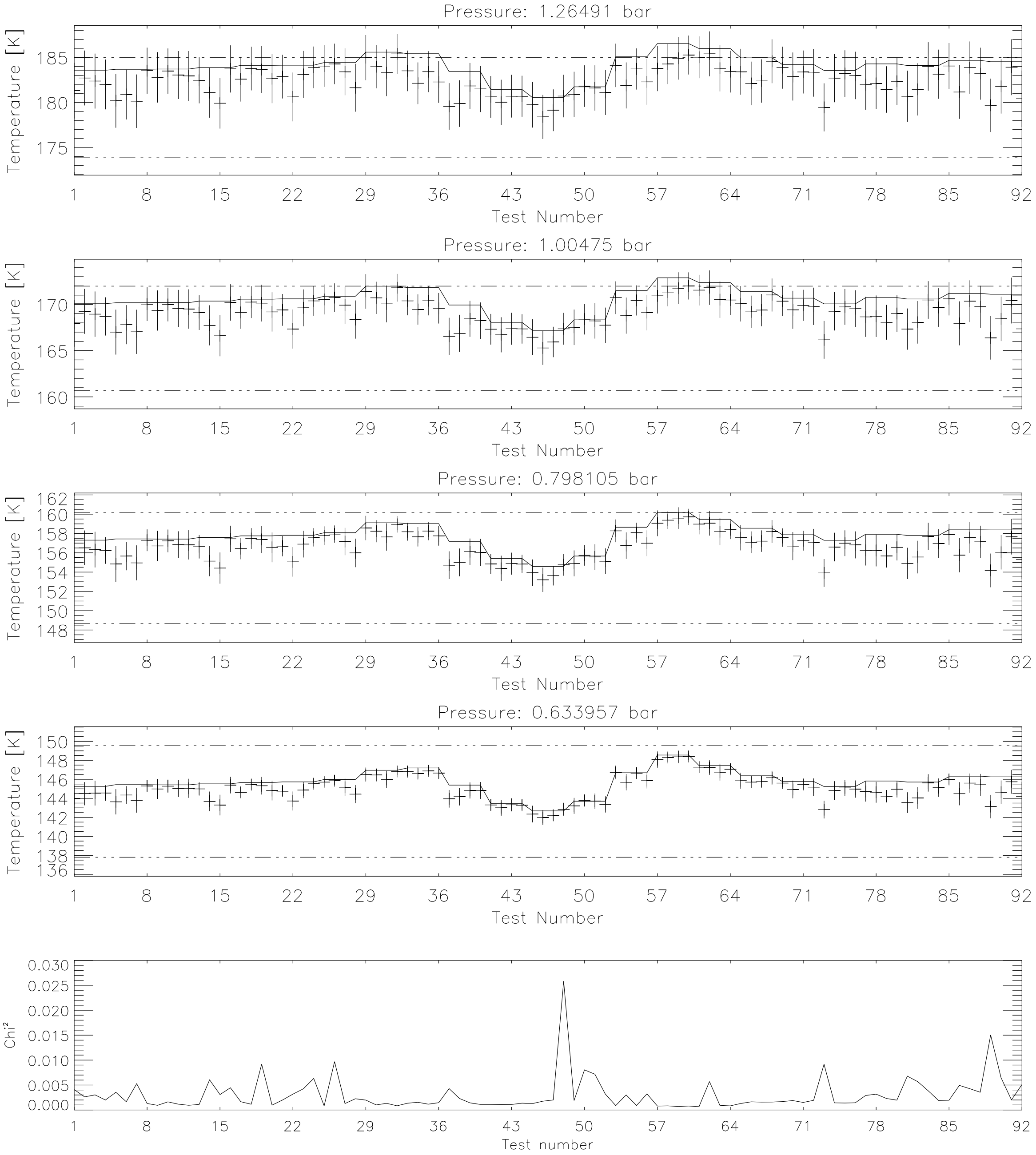
Pressure: 1.26491 bar

Pressure: 1.00475 bar

Pressure: 0.798105 bar

Pressure: 0.633957 bar

Figure 4.2: Retrieval validation: temperature. The solid line is the original value used to generate the synthetic spectrum and the dotted lines show the *a priori* estimates ± the *a priori* error. The fitted values are indicated by the + symbols, where the vertical extent is set to the model variance.
The inability of the retrieval model to retrieve high values of haze opacity is due to the significant correlation between temperature and cloud *circa* 1 bar. This is revealed by a test-by-test comparison of the temperatures presented here and the hazes in Figure 4.1. It is unknown why high opacity would restrict the model from retrieving either temperature or cloud accurately. Only pressure-temperatures between 1.3 and 0.6 bar are shown for the sake of brevity and because temperatures outside this range range appear unaffected.

The four panels at the top of Figures 4.1 and 4.2 are the retrieved parameters for all 92 cases with the corresponding *chi*-squared[2] fit (bottom panel):

$$\chi^2 = [\mathbf{y} - \mathbf{F}(\mathbf{x})]^T \mathbf{S}_\varepsilon^{-1} [\mathbf{y} - \mathbf{F}(\mathbf{x})]. \tag{4.2}$$

The calculated spectra fit the synthetic spectra to a high degree of accuracy ($\ll 1$, where $\bar{\chi}^2 = 0.003$), with over half the cases within one standard deviation of the retrieved mean. The agreement between the true and fitted parameters for both composition and temperature of Figures 4.3 and 4.4 is also good. This simple analysis shows that the retrieval scheme works well and the selection of *a priori* values reproduces realistic conditions found on Jupiter.

Although the inversion works as expected, potential errors could still exist. Systematic error in the model could influence the retrieval, biasing the results. Bias arises when the retrieval method is poorly-behaved or ill-suited to the inverse problem employed (*e.g.* when linearization is carried out about a state other than *a priori*). Another source of uncertainty is the error associated with the forward model. Forward-modelling error arises from an incomplete knowledge of the physical system the forward model is trying to describe. Example forward-modelling errors include neglected physics or incorrect/missing state vector elements. Known forward-modelling errors within the CIRS project include the assumption of LTE, potentially incorrect spectral-line strengths and/or positions and the correlated-k approximation. For these inaccuracies, a forward-modelling error of 5% of the measurement radiance is added to the retrieval uncertainty – the value having

---

[2] The "reduced *chi*-squared" $\equiv \chi^2$ / the degrees of freedom, is meant in all cases.

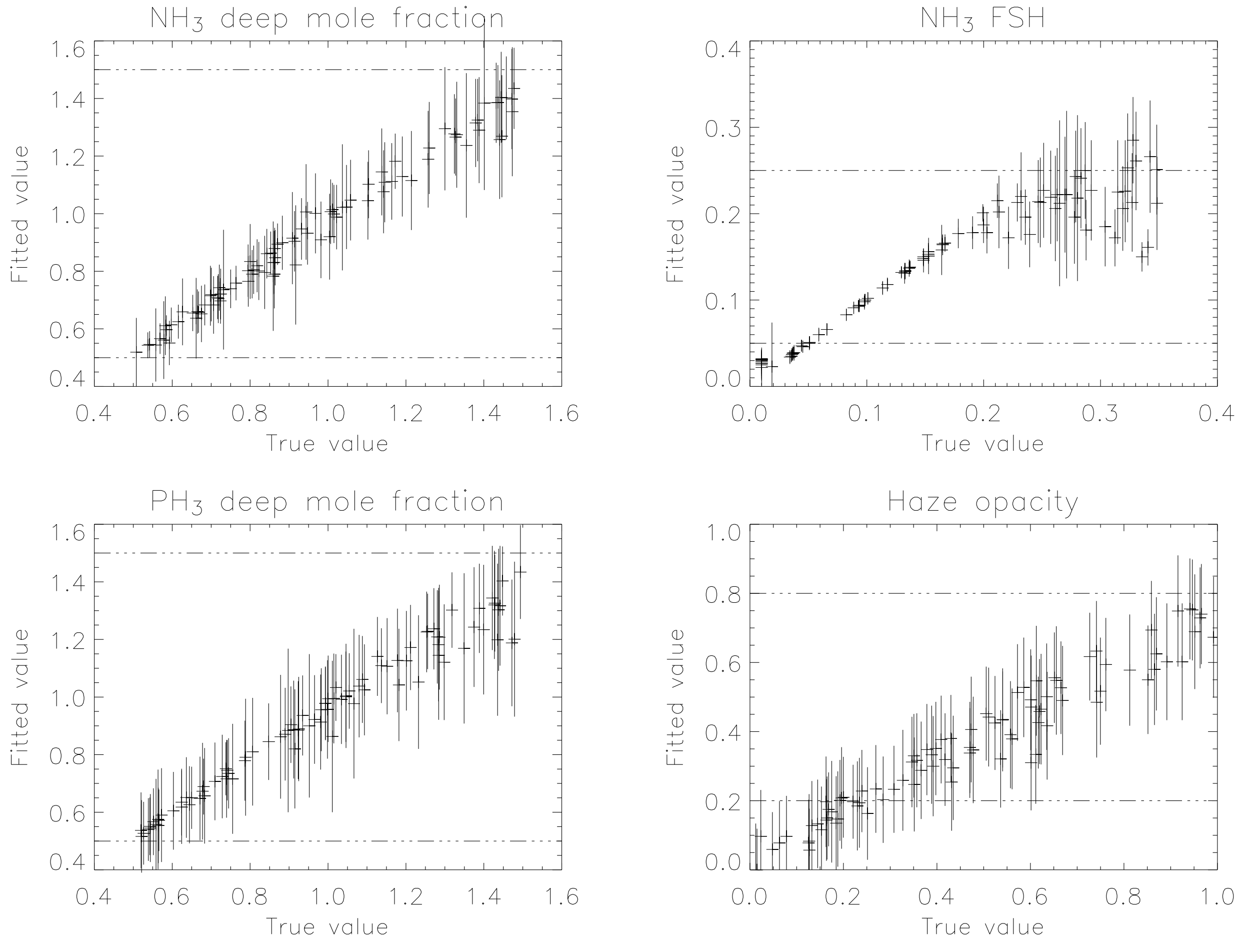

Figure 4.3: Retrieval validation: correlation between true and fitted composition. Note that the vertical and horizontal scales are different for each plot. The vertical extent of the + symbols is set to the model variance where the dotted lines are the ± *a priori* error. The increasing variance of NH$_3$ FSH at true values greater than 0.2 is due to the saturation of NH$_3$ in the forward model.

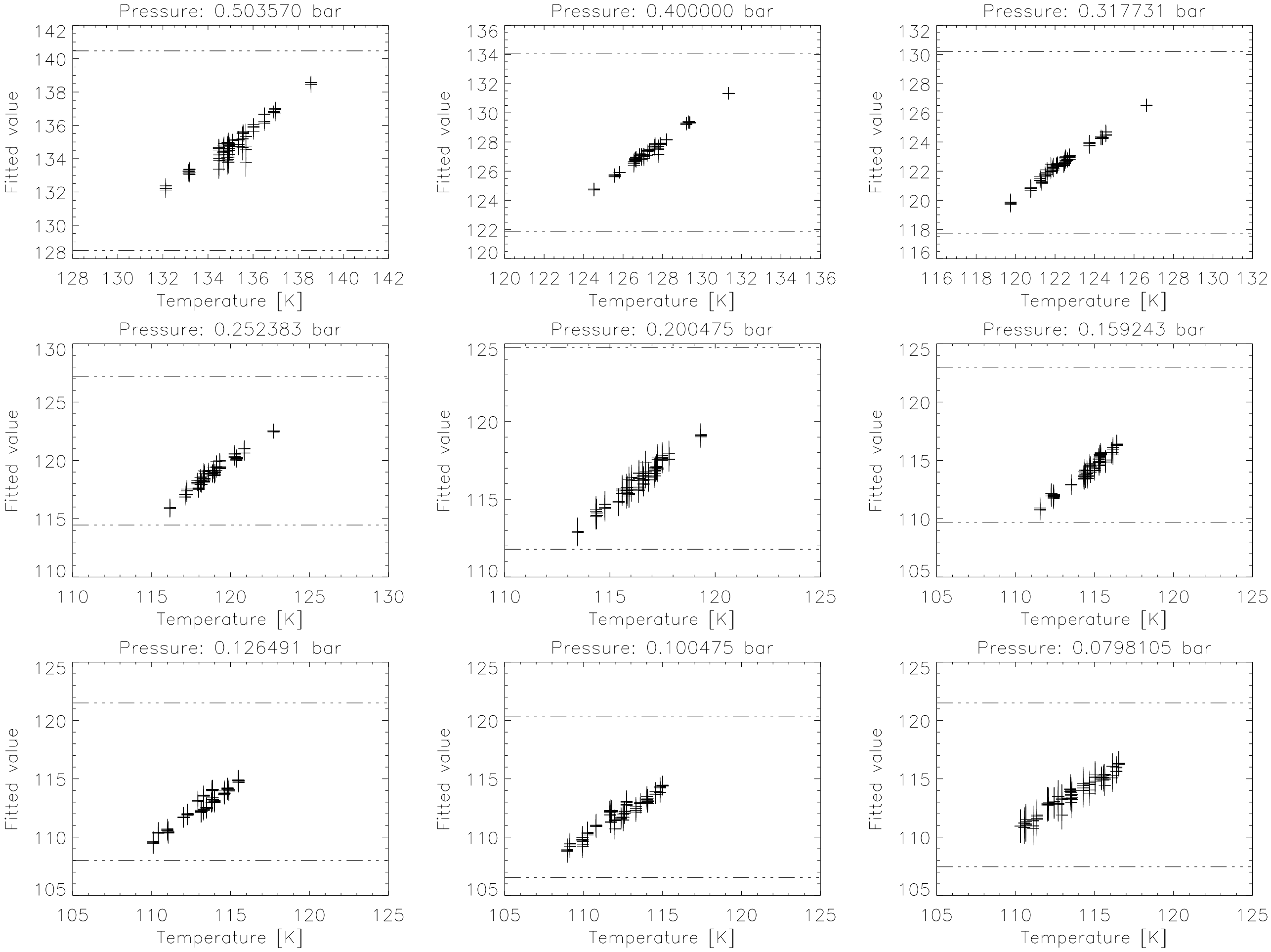

Figure 4.4: Retrieval validation: correlation between true and fitted temperature [K]. Note that the vertical and horizontal scales are different for each plot. The vertical extent of the + symbols is set to the model variance where the dotted lines are the ± *a priori* error. Only pressure-temperatures between 0.5 and 0.08 bar are shown for the sake of brevity.

been derived from intercomparisons with other radiative-transfer models [26].

4.2 Retrieval Scheme

The validated retrieval model was used to analyse spectra from ATMOS observations A through D using the selection criteria outlined in §2.4. As previously described (§2.4.3), a calibration shift occurred halfway through the ATMOSB observation biasing all the resulting analyses. ATMOSB results are shown regardless for completeness. However, analysis of the averaged radiance from ATMOS maps A, C and D (“ATMOSACD”) is sometimes shown for diagnostic purposes.

The size of the retrieval bins (6°) was chosen to be wide enough to create useful averages, but small enough that localised phenomena might be observable. At 16° diameter, the mildly-elliptical GRS is approximately twice the size of the next largest feature – the white oval of the South South Temperate domain (32.6°S), and possibly the only atmospheric feature that can be seen within the retrieval maps (aside from the belt-zone pattern, *cf.* Figure 4.5). On average, there were five spectra from each focal plane per bin (for ATMOSACD, the value was approximately 14).

The radiance uncertainty was either the NESR/$\sqrt{N}$ (where N is the number of spectra within the bin) or the standard-deviation-of-the-mean radiance within the bin (whichever was larger at the measurement wavenumber) and included a forward-modelling error of five percent. Although the forward-modelling error was incorporated into the error budget, it was assumed in the course of the thesis that measurement uncertainty would exceed systematic errors in such a way that they could be ignored. This is sup-

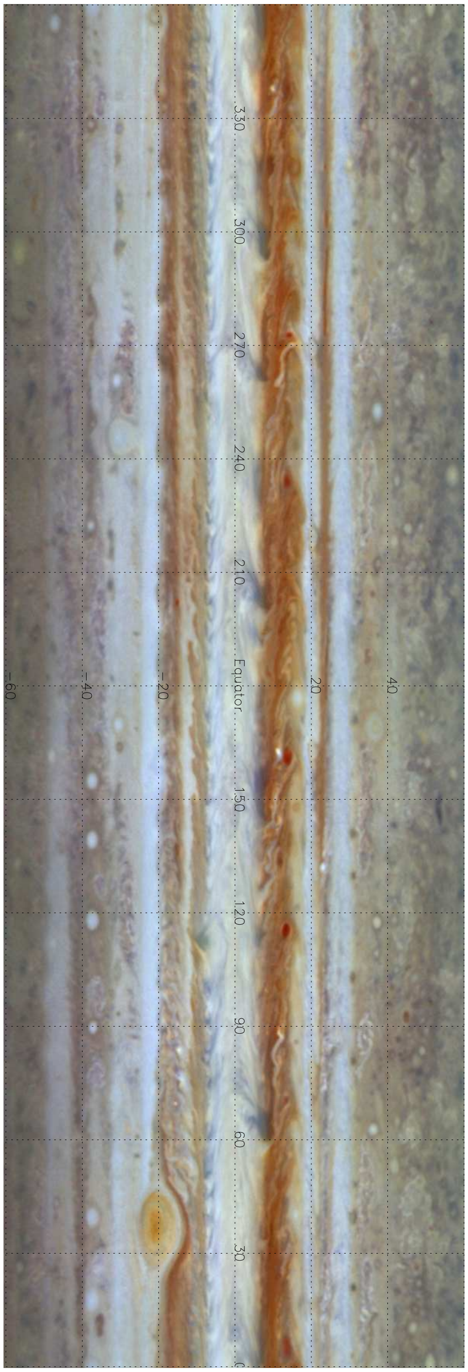

Figure 4.5: Cylindrical projection of Jupiter's circumference as viewed by Cassini's Imaging Science System (ISS). This averaged mosaic, spanning 24 rotations in early November 2000, was taken by the narrow-angle camera using red, green and blue filters. The smallest visible features near the Equator are about 0.2°/600 km. [152]
As the GRS is known to drift slowly (8°/month, westward) in longitude [197], by the time of the ATMOS observations in January 2001, it had moved to approximately 54° west longitude. [NASA]

ported by the observation that the radiometric variance within the bin was typically ten times the one-standard deviation uncertainty provided by the preflight NESR.

The transmission-weighting and contribution function peaks for the CIRS mid-IR spectral range can be found in Figure 4.6. The distinction between the two functions is the Planck function's gradient with height. If the variation of $B(\tilde{\nu}, T)$ with height is small compared to that of $d\tau/dz$ in Equation 3.8, then the weighting function peak defines the level of greatest contribution. If however, the variation of $B(\tilde{\nu}, T)$ with z is not small, then the contribution function maximum is more appropriate for determining the level of maximum sensitivity. As the contribution function more accurately describes the altitude at which most of the radiation is being emitted (in a non-isothermal atmosphere), it was used to quantify the heights/pressure-levels quoted in the thesis; selected contribution functions *versus* height/pressure are presented in Figure 4.7.

Also shown in Figure 4.6 are the selected temperature and "composition" retrieval windows. Whereas the CIA translation-rotation lines sound the upper troposphere from 0.15 to 0.4 bar and are useful in the retrieval of temperature, the contribution/weighting function peaks for the composition retrieval window range from the uppermost cloud level (0.4 bar) to pressures greater than one bar. In principle, the inference of temperature in the upper-troposphere is provided by the temperature retrieval window while the profile assumptions (*e.g.* dry adiabatic lapse rate, barotropic stability) keep the values accurate at greater depths.

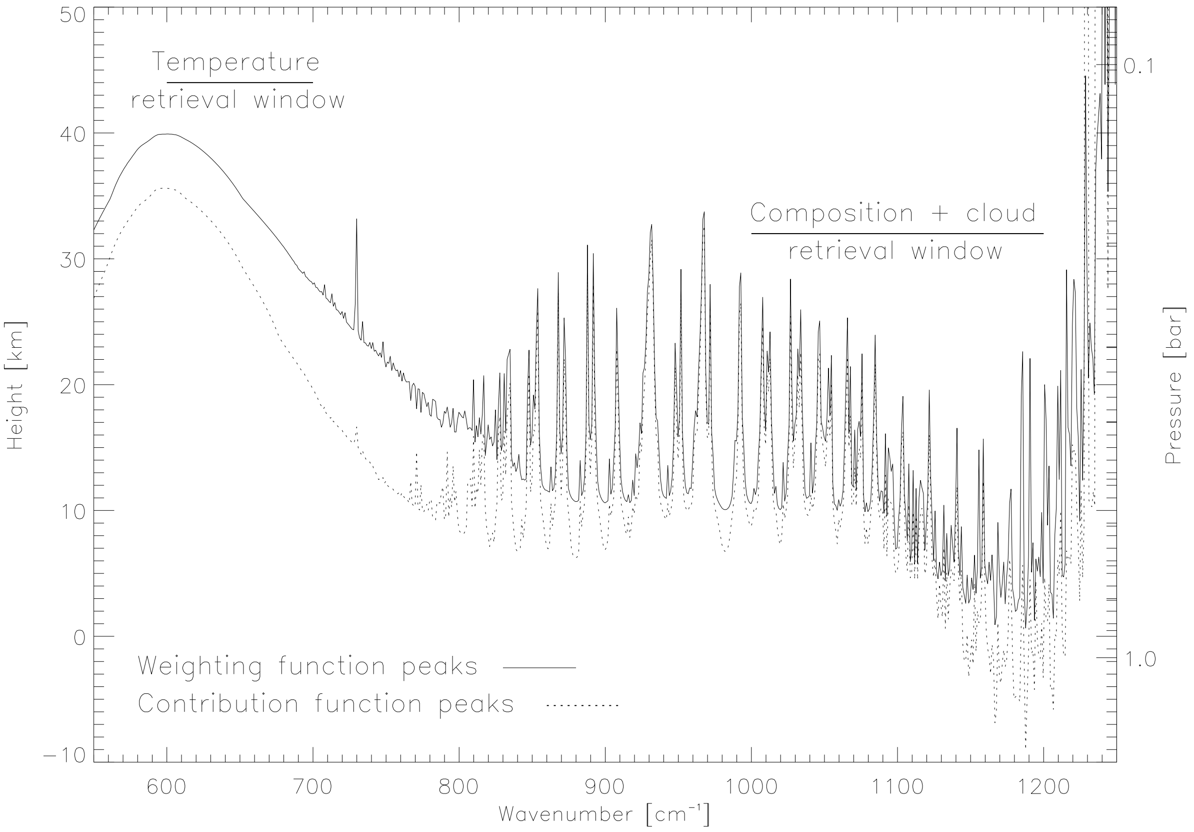

Figure 4.6: CIRS transmission-weighting, and contribution, function peaks at one wavenumber resolution. While both functions are useful in determining the pressure level at which the spectral information is retrieved (note the temperature and "composition" retrieval windows at 600 to 700 cm^{-1} and 1000 to 1200 cm^{-1} respectively), the contribution function is the transmission-weighting function multiplied by the Planck function and consequently peaks at the altitude where most of the radiation is emitted. The peak variation was computed with the same, assumed equatorial, *a priori* temperature and composition profiles of Table 3.1; the relative strengths of various contributions may however be different at higher latitudes. LTE was assumed in all levels at which there is significant radiative activity.

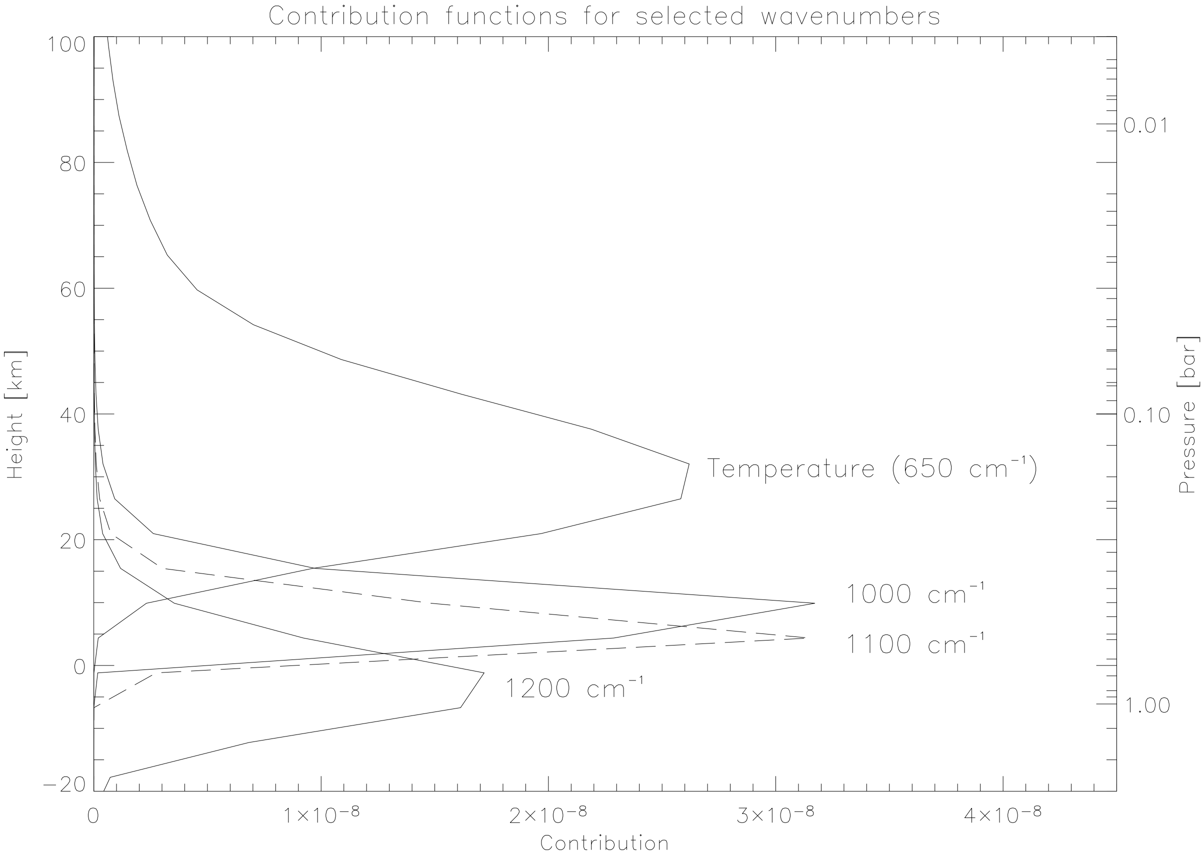

Figure 4.7: Selected CIRS contribution functions *versus* height (same as those presented in Figure 4.6 assuming a nadir observation). Adopting the FWHM as a measure of the vertical resolution, the accuracy of the contribution functions can be seen to be on the order of a Jovian scale height (approximately 25 kilometres) or greater.

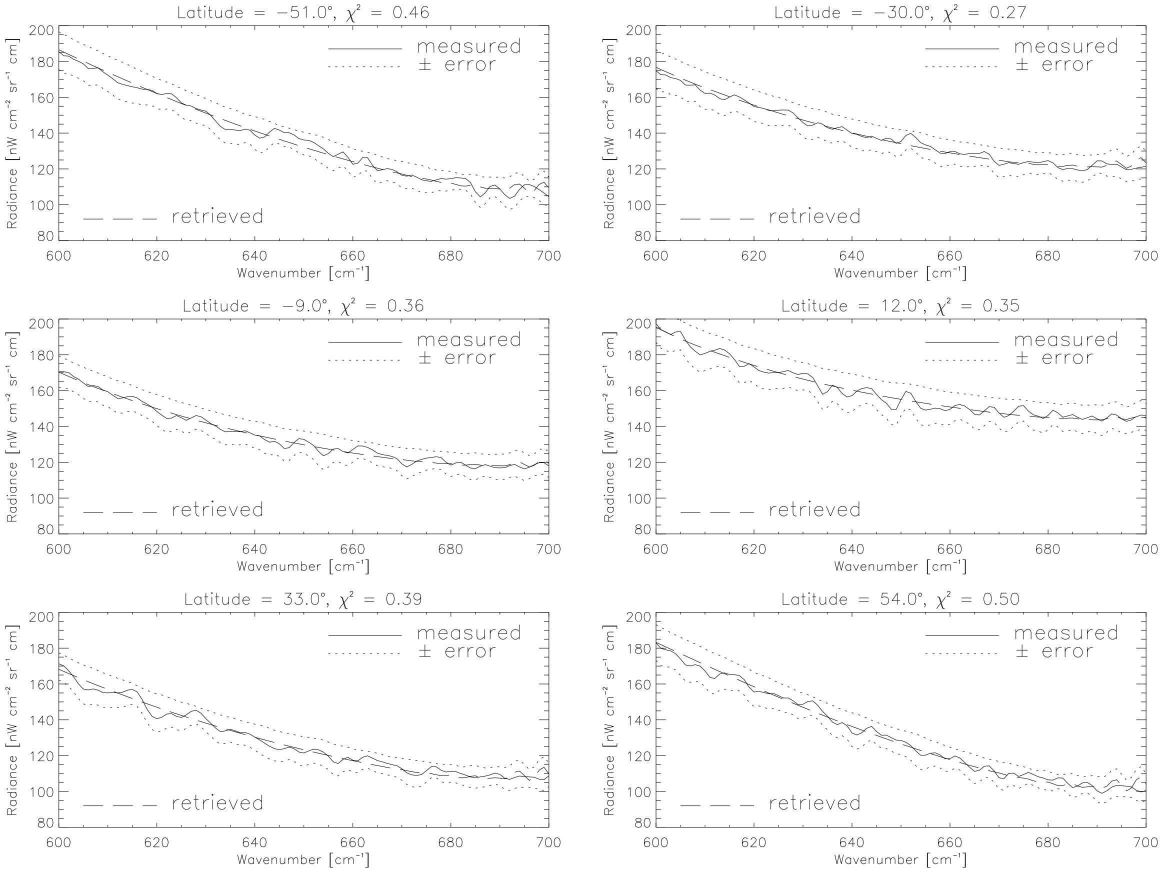

Figure 4.8: Example inverse-model fits for the temperature retrieval-window: the measured and retrieved spectrums. ATMOSACD spectra, 48° - 54° west longitude.

4.3 Retrieved Temperature

Six example, measurement *versus* inverse-model fits for the temperature retrieval window are shown in Figure 4.8 – note the quality of χ^2 (all less than one) signifying acceptable agreement. Plots of retrieved temperature from Cassini/CIRS observations can be seen in Figures 1.4, 4.9, 4.10, 4.11 and 4.31. The temperature retrievals were found to be in good agreement with the retrievals of contemporary CIRS analyses [61, 139] and broadly consistent with those obtained from the Pioneer and Voyager data-sets. Overall, the latitudinal variation at a particular pressure level rarely exceeds 10 K with the tropopause coldest at the Equator and within the South Tropical Zone (STrZ) – the minimum temperature occurring over the GRS (centred at 22°S, 54°W). This is in agreement with the findings of Lara *et al.* 1998 – hereafter referred to as L98[3], and Voyager/IRIS retrievals [59, 81, 169].

There also appears to be slight north-south asymmetry with warmer and higher-altitude temperatures in the north at the millibar level. The asymmetry is notably weak (perhaps only 3 K) and was similarly determined by Pioneer and Voyager/IRIS [82, 93]. The stratospheric waves observed at these levels are likely propagating disturbances from the troposphere and may indicate wave activity associated with a QQO. For example, the regularly-spaced features of the temperature maps at 0.25 bar (Figure 4.11) are similar to those previously identified in both ground-based [49, 149] and Voyager/IRIS [125] measurements. Although some of the features within the stratosphere have been shown to possess a westward drift [61], the tropospheric counterparts appear to remain stationary (± a couple degrees latitude from ATMOSA to ATMOSD) despite being embedded in large meridional wind currents.

4.4 Retrieved Ammonia

Good agreement is also found between measured and inverse-modelled spectra within the "composition" (actually composition and cloud) retrieval window (Figure 4.12). Although acceptable, the χ^2 fits within FP4 are in fact much better than those displayed

---

[3] Using the Infrared Telescope Facility in Mauna Kea, Lara *et al.* 1998: [112] observed Jupiter at several different longitudes between 40°S to 10°S (including that of the GRS). The spectra were recorded at high spectral resolution (approximately 0.1 cm^{-1}) for two separate wavelength channels: 10.5 to 11.2-μm (956 to 891 cm^{-1}) and 12.8 to 17.8-μm (781 to 562 cm^{-1}).

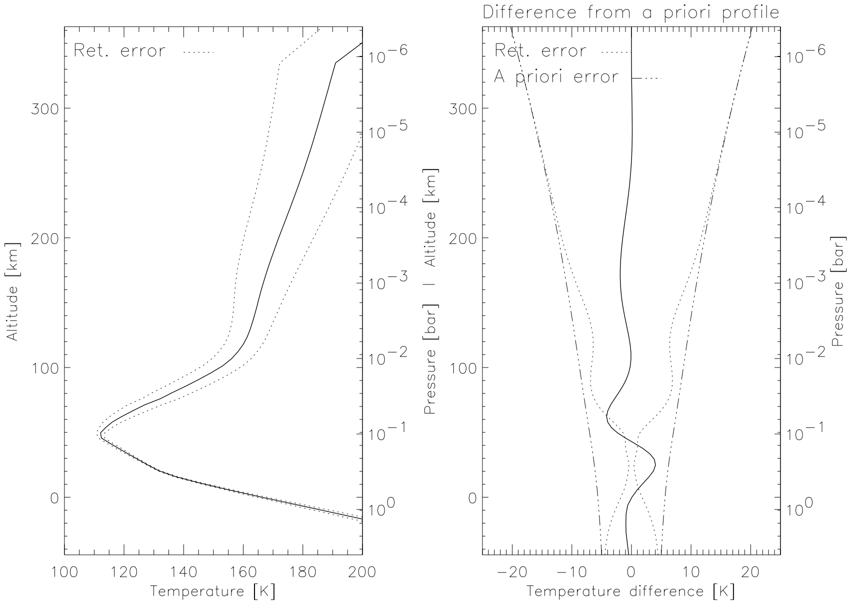

Figure 4.9: Retrieved NEB temperature profile and the difference with respect to the *a priori* temperature profile. Note that, for pressures less than 10 mbars and greater than one bar, there is little spectral sensitivity to temperature and therefore the values in these regions tend towards the *a priori* values. ATMOSACD spectra, 48° - 54° west longitude.

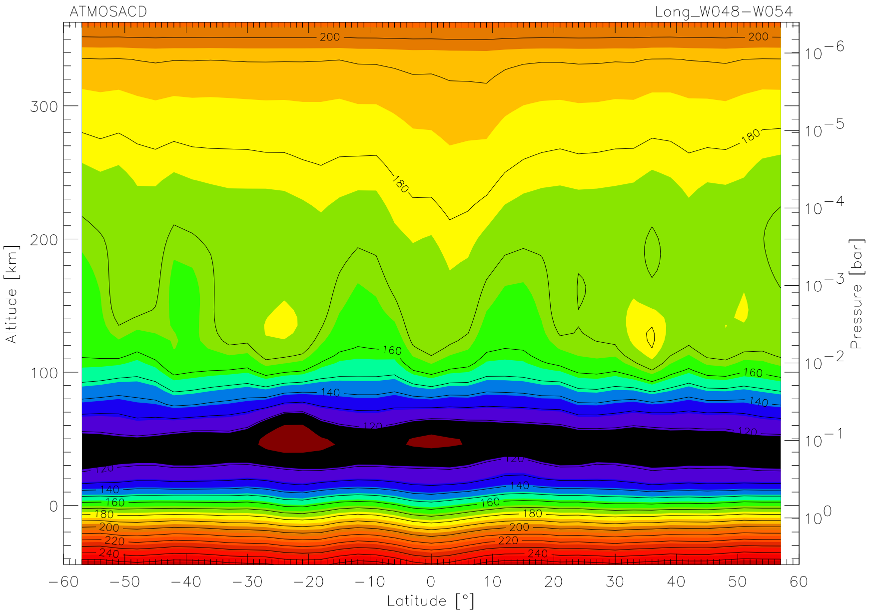

Figure 4.10: Temperature profile as a function of latitude. Note the barotropic conditions at P > 1 bar and the GRS at 22°S, 50 km altitude (0.1 bar). ATMOSACD spectra, 48° - 54° west longitude.

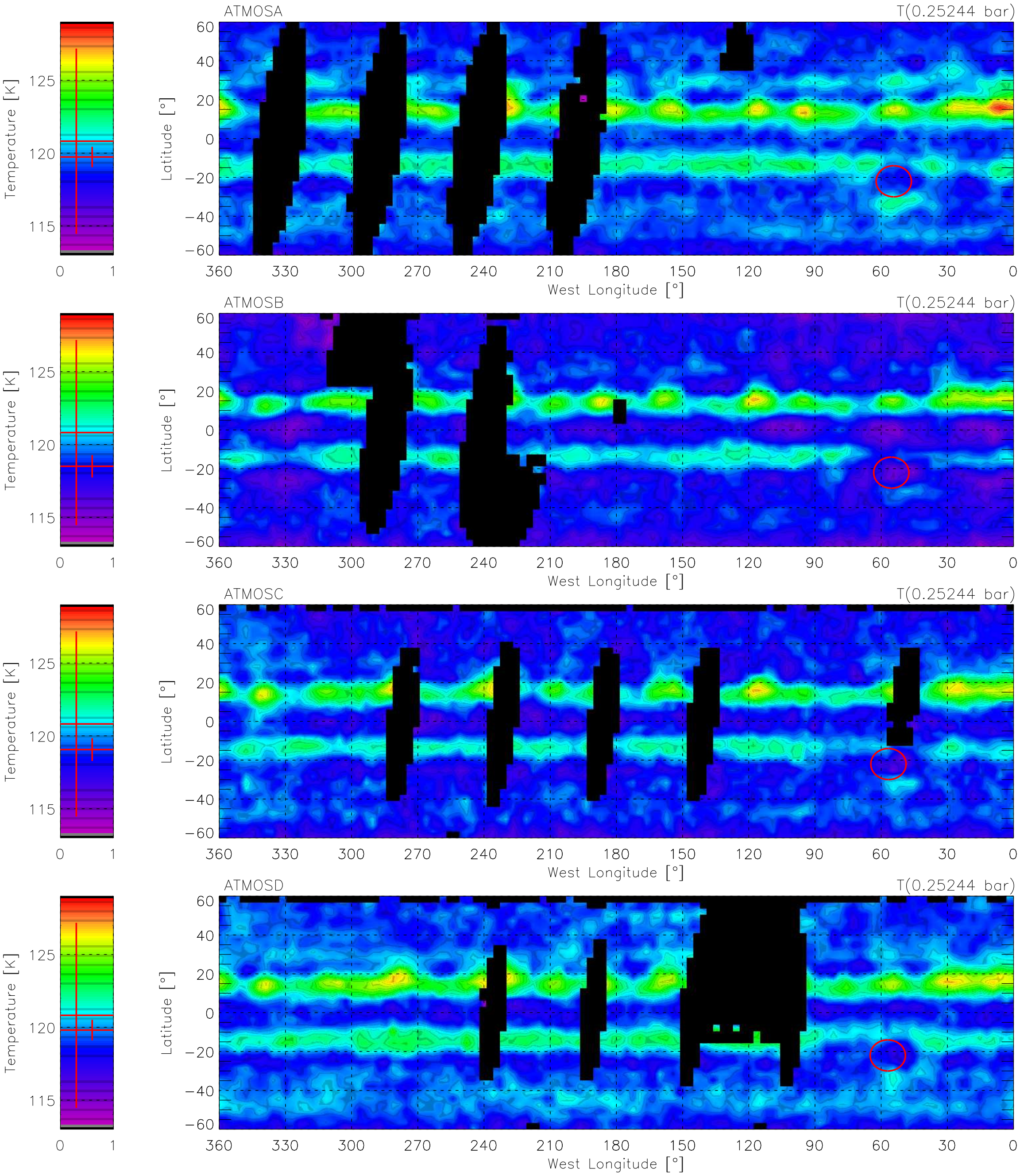

Figure 4.11: Retrieved temperature at 0.25 bar maps – ATMOSA through D. The circular outlines are the calculated locations of the GRS during ATMOS observations A through D. The GRS was assumed to be 16° in diameter, drifting slowing westward at 8°/month [197]. Plotted within the key are the *a priori* value ± the *a priori* error (left) and the mean retrieved value ± the mean retrieved error (right). The black, near-vertical stripes designate no data.

as (occasional) negative radiances at 1033 cm^{-1} and greater noise inhibit the accurate fitting of the NH_3 bands within FP3.

In the upper-troposphere/lower Jovian stratosphere, the NH_3 abundance decreases rapidly with altitude due to both condensation and UV photolysis. From the ultraviolet [54], through the infrared [38, 110, 129] to centimetre wavelengths [120], the abundance of NH_3 has been shown to decrease from a few 10^{-4} at 1.0 bar to as low as 10^{-9} around 0.25 bar. Variation (at a given pressure level) is also found in terms of both latitude and longitude. As previously discussed (§3.4.2), this non-uniformity in the NH_3 abundance is mimicked using a combination of retrieved deep abundance and retrieved fractional scale height. Spectral information on NH_3 and NH_3 FSH come from the 850 to 1050 cm^{-1} band whose vertical sensitivity spans 0.2 to 0.8 bar.

4.4.1 Ammonia Deep Abundance

Figure 4.13 presents the retrieved, deep mole fraction for each of the ATMOS maps. The deep abundance maps are plotted at 0.4 bar because this is the pressure level most sensitive to the centre of the NH_3 band at 950 cm^{-1}. Unfortunately, the variation across the planet is insignificant compared to the retrieval error extrapolated to 0.4 bar such that no spatial information about NH_3 deep abundance can be inferred. Thus, the deep abundance (2.2×10^{-4}) derived by Lindal *et al.* 1981: [120] is assumed when determining the NH_3 FSH results of §4.4.2.

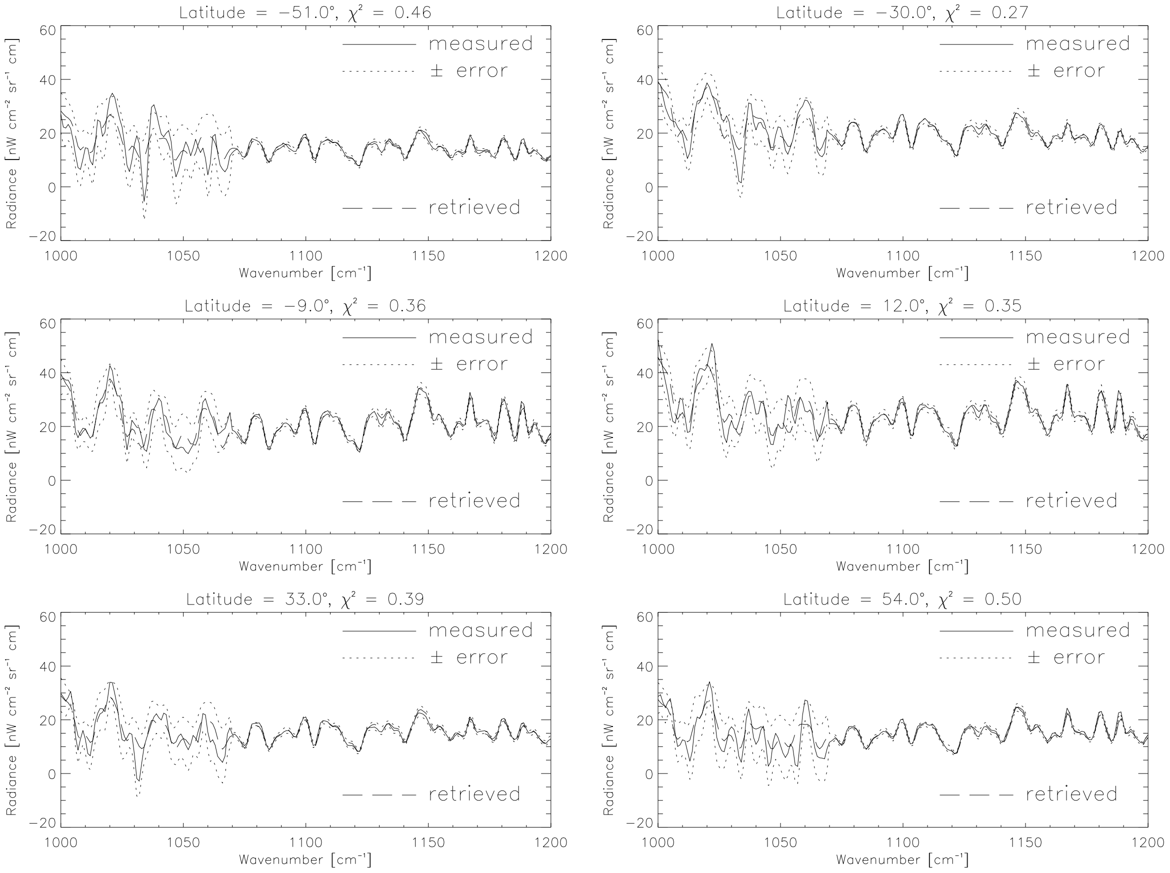

Latitude = $-51.0°$, χ^2 = 0.46

Latitude = $-30.0°$, χ^2 = 0.27

Latitude = $-9.0°$, χ^2 = 0.36

Latitude = $12.0°$, χ^2 = 0.35

Latitude = $33.0°$, χ^2 = 0.39

Latitude = $54.0°$, χ^2 = 0.50

Figure 4.12: Example inverse-model fits for the composition retrieval-window: the measured and retrieved spectrums. ATMOSACD spectra, 48° - 54° west longitude.

4.4.2 Ammonia Fractional Scale Height

Conversely, retrieved NH_3 FSH (Figure 4.14) shows clear meridional variation with higher values within the Equatorial Zone (EZ) and lower values over the North and South Equatorial Belts (NEB and SEB respectively). This appearance is consistent with the canonical view of rapid uplift or strong vertical mixing in the zones and subsidence over the belts [190]. NH_3 FSH also appears somewhat reduced over the GRS.

The meridional depletion and enhancement of NH_3 at latitudes of subsidence and upwelling (respectively) has been well documented. Observations of Jupiter's radio emission

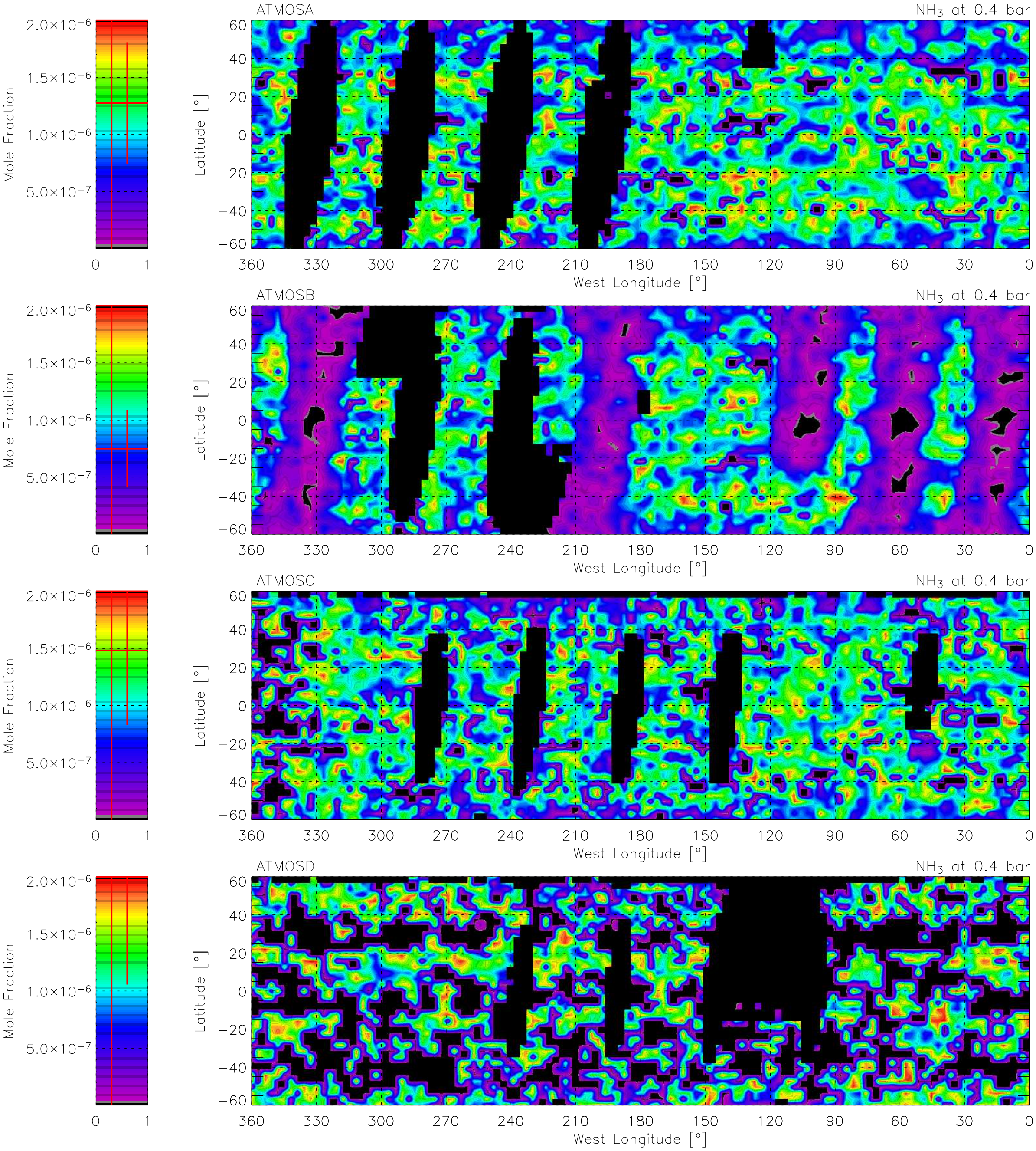

Figure 4.13: Retrieved ammonia abundance at 0.4 bar maps – ATMOSA through D. As the NH_3 variance at 0.4 bar is insignificant compared to the retrieval error (extrapolated to 0.4 bar), no spatial information about the NH_3 deep abundance can be inferred. However, note the banding in ATMOSB at 20°, 60°, 100°, 200° and 330° west longitude. The banding is due to a calibration shift (see §2.4.3) which occurred halfway through the observation. The black, near-vertical stripes designate no data.

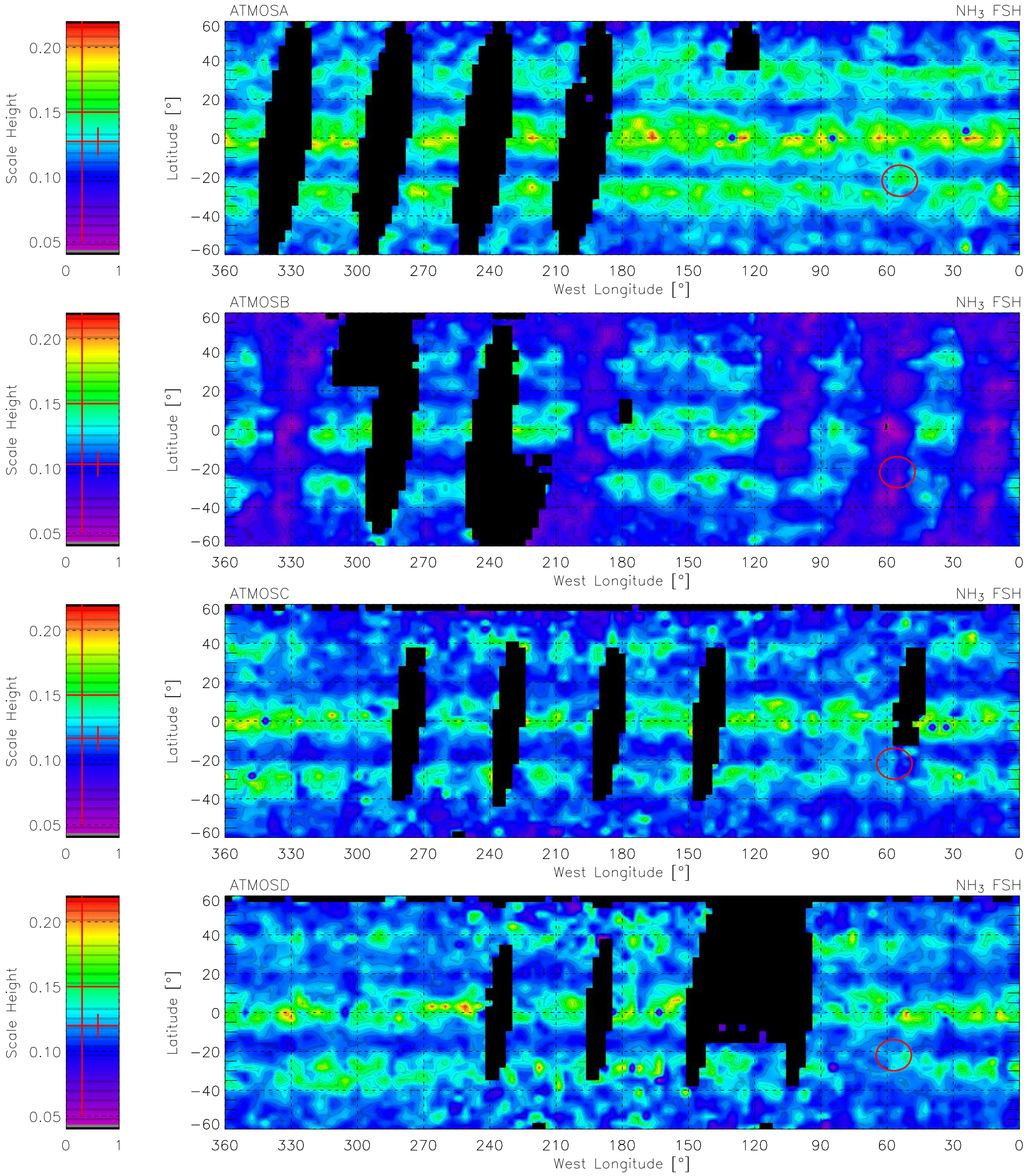

Figure 4.14: Retrieved ammonia fractional scale height maps – ATMOSA through D. The FSH is a useful measure of how a species falls off with altitude; the larger the value, the greater the upwelling. The circular outlines are the calculated locations of the GRS during ATMOS observations A through D. The GRS was assumed to be 16° in diameter, drifting slowing westward at 8°/month [197]. Plotted within the key are the *a priori* value ± the *a priori* error (left) and the mean retrieved value ± the mean retrieved error (right). The black, near-vertical stripes designate no data.

from 2 to 0.5 bar [48], Voyager/IRIS retrievals at 0.68 bar [73] and ground-based, 10-μm observations sounding 0.3 bar [194] have all confirmed the relative depletion of the belts in comparison to the zones. The zone-belt theory of alternating ascending and descending currents is also consistent with the NH_3 results of L98 and Edgington *et al.* 1999 – henceforth E99[4].

The retrieved NH_3 fractional scale height values are also consistent with both previous investigations [98, 203] and CIRS collaborators: Abbas *et al.* 2003: [1], Achterberg *et al.* 2004: [2] and Fouchet *et al.* 2003: [64]. All three sets of authors derive similar NH_3 abundances despite using three separate retrieval models (and a slightly different wavenumber range – 900 cm^{-1} to 940 cm^{-1}, in the case of Fouchet *et al.*). The implications of the NH_3 results will be discussed in the context of the PH_3 retrievals.

4.5 Retrieved Phosphine

Phosphine has a clear spectral signature *circa* 5 μm for which a number of studies (*e.g.* [27, 50, 98]) have determined an approximate mole fraction of 6.0×10^{-7} at one bar. Although PH_3 has additional spectral features in the infrared (at 1000 cm^{-1}/10 μm) and at UV and submillimetre wavelengths, low SNR, uncertainties in the line strengths and overlapping transitions from other gases have prevented more accurate abundance determinations. These alternate regions have however been used to constrain the vertical variation of PH_3 at pressures less than one bar. Here, the abundance of PH_3 decreases according to the rate of vertical mixing and photolysis [191] and may be quanti-

---

[4] Edgington *et al.* 1999 analysed UV spectra (160 to 230 nm) from the HST Faint Object Spectrograph at selected locations in Jupiter's northern and southern hemispheres.

fied by the fractional scale height. The FSHs determined from Voyager/IRIS (mid-IR), Galileo/NIMS (5 μm) and Cassini/CIRS (far-IR) spectra are 0.3 [38], 0.271 ± 0.014 [98] and 0.26 ± 0.02 [63] respectively. Of these, as the Voyager/IRIS mission most closely resembles that of Cassini/CIRS, 0.3 was adopted for PH_3 FSH and, because it is assumed to be constant, just the deep VMR fitted.

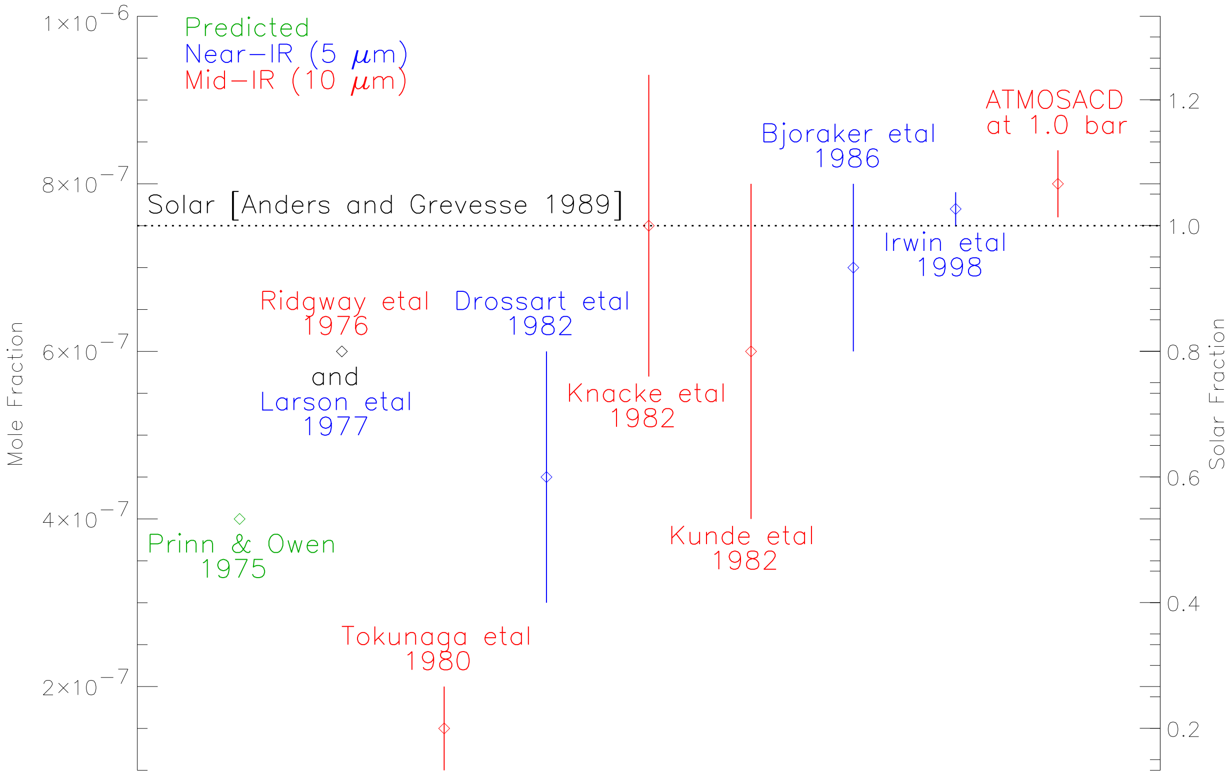

Figure 4.15: Comparison of retrieved PH_3 abundances: mole fraction to the left, fraction relative to solar P/H ratio on the right.

In general, the retrieved abundances are slightly greater than previous investigations (Figure 4.15). As can be seen in Figures 4.16 and 4.17, the pattern of depletion in the equatorial belts and enhancement of the EZ seen in the NH_3 FSH maps is also repeated in the PH_3 deep abundance maps (the abundances, sounded at deeper levels than NH_3,

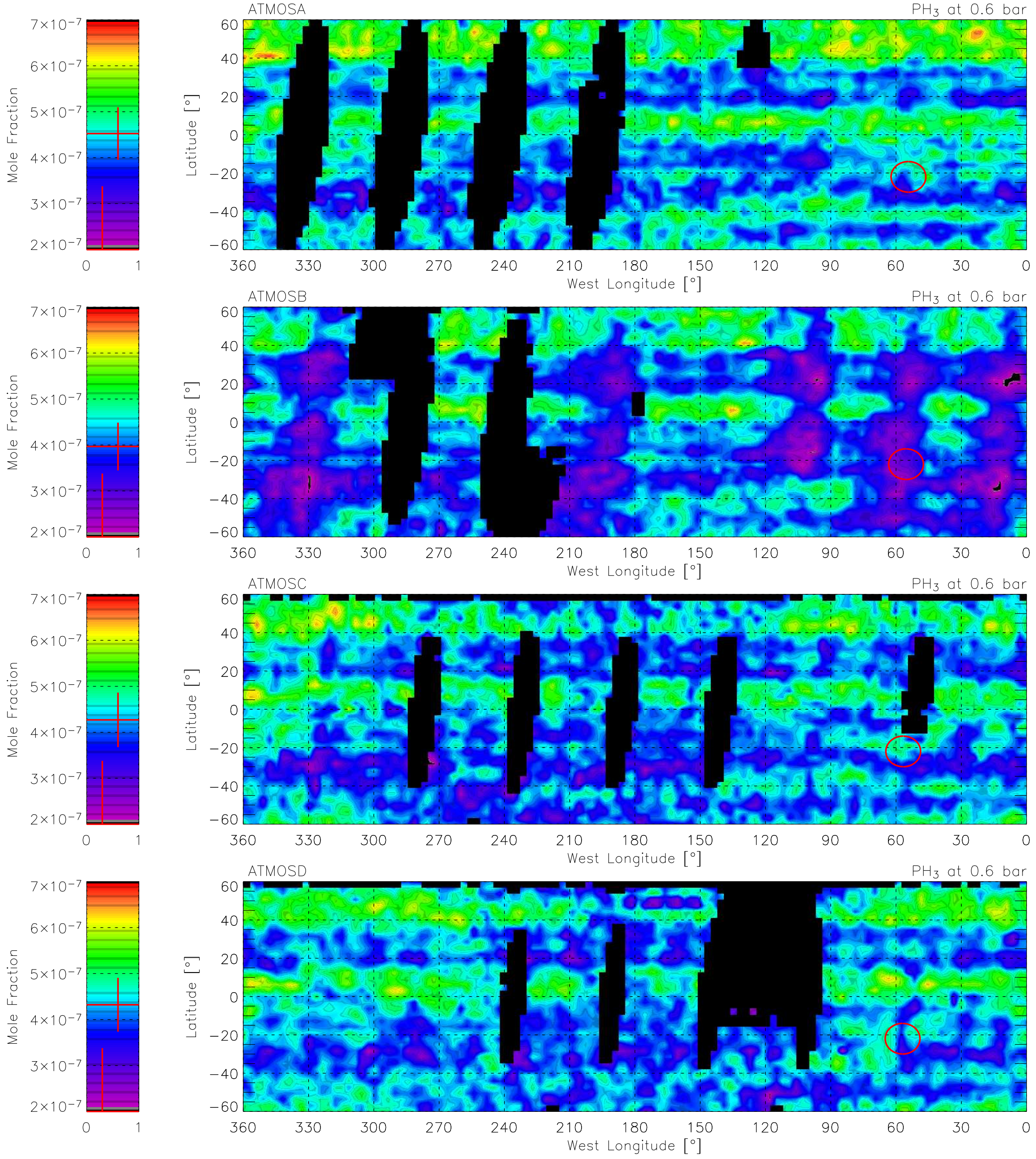

Figure 4.16: Retrieved phosphine abundance at 0.6 bar maps – ATMOSA through D. The circular outlines are the calculated locations of the GRS during ATMOS observations A through D. The GRS was assumed to be 16° in diameter, drifting slowing westward at 8°/month [197]. Plotted within the key are the *a priori* value ± the *a priori* error (left) and the mean retrieved value ± the mean retrieved error (right). The black, near-vertical stripes designate no data.

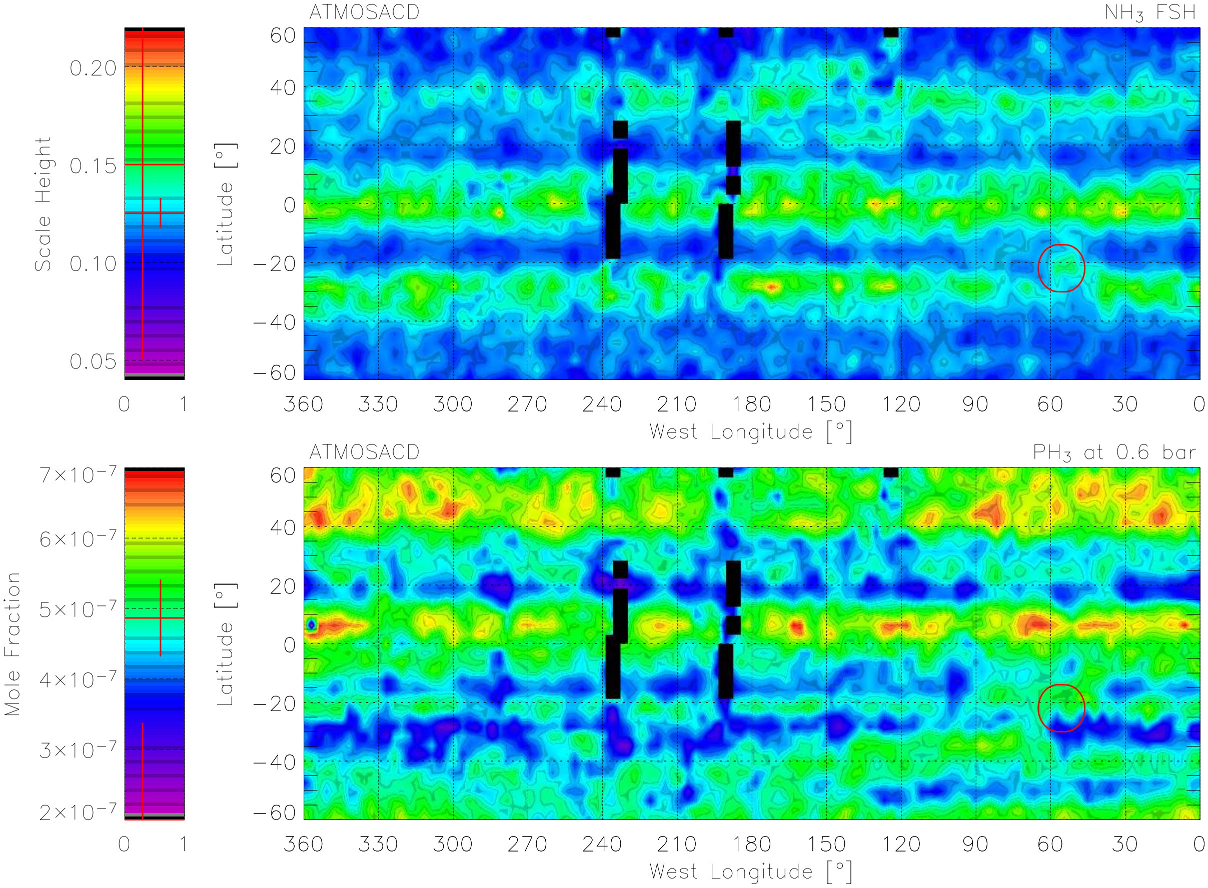

Figure 4.17: Retrieved composition maps – ATMOSACD: ammonia fractional scale height and phosphine abundance at 0.6 bar. The circular outlines are the calculated locations of the GRS during ATMOS observations A, C and D. The GRS was assumed to be 16° in diameter, drifting slowing westward at 8°/month [197]. Plotted within the key are the *a priori* value ± the *a priori* error (left) and the mean retrieved value ± the mean retrieved error (right). The black, near-vertical stripes designate no data.

are plotted at 0.6 bar because this is the pressure level most sensitive to the PH_3 feature at 1120 cm^{-1}). In the PH_3 maps however, the EZ enhancement is slightly offset to the north and there is additional enhancement seen at northern mid-latitudes (45°N). Close inspection also reveals the moderate enhancement (30%) of PH_3 over the GRS.

A number of studies (*cf.* Figure 4.15) have been conducted to investigate the spatial variation of ammonia and phosphine on Jupiter. The observed variations, characterised by regions of strong vertical transport, are a consequence of active Jovian meteorology. Such regions, for example the GRS and the turbulent wake immediately to its northwest, the equatorial region and at mid-latitudes, each have their own characteristic features and are discussed individually below.

4.5.1 Equatorial Zone

Both NH_3 and PH_3 were shown by L98 to increase towards the Equator commensurate with the EZ being a region of significant upwelling, or vigorous vertical mixing. NH_3 was determined to be the more spatial inhomogeneous of the two, exhibiting large variability in both latitude and longitude.

While both NH_3 and PH_3 appear locally enhanced within the EZ (Figure 4.17), phosphine's enhancement is slightly offset to the north. The NEB exerts a controlling influence on the cloud systems here (6° to 9°), with "projections" intruding into the EZ. These are commonly referred to as 5-μm hot-spots because of their transparency to planetary emission near 5 μm. Although hot-spots cover just 1% of Jupiter's disc, they are concentrated just north of the Equator where they encompass 15% of the equatorial

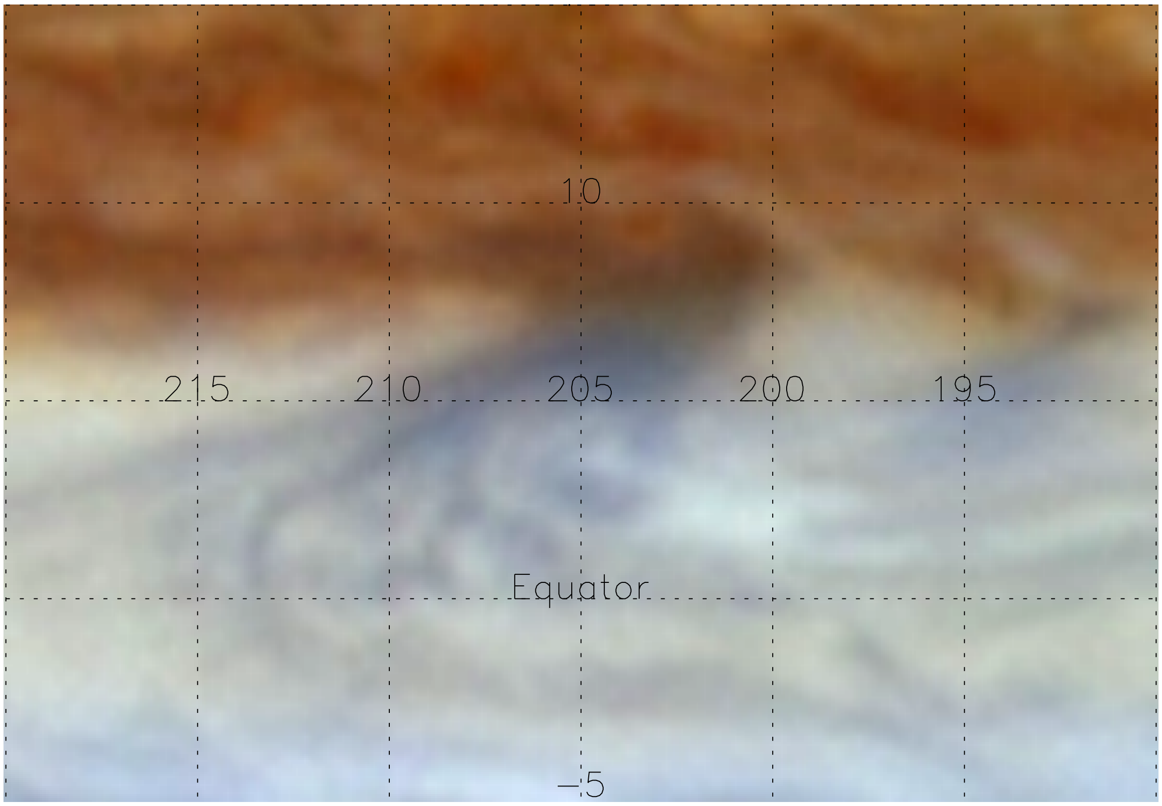

Figure 4.18: Example hot-spot as viewed by Cassini/ISS (enlarged from Figure 4.5 – see the caption for details). The dark projection running southwest to northeast at the centre of the image is the hot-spot: a region of decreased cloud opacity which appears bright in 5-μm thermal-emission images. Highly-reflective, oval- or plume-shaped clouds can be seen to the west and south-southeast of the hot-spot; the relationship between the hot-spot and the plumes is not well understood. [NASA]

surface area [143, 147] – an example hot-spot from the Millennium Fly-by can be seen in Figure 4.18.

The existence of equatorially-trapped Rossby waves, as originally proposed by Allison 1990: [3], have regularly been used to explain the spatial periodicities of the hot-spots. If Rossby waves prove to be the source of the variation in the northern EZ (more on this in §4.8) then the PH_3 enhancement likely corresponds to increased concentration within the plumes. Although the plumes were found to lie slightly to the south of the hot-spots [11], the gross spatial resolution of this study prevents any such discrimination. It is believed that NH_3 is not similarly enhanced in the northern EZ because of condensation (the air having been lifted to 1 bar from an initial pressure of 2 to 5 bars). This explanation would dovetail nicely with the increased concentration of fresh, spectrally-identifiable ammonia-ice clouds observed between 2°N and 7°N [11].

4.5.2 Mid-latitudes

While NH_3 is to first order symmetric in latitude within the retrieved abundance maps, PH_3 shows a distinct north-south asymmetry at mid-latitudes[5]. While the origin of the asymmetry is unclear, it is not unprecedented (*e.g.* NEB hot-spots and the propensity of large anticyclonic eddies – such as the GRS, to occur in the southern hemisphere [181]). Nor is the enhancement of PH_3 at northern mid-latitudes new. For example, Drossart *et al.* 1990: [51], observed a 60% enhancement in phosphine at mid-latitudes compared to

---

[5] The mid-latitudes can be said to fall between the outermost Temperate domain and the polar regions. Here, the bands are highly variable in appearance (Figure 4.30) and do not resemble the structured pattern observed near the Equator. In fact, the bands are seldom complete, instead appearing as short segments with frequent discontinuities.

both the NEB and GRS.

4.5.3 GRS Environs

The Great Red Spot environs (Figure 4.19) are uniquely complex and highly dynamic. While the latitudinal position and extent of the GRS are known to be nearly constant, the spot has been shown to be both drifting and shrinking in longitude. At the time of the Voyager encounters, the GRS was located at 77.5°W (Voyager 1) and 110.0°W (Voyager 2) with dimensions of 9.6 ± 0.1° latitude by 18.6 ± 0.6° longitude [169]. The location of the GRS in the retrieval maps agrees well with both the 50-year mean latitude (22.4 ± 0.5°S [162]) as well as the System III longitude of the January 2001 observations [145]. Assuming a shrinkage rate of 0.15 ± 0.05°/year [180], the GRS should have a longitudinal extent of approximately 16 ± 1° during the Cassini-Huygens Jupiter encounter.

As the GRS is thought to be a region of upwelling and divergence at pressures greater than 0.5 bar [43, 59], the abundances of volatiles are expected to be locally enhanced. Accordingly, the measurement of abundant volatiles like ammonia and phosphine within and around the GRS have been pursued by many authors – Figures 4.20 and 4.21 respectively. However, no enhancement of PH_3 has yet been observed and indeed the abundance of NH_3 appeared, unexpectedly, to be depleted. For example, whereas L98 found a slight enhancement in NH_3 over the GRS compared to the surrounding regions, E99 determined a 25% depletion (the L98 enhancement was however, only marginally significant with respect to the modelling uncertainties). Earlier observations by Griffith *et al.* 1992 – G92[6] derived a similar depletion in NH_3 as E99. In contrast, E99 was only able to

---

[6] Griffith *et al.* 1992's work involved three averages of Voyager/IRIS spectra at essentially the same

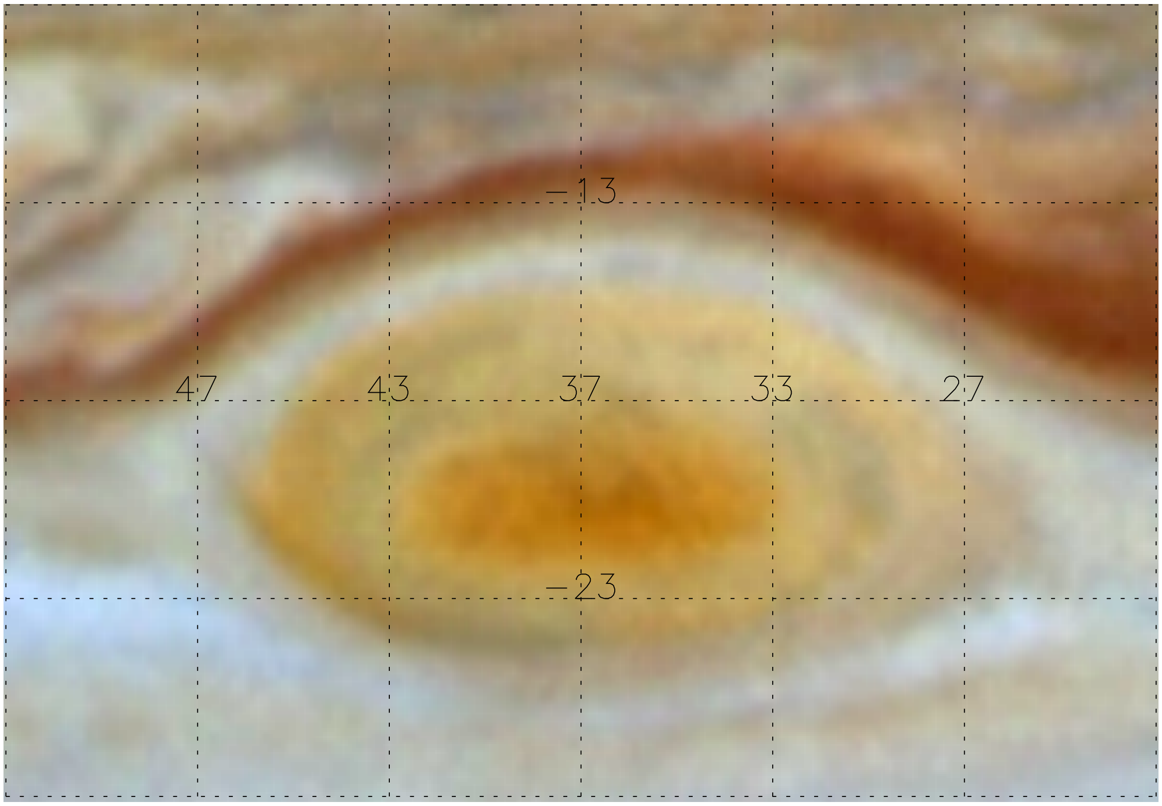

Figure 4.19: The Great Red Spot as viewed by Cassini/ISS in early November 2000 (enlarged from Figure 4.5 – see the caption for details). The GRS, which spans the entire STrZ and intrudes into the SEB, is bound poleward by a relatively mild eastward current and equatorward by the strongest westward jet on the planet. Material approaches the GRS from the east and proceeds to circulate in an anticyclonic (counterclockwise) direction. Material not absorbed either is carried away (westward) by the SEB current, or is displaced eastward by the strong equatorial stream (on the other side of the SEB!). [NASA]

determine an upper-limit PH_3 abundance at the tropopause. And while G92 and L98 sounded deeper levels, neither study was able to discern an enhancement in PH_3 within their respective uncertainties. Several other authors have searched for the enhancement of NH_3 and/or PH_3 as well, however with limited success. In this study, both NH_3 FSH and PH_3 appear marginally enhanced, but at different spatial locations (Figure 4.22). While NH_3 FSH appears slightly enhanced within the GRS itself, the enhancement of PH_3 occurs northeast of the GRS. Both trends are however on the edge of detection and can only be considered mildly significant.

The differences between this study's result and that of G92 and L98 (*cf.* Figures 4.16, 4.15 and 4.21) may be due to the way the analyses were conducted. For example, G92's longitudinal averaging is likely to have smoothed-out strong localised abundance gradients resulting in a weak GRS trend with respect to its surroundings. The discrepancy between this study and that of L98 would appear radiative-transfer model related, differing in several key respects:

- they used a line-fitting retrieval program,
- they investigated three doublets between 945 and 975 cm^{-1} – a wavenumber region more sensitive to NH_3 absorption and cloud opacity than PH_3,
- they assumed PH_3 varied with constant FSH above 1.25 bar,
- and they included a cloud layer between 0.65 and 0.3 bar in their model.

---

latitude: two of the STrZ and one of the GRS. The same number of spectra were considered in each average with the GRS spectra taken during closest approach. Only the spectral intervals 200 to 600 cm^{-1} and 800 to 1140 cm^{-1} were considered.

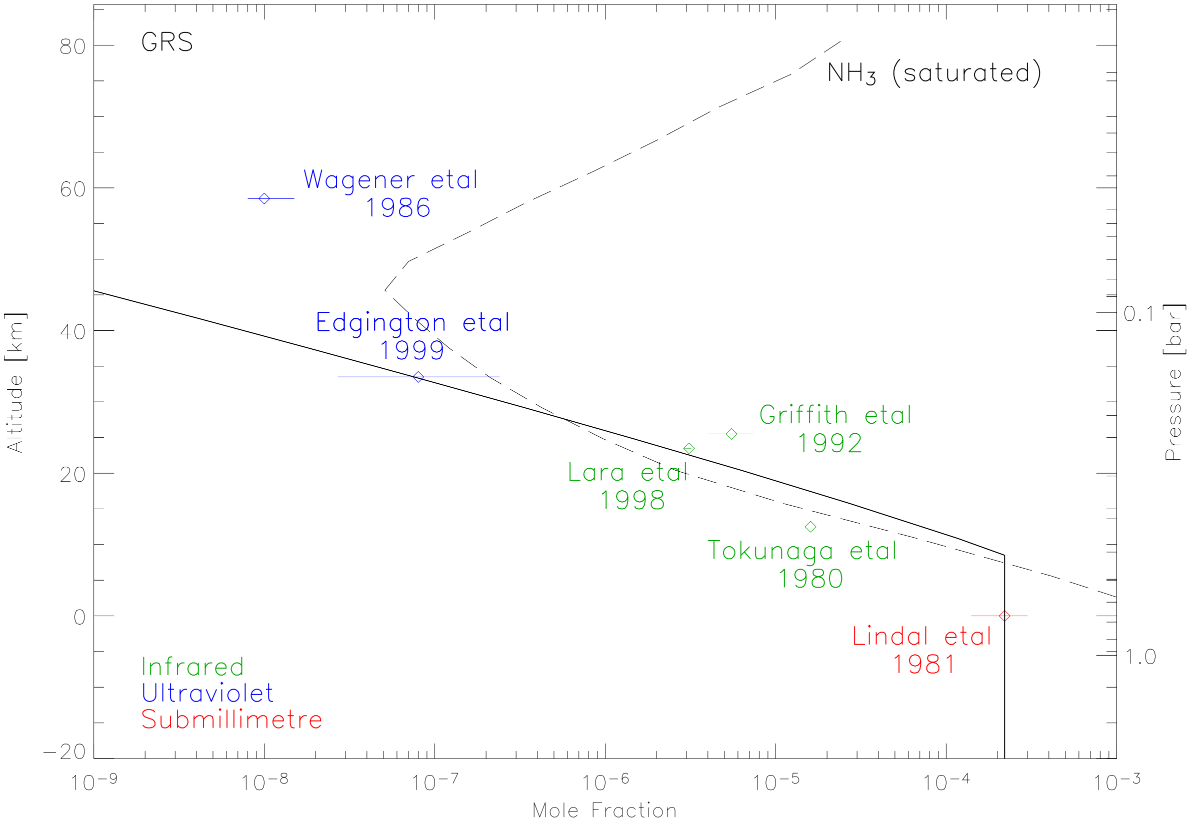

Figure 4.20: Ammonia mole fraction *versus* altitude – GRS. The deep abundance was assumed to be that of Lindal *et al.* 1981: [120], $(2.2 \pm 0.8) \times 10^{-4}$, falling off above 0.7 bar (the condensation level) according to the retrieved FSH (1.36 ± 0.01). In this way, the NH_3 abundance at 0.5 bar and 0.3 bar is $(1.7 \pm 0.7) \times 10^{-5}$ and $(3.4 \pm 2.5) \times 10^{-7}$ respectively. For reference, the solar N/H mole fraction is 1.12×10^{-4} [5].

The infrared results may, at first, appear spurious as they are all nearly supersaturated. However, should the upwelling within the GRS be significant, it is plausible the NH_3 near the cloud tops is not in equilibrium with the surroundings having been quickly transported from below. Furthermore, the validity of the saturation curve is based on an assumed condensate purity and is dependent upon the accuracy of the accompanying temperature-retrieval.

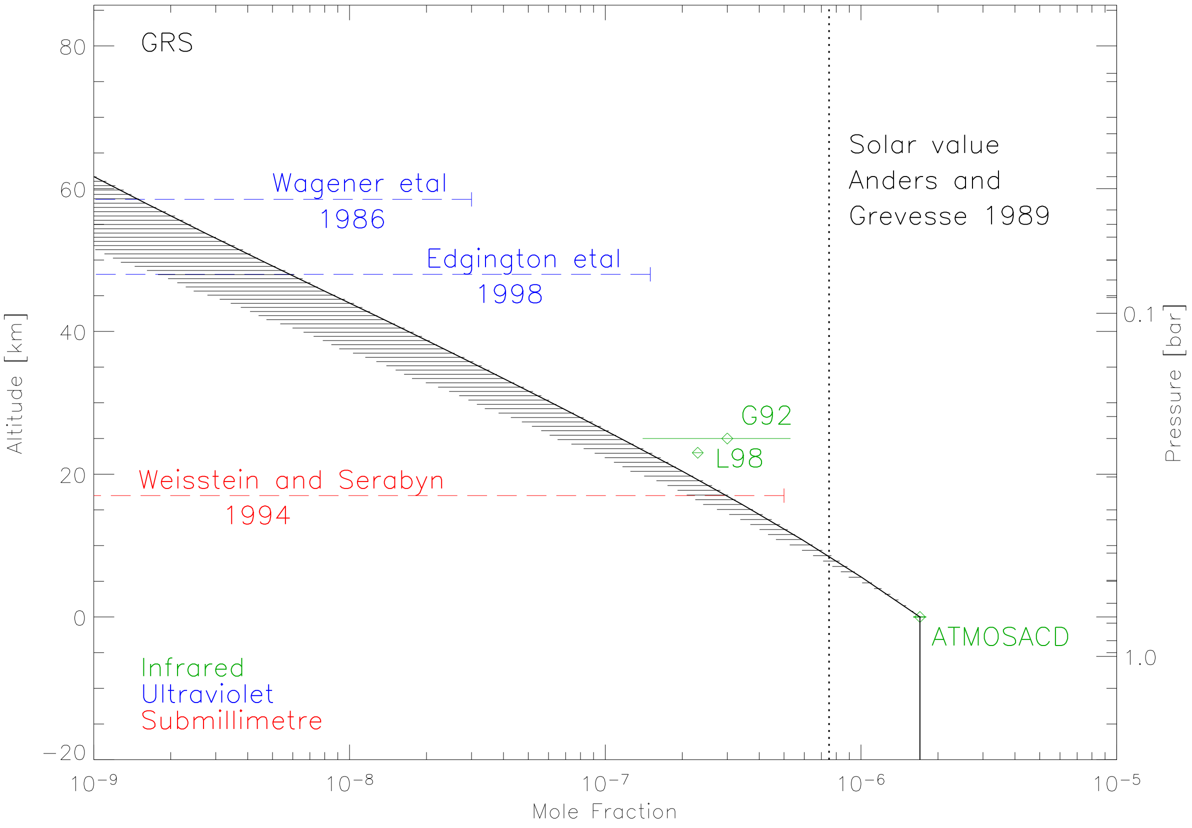

Figure 4.21: Phosphine mole fraction *versus* altitude – GRS. Unlike the NH_3 profile, the PH_3 profile was constructed assuming a constant FSH (0.3) above the retrieved, deep (1.0 bar) abundance. In the presented distribution, the phosphine abundance at pressures greater than one bar is $(1.6 \pm 0.1) \times 10^{-6}$ falling off to $(3.4 \pm 0.3) \times 10^{-7}$ at 0.5 bar and $(1.2 \pm 0.1) \times 10^{-7}$ at 0.3 bar. The shaded region represents PH_3 abundances if a FSH ranging between 0.26 and 0.3 were chosen.

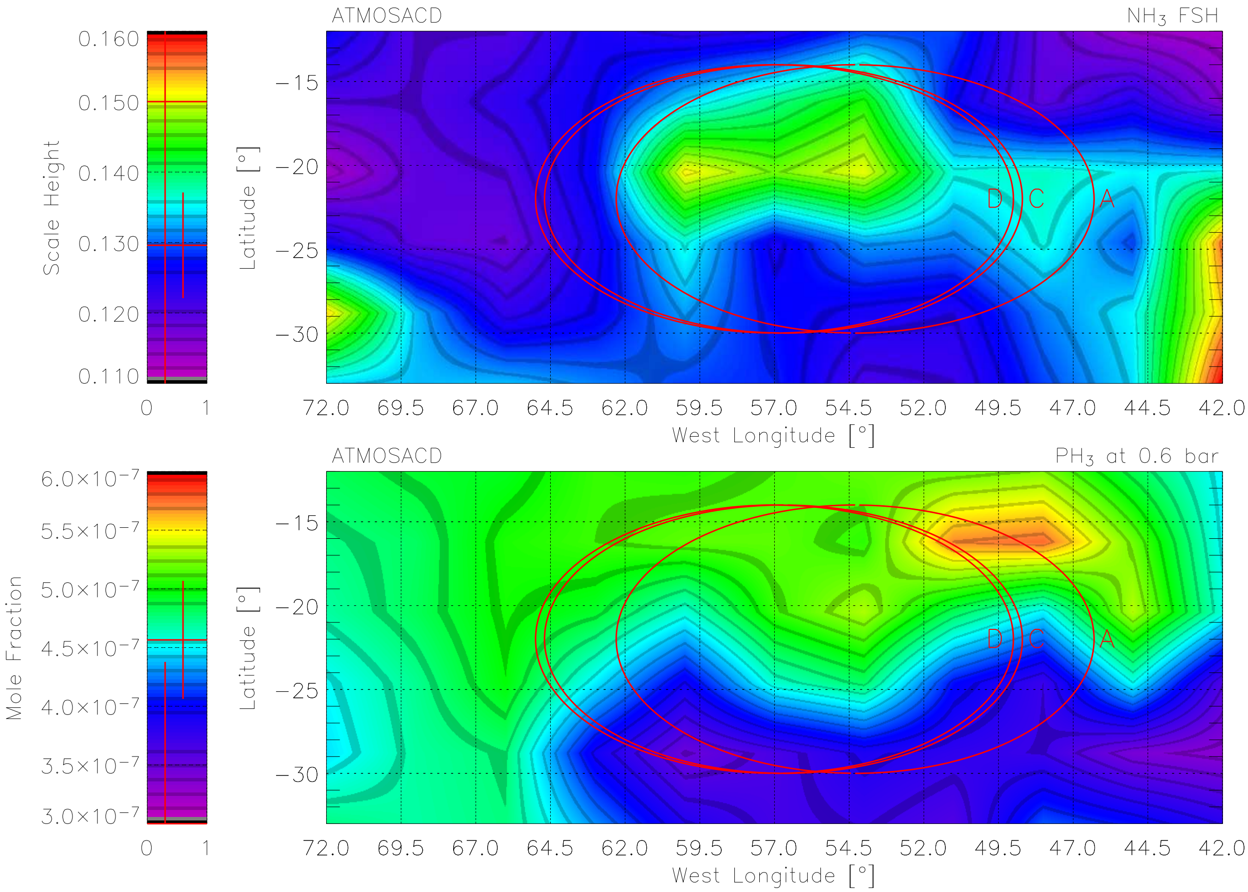

Figure 4.22: Retrieved composition maps – GRS environs: ammonia fractional scale height and phosphine abundance at 0.6 bar. *N.b.*, the colour contrast has been enhanced from that displayed in Figures 4.16 and 4.17. The circular outlines are the calculated locations of the GRS during ATMOS observations A, C and D. The GRS was assumed to be 16° in diameter, drifting slowing westward at 8°/month [197]. Plotted within the key are the *a priori* value ± the *a priori* error (left) and the mean retrieved value ± the mean retrieved error (right). ATMOSACD spectra.

It is then no surprise that this study also does not agree with the other result of L98, that PH_3 smoothly decreases with latitude from 10°S to 35°S. In the case of NH_3, spectral incompatibilities and observational limitations between G92, L98 and E99 prevent a direct intercomparison of the retrieved values.

4.6 Retrieved Haze Opacity

Like NH_3 FSH and PH_3, the retrieved haze opacity (Figure 4.23) matches the belt-zone albedo variations observed in the visible. Unfortunately however, the opacity due to aerosols is less well-known than that due to gases and is viewed with an element of uncertainty. Whereas both NH_3 and H_2O ice have been detected in Jupiter's atmosphere, they are non-uniformly distributed and only amount to a few percent of the planet's disc at any one time [11, 179]. For the most part, the chemical composition and the spectroscopic properties of the particulate absorbers are unknown (although large radii has been inferred to provide the necessary opacity in the thermal infrared [34, 73, 146]).

The cloud used in this study was patterned on the inhomogeneous NH_3 cloud properties of the uppermost cloud level but based at one bar to mutually account from the variability in thermal emission at both 8.5 μm and 45 μm and at 5 μm. Despite grey-absorbing aerosols being indistinguishable from a cloud-free atmosphere with suitably adjusted temperature profile, the aerosol opacity was assumed to be spectrally-grey over the limited spectral ranges considered. This is so that both temperature and cloud opacity may be utilised as free parameters with which to minimise the difference between the synthetic and measured spectra in regions away from NH_3 and PH_3 absorption features.

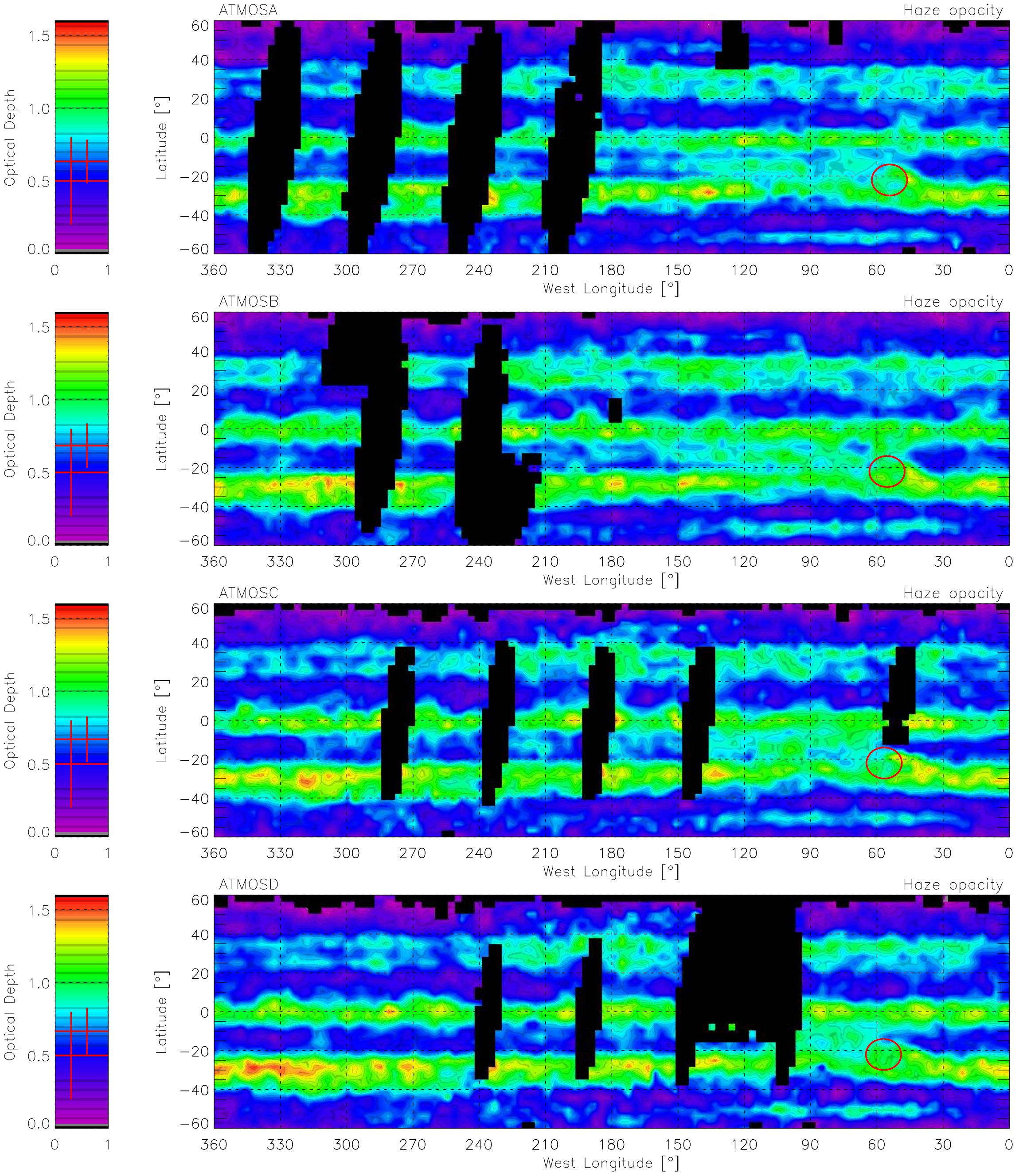

Figure 4.23: Retrieved haze opacity maps – ATMOSA through D. The circular outlines are the calculated locations of the GRS during ATMOS observations A through D. The GRS was assumed to be 16° in diameter, drifting slowing westward at 8°/month [197]. Plotted within the key are the *a priori* value ± the *a priori* error (left) and the mean retrieved value ± the mean retrieved error (right). The black, near-vertical stripes designate no data.

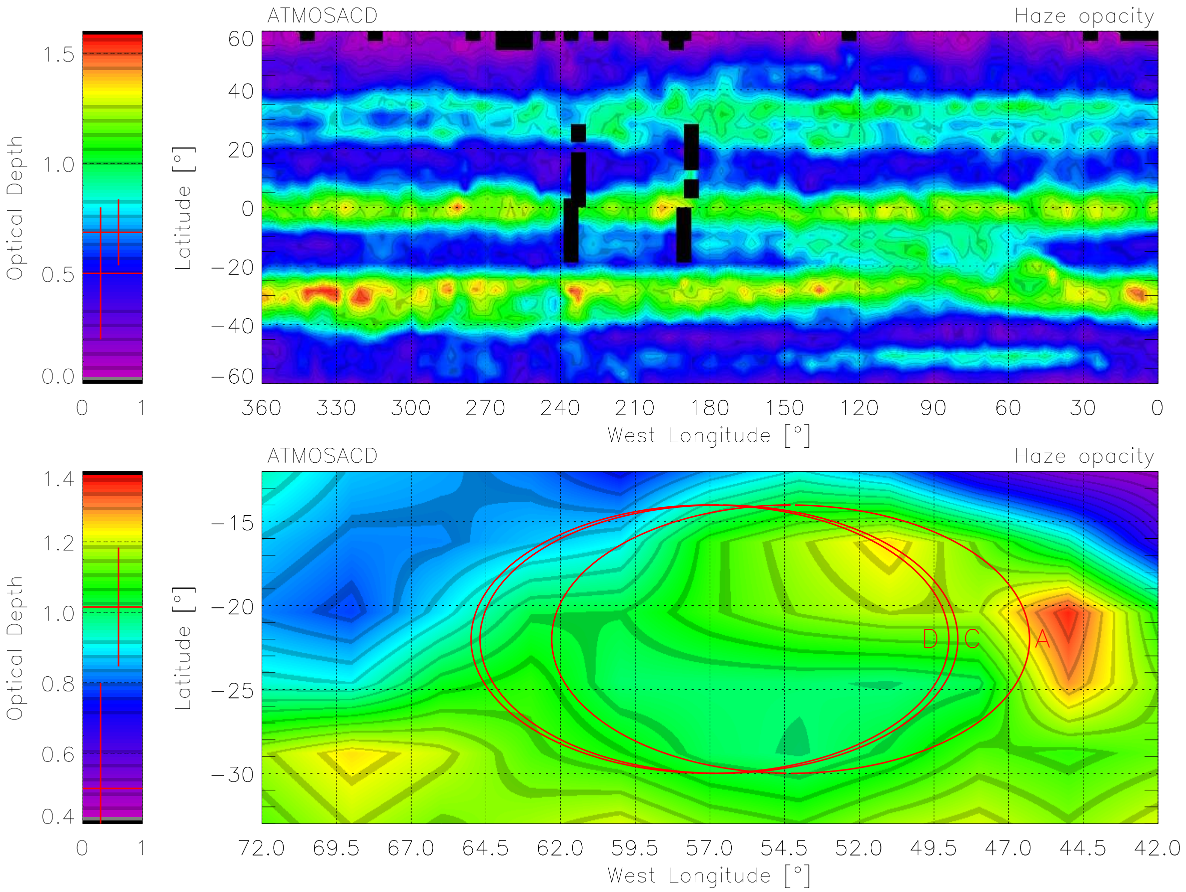

Figure 4.24: Retrieved haze opacity maps – ATMOSACD, GRS environs. *N.b.*, the colour contrast has been enhanced in the bottom plot from that displayed at the top and in Figure 4.23. The circular outlines are the calculated locations of the GRS during ATMOS observations A, C and D. The GRS was assumed to be 16° in diameter, drifting slowing westward at 8°/month [197]. Plotted within the key are the *a priori* value ± the *a priori* error (left) and the mean retrieved value ± the mean retrieved error (right).

If the increased optical depth viewed in the maps can be accurately interpreted as extended path-lengths associated with clouds, then the retrieved haze opacity agrees well with post-Voyager analyses [44, 203]. This includes the asymmetric nature of the opacity about the Equator and increased opacity over the EZ and STrZ. The haze opacity over the GRS (Figure 4.24) was found to resemble that of the surrounding STrZ. This is in agreement with both G92 and Galileo/NIMS observations [12] despite the average optical depth (1.0) being up to two times the values for these studies (0.45 and 0.7 respectively). However, if the pressure level the studies probe are considered (~ 0.3 bar *versus* 1.0 bar for this study), the discrepancy is qualitatively explained.

4.7 Radiance Differencing

Retrieving atmospheric composition from remotely-sensed spectra is a classic ill-posed problem. Due to uncertainties in the spectra and approximations in the forward model, there are many combinations of profiles that generate results which are consistent with the observed spectra. In attempted validation of the retrieval model, a simple radiance-differencing scheme is used for extracting the spatial distribution of phosphine abundance directly from the radiances.

4.7.1 Wavelength-Pair Selection

The synthetic, and rate-of-change, radiances of Figure 3.8 were searched for wavenumber pairs of equal brightness temperature which were equally affected by changes in temperature, ammonia and haze opacity, but differentially affected by variations in the phosphine abundance. The optimum pair would have as small a wavenumber separation as possible so that the assumption of grey cloud absorption remains valid. If two such wavenumbers could be found, then a rough map of the phosphine-abundance variation may be constructed.

The same forward model run used in the creation of the transmission-weighting and contribution functions was used to calculate the change in brightness temperature (T_B) when the *a priori* ammonia (deep VMR and FSH), phosphine (deep VMR and FSH) and haze opacities were changed by 50%. The optimum pair, found at T_B = 154.0 K ($\sim$ 0.7 bar), was determined to be 1186.94 cm^{-1} and 1189.66 cm^{-1}. Such high precision is possible despite using a one-wavenumber resolution forward model because the selection routine does not test the spectral points themselves, but samples the interpolated radiance at 154 K. Figure 4.25 shows the forward model-synthesised spectrum in the region of this pair together with the differences introduced by varying the composition and cloud structure; as the pair represent equal brightness temperature, they are also roughly at the same altitude. By preparing brightness temperature maps at these two wavenumbers and subtracting them, any variations observed should be attributable to phosphine variation alone.

4.7.2 Validation and Application

The set of 92 test spectra previously used to validate the retrieval model (§4.1) was also used here in the validation of the radiance-differencing technique. For each variable parameter, the brightness-temperature difference, $\Delta T_B = T_B(\tilde{\nu_2})$ - $T_B(\tilde{\nu_1})$, was plotted

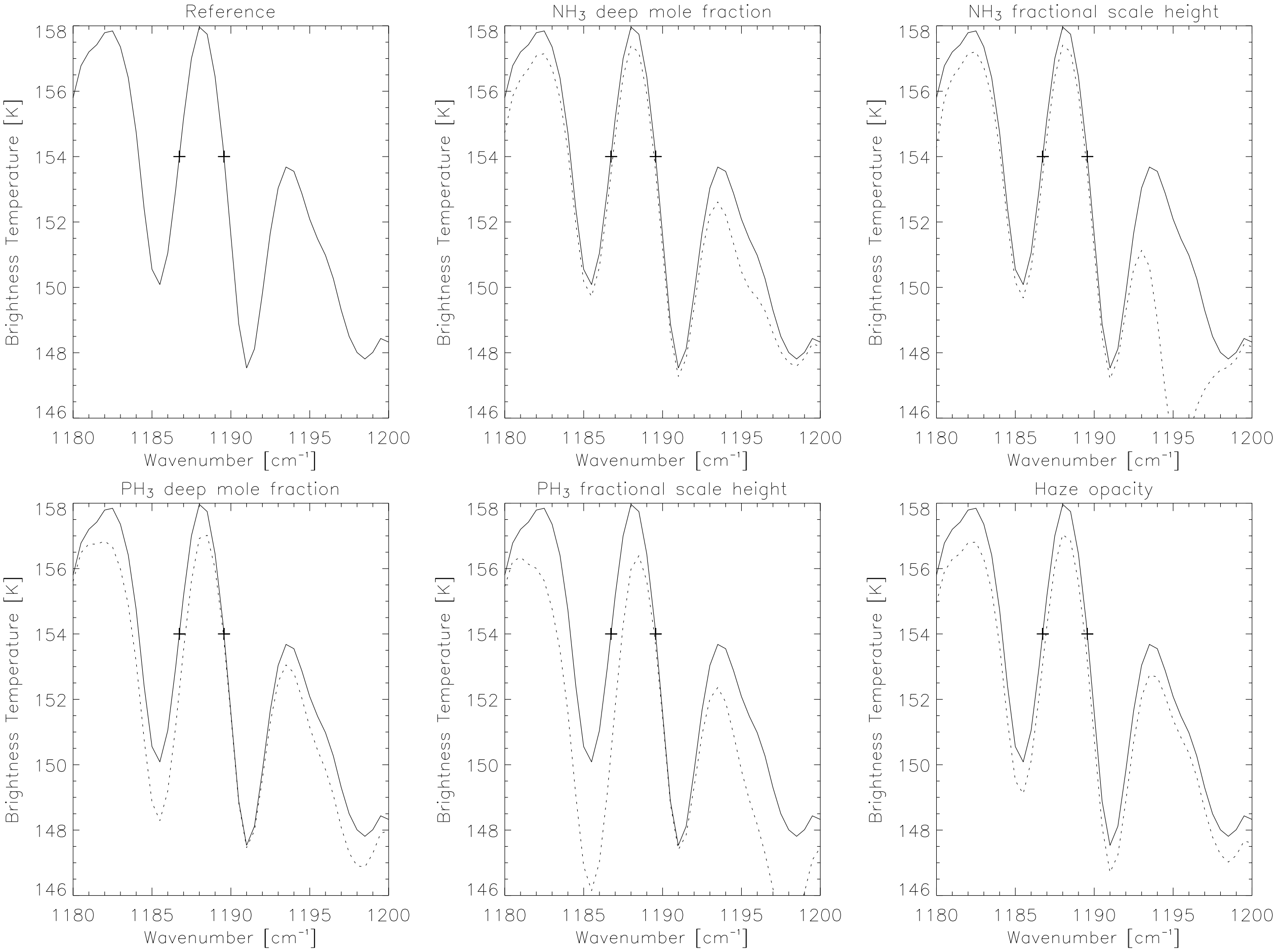

Figure 4.25: Wavenumber-pair selection for use in radiance differencing. The differential sensitivity to PH$_3$ for the 1186.94 cm^{-1} and 1189.66 cm^{-1} pair (indicated by the + symbols) *versus* the other parameters is clear. The pair is assumed to have minimum sensitivity to temperature as the brightness temperatures were used in their determination.

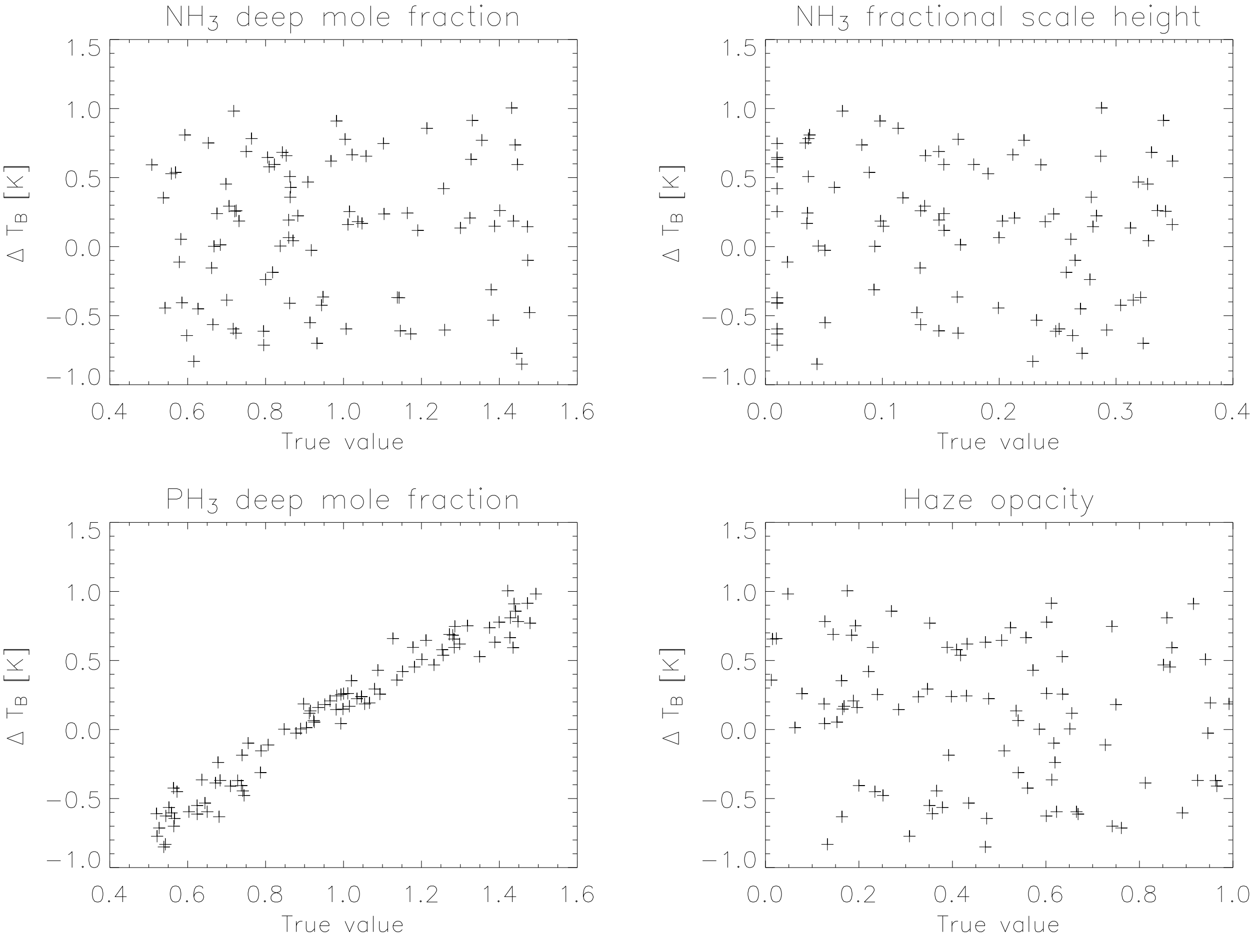

Figure 4.26: Scatter plots of brightness-temperature difference *versus* composition.

against the original values of ammonia, phosphine, cloud and temperature used to generate the spectra ("true value"). The results are shown in Figures 4.26 and 4.27. A clear correlation with phosphine abundance can be seen, as can be the non-dependence of the other parameters (including temperature).

The same procedure was then applied to the ATMOS data-set. To ensure that the same features from the forward model were selected within the ATMOS maps, the syn-

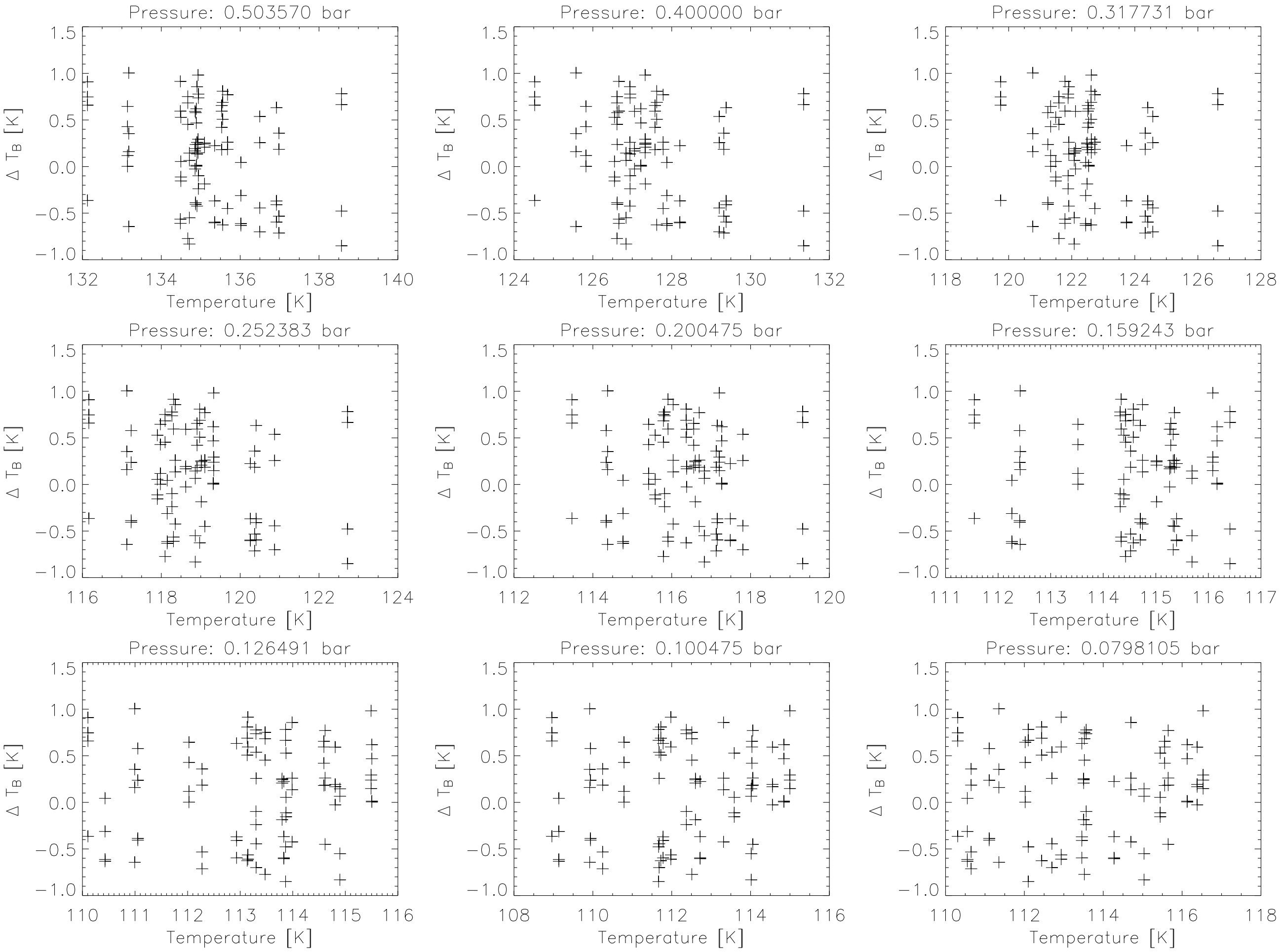

Figure 4.27: Scatter plots of brightness-temperature difference *versus* temperature. Although ΔT_B was found to be uncorrelated with variation at all levels, only the temperatures between 0.5 to 0.08 bar are shown for the sake of brevity.

Map Designation	T_B **offset**	**Optimum pair** $\tilde{\nu}_1$	**Optimum pair** $\tilde{\nu}_2$
ATMOSA	6.0 K	1187.7 cm^{-1}	1190.1 cm^{-1}
ATMOSB	4.8 K	1187.7 cm^{-1}	1190.0 cm^{-1}
ATMOSC	5.7 K	1187.6 cm^{-1}	1190.1 cm^{-1}
ATMOSD	6.1 K	1187.7 cm^{-1}	1189.7 cm^{-1}
ATMOSACD	5.9 K	1187.7 cm^{-1}	1189.8 cm^{-1}

Table 4.1: ATMOS brightness-temperature offsets and wavenumber-pairs. As the radiance-differencing method is particularly wavelength sensitive, the small variation of the wavelength-pairs ($\sim$ 0.2 cm^{-1}) between the ATMOS maps was allowed to set the precision of the experiment.

thetic brightness temperatures were vertically offset to match the measured radiances converted into brightness temperature. The measured brightness temperatures were then searched for wavenumber pairs at the new ($T_B = 154$ K + offset) brightness temperature which matched the selection criteria – the brightness temperature offset and the selected wavenumber pairs are listed in Table 4.1, while the ΔT_B maps for the individual ATMOS observations and ATMOSACD can be seen in Figures 4.28 and 4.29.

Just as with the forward model, the spacing between the ATMOS wavenumber pairs is greater than the spectral resolution, but only just. Yet there is no reason to believe the correlation displayed in Figure 4.26 cannot be achieved using a wavenumber pair one spectral interval apart. Indeed, the radiance-differencing method produces the gross meridional structure observed within the PH_3 retrieval maps totally disregarding the relative enhancement within the GRS, over the EZ (again, slightly offset to the north) and in pockets at northern mid-latitudes – the main results of this work.

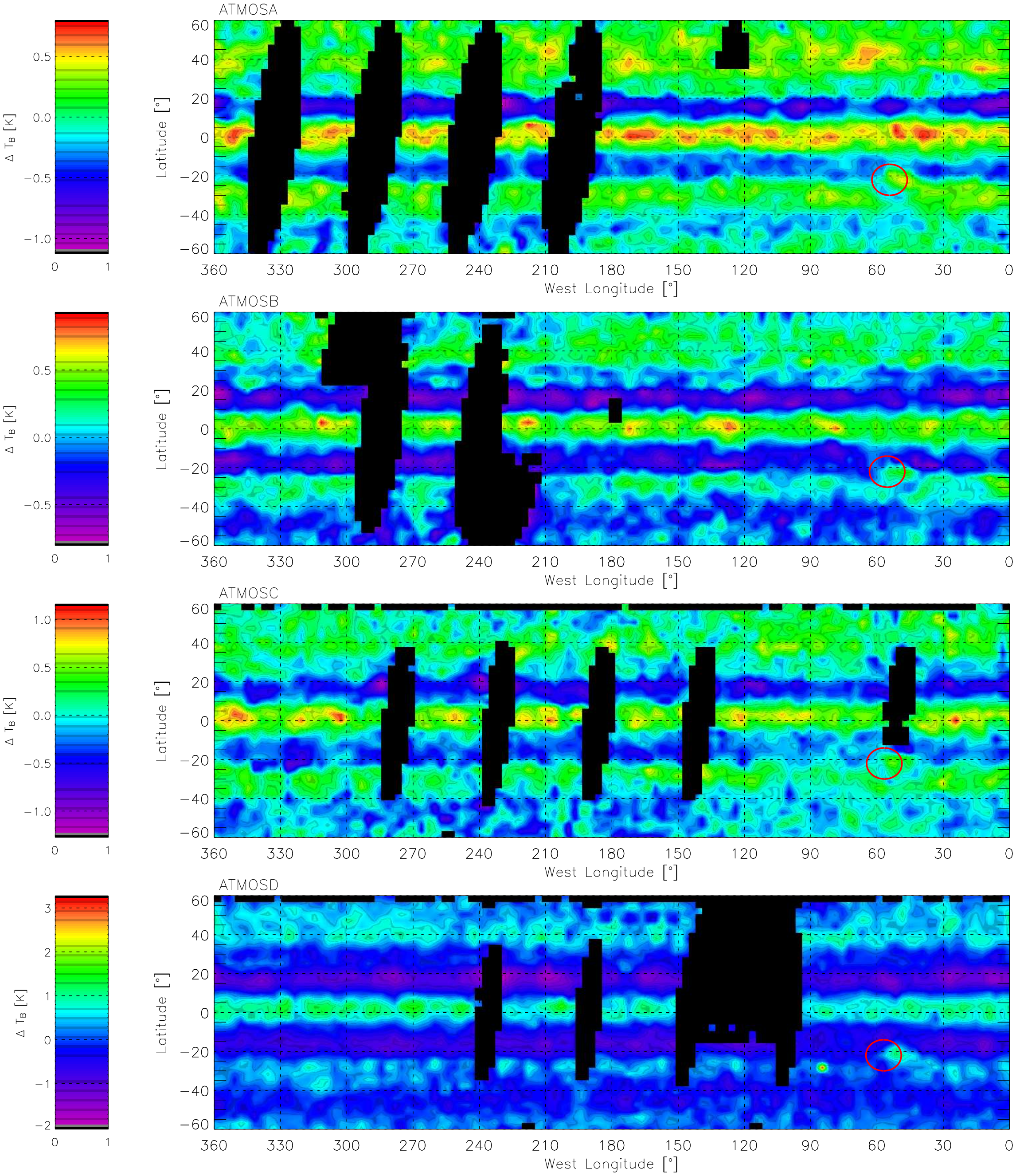

Figure 4.28: Brightness-temperature difference maps – ATMOSA through D. *N.b.*, the maps are not plotted on the same ΔT_B scale. The circular outlines are the calculated locations of the GRS during ATMOS observations A through D. The GRS was assumed to be 16° in diameter, drifting slowing westward at 8°/month [197]. The black, near-vertical stripes designate no data.

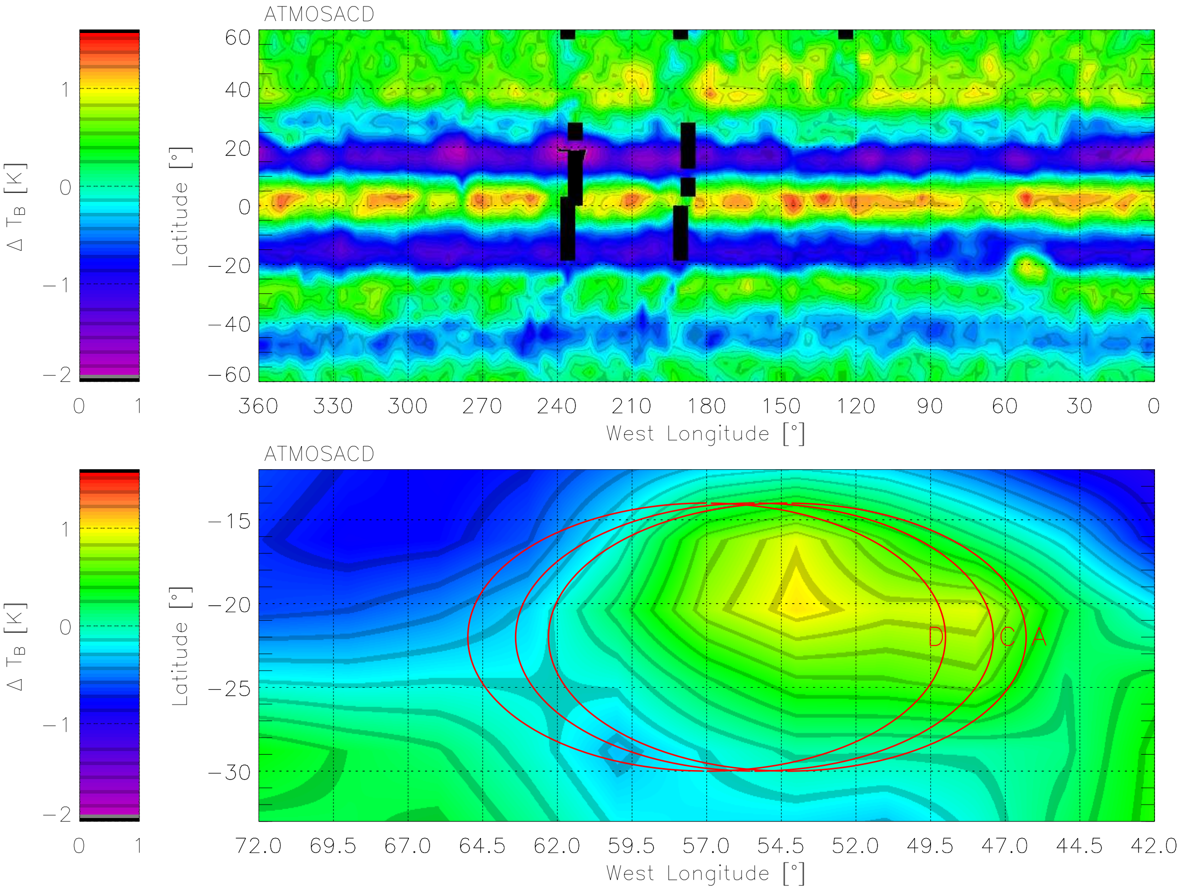

Figure 4.29: Brightness-temperature difference maps – ATMOSACD, GRS environs. The circular outlines are the calculated locations of the GRS during ATMOS observations A, C and D. The GRS was assumed to be 16° in diameter, drifting slowing westward at 8°/month [197]. The black, near-vertical stripes designate no data.

4.8 Discussion

Two methods of analysis have been employed to investigate the spatial distribution of phosphine on Jupiter. The results complement and/or extend previous investigations. The following discussion expands upon the text in an attempt to inter-relate the results and validate the approach and interpretation.

4.8.1 5-μm Hot-spots

Historical observations of the hot-spots at 5-μm show little in the way of general patterns or principles governing their time-dependent behaviour. These observations also reveal that only one hemisphere is active with hot-spots at any given time – the transition to the north occurring at the turn of the twentieth century [162]. Observations by spacecraft have slightly complicated the issue however. It turns out the southern EZ is not as quiet as the historical observations suggest, for a solitary projection was observed during the Voyager encounters [3]. In addition, observations by Galileo showed a cloud morphology within the SEB resembling the cloud structure associated with the hot-spots north of the Equator, however on a smaller scale and inverted with respect to latitude [197].

Two competing theories have been proposed to explain the hot-spots. The first describes hot-spots as a phenomena of local meteorology. Under this proposal [197], a hot-spot may be interpreted as an anticyclonic vortex lying in the shear region between two cyclonic regions to the west and southeast and would account for the dry and cloud-free nature of the hot-spots [158, 167]. Alternatively, the regular nature of the hot-spots, their motion as a coherent pattern relative to the mean zonal wind and the reflection about the Equator suggest the influence of an atmospheric wave [3, 143].

Radio occultation and infrared measurements provide a variety of observational evidence for the latter option. For example, time-series analysis [86, 143] has shown hot-spots of planetary-wavenumbers[7] 8, 9 and 10 propagating west (counter to the prevailing flow) in excess of 100 m/s. Many authors (*e.g.* [3, 49, 143]) interpret this as a vertically-propagating Rossby wave which alternatively stretches and compresses the vertical air column to form the 5-μm hot-spots and plumes respectively. Non-linear simulations of the hot-spots [175] show that the extent of the compression/stretching could be a factor of two or more. This in accordance with Galileo probe observations in which the NH_3, H_2S and H_2O condensation levels appear to have been forced downwards (from 1, 2 and 5 bars to 8, 16 and $>$ 20 bars respectively) [135].

It is important to note that, although the temperature retrievals were found to be consistent with Pioneer and Voyager results (including the appearance of the QQO at tropospheric pressures), no correlation between the location of the 5-μm hot-spots and the upper-troposphere/lower stratosphere oscillation have been observed [67, 147]. Furthermore, with velocities in excess of 100 m/s ($\sim 7^\circ$/day [143]) and observation times close to two sidereal rotation periods, the spatial response within the north EZ is likely to be horizontally-smeared with spectra from the hot-spots/plumes propagating from one bin to the next. This is unlikely to be a problem for everything except the hot-spots because of nature in which the north-to-south scans were conducted and because of the lack of organised features within the jets.

---

[7] The number of wavelengths in one planetary circumference.

4.8.2 Northern Mid-latitudes

Although thermal waves are ubiquitous in the Jovian atmosphere [60, 86, 125], the relative enhancement of PH_3 at northern mid-latitudes cannot however be described in the same terms as those used for hot-spots. This is because long-period planetary-waves are unable to propagate vertically at mid-latitudes due to the frequency being less than the mid-latitude Coriolis frequency [143].

The relative PH_3 enhancement is then likely related to increased vertical advection. As the deep mole fraction of PH_3 was retrieved (*vice* PH_3 FSH), the advection would be presumed to occur at a deep level. Evidence for deep convection at mid-latitudes, at least as deep as water condensation, comes from a variety of sources. For example, water clouds were inferred at mid-latitudes using Voyager/IRIS [179]. Although the water-ice study exhibited a preference for southern mid-latitudes (50°S), the balance is somewhat redressed with all of the mid-latitude, spectrally-identifiable ammonia-ice clouds being observed in the north [11] – spectrally-identifiable ammonia-ice clouds were also observed during the Millennium Fly-by as exemplified in Figure 4.30). Independent evidence for deep convection at mid-latitudes for both hemispheres comes from lightning studies performed with Voyager and Galileo imaging data [28, 123].

While a suitable explanation for ammonia and water clouds occurring in separate hemispheres has yet to be given, convective activity at mid-latitudes can be seen to persist well into the upper-troposphere. Here, continued advection is determined by external influences such as insolation and auroral precipitation.

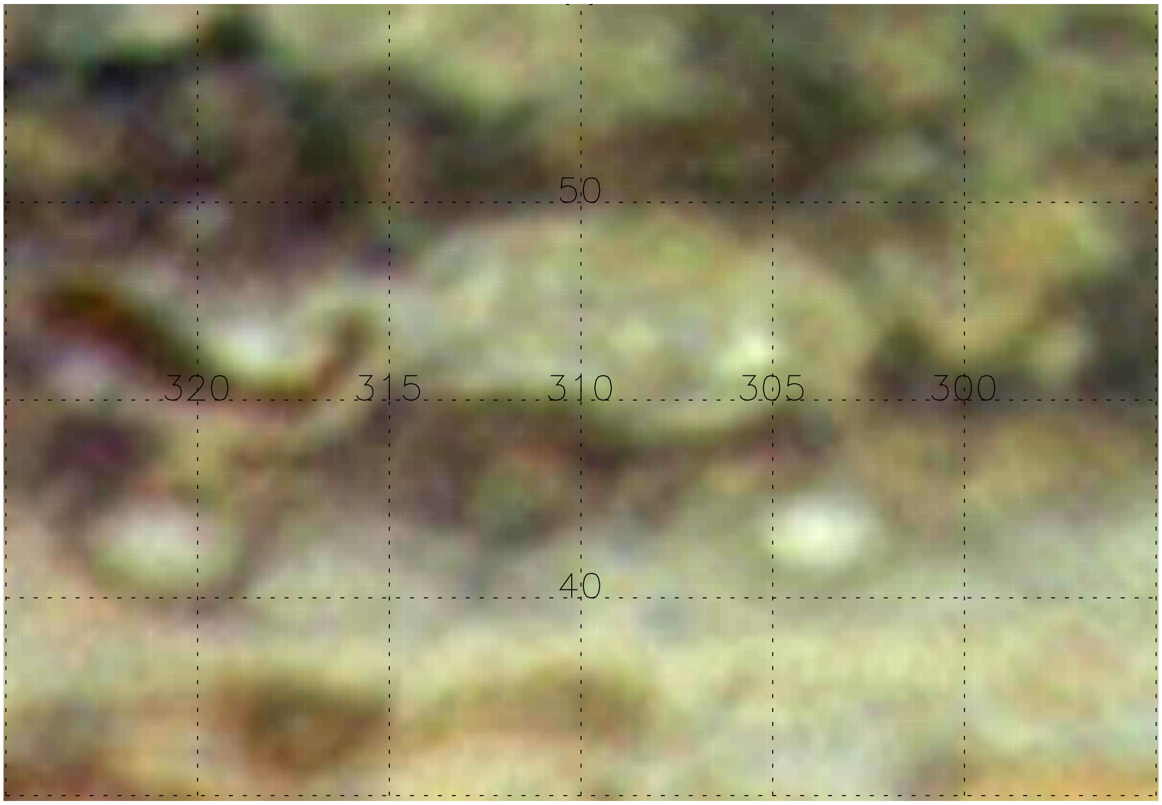

Figure 4.30: The northern mid-latitudes as viewed by Cassini/ISS (enlarged from Figure 4.5 – see the caption for details). The northern mid-latitudes, from 40°N to 50°N, are represented by the North North Temperate Zone and North North North Temperate Belt pair. The latitudinal extent of the pair, based on their 50-year means, is (39.1 ± 0.7°N) to (47.0 ± 1.0°N) and are separated by the North North Temperate Current at (42.7 ± 1.0°N) [162]. [NASA]

As Jupiter's plasma environment is known to produce observable features within the polar regions [36, 37], the lull in the relative-enhancement of PH_3 at northern mid-latitudes (from 240°W to 90°W – see Figure 4.17), seemed, at least initially, very inviting. It was originally thought that collisional-heating within the northern auroral oval[8] could be responsible for the suppression of advection within this region. However, the lull is now believed to be no more significant than an artificial artefact of the data and/or plotting routine. For one thing, the same suppression does not appear in the radiance-differencing maps. More critically, the particle flux would either need to penetrate suitably deep or evaporate the overlying haze so that the incident radiation could suppress the internal upwelling. Neither proposal readily agrees with established theory. While the depth penetrated by the precipitating particles is not well documented, it is believed unable to reach pressures greater than 0.01 bar [61, 104]. Additionally, the northern onset of the polar hood/increased stratospheric haze occurs at 35°N [159].

Similarly, while insolation is known to play an active part in stratospheric dynamics at mid-latitudes, its influence at tropospheric pressures (whether direct, indirect, or none at all) is debated. As the number of photons available for photodissociation is less at mid-latitudes, insolation's direct influence would be the apparent increase in phosphine concentration at mid-latitudes. However, as PH_3 is photolysed *circa* 80 mbars [191] and no insolational heating is observed below this level (Figure 4.31), the explanation would require efficient dynamical connection between the troposphere and the stratosphere

---

[8] The auroral ovals (of which there are two, one in the northern and southern hemispheres) mark the boundary between open and closed magnetic-field lines. Their significance in atmospheric studies results from the precipitation of charged particles on the open field lines resulting in heating of the upper-atmosphere (20 μbar or higher). During the Jupiter encounter, the northern auroral oval (centred at 65°N, 180°W with approximate 20° diameter) was observed to dip equatorward of 60°N on several occasions [61, 153]. The southern auroral oval is off the map at 75°S, 30°W [61].

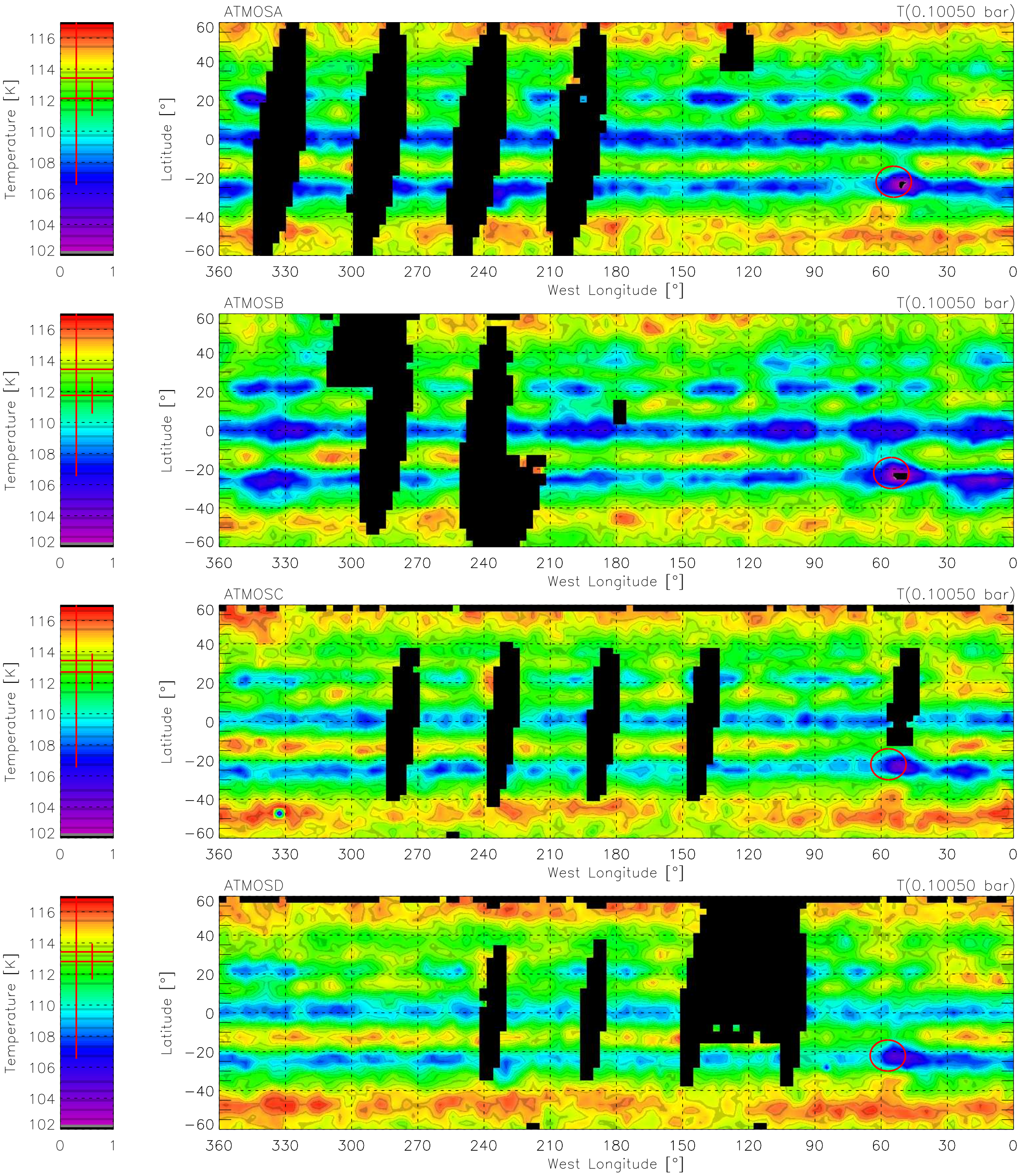

Figure 4.31: Retrieved temperature at 0.1 bar maps – ATMOSA through D. Note the cold temperatures over the GRS at 22°S, 55°W. The circular outlines are the calculated locations of the GRS during ATMOS observations A through D. The GRS was assumed to be 16° in diameter, drifting slowing westward at 8°/month [197]. Plotted within the key are the *a priori* value ± the *a priori* error (left) and the mean retrieved value ± the mean retrieved error (right). The black, near-vertical stripes designate no data.

(which is unlikely considering the strongly stratified nature of the stratosphere [203]).

Alternatively, insolation is conjectured to indirectly affect mid-latitudes by suppressing the lapse rate within the equatorial upper-troposphere causing atmospheric motions to counter-balance the differential solar-heating at higher latitudes [92, 151]. The increased advection under this scenario would support the enhancement of PH_3 observed at northern mid-latitudes. However, the Millennium Fly-by took place slightly after northern summer solstice when insolation at 45°N exceeds the winter by 34%[9] [18]. The seasonal increase in insolation at mid-latitudes should suppress the advection thought to be responsible for the observation of PH_3 at northern mid-latitudes.

This would be the case were it not for the thermal inertia of the atmosphere to radiative forcing. The inertia delays the radiative influence, producing a response time thought to be on the order of season (10^8 s) for the upper-troposphere [73]. Although the mid-latitudes were not observed in great detail during the Voyager encounter (1.75 Jovian years earlier), the 60% PH_3 enhancement reported by Drossart *et al.* 1990 is just over one Jovian year prior to these observations. Yet, despite the response appearing to be in phase with the insolation effect, the observations and the theory are still contradictory as the PH_3 enhancement is anti-correlated with increased insolation.

It is also possible that insolation plays no part in tropospheric dynamics. Instead fractionation and planetary contraction would be the impetus for transport. Under this scenario, the observed advection is not cloud convection but internal circulation. While

---

[9] As the northern summer solstice is nearly coincident with perihelion, the variation in insolation over the Jovian year (11.86 Earth years, approximately 4×10^8 s) tends to reinforce the seasonal effect in the north and counteract it in the south – only a 9% seasonal difference is observed at 45°S. The seasonal effect is despite Jupiter having an obliquity and eccentricity of 3° and 0.05 respectively.

the energy source driving Jupiter's active meteorology is not understood, Galileo observations of moist convection have suggested that the energy transported over the entire planet is comparable to the flux generated by Jupiter's interior [74][10]. If valid, the observations provide an efficient means for the dissipation of heat at the Equator and is supported by Cassini/ISS observations of convective storms within the equatorial belts [153]. More importantly, the observations also suggest large-scale convergence at low-levels in the atmosphere. This is seen as a crucial endorsement of the globally-distributed NH_3- [11, 204] and H_2O-ice clouds [179] and is important to this study because it suggests that PH_3 enhancement would also be observed at southern mid-latitudes if the haze opacity wasn't so concentrated there. This is an issue that the direct- and indirect-influence proposals failed to address. Moreover, there is no need to invoke thermal inertia and radiative-time constants to reconcile this study's PH_3 enhancements with that of Drossart *et al.* 1990.

4.8.3 Great Red Spot

Although the relative-enhancements of ammonia and phosphine with the GRS could have a dynamical origin or be the result from some unidentified chemical process(es), the observed trends are not in agreement with the canonical model of the spot. In the first instance, the enhancements attributed to NH_3 and PH_3 (the retrieved values) are not mutually compatible. According to established doctrine, the GRS is thought to be an area

---

[10] The authors observed a storm system west of the GRS and measured the vertical energy transport due to moist convection. Assuming all lightning storms on Jupiter were like this one storm, the authors then multiplied the derived value by the frequency of storms. The resulting estimate of the global rate of energy outflow (3.3 W/m^2) was found to be comparable to the internal heat flux (5.7 W/m^2).

of uplift at depth, but stagnant at upper levels (meaning pressures less than 50 mbars) [43, 59]. Thus, as NH_3 is sampled at higher altitudes than PH_3 at these wavelengths, high values of phosphine would be expected to coincide with low values of ammonia (as the stagnant conditions allow condensation, divergence and/or photodissociation to occur). This is not however what is observed (ignoring the meridional divergence) as both NH_3 and PH_3 are enhanced (if only moderately so).

The spatial discrepancy (that is, PH_3 being slightly offset to the north) is somewhat explained by Voyager/IRIS temperature retrievals [59, 169] which revealed that the centre of the GRS at high altitudes is further south than the centre at lower altitudes. Hence, PH_3 enhancement would be expected to occur slightly to the north of NH_3 depletion. This is observed within the retrieval maps (minus the NH_3 depletion at previously addressed), but there is still the issue of the enhancements occurring at different longitudes. As the turbulent wake to the northwest of the GRS is often associated with localised convection and spectrally-identifiable NH_3-ice clouds [11, 74], the calculated position of the GRS[11] could be in error. Under this scenario, the GRS would be positioned further to the east such that the enhancements attributed to NH_3 and PH_3 are, respectively, located off the western edge, and within the northern cusp, of the ATMOS footprints. This proposal would however require a negative drift, as the spot's central meridian ($\sim 51°$) would be in conflict with 30+ years of observational history [162] and ground-based observations

---

[11] As the GRS drifts erratically in longitude, the location of the GRS during the ATMOS observations had to be estimated using the 3.9 m/s drift-rate reported by Galileo [197] and the last reported location of the GRS in late December 2000 [145]. For confirmation, the drift-rate (which works out to be approximately 8.0°/month) was compared to the published locations of the GRS from the Voyager [169], IUE [200], Galileo [197] and Cassini [152, 153] missions. Lacking further information (and assuming linear movement in longitude for a circular GRS of 16° diameter), the central meridian of the GRS for ATMOSA through D are 54.3°, 55.4°, 56.7° and 57.0° west longitude (respectively).

which centred the GRS at 53° west longitude in late December 2000 [145].

Furthermore, the enhancement attributed to PH_3 by the radiance-differencing method (Figure 4.29) also agrees with the calculated location of the GRS. However, its enhancement is a bit more difficult to reconcile with the retrieved results. While there is an allusion to both the north and the east in the ΔT_B map, the overall structure of the GRS environs is different between the two methods, with the radiance-differencing map more like what was expected (centrally-located, stronger enhancement, clear to the northwest).

The radiance-differencing method however is not without its own inherent shortcomings. In particular, the results exhibit a discernible sensitivity to the radiometric calibration. For example (*cf.* Figure 4.32), the ΔT_B scale is several times greater, and the GRS more prominent, in ATMOSD than in the other ATMOS maps. As reference spectra were not hand-picked for ATMOSD (see §2.4.1), the process used to produce the calibrated spectra for ATMOSA through C is thought to be non-ideal for the application of the radiance-differencing method. This likely is a consequence of the large number of deep-space and shutter interferograms that went into the hand-picked dataset, resulting in homogeneous spectra for which it is difficult to distinguish the PH_3 signature. The benefits of the hand-picking technique within the calibration process, which is still on-going, have never been quantitatively evaluated [138].

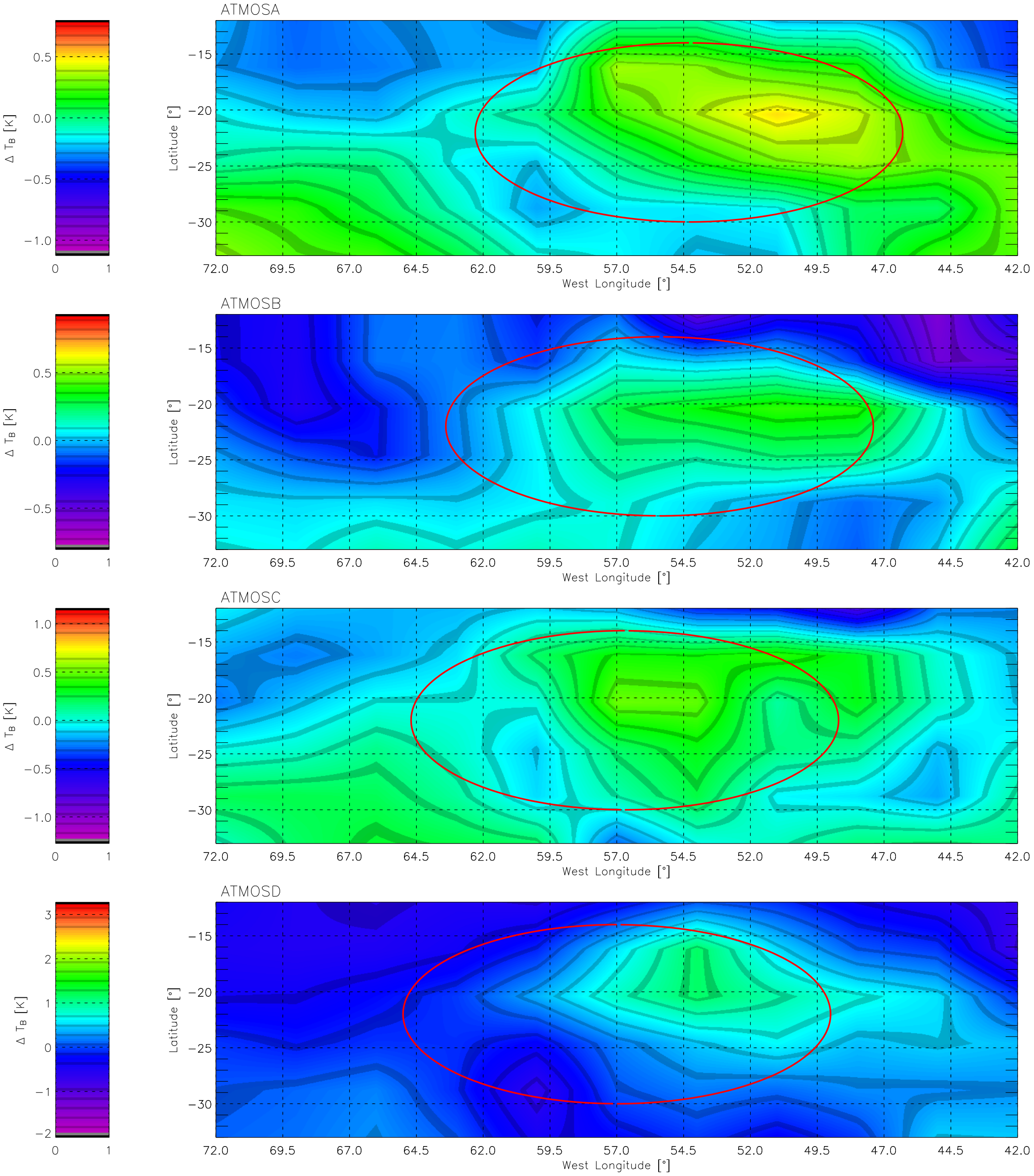

Figure 4.32: Brightness-temperature difference maps – GRS environs. *N.b.*, the maps are not plotted on the same ΔT_B scale. The circular outlines are the calculated locations of the GRS during ATMOS observations A through D. The GRS was assumed to be 16° in diameter, drifting slowing westward at 8°/month [197].

Chapter 5

Dynamics Modelling

Contents

The initial detection of phosphine [113, 160] complicated the understanding of Jovian dynamics because, as a non-equilibrium species, it is incompatible with established thermochemical models. By making a few assumptions about the Jovian atmosphere, it is possible to model the conditions which allow the PH_3 abundances of Chapter 4 to be observed. This chapter considers a simple dynamical model incorporating both transport and chemistry.

5.1 A Simple Dynamical Model of Jupiter

Above the cloud tops, PH_3 is photodissociated. Beneath the clouds, to a "quench" level where equilibrium prevails, PH_3 is thermochemically decomposed. The fact that PH_3 is nonetheless detected within the upper troposphere is thought [155] to be due to significant mixing and/or strong uplift from depths where the molecule is stable. Regardless of mechanism, the vertical distribution of PH_3 at all locations is described by the continuity equation:

$$\frac{\partial n_i}{\partial t} + \frac{\partial \psi_i}{\partial z} = P_i - L_i \tag{5.1}$$

where n_i is the number density, ψ_i the flux and P_i and L_i the respective chemical-production and -loss rates of the i^{th} constituent. The continuity equation describes the overall composition of Jupiter's atmosphere in terms of production, loss and transport. However, because of the required knowledge about photochemical pathways and reaction-rates, Equation 5.1 is too complex to be considered here. Instead, simple advection, mixing and (photo)chemistry are modelled.

5.1.1 Vertical Wind

Neglecting mixing and chemistry for the moment, the updraft velocity, w, may be determined directly from thermodynamic principles [45] via:

$$\frac{\partial T}{\partial t} + \frac{N^2 \, H}{R_{gas}} \, w = \frac{T_E - T}{t_R}, \tag{5.2}$$

where R_{gas} is the Jovian gas constant, T_E is the radiative-equilibrium temperature, t_R

Parameter	**Symbol**	**Value**	**Reference**
Mean molecular weight	μ	2.3 amu or g/mol	[83, 172]
Gravitational acceleration	g	23.3 m/s^2	[124, 172]
Jovian gas constant	R_{gas}	3.6×10^3 J/(kg K)	[3, 172]
Specific heat at constant pressure	c_P	1.1×10^4 J/(kg K)	[3, 172]
Radiative-equilibrium time	t_R	1.0×10^8 s, 3.2 years	[73]
Radiative-equilibrium temperature	T_E	adiabatic 119 K zonal mean	P > 0.3 bar 0.3 bar P < 0.3 bar

Table 5.1: Vertical wind calculation parameters.

is the radiative-time constant and N is the Brunt-Väisälä frequency[1]. This expression balances the stability-restoring qualities of the Brunt-Väisälä frequency:

$$N^2 = \frac{g}{T} \left(\frac{dT}{dz} + \frac{\mu\, g}{c_P} \right), \tag{5.3}$$

(where μ is the mean molecular weight, g is gravity and c_P is the specific heat capacity at constant pressure) with radiative heating. Assuming a steady-state solution and adopting the model parameters of Table 5.1, the vertical wind may be reduced to being directly proportional to the departure of retrieved temperature from radiative-equilibrium.

As the upper-troposphere is assumed to be in radiative equilibrium, an air parcel thrust up from below is colder than the surroundings due to adiabatic expansion. Thus, regions of colder temperature may be described as locations of uplift and the modelled vertical wind speed at 0.3 bar (Figure 5.1) is the inverse of retrieved temperature at 0.3 bar (Figure 4.11). The localised increases in vertical wind over the Equatorial Zone and

---

[1] The buoyancy or characteristic restoring-frequency of an air parcel displaced from its equilibrium position. Large values of N reflect static stability.

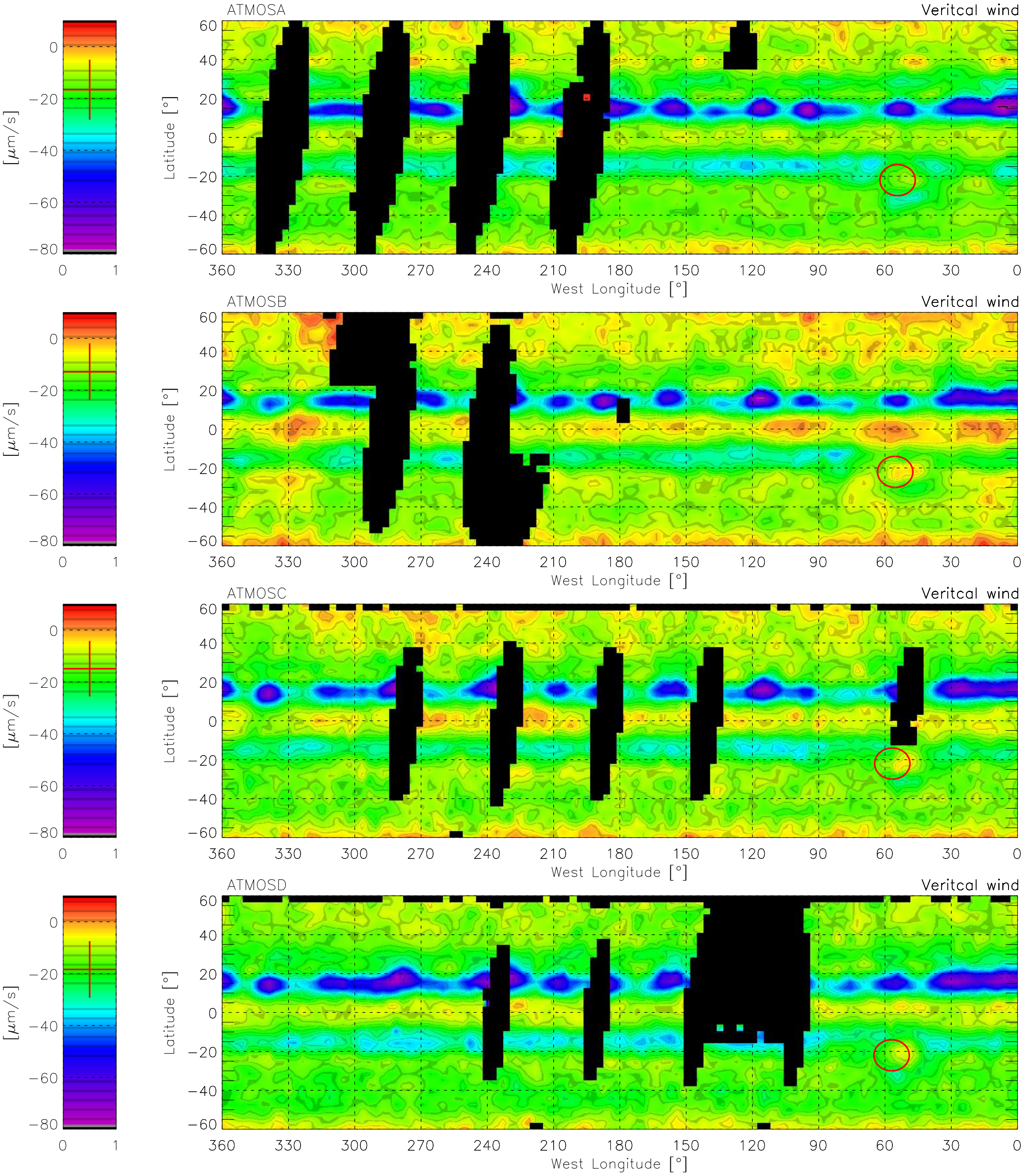

Figure 5.1: Vertical wind speed at 0.5 bar maps – ATMOSA through D. Positive values denote uplift. The circular outlines are the calculated locations of the GRS during ATMOS observations A through D. The GRS was assumed to be 16° in diameter, drifting slowing westward at 8°/month [197]. The mean vertical wind ± the standard deviation is plotted within the key. The black, near-vertical stripes designate no data.

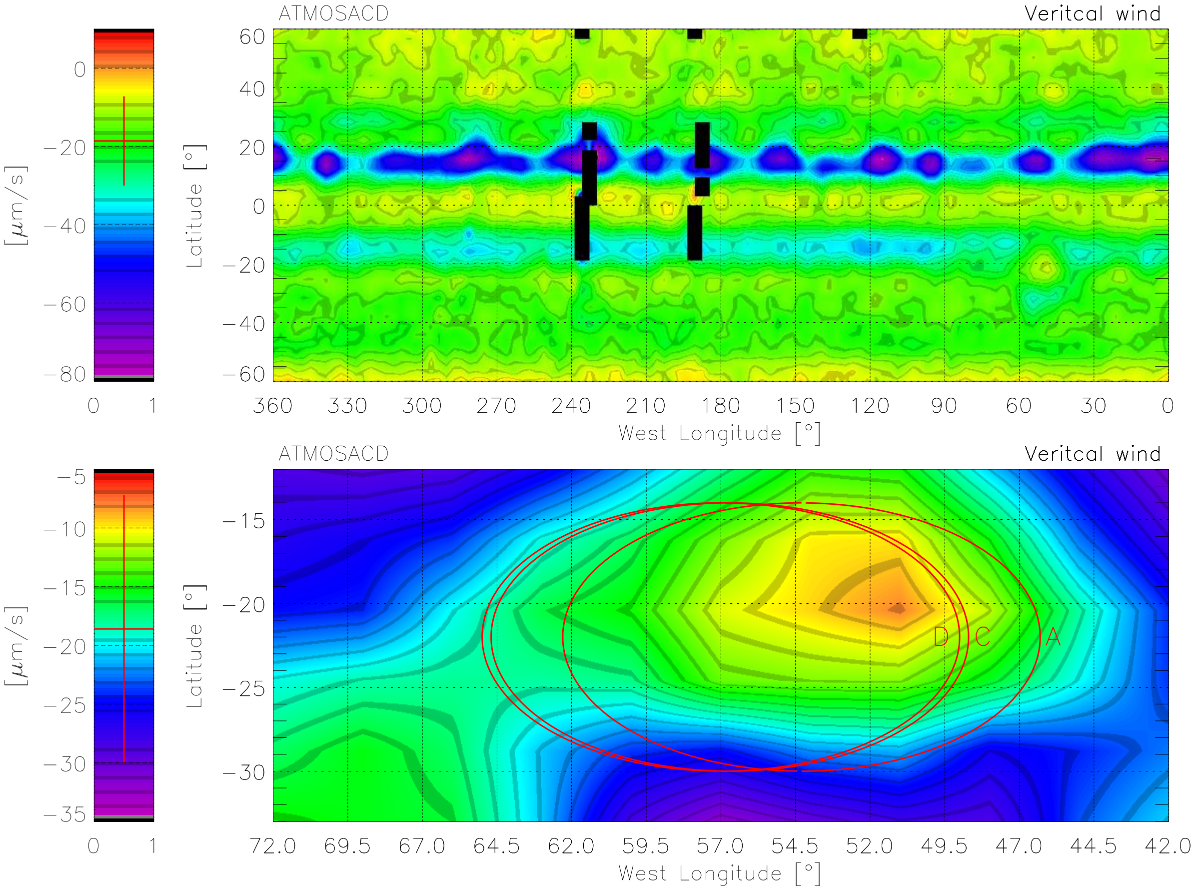

Figure 5.2: Vertical wind speed at 0.5 bar maps – ATMOSACD, GRS environs. *N.b.*, the colour contrast has been enhanced in the bottom plot from that displayed at the top and in Figure 5.1. Positive values denote uplift. The circular outlines are the calculated locations of the GRS during ATMOS observations A, C and D. The GRS was assumed to be 16° in diameter, drifting slowing westward at 8°/month [197]. The mean vertical wind ± the standard deviation is plotted within the key. The black, near-vertical stripes designate no data.

the North and South Tropical Zones is consistent with the interpretation that composition and clouds are concentrated where w is largest (it should be noted that the same effect may be achieved if eddy mixing is more active over the zones). Enhanced uplift is also observed over the GRS (Figure 5.2), however turbulent mixing and the convergence of heat by large-scale eddies was not included in Equation 5.2 and so it cannot be considered accurately-modelled.

The maps resemble the Voyager/IRIS vertical wind speeds in two respects: first,

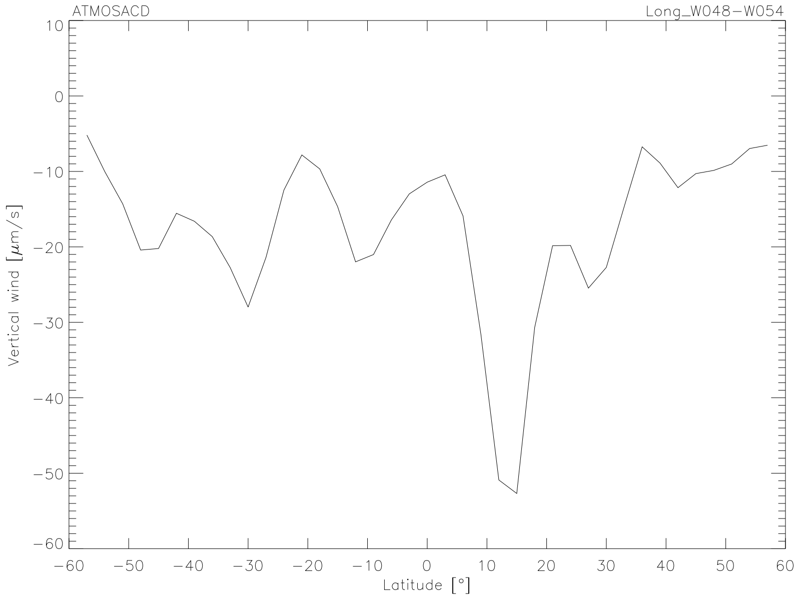

Figure 5.3: Vertical wind speeds at 0.5 bar *versus* latitude. Positive values denote uplift. ATMOSACD spectra; 48° to 54° west longitude.

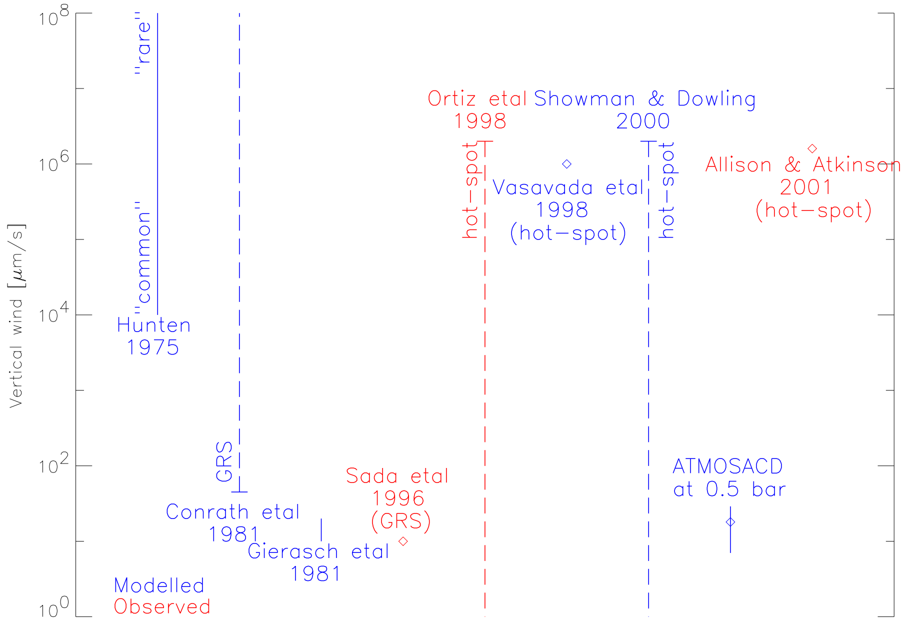

Figure 5.4: Comparison of vertical wind speeds.

broadly speaking, upward motion is observed at the equatorial edges of prograde jets (*cf.* the plotted values of Figure 5.3 to the vertical axis of Figure 1.7) [45, 73]. Secondly, while basic in approach, the values are comparable to those determined previously (also Figure 5.4). The wide discrepancy between the modelled and observed values arises from the vertical motion occurring on a very-localised scale. To illustrate this point, consider the Galileo/Solid State Imager example where clouds were observed to move swiftly (30 to 50 m/s) towards the centre of a hot-spot where they appear to evaporate [197]. Assuming the 40 m/s air enters the southern boundary of a 5000 × 2000-km hot-spot, the convergence rate is approximately 10^{-5} /s and the resulting downdraft velocity is 10 cm/s. Although the input values are variable, this is approximately the value derived from Galileo probe Doppler residuals [4]. Assuming no nearby sources or sinks and a continuity-balance between minor circulations, the 10 cm/s value equates to an area-weighted vertical velocity of 1000 μm/s for a CIRS footprint near the Equator. This is only couple magnitude larger than the mean value derived using Equation 5.2.

5.1.2 Diffusion and Flux

Besides vertical transport, diffusion is another means by which material is bulk-advected. The diffusive flux at any given level is the combination of molecular and eddy mixing. Of the two, empirically-determined eddy diffusion ($\mathcal{K}$), is generally used to quantify the turbulent, convective mixing in atmospheric applications. Eddy-diffusion processes dominate below the homopause, the level above which the atmosphere ceases to be well-mixed and the species are diffusely separated according to their own scale heights.

Neglecting molecular diffusion which is negligible in the troposphere, a rough estimate of the time to reach diffusive-equilibrium can be made based on mixing-length theory[2]. But first, the vertical eddy-diffusion coefficient must be determined. Even though turbulence results from small-scale motions, as eddy mixing tends to homogenise the atmosphere, it is used to conveniently describe motions both large and small and may be approximated:

$$\mathcal{K} \sim w_{\mathcal{K}} \, L, \tag{5.4}$$

where $w_{\mathcal{K}}$ is the eddy velocity and L a length scale. Since the constituents within the homosphere are distributed according to the mean atmospheric scale height, H, is a natural assumption for L. However, it has been shown [184] that more consistent results can be obtained using $L \sim 0.1\ H$, an expression based on the e-folding time scales for convective dynamics in the giant planets. Thus, in the absence of chemistry, the eddy-mixing time is:

$$t_{\mathcal{K}} = \frac{L^2}{\mathcal{K}} \sim \frac{0.1\,H}{w_{\mathcal{K}}}. \tag{5.5}$$

As the vertical wind speeds of §5.1.1 are likely to be highly sheared and effectively horizontal as a result of deep zonal winds in excess of 100 m/s [6], they may be assumed to be approximately $w_{\mathcal{K}}$; the calculated diffusive-equilibrium times for the NEB, GRS, EZ and northern mid-latitudes can be found in Figure 5.5.

---

[2] According to Prandtl's mixing-length theory, a parcel of air displaced vertically will maintain its identity a characteristic distance, L, before being mixed with the surrounding fluid. The displacement creates a turbulent fluctuation in the composition of the new level resulting in rapid, small-scale overturning of material in a process called *convection.* It should be noted that the characteristic distance does not describe something physical about convective motions (*i.e.* it does not imply that convection is arranged into cells of dimension L). It is merely a parameter that allows an accurate approximation of the abundance at observable levels.

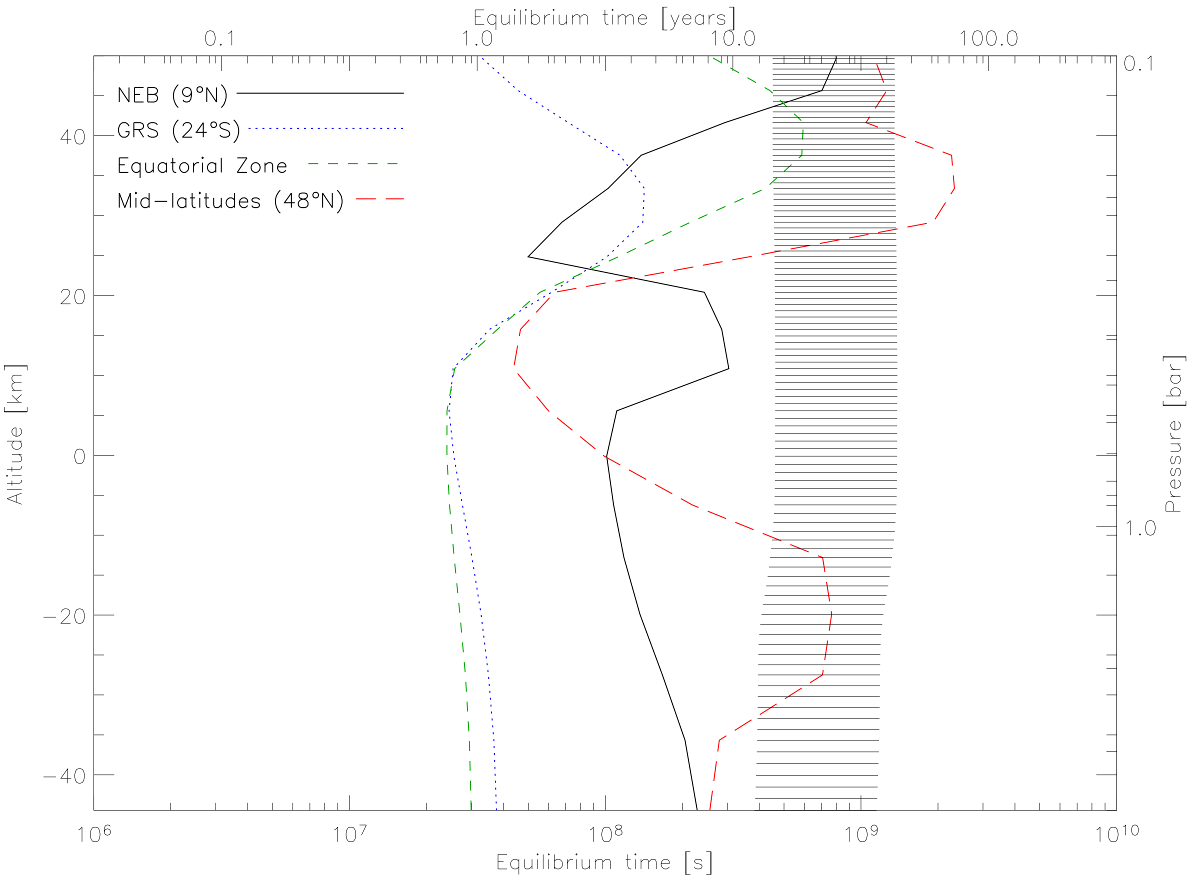

Figure 5.5: Eddy-mixing times for the NEB, GRS, EZ and northern mid-latitudes. The shaded profile is the global mean eddy-mixing time ± 50%. *N.b.*, the profiles were smoothed slightly for presentation. ATMOSACD spectra; 48° to 54° west longitude.

The mixing times can be seen to range from several years, to decades or even hundreds of years within the upper-troposphere/lower stratosphere. These values are in agreement with both Voyager/IRIS [43] and UV occultation [8] data which estimated vertical mixing times to range from 20 to 300 years. As expected, the regions of enhancement in the retrieved-PH_3 maps (EZ, GRS and northern mid-latitudes) have an upper-tropospheric ($P > 0.1$ bar) mixing time less than the mean. However, the tropospheric mixing time for northern mid-latitudes exceeds the NEB value and is several factors greater than either the EZ or GRS.

It is also possible to model the flux directly. Restricting motion to the vertical, the tropospheric flux attributable to eddy diffusion may be written [7]:

$$\psi_i = -\mathcal{K}\left(\frac{dn_i}{dz} + \frac{n_i}{H} + \frac{n_i}{T}\frac{dT}{dz}\right). \tag{5.6}$$

If the eddy-diffusion coefficient profile from Fouchet *et al.* 2003: [66] is adopted, the flux of PH_3 can be calculated from the retrieved temperature and number densities (Figure 5.6). As thermal escape is very slow on Jupiter, Equation 5.6 was solved with zero-flux upper-boundary conditions. The lower-boundary conditions were allowed to be dictated by the temperature distribution at the base of the profile.

The derived fluxes resemble (both qualitatively and quantitatively) the Jovian streamfunctions modelled by Conrath *et al.* 1990: [45] based on Voyager/IRIS data. In both studies, heightened streamfunctions appear to emanate from either side of the equatorial region, plateauing or even increasing at northern mid-latitudes. Reduced fluxes are observed over the North and South Tropical Zones at all longitudes (including that of the Great Red Spot).

While this and previous analyses yield results consistent with a range of observations and constraints, it is based on a number of simplifying assumptions that may not be appropriate. This is especially the case in terms of the eddy-diffusion coefficient which is exceedingly complex and susceptible to gross uncertainty [8, 66]. Thus, the assumptions may, at best, yield only qualitatively useful results (*e.g.* the modelled fluxes which imply a number density in excess of the mean atmospheric density).

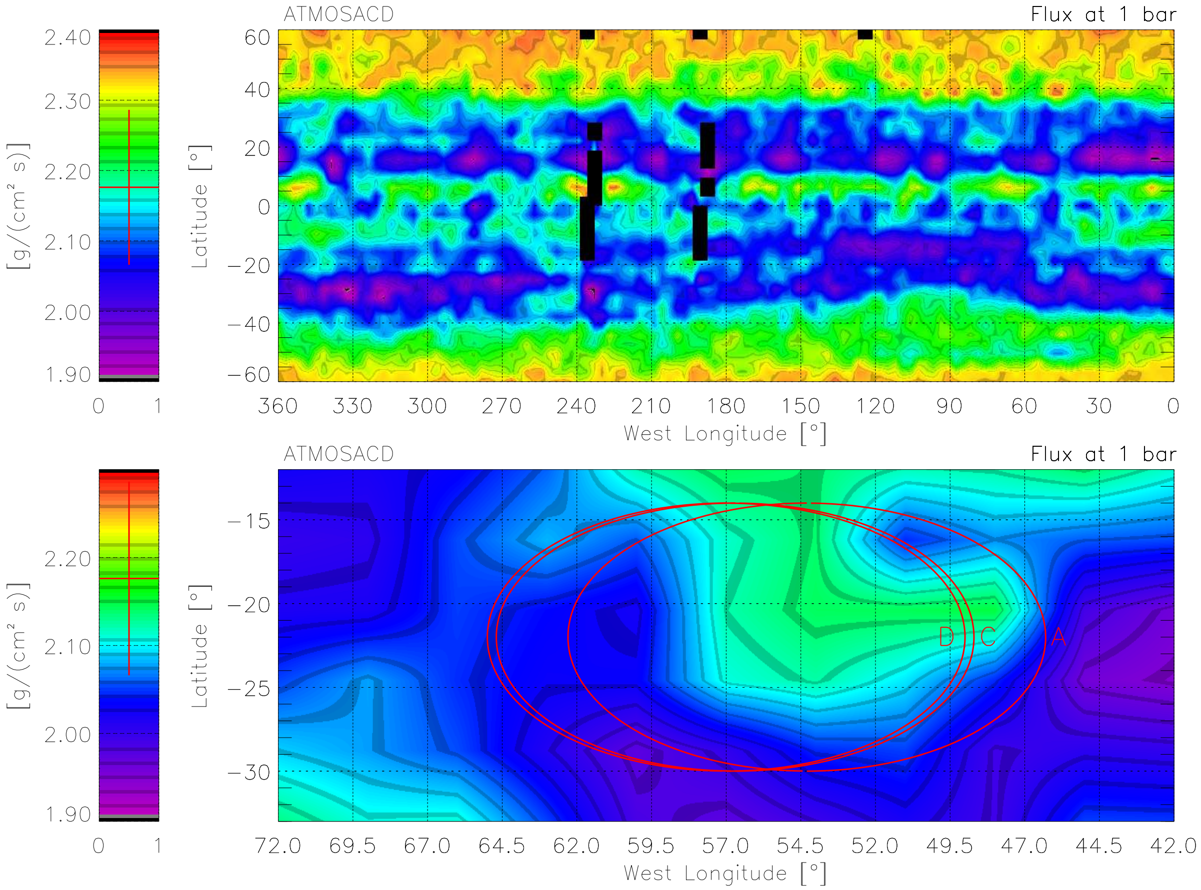

Figure 5.6: Flux at 0.3 bar – ATMOSACD, GRS environs. The circular outlines are the calculated locations of the GRS during ATMOS observations A, C and D. The GRS was assumed to be 16° in diameter, drifting slowing westward at 8°/month [197]. The mean flux ± the standard deviation is plotted within the key. The black, near-vertical stripes designate no data.

5.1.3 Chemistry considerations

Since its detection on Jupiter [160], phosphine has been extensively studied because of its role in the creation of triclinic red phosphorus (P_4), a potential chromophore. As a product of PH_3 photolysis, P_4 was thought to produce the red colouring observed on Jupiter [155]. However, long before the Cassini encounter, several authors [33, 178, 203] disputed P_4's ability to produce the observed colours. Regardless, it was hoped the CIRS spectra might help to constrain PH_3's enigmatic existence at observable levels. This is perhaps best understood by considering Jupiter's tropospheric chemistry.

As a non-equilibrium species, the detection of PH_3 implies abundances in excess of those predicted by dynamical models given thermochemical-equilibrium conditions. Abiding by the "quench-level" approximation[3], the observed mixing ratio is representative of levels where the time constant for the destruction of PH_3 is less than the characteristic time for convective mixing. Despite the mechanism, kinetics and deep abundances of oxygen and phosphorus being poorly understood [29, 57], Barshay and Lewis 1978: [15] proposed oxidation with water vapour:

$$\mathrm{PH_3} + h\,\nu \rightarrow \mathrm{PH} + \mathrm{H_2} \tag{5.7}$$

$$\mathrm{H_2O} + h\,\nu \rightarrow \mathrm{OH} + \mathrm{H} \tag{5.8}$$

$$\mathrm{PH} + \mathrm{OH} \rightarrow \mathrm{PO} + \mathrm{H_2} \tag{5.9}$$

---

[3] The quench-level approximation is generally used to estimate the observed abundances of chemically-reacting species in the presence of convective dynamics. The quench level itself is the temperature/pressure/height where the time scales for the chemical reaction and the convective dynamics are equal. Below the quench level chemical processes dominate and abundances maintain their equilibrium values. Above the quench level, the chemical time scales become so long so quickly that the reaction is effectively "quenched" (*i.e.* extinguished, eliminated, satiated), leaving abundances near their equilibrium value at the quench level [182].

$$PO + OH \rightarrow PO_2 + H \tag{5.10}$$

$$2PO + 2PO_2 + 2M \rightarrow P_4O_6 + 2M \tag{5.11}$$

(where h is the Planck constant and M is a neutral body) as the principal means PH_3 is decomposed in the deep atmosphere of Jupiter. Under this scenario, PH_3 is the most abundant phosphorus-bearing species within the troposphere prior to phosphorus trioxide dimer (P_4O_6 – no known spectral signature within the CIRS spectral range) usurping the top spot from 1000 K to approximately 300 K when PH_3 regains its previous dominance. PH_3's lifetime for irreversible oxidation to P_4O_6 was calculated [154] to be just six days. This value is seen to be a order of magnitude less than the eddy-mixing times estimated in §5.1.2.

However, Borunov *et al.* 1995: [29] argue that P_4O_6 does not take part in the phosphorus cycle at all and that PH_3 is the most abundant equilibrium phosphorus gas from 2000 to 300 K. The authors base their assertion on the use of an erroneous enthalpy of formation in the Barshay and Lewis model which produces a P_4O_6 abundance 30 to 80 orders of magnitude (!) larger than similarly-oxidized states: P_4O_7, P_4O_8, P_4O_9, P_4O_{10}.

The formation-rate discrepancy has yet to be resolved with both sets of authors calling for new experimental determinations. While the net results are different, both sets of authors agree PH_3 will remain at least “weakly” non-equilibrium as condensation of ammonium dihydrogen phosphate ($NH_4H_2PO_4$) within the troposphere rapidly reduces its abundance at temperatures less than 500 K

5.2 Dynamical Implications

The northern mid-latitude, tropospheric mixing-time result was unexpected. If, as outlined in §4.8.2, uplift is due to internal circulation (that is to say, large-scale convergence at low-levels as a result of planetary contraction and internal differentiation), then the three principal regions of PH_3 enhancement observed in Chapter 4 could be expected to exhibit similar mixing properties. As they do not (based on this gross-simplification), it is conceivable the tropospheric mechanism for uplift at northern mid-latitudes is different from that within the EZ and/or GRS.

While the cold temperatures, high divergence and anticyclonic motion of the GRS are all consistent with a local high pressure system and forced upward motion, its origin, evolution and nature are not well known. The modelling presented here has not changed this view. Regardless, the PH_3 enhancement observed is believed to result from a different mechanism than that seen within the northern EZ as the Rossby-wave description (the vertical stretching and compressing of isentropic surfaces: §4.8.1) is confined to a small range of latitudes near the Equator.

Alternatively, the vertical wind and flux results suggest that eddy mixing is responsible for the enhancement observed at northern mid-latitudes. Despite $\mathcal{K}$ being shown to decrease with latitude [54], if the observed variability was due to increased eddy mixing, then other non-equilibrium species (*e.g.* AsH_3, CO, GH_4, HCN) would show the same qualitative behaviour. Of these, CO is thought to be the most similar to PH_3 because it does not exhibit photochemical destruction in the troposphere (under the weakly non-equilibrium scenario discussed in §5.1.3). Recent observations of CO within the hot-spots and in association with the SL9 impacts offer contradictory insight into its deep abundance. On one hand, the SL9 observations ($\sim 45°$S) indicate that the comet fragments did not penetrate the H_2O cloud *circa* 5 bars such that the tropospheric abundances were fit with a constant mixing ratio (*i.e.* no mixing) [142]. The authors' methods were later called into question by a study of CO in the hot-spots. In this later study, the non-equilibrium thermochemistry was re-evaluated pointing to both an internal source for the abundance observed at six bars [25]. Thus, while the enhancement of weakly non-equilibrium species is corroborated, the mixing at mid-latitudes remains unestablished.

Regardless, if PH_3 is weakly non-equilibrium and consequently sensitive to the strength of K, then, like CO, it should be close to its quench-level abundance. PH_3's quench-level abundance is dependent on the isotopic abundance of phosphorus within the deep atmosphere. If the evolutionary model favoured by Owen *et al.* 1999: [150] is correct[4], then volatiles, like phosphorus, should have an enrichment of several times solar. Phosphorus' measured isotopic abundance is approximately unity however (0.82), having been based on the Voyager/IRIS determination of PH_3 at one bar [110]. The slightly greater than solar abundance PH_3 retrieved by this study (1.1 times solar: Figures 4.15 and 4.21) suggest this value is in error. If PH_3 is indeed weakly non-equilbrium, then it is plausible the values observed in this study are indicative of a greater abundance within the deep atmosphere. This would reconcile the discrepancy-in-enrichment observed for Ar,

---

[4] In this evolutionary model, the "metals" (elements heavier than helium) came to the planet in icy planetesimals formed at very low temperatures. Laboratory studies of the trapping of volatile gases in amorphous ice indicate that, at very low temperatures (≤ 30 K), solar proportions of these elements are possible. This is in conflict the model proposed by Gautier *et al.* 2001: [72] where the metals were trapped in clathrate hydrates. The characteristics of clathrates require a large overabundance (greater than nine times solar) of H_2O to reproduce the noble gas enrichments observed by the GPMS.

Kr, Xe, C, S and O (which all range from two to three times solar [25, 126]) and the phosphorus-to-hydrgogen ratio for Saturn (five to ten times solar [9]).

Chapter 6

Summary and Conclusions

Contents

The determination of upper-tropospheric phosphine has been considered in this thesis. The data, thermal-infrared spectra returned by the Cassini/CIRS instrument during and immediately after closest approach with Jupiter, have allowed the systematic, global-mapping of PH_3 for the first time. The three-dimensional distribution and temporal variation of temperature, clouds and simple dynamics were also considered. The results, complementing and/or extending the scientific advances made by Voyager/IRIS, reflect the unprecedented combination of the high spatial, and medium spectral resolution. In this chapter I initially summarise the results of the thesis, offer suggestions how this study might be extended and then discuss future missions to Jupiter.

6.1 Summary

The model atmosphere, radiative-transfer code and *a priori* values have been largely successful in reproducing the observed Jovian conditions. In particular, the banded structure which distinguishes Jupiter from the other gas giants is readily apparent in the presented maps. Furthermore, the temperature, composition and cloud retrievals are broadly consistent with the temperature and compositional results obtained during the Voyager encounters. Of these, the temperature results show the most variation, including propagating disturbances associated with the quasi-quadrennial oscillation.

Waves also feature in the composition maps for which two methods are used to investigate the spatial distribution of ammonia and phosphine. In general, ammonia fractional scale height and phosphine are found to be enhanced in two principal regions: within the Equatorial Zone and in or immediately adjacent to the Great Red Spot. Coupled with the belt-zone structure, the enhancements are consistent with the known atmospheric circulation on Jupiter.

The wave reference above pertains to PH_3's EZ enhancement, which is slightly offset to the north where it corresponds with the latitude that spectrally-identifiable ammonia-ice clouds and 5-μm hot-spots are observed. The pattern of vertically stretched (hot-spots) and compressed (NH_3-ice clouds) air columns are thought to result from a Rossby wave system [3, 49, 143].

Alternatively, the NH_3 FSH and PH_3 enhancements observed for the GRS environs suggest no general pattern or governing principles. This is commensurate with the region being uniquely complex and highly dynamic. While the temperature and cloud opacity results resemble those obtained by previous investigators, the composition results have proved more difficult to reconcile. Yet, regardless of the spatial and abundance variations, the overall trend is one of enhancement, and hence uplift, in agreement with the canonical model of the GRS as a site of uplift at tropospheric pressures. Though it must be said, the vertical transport observed is only modestly enhanced compared to adjacent regions.

While NH_3 is to all intents and purposes symmetric about the Equator, PH_3 is found to be enhanced at northern mid-latitudes. Although the PH_3 enhancement at northern mid-latitudes is not a new finding, along with Voyager observations of H_2O-ice clouds at southern mid-latitudes, these results point to large-scale convergence at low-levels of the atmosphere. Although insolation is also thought to influence the dynamics suggested by these enhancements, the available observations were shown not to support the theory (for the record, insolation *is* observed, but only in the studies of contemporary CIRS authors focusing on stratospheric temperatures and hydrocarbons [61, 140]).

Careful attention has been paid to test the sensitive methods of analysis and to validate the approach. Although grossly-simplified, a dynamical model was constructed to verify the interpretations made from the analysis methods. As anticipated, the principal regions of PH_3 enhancement were shown to experience rapid turnover. The northern mid-latitudes were, on the other hand, shown to undergo mixing at a rate slower than the global mean. This is in conflict with the notion that PH_3 is a non-equilibrium species. For if mixing was weak, thermochemical modelling would dictate that it should not reach observable levels, especially in enhancement.

It was subsequently shown that the prevailing thermochemical models had used an erroneous formation rate in the determination upper-tropospheric PH_3. While the calorimetric discrepancy still needs to be resolved, the combination of this study and the questionable outcome of the thermochemical models implies that the quasi-solar PH_3 abundance observed at cloud levels may not be fortuitous. Instead, PH_3 is weakly non-equilibrium with the observation at northern mid-latitudes arising from a unique set of conditions which allow a deep sounding of the atmosphere.

Taken as a whole, the results are of interest owing to the favourable spectral and spatial resolutions, global distribution and sensitivity compared to that of Voyager/IRIS. The high-quality data and robust approach complement and/or extend previous investigations of Jovian temperature and phosphorus-composition by confirming, refining or improving the derived results.

6.2 Further Work and Recommendations

Preliminary CIRS results have been presented at various conferences with mature findings in print (in Flasar *et al.* 2003: [61] and Wong *et al.* 2003: [204]) or soon to be so (Abbas *et al.* 2004: [1], Achterberg *et al.* 2004: [2], Fouchet *et al.* 2004: [64], Kunde *et al.* 2004: [109] and Nixon *et al.* 2004: [140]). An outline of this work is due to be published in the journal, *Icarus* in early 2004.

Several shortcomings in the analysis methods were encountered that in hindsight may be addressed. For example, the inversion code could use a bit of frequency “stretch” so that wavelength-calibration issues do not artificially-inhibit the model’s ability to fit the measured spectra. In addition, while outer-planet observation lack the same wealth in measurement enjoyed by Earth-observing programs, a technique which maximises the available information content (or some other figure of merit) could be used to make the optimal estimation truly optimal. In simple terms, this may be realised via the automated selection of spectral windows or a quantitative improvement in the precision or accuracy of the retrieved product. Speaking of information content, in light of the inability to retrieve NH_3 deep abundance, perhaps both NH_3 and PH_3 should be retrieved as a profile, much like temperature. What with all the various factors removing these species from the atmosphere, it is likely that the simplified two-parameter profile is unable to characterise these complex, compositional trends. And finally, new and refined PH_3 linedata [106] for the mid-infrared has become available providing a much needed update to the two decade old information used in this work.

On the issue of calibration, the radiance-differencing results strongly suggest that different data-sets may be better for different purposes. For example, it is probable, that one method of calibration produces less noisy single spectra, but another produces spectra which will “co-add” better. As each spectrum is really three different things in one, there are good arguments for the calibration to be part of the analysis process, examining all of the individual elements and adding the right ingredients for the type of science to be completed.

If NASA’s gambit to establish a permanent lunar base and send a human to Mars [20] (or, for that matter, ESA’s Aurora programme or the Chinese Space Agency’s proposal to send a spacecraft to the Moon) is backed up with action, it is unlikely any new mission proposal to the outer planets will see the light of day. This relegates near-term observations of Jupiter's atmosphere to ground-based astronomers. Having said that, Southwest Research Institute, the body responsible for NASA's Pluto-Kuiper Belt mission, have announced that they will test the spacecraft's instruments during a fly-by of the giant planet in late 2006 or early 2007 [186]. Akin to Cassini-Huygens' leisurely tour of the Jovian system, the five-month fly-by will allow the scientists to test the spacecraft's cameras, spectrometers, radiometer and space plasma and dust sensor.

Appendix A

FP1 Polarization-Modulation

Contents

The far-IR interferometer aboard CIRS (FP1) uses polarisation-modulation [130] to remove the constant, or direct-current, component from the resulting interferogram making FP1 less susceptible to instrument drifts. The advantages of this design over those used in standard amplitude-splitting interferometers are that it is efficient over a wide range of wavenumbers and tends to reject substrate bias.

The construction of a polarising interferometer (Figure A.1) is similar to the classic interferometer design in that the incident radiation is initially collimated and then divided at a beam splitter into two beams of equal amplitude. However, within a polarising interferometer, the incident radiation is initially polarised at an input polariser. The beams are then reflected back on themselves by roof-top mirrors rotating the polarisation of the beams 90° in the process. The beams subsequently strike the beam splitter again, where they are recombined and directed towards the image planes.

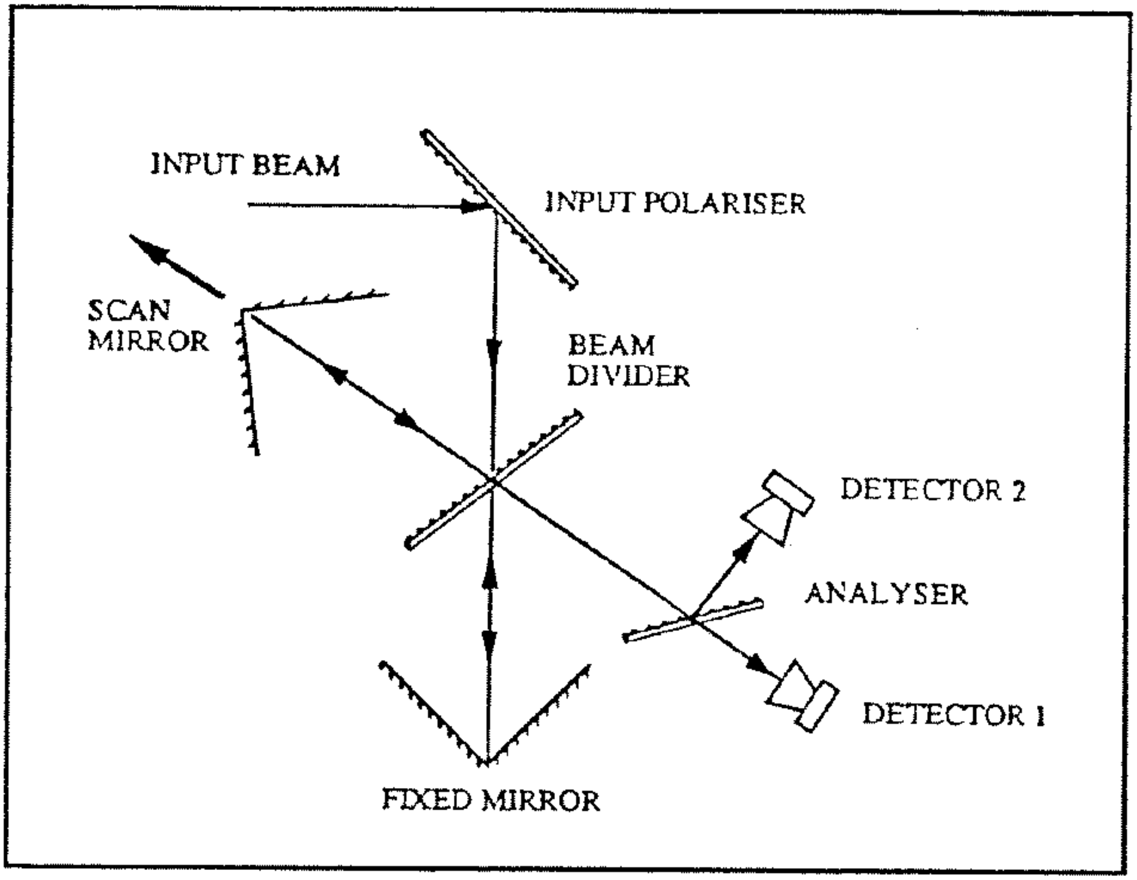

Figure A.1: Schematic of the far-infrared interferometer (some "folding" mirrors are omitted). [35]

Here is where the two designs differ. In the classic design, the two components of the recombined beam interfere with each other and form circular fringes on the image plane whose intensity (the interferogram) depends upon the different paths traversed by the two beams prior to recombination. As the one mirror moves, the path length of one beam changes so that if the two-beams differ by an integral number of wavelengths (at a particular frequency), then the light will interfere constructively. Other wavelengths which do not meet this criterion will interfere destructively. In a polarising interferometer, the effect of moving the scan mirror changes the instantaneous state of the polarisation, slowly rotating it as the mirror is scanned. The resulting beam is consequently elliptically-polarised for which an analyser grid and a pair of detectors are used to determined the difference in measured intensity.

A.1 Derivation

Consider the parallel and perpendicular electric field components ($E_{\|}$ and $E_{\perp}$ respectively) of the elliptically-polarised beam prior to the polarising analyser grid:

$$E_{\|} = E_0 \cos(wt + \phi), \tag{A.1}$$

$$E_{\perp} = E_0 \cos(wt). \tag{A.2}$$

The two components differ by ϕ, a phase introduced by the difference in path length in the arms of interferometer. The analyser grid reflects half the recombined beam to Detector 1 while transmitting the other half (in this derivation, $E_{\|}$) to Detector 2. Thus, the electric field at the respective detectors is:

$$E_1 = E_{\|} + E_{\perp} = E_0 \left[\cos(wt + \phi) + \cos(wt)\right], \tag{A.3}$$

$$E_2 = E_{\|} - E_{\perp} = E_0 \left[\cos(wt + \phi) - \cos(wt)\right], \tag{A.4}$$

which, according to Simpson's formulae:

$$\cos\alpha + \cos\beta = 2\cos\left(\frac{\alpha + \beta}{2}\right)\cos\left(\frac{\alpha - \beta}{2}\right), \tag{A.5}$$

$$\cos\alpha \;-\; \cos\beta \;=\; -2\,\sin\left(\frac{\alpha\,-\,\beta}{2}\right)\,\sin\left(\frac{\alpha\,+\,\beta}{2}\right), \tag{A.6}$$

may be simplified to:

$$E_1 \;=\; 2\,E_0\,\cos\left(\frac{\phi}{2}\right)\,\cos\left(wt\,+\,\frac{\phi}{2}\right), \tag{A.7}$$

$$E_2 \;=\; -2\,E_0\,\sin\left(wt\,+\,\frac{\phi}{2}\right)\,\sin\left(\frac{\phi}{2}\right). \tag{A.8}$$

The time-dependence of Equations A.7 and A.8 presents a problem because the measured intensity, I, is the root-mean-square value. Thus, time must be factored out. Utilising the fact that the intensity is the time-average of the Poynting vector:

$$I \;\equiv\; |\,\mathbf{S}_{\text{average}}\,| \;=\; \frac{E_0^2}{2} \tag{A.9}$$

(assuming an electromagnetic wave in free space where the permittivity equals 1) removes the time-dependence such that Equations A.7 and A.8 can be rewritten:

$$I_1 \;=\; 2\,E_0^2\,\cos^2\left(\frac{\phi}{2}\right), \tag{A.10}$$

$$I_2 \;=\; 2\,E_0^2\,\sin^2\left(\frac{\phi}{2}\right). \tag{A.11}$$

What remains can then be further simplified using the half-angle relations:

$$\cos^2\left(\frac{\phi}{2}\right) \;=\; \frac{1\,+\,\cos\phi}{2}, \tag{A.12}$$

$$\sin^2\left(\frac{\phi}{2}\right) \;=\; \frac{1\,-\,\cos\phi}{2}, \tag{A.13}$$

resulting in:

$$I_1 = A(\tilde{\nu})\,[1 + \cos\phi], \tag{A.14}$$

$$I_2 = A(\tilde{\nu})\,[1 - \cos\phi], \tag{A.15}$$

where $A(\tilde{\nu}) \equiv I_1 = I_2 = E_0^2$, is the intensity of either wave. Thus, the difference in intensity between the two detectors is:

$$I_1 - I_2 = A(\tilde{\nu})\,\cos\phi, \tag{A.16}$$

where the constant component has been removed; *quod erat demonstrandum.*

Appendix B

CIRS Observations at Jupiter

Contents

After launch on 15 October 1997, Cassini-Huygens flew the circuitous route past Venus twice, Earth and then Jupiter on its way to Saturn. The project elected to take advantage of the Jupiter encounter to test the instruments in preparation for the 4-year tour of the Saturnian system. Unlike the Jupiter fly-bys conducted by the Voyager spacecraft, the Cassini-Huygens fly-by was leisurely with observations planned for the 90 days both before and after closest approach (CA).

For ease in sequence design, the Jupiter fly-by was divided into seven Subphases (A through G) with the observations outside of CA ± 20 days dictated by the repetitive use of 5-day templates. For observations within CA ± 20 days, specialised observations were used. Examples of the specialty observations include north/south maps of which there are two types: the standard north/south map designed to produce maps of the individual northern and southern hemispheres, and “Beachballs” which mapped the entire disk. “Feature Tracks”, on the other hand, were designed to observe spatial variations in dynamically interesting features (*e.g.* the 23°N jet, GRS or white oval). Another example, the “Ring Phases”, had the dual objectives of determining the composition and particle-size distribution of Jupiter’s rings at 15° to 120° phase angle. An abbreviated summary of the CIRS observations is included below.

Jupiter Subphase A (CA -90^d to -55^d):

- Seven repetitions of Subphase A template: sit-and-stare integration of Jupiter at three different resolutions and two 1x4 satellite searches.

Jupiter Subphase B (CA -55^d to -25^d):

- Two additional repetitions of Subphase A template.
- Four repetitions of Subphase B template: 2x2 mosaic of Jupiter incorporating a north to south slew for greater spatial coverage.

Jupiter Subphase C (CA -25^d to -11^d):

- One additional repetition of Subphase B template.
- Implementation of five blocks of varying observational routines:
  - Block 1: Four repetitions of 2x2 mosaic and FP1-stare directed at Jupiter’s centre.
  - Block 2: Six repetitions of 1x2 integration of central meridian and rings.

  - Block 3: Six additional repetitions of 1x2 integration of central meridian and rings, twelve north pole/aurora integrations and six Callisto observations.
  - Block 4: First north/south map.
  - Block 5: First Ring Phase.

Jupiter Subphase D (CA -11^d to CA):

- Four additional north/south maps, the first three Feature Tracks (including that for the GRS), multiple Galilean-satellite observations (including a 15-hour integration on Io with FP1) and four additional Ring Phases.

Jupiter Subphase E (CA to CA +14^d):

- Remaining three Feature Tracks, two additional Ring Phases, four Beachball maps (ATMOSA through D), two aurora observations coordinated with HST and several additional satellite observations.

Jupiter Subphase F (CA +14^d to +71^d):

- Final Ring Phase, final HST-aurora observation and six repetitions of 1x2 integration of central meridian and rings.

- Ten repetitions of Subphase F template: similar to Subphase B template modified for looking at the night side of Jupiter.

Jupiter Subphase G (CA +71^d to +90^d):

- Two additional repetitions of Subphase F template.

- CIRS boresight calibration.

B.1 Mission Status and Update

At the time of writing, Cassini-Huygens is in an excellent state of health and is operating normally; most of the instruments are in sleep mode as the spacecraft continues its cruise to the Saturnian system. However, two events during the Jupiter encounter conspired to reduce the amount of data returned by CIRS and are summarised below.

Observations were temporarily suspended on 17 December 2000 as Cassini-Huygens unexpectedly switched to its back-up maneuvering system. The spacecraft, using a trio of electrically-driven reaction wheels for orientation, automatically resorted to using hydrazine-burning thrusters after one of the reaction wheels required more than the normal amount of force to function. While the incident was investigated, all observations requiring pointing were suspended so as to conserve the limited-supply of hydrazine for Cassini-Huygens' primary mission at Saturn. On 29 December 2000, observations were resumed on reaction wheels at the point in the observing-sequence assuming no interruption occurred.

The source of the excess friction within the reaction wheel is still unknown. The probable cause is suggested to be viscosity-related due to the reaction wheel assembly (RWA) not being properly "de-spun" so as to distribute the bearing lubrication during the extended Jupiter observations. A thorough review of the situation has been conducted by the Jet Propulsion Laboratory and as a result of which, the RWA is now treated as a consumable that is to be used selectively with additional flight rules concerning regular monitoring and preventative-measures.

The suspension of observations however proved costly in terms of Jupiter encounter data since it occurred immediately prior to CA. In short summary, Block 5 of Subphase C and a significant portion of Subphase D were not executed including all of the rings observations where CIRS was the prime instrument, four of the five north/south maps, half of the Feature Tracks (including that for the Great Red Spot!), several satellite observations and numerous deep-space calibrations were lost. To top it all off, the reaction wheel which was at the center of the incident is starting to stick again [94] possibly necessitating use of the spare reaction wheel to ensure a successful Saturn tour.

In February 2000, an in-flight check-out of the Huygens probe revealed the "non-optimal behaviour of the communication subsystem" [121]. The anomaly turned out to be a design flaw which prevents the Huygens receiver aboard Cassini from compensating for the Doppler shift between the probe and the orbiter. If undealt with, the anomaly could have a significant and adverse impact on data recovery during the probe's descent at Titan. After an investigation, a work-around in the flight plan stipulating a new probe release date and geometry-of-descent was arranged. The changed itinerary, which is seven weeks later than originally planned and will consume up to one-third of the reserve fuel supply, shortens Cassini's initial two orbits around Saturn and adds an additional fly-by of Titan. The additional fly-by will provide the conditions for which a successful descent onto Titan by Huygens can take place. At more than 50 times the altitude formerly planned, Cassini will be travelling further out in its orbit (at consequently reduced speed) during the probe's descent thereby reducing the Doppler-shift which had threatened the success of the mission.

To support the diagnostics that led to an accurate determination of the communications anomaly, observations from 31 January through 6 February 2001 were replaced with a sequence to conduct an in-flight check-out of the communications link between the Huygens probe and the Cassini spacecraft. Several additional atmospheric observations of Jupiter by CIRS planned for this period were cancelled.

Appendix C

The cassini_cirs database

Contents

Cassini_cirs is the molecular-absorption database used extensively in the analysis of the CIRS spectra. The purpose of creating cassini_cirs was twofold: to create a repository with standard format and input, and, as the project advanced, to facilitate updating the existing spectral line-data where and when it was found to be lacking. The following is a brief summary of the considerations that went into the creation of the cassini_cirs database and the k-tables that were produced from it.

C.1 Line-data

Line-data for acetylene (C_2H_2), ethylene (C_2H_4), ethane (C_2H_6) and diacetylene (C_4H_2) were extracted from the *Gestion et Etude des Informations Spectroscopiques Atmosphériques 1997* (GEISA-97) release. Line-data for phosphine[1] (PH_3) was similarly taken from GEISA-97, however, in accordance with Lellouch *et al.* 2001: [114], the line-data were corrected for an error in the treatment of the axial angular-momentum quantum number. Two transitions appear within GEISA-97, whereas only one component is allowed by selection rules. The transition given in Table II of Tarrago *et al.* 1981: [192], was retained. The approximately one hundred lines removed from the GEISA-97 linelisting can be found in Table C.1.

Updated line-data for ammonia (NH_3) and methane (all three isotopes: CH_4, $^{13}CH_4$, CH_3D) were procured from the High Resolution Transmission Molecular Absorption Database 2000 (HITRAN-2K) release. The line-data were extracted, converted into GEISA format, concatenated from 0 to 1500 cm^{-1} and merged together with the other line-data to create the cassini_cirs database.

The line-data manifest themselves as spectral line strengths/intensities, S, at standard pressure (1.0 atm = 1.013 bar, P_0) and temperature (296 K, T_0). The monochromatic absorption coefficient, k, at wavenumber, $\tilde{\nu}$, is given by:

$$k_{\tilde{\nu}} = S\, f(\tilde{\nu} - \tilde{\nu}_0), \tag{C.1}$$

---

[1] Phosphine has a pyramidal shape with phosphorus at the apex and the three hydrogen nuclei at the corners of an equilateral triangle. This structure has two out of three moments of inertia equal, making phosphine a symmetric-top (also sometimes known as a symmetric-rotator or "rotor"). As PH_3's three moments of inertia are not all equal, the effect of rotation on the spectrum requires the description of two quantum numbers: the total and axial angular-momentum quantum numbers respectively.

$\tilde{\nu}$ [cm^{-1}]	**Line Strength at 296 K**	$\tilde{\nu}$ [cm^{-1}]	**Line Strength at 296 K**	$\tilde{\nu}$ [cm^{-1}]	**Line Strength at 296 K**
896.504	3.69E-28	1116.682	1.25E-23	1122.289	2.99E-21
906.615	1.86E-27	1116.754	6.27E-24	1122.302	7.38E-21
916.532	5.99E-27	1118.052	2.89E-23	1122.321	8.92E-22
926.264	1.74E-26	1118.136	1.45E-23	1122.340	4.81E-21
935.823	4.75E-26	1119.040	7.82E-21	1122.408†	9.74E-21
945.222	1.26E-25	1119.196	6.41E-23	1122.502	1.51E-21
954.473	3.23E-25	1119.294	3.22E-23	1122.521	5.52E-21
963.592	7.97E-25	1119.413	1.37E-20	1122.584	2.45E-21
972.593	1.90E-24	1119.879	1.98E-20	1122.585	3.77E-21
981.490	4.40E-24	1120.132	1.36E-22	1137.219	1.46E-21
990.299	9.82E-24	1120.243	6.83E-23	1146.581	1.70E-21
999.033	2.13E-23	1120.358	2.47E-20	1155.946	1.22E-21
1007.707	4.46E-23	1120.801	3.65E-21	1165.259	6.59E-22
1016.332	9.10E-23	1120.888	7.99E-23	1174.499	2.93E-22
1024.920	1.81E-22	1121.002	1.39E-22	1183.666	1.13E-22
1033.479	3.49E-22	1121.179	2.63E-20	1192.762	3.77E-23
1042.015	6.58E-22	1121.274	1.51E-20	1201.784	1.03E-23
1050.530	1.21E-21	1121.345	1.24E-20	1210.718	1.09E-24
1059.020	2.14E-21	1121.445	5.37E-22	1219.572	1.35E-25
1067.478	3.60E-21	1121.453	1.52E-20	1228.310	3.48E-26
1075.897	5.54E-21	1121.507	2.33E-20	1236.922	1.90E-25
1084.292	7.43E-21	1121.589	2.70E-22	1245.390	2.57E-25
1092.711	8.69E-21	1121.590	1.64E-20	1253.694†	2.32E-25
1101.234	7.54E-21	1121.758	1.75E-20	1261.813	1.70E-25
1108.663	1.23E-21	1121.789	6.18E-22	1269.727	1.09E-25
1108.684	1.44E-25	1121.864	1.40E-21	1277.415	6.30E-26
1109.929	5.35E-21	1121.919	1.48E-20	1284.854	3.36E-26
1111.070	7.85E-25	1122.014	1.48E-20	1292.027	1.65E-26
1111.109	3.93E-25	1122.023	5.02E-22	1298.912	7.64E-27
1113.205	2.06E-24	1122.094	1.26E-20	1305.490	3.04E-27
1113.254	1.03E-24	1122.135	1.77E-21	1311.745	1.13E-27
1115.072	5.18E-24	1122.190	1.07E-20	1317.660	3.75E-28
1115.132	2.59E-24	1122.261	1.01E-20		

Table C.1: PH_3 lines in error within the GEISA-97 spectroscopic database [114] – line strengths are in units of cm^{-1}/(molec. cm^2). †: the first of two entries at the same wavenumber.

Ordinates	Weights
1.3046736E-02	3.3335671E-02
6.7468315E-02	7.4725673E-02
0.1602952	0.1095432
0.2833023	0.1346334
0.4255628	0.1477621
0.5744371	0.1477621
0.7166977	0.1346334
0.8397048	0.1095432
0.9325317	7.4725673E-02
0.9869533	3.3335671E-02

Table C.2: Gauss-Legendre quadrature ordinates and weights.

where f is the shape factor of the spectral line. The absorption coefficients were then used to calculate the k-distributions. The k-distributions were integrated using a ten-point Gaussian-Legendre quadrature with the ordinates and weights of Table C.2.

C.2 K-tables

Pre-tabulated tables of k-distributions for use with the correlated-k method were created from the cassini_cirs database. A base k-table of point-spacing 0.25 cm^{-1} between 5 and 1450 cm^{-1} was created for each gas: CH_4 (and its isotopes CH_3D, $^{13}CH_4$), C_2H_2, C_2H_4, C_2H_6, C_4H_2, NH_3 and PH_3. Five additional k-tables of point-spacings 0.5, 1.0, 2.5, 5.0 and 10.0 cm^{-1} were then averaged from the base k-table for use with the various spectral resolutions returned by the CIRS instrument.

The six k-tables were convolved with a boxcar FWHM set equal to the point-spacings so as to create a triangular line shape. The triangular line shape was found to be a convenient and sufficiently accurate approximation to the Hamming apodisation applied

Pressures [bar]	**Temperatures [K]**
1.6701701E-05	100.0000
4.2270196E-05	117.8571
1.0698119E-04	135.7143
2.7075780E-04	153.5714
6.8525871E-04	171.4286
1.7343147E-03	189.2857
4.3893605E-03	207.1429
1.1108996E-02	225.0000
2.8115654E-02	242.8571
7.1157642E-02	260.7143
0.1800923	278.5714
0.4557941	296.4286
1.153564	314.2857
2.919547	332.1429
7.389056	350.0000

Table C.3: K-table pressures and temperatures at which k-distributions were calculated.

to the CIRS spectra during calibration. Additional considerations in the compilation of the k-tables include line wings and shapes and pressure and temperature corrections.

C.2.1 Pressure and Temperature

The k-distributions were computed on a grid of 15 equally-spaced temperatures between 100 and 350 K and 15 equally-spaced pressures from $-11 \leq \log \mathrm{P} \leq +2$ (1.7×10^{-5} and 7.5 bar respectively – the individual pressures and temperatures are in Table C.3).

C.2.2 Line Shape

The pressure-temperature dependence of a line-shape's half-width-at-half-maximum (γ) for a gas at pressure, P, temperature, T, is:

$$\gamma(P,T) \;=\; [(1 \;-\; \mathrm{VMR})\,\gamma_{\mathrm{foreign}}(P_0,T_0) \;+\; \mathrm{VMR}\,\gamma_{\mathrm{self}}(P_0,T_0)] \left(\frac{P}{P_0}\right) \left(\frac{T_0}{T}\right)^{\alpha}, \qquad \text{(C.2)}$$

where $\gamma_{\mathrm{foreign}}$ and γ_{self} are the reference foreign- and self-broadened half-width-at-half-maximums, α is the coefficient of temperature dependence and VMR is the volume mixing ratio. The pressure-broadening of each species was set to be completely foreign-broadened due to the hydrogen-dominated Jovian conditions in which molecules of the same species are unlikely to come in contact with one another. The half-widths were determined assuming a Voigt line-shape which considers a mixed Doppler and Lorentz line-profile (whichever is larger at the calculation pressure and temperature) and was chosen as the standard for those working on CIRS radiative-transfer modelling for intercomparison purposes.

Collision-induced absorption (CIA), that which defines the continuum line-shape, was also considered. CIA was determined for H_2, He and CH_4 based on the studies of Borysow *et al.* 1985, 1987, 1988: [30, 31, 32]. For the purposes of intercomparison, formally agreed-upon half-widths and coefficients of temperature-dependence were prescribed for the major species within the Jovian atmosphere; these values can be found in Table C.4.

The line-broadening parameters for PH_3 were however determined independently.

Species	**Pressure-broadened γ [cm^{-1}/atm] at 296 K**	**Coefficient of Temperature Dependence**
CH_4 $^{13}CH_4$ CH_3D	0.061	0.45
C_2H_2	0.085	0.75
C_2H_4	0.101	0.63
C_2H_6	0.105	0.94
NH_3	0.072	0.73
PH_3	0.093	0.68

Table C.4: Line-broadening parameters – no values were prescribed for C_4H_2.

The H_2- and He-broadening of PH_3 was found [116] to follow the empirical relations:

$$\gamma_{H_2} = 0.1078 - (0.0014\,\kappa), \tag{C.3}$$

$$\gamma_{He} = 0.0618 - (0.0014\,\kappa), \tag{C.4}$$

where κ is the total angular-momentum quantum number[2]; the corresponding empirically-determined [117] coefficients of temperature-dependence are 0.732 and 0.303 (for H_2- and He-broadening respectively). Using the H_2 and He relative-abundances (0.863 and 0.134 respectively) to simulate Jovian conditions, the pressure-broadened half-width and coefficient of temperature-dependence equal 0.099 and 0.672 respectively (for $\kappa = 1$). These values compare favourably to the values prescribed for PH_3 for intercomparison: 0.093 and 0.68 [Table C.4].

---

[2] Note that most studies use J to represent the total angular-momentum quantum number.

Species	α	β	γ	δ
CH_4	-0.26479E+02	+0.11557E+01	+0.26831E-02	+0.15117E-05
$^{13}CH_4$	-0.52956E+02	+0.23113E+01	+0.53659E-02	+0.30232E-05
CH_3D	-0.21577E+03	+0.93318E+01	+0.21779E-01	+0.12183E-04
C_2H_2	-0.83088E+01	+0.14484E+01	-0.25946E-02	+0.84612E-05
C_2H_4 C_2H_6 C_4H_2	-0.30755E+02	+0.63608E+01	+0.43890E-03	-0.23683E-06
NH_3	-0.42037E+02	+0.25976E+01	+0.13073E-01	-0.62230E-05

Table C.5: The partition-function coefficients used to determine the line strength at temperatures away from 296 K. As there was no known partition-functions for C_2H_4, C_2H_6 and C_4H_2, the coefficients for these species were set to a reasonable approximation ($\sim T^{1.5}$) for the rotation partition-function of a polyatomic rotor.

C.2.3 Spectral Strength Temperature Correction

To obtain the absorption line strength at temperatures away from T_0, the total partition function must be determined. The total partition function is useful in determining the distribution of molecules amongst the various energy states at a particular temperature [70]. Assuming separability of the electronic, vibrational, rotational and translational energy states, a direct summation of the respective energies (including any degeneracies) is obtainable, but computationally expensive.

Instead, the total partition function can be accurately approximated as the product of the vibrational and rotational partition-functions alone. Utilising coefficients representing the geometric properties of the molecule, the four-term polynomial expression:

$$\frac{S(T)}{S(T_0)} = \frac{\alpha + \beta T_0 + \gamma T_0^2 + \delta T_0^3}{\alpha + \beta T + \gamma T^2 + \delta T^3}, \tag{C.5}$$

may be used to approximate the sum to high accuracy. The partition-function coefficients for an assortment of Jovian gases used in the thesis (originally taken from HITRAN-2K) can be found in Table C.5.

C.2.4 Line-wing Cut-off

Line-wings, while not as important as line centers in determining the molecular absorption, contain information about the underlying continuum [77]. However, in the interests of computational efficiency, a maximum distance within which to consider the contribution of the line wings, is prescribed. This is referred to as the line-wing cut-off. A line-wing cut-off of 35 cm^{-1} was chosen as the standard for those working on CIRS radiative-transfer modelling for intercomparison purposes.

Bibliography

[1] Abbas, M. and LeClaire, A. (2004). Nitrogen isotopic ratio in Jupiter's atmosphere from observations by the Composite Infrared Spectrometer (CIRS) on the Cassini spacecraft. in preparation.

[2] Achterberg, R., Conrath, B., Gierasch, P., Flasar, M., and Simon-Miller, A. (2004). Cassini CIRS retrievals of temperature and ammonia in Jupiter's upper-troposphere: implications for atmospheric dynamics. in preparation.

[3] Allison, M. (1990). Planetary waves in Jupiter's equatorial atmosphere. *Icarus*, 83(2):282–307.

[4] Allison, M. and Atkinson, D. (2001). Galileo probe doppler residuals as the wave-dynamical signature of weakly stable, downward-increasing stratification in Jupiter's deep wind layer. *J. Geophys. Res.*, 28(14):2747–2750.

[5] Anders, E. and Grevesse, N. (1989). Abundances of the elements: meteoritic and solar. *Geochim. Cosmochim. Acta*, 53(1):197–214.

[6] Atkinson, D., Pollack, J., and Seiff, A. (1998). The Galileo probe doppler wind experiment: measurement of the deep zonal winds on Jupiter. *J. Geophys. Res.*, 103(E10):22911–22928.

[7] Atreya, S. (1986). *Atmospheres and ionospheres of the outer planets and their satellites*. Springer-Verlag, Heidelberg, Germany, 1st edition.

[8] Atreya, S., Donahue, T., and Festou, M. (1981). Jupiter: structure and composition of the upper atmosphere. *Astrophys. J.*, 247(1):L43–L47.

[9] Atreya, S., Mahaffy, P., Niemann, H., Wong, M., and Owen, T. (2003). Composition and origin of the atmosphere of Jupiter – an update, and implications for the extrasolar giant planets. *Plan. & Space Sci.*, 51(2):105–112.

[10] Atreya, S., Wong, M., Owen, T., Mahaffy, P., Niemann, H., de Pater, I., Drossart, P., and Encrenaz, T. (1999). A comparison of the atmospheres of Jupiter and saturn: deep atmospheric composition, cloud structure, vertical mixing and origin. *Plan. & Space Sci.*, 47(10-11):1243–1262.

[11] Baines, K., Carlson, R., and Kamp, L. (2002). Fresh ammonia ice clouds in Jupiter: I. spectroscopic identification, spatial distribution, and dynamical implications. *Icarus*, 159(1):74–94.

[12] Baines, K., Carlson, R., and Newman, E. (1996). The vertical and dynamical structure of the Great Red Spot and environs as determined by Galileo/NIMS. *Bull. Amer. Astron. Soc.*, 28:1136.

[13] Banfield, D., Gierasch, P., Bell, M., Ustinov, E., Ingersoll, A., and Vasavada, A. (1998). Jupiter's cloud structure from Galileo imaging data. *Icarus*, 135(1):230–250.

[14] Banwell, C. and McCash, E. (1994). *Fundamentals of molecular spectroscopy.* McGraw-Hill Publishing Co., USA, 4th edition.

[15] Barshay, S. and Lewis, J. (1978). Chemical structure of the deep atmosphere of Jupiter. *Icarus*, 33(3):593–611.

[16] Baum, W. (1953). A photometric observation of the occultation of σ Arietis by Jupiter. *Astron. J.*, 58:108–112.

[17] Beebe, R. (1995). *Jupiter: The Giant Planet.* Academic Press, USA, 1st edition.

[18] Beebe, R., Suggs, R., and Little, T. (1986). Seasonal north-south asymmetry in solar radiation incident on Jupiter's atmosphere. *Icarus*, 66(2):359–365.

[19] Beebe, R. and Youngblood, L. (1979). Pre-Voyager velocities, accelerations and shrinkage rates of Jovian cloud features. *Nature*, 280:771–772.

[20] Berger, B. (2004). Back to the moon, on to mars. Space News online: http://www.space.com.

[21] Bergin, E., Lellouch, E., Harwit, M., Gurwell, M., Melnick, G., Ashby, M., Chin, G., Erickson, N., Goldsmith, P., Howe, J., Kleiner, S., Koch, D., Neufeld, D., Patten, B., Plume, R., Schieder, R., Snell, R., Stauffer, J., Tolls, V., Wang, Z., Winnewisser, G., and Zhang, Y. (2000). Submillimeter Wave Astronomy Satellite observations of Jupiter and Saturn: detection of 557 GHz water emission from the upper atmosphere. *Astrophys. J.*, 539(2):L147–L150.

[22] Betremieux, Y., Yelle, R., and Griffith, C. (2003). HST observation of the atmospheric composition of Jupiter's equatorial region: evidence for tropospheric C_2H_2. *Icarus*, 163(2):414–427.

[23] Bézard, B., Drossart, P., Encrenaz, T., and Feuchtgruber, H. (2001). Benzene on the giant planets. *Icarus*, 154(2):492–500.

[24] Bézard, B., Griffith, C., Lacy, T., and Owen, T. (1995). Non-detection of hydrogen cyanide on Jupiter. *Icarus*, 118(2):384–391.

[25] Bézard, B., Lellouch, E., Strobel, D., and Drossart, P. (2002). Carbon monoxide on Jupiter: evidence for both internal and external sources. *Icarus*, 159(1):95–111.

[26] Bézard, B. and Orton, G. (2000). *Report on the radiative-transfer model comparisons.* CIRS radiative transfer team, Obs. Meudon, Paris, France.

[27] Bjoraker, G., Larson, H., and Kunde, V. (1986). The abundance and distribution of water-vapour in Jupiter's atmosphere. *Astrophys. J.*, 311(2):1058–1072.

[28] Boruki, W. and Magalhães, J. (1991). Analysis of Voyager 2 images of Jovian lightning. *Icarus*, 96(1):1–14.

[29] Borunov, S., Doropeeva, V., Khodakovsky, I., Drossart, P., Lellouch, E., and Encrenaz, T. (1995). Phosphorus chemistry in the atmosphere of Jupiter: a reassessment. *Icarus*, 113(2):460–464.

[30] Borysow, J. and Frommhold, L. (1987). Collision-induced rototranslational absorption-spectra of CH_4-CH_4 pairs at temperatures from 50 K to 300 K. *Astrophys. J.*, 318(2):940–943.

[31] Borysow, J., Frommhold, L., and Birnbaum, G. (1988). Collision-induced rototranslational absorption spectra of H_2-He pairs at temperatures from 40 to 3000 K. *Astrophys. J.*, 326(1):509–515.

[32] Borysow, J., L., T., Frommhold, L., and Birnbaum, G. (1985). Modelling of pressure-induced far-infrared absoprtion spectra: molecular hydrogen pairs. *Astrophys. J.*, 296(2):644–654.

[33] Boudon, V., Mkadmi, E., Bürger, H., and Pierre, G. (1999). High-resolution Fourier transform infrared spectroscopy and analysis of the ν_3 fundamental band of P_4. *Chem. Phys. Lett.*, 305:21–27.

[34] Brooke, T., Knacke, R., Drossart, P., Encrenaz, T., Crisp, D., and Feuchtgruber, H. (1998). Models of the ISO 3-μm reflection spectrum of Jupiter. *Icarus*, 136(1):1–13.

[35] Calcutt, S., Taylor, F., Ade, P., Kunde, V., and Jennings, D. (1992). The Composite Infrared Spectrometer. *J. Brit. Interplan. Soc.*, 45(1):811–816.

[36] Caldwell, J., Halthore, R., Orton, G., and Bergstralh, J. (1988). Infrared polar brightening on Jupiter iv: spatial properties of methane emission. *Icarus*, 74(2):331–339.

[37] Caldwell, J., Tokunaga, A., and Gillett, F. (1980). Possible infrared aurorae on Jupiter. *Icarus*, 44(3):667–675.

[38] Carlson, B., Lacis, A., and Rossow, W. (1993). Tropospheric gas composition and cloud structure of the Jovian North Equatorial Belt. *J. Geophys. Res.*, 98(E3):5251–5290.

[39] Carlson, R. (2002). *CIRS spectral resolution as a function of scan time.* SSAI/NASA Goddard Space Flight Center, Code 693.0, Greenbelt, MD, USA.

[40] Carlson, R., Smythe, W., Baines, K., Barbinis, E., Becker, K., Burns, R., Calcutt, S., Calvin, W., Clark, R., Danielson, F., Davies, A., Drossart, P., Encrenez, T., Fanale, F., Granahan, J., Hansen, G., Herrera, P. Hibbitts, C., Hui, J., Irwin, P., Johnson, T., Kamp, L., Kieffer, H., Leader, F., Lellouch, E., Lopes-Gautier, R., Matson, D., McCord, T., Mehlman, R., Ocampo, A., Orton, G., Ross-Serote, M., Segura, M., Shirley, J., Soderblom, L., Stevenson, A., Taylor, F., Torson, J., Weir, A., and Weissman, P. (1996). Near infrared spectroscopy and spectral mapping of Jupiter and the Galilean satellites: results from Galileo's first orbit. *Science*, 274(5286):385–388.

[41] Carlson, R., Weissman, P., Smythe, W., and Mahoney, J. (1992). Near-Infrared Mapping Spectrometer experiment on Galileo. *Space Sci. Rev.*, 60(1-4):457–502.

[42] Chou, M.-D., Ridgway, W., and Yan, M. (1993). One-parameter scaling and exponential-sum fitting for water vapor and CO_2 infrared transmission functions. *J. Atmos. Sci.*, 50(14):2294–2303.

[43] Conrath, B., Flasar, M., Pirraglia, J., Gierasch, P., and Hunt, G. (1981). Thermal structure and dynamics of the Jovian atmosphere. II: visible cloud features. *J. Geophys. Res.*, 86(A10):8769–8775.

[44] Conrath, B. and Gierasch, P. (1986). Retrieval of ammonia abundances and cloud opacities on Jupiter from Voyager IRIS spectra. *Icarus*, 67(3):444–455.

[45] Conrath, B., Gierasch, P., and Leroy, S. (1990). Temperature and circulation in the stratosphere of the outer planets. *Icarus*, 83(2):255–281.

[46] Davis, S., Abrams, M., and Brault, J. (2001). *Fourier transform spectrometry.* Academic Press, USA, 1st edition.

[47] de Graauw, T., Feuchtgruber, H., Bézard, B., Drossart, P., Encrenaz, T., Beintema, D., Griffin, M., Heras, A., Kessler, M., Leech, K., Lellouch, E., Morris, P., Roelfsema, P., Roos-Serote, M., Salama, A., Vandenbussche, B., Valentijn, E., Davis, G., and Naylor, D. (1997). First results of ISO/SWS observations of Saturn: detection of CO_2 CH_3C_2H, C_4H_2 and tropospheric H_2O. *Astron. Astrophys. Rev.*, 321(2):L13–L16.

[48] de Pater, I. (1986). Jupiter's zone-belt structure at radio wavelengths. II: comparison of observations with model atmosphere calculations. *Icarus*, 68(2):344–365.

[49] Deming, D., Reuter, D., Jennings, D., Bjorker, G., McCabe, G., Fast, K., and Wiedemann, G. (1997). Observations and analysis of longitudinal thermal waves on Jupiter. *Icarus*, 126(2):301–312.

[50] Drossart, P., Encrenaz, T., Kunde, V., and Combes, M. (1982). An estimate of the PH_3, CH_3D and GH_4 abundances on Jupiter from the voyager IRIS data at 45 μm. *Icarus*, 49(2):416–426.

[51] Drossart, P., Lellouch, E., Bézard, B., Maillard, J., and Tarrago, G. (1990). Jupiter: evidence for a phosphine enhancement at high northern latitudes. *Icarus*, 83(2):248–253.

[52] Dwyer, J. (2003). A fundametnal limit on electric fields in air. *Geophys. Res. Lett.*, 30(20):2055.

[53] Edgington, S., Atreya, S., Trafon, L., Caldwell, J., Beebe, R., Simon, A., West, R., and Barnet, C. (1998). On the latitude variation of ammonia, acetylene and phosphine

altitude profiles on Jupiter from HST Faint Object Spectrograph observations. *Icarus*, 133(1):192–209.

[54] Edgington, S., Atreya, S., Trafton, L., Caldwell, J., Beebe, R., Simon, A., and West, R. (1999). Ammonia and eddy mixing variations in the upper troposphere of Jupiter from HST Faint Object Spectrograph observations. *Icarus*, 142(2):342–356.

[55] Encrenaz, T. (1999a). The planet Jupiter. *Astron. Astrophys. Rev.*, 9(3-4):171–219.

[56] Encrenaz, T., Drossart, P., Feuchtgruber, H., Lellouch, E., Bézard, B., Fouchet, T., and Atreya, S. (1999b). The atmospheric composition and structure of Jupiter and Saturn from ISO observations: a preliminary review. *Plan. & Space Sci.*, 47(10-11):1225–1242.

[57] Fegley, B. and Lodders, K. (1994). Chemical models of the deep atmospheres of Jupiter and Saturn. *Icarus*, 110(1):117–154.

[58] Feuchtgruber, H., Lellouch, E., de Graauw, T., Bézard, B., Encrenaz, T., and Griffin, M. (1997). External supply of oxygen to the atmospheres of the giant planets. *Nature*, 389(6647):159–162.

[59] Flasar, M., Conrath, B., Pirraglia, J., Clark, P., French, R., and Gierasch, P. (1981). Thermal structure and dynamics of the Jovian atmosphere. I: the Great Red Spot. *J. Geophys. Res.*, 86(A10):8759–8767.

[60] Flasar, M. and Gierasch, P. (1986). Mesoscale waves as a probe of Jupiter's deep atmosphere. *J. Atmos. Sci.*, 43(22):2683–2707.

[61] Flasar, M., Kunde, V., Achterberg, R., Conrath, B., Simon-Miller, A., Nixon, C., Gierasch, P., Romani, P., Bézard, B., Irwin, P., Bjoraker, G., Brasunas, J., Jennings, D. Pearl, J., Smith, M., Orton, G., Spilker, L., Edberg, S., Carlson, R., Calcutt, S., Read, P., Taylor, F., Fouchet, T., Parrish, P., Barucci, A., Courtin, R., Coustenis, A., Gautier, D., Lellouch, E., Marten, A., Biraud, Y., Ferrari, C., Prangé, R., Owen,

T., Abbas, M., Samuelson, R., Raulin, F., Ade, P., Césarsky, C., Grossman, K., and Coradini, A. (2003). An intense stratospheric jet on Jupiter. *Nature*, 427(6969):132–135.

[62] Forman, M., Steel, W., and Vanasse, A. (1966). Correction of the asymmetric interferograms obtained in Fourier spectroscopy. *J. Opt. Soc. Amer.*, 56(1):59–63.

[63] Fouchet, T. (2003). Private communication.

[64] Fouchet, T., Irwin, P., Parrish, P., Calcutt, S., Taylor, F., and Owen, T. (2004). Search for spatial variation in the Jovian ^{15}N/^{14}N ratio from Cassini/CIRS observations. accepted Icarus.

[65] Fouchet, T., Lellouch, E., Bézard, B., Feuchtgruber, H., Drossart, P., and Encrenaz, T. (2000). Jupiter's hydrocarbons observed with ISO-SWS: vertical profiles of C_2H_6 and C_2H_2, detection of CH_3C_2H. *Astron. Astrophys. Rev.*, 355(1):L13–L17.

[66] Fouchet, T., Lellouch, E., and Feuchtgruber, H. (2003). The hydrogen ortho-to-para ratio in the stratospheres of the giant planets. *Icarus*, 161(1):127–143.

[67] Friedson, A. (1999). New observations and modelling of a QBO-like oscillation in Jupiter's stratosphere. *Icarus*, 137(1):34–55.

[68] Fu, Q. and Liou, K.-N. (1992). On the correlated k–distribution method for radiative transfer in nonhomogeneous atmospheres. *J. Atmos. Sci.*, 49(22):2139–2156.

[69] Galileo (2003). Galileo end of mission status. http://galileo.jpl.nasa.gov/news/.

[70] Gamache, R., Hawkins, R., and Rothman, L. (1990). Total internal partition sums in the temperature range 70-3000 K: atmospheric linear molecules. *J. Molec. Spectro.*, 142(2):205–219.

[71] García-Melendo, E. and Sánchez-Lavega, A. (2001). A study of the stabilitity of Jovian zonal winds from HST images: 1995-2000. *Icarus*, 152(2):316–330.

[72] Gautier, D., Hersant, F., Mousis, O., and Lunine, J. (2001). Enrichments in volatiles in Jupiter: a new interpretation of the Galileo measurements. *Astrophys. J.*, 550(2):L227–L230. erratum in *Astrophys. J.* 559, L183.

[73] Gierasch, P., Conrath, B., and Magalhães, J. (1986). Zonal mean properties of Jupiter's upper troposphere from Voyager infrared observations. *Icarus*, 67(2):456–483.

[74] Gierasch, P., Ingersoll, A., Banfield, D., Ewald, S., Helfenstein, P., Simon-Miller, A., Vasavada, A., Breneman, H., Senske, D., and the Galileo Imaging Team (2000). Observation of moist convection in Jupiter's atmosphere. *Nature*, 403(6770):628–630.

[75] Gladstone, G., Allen, M., and Yung, Y. (1996). Hydrocarbon photochemistry in the upper atmosphere of Jupiter. *Icarus*, 119(1):1–52.

[76] Goody, R., West, R., Chen, L., and Crisp, D. (1989). The correlated-k method for radiation calculations in nonhomogeneous atmospheres. *J. Quant. Spectro. Rad. Trans.*, 42(6):539–550.

[77] Goody, R. and Yung, Y. (1989). *Atmospheric radiation.* Oxford Univ. Press, UK, 2nd edition.

[78] Griffith, C., Bézard, B., Owen, T., and Gautier, D. (1992). The tropospheric abundances of NH_3 and PH_3 in Jupiter's Great Red Spot, from Voyager IRIS observations. *Icarus*, 98(1):82–93.

[79] Guillot, T. (1999). A comparison of the interiors of Jupiter and Saturn. *Plan. & Space Sci.*, 47(10-11):1183–1200.

[80] Guillot, T., Chabrier, G., Morel, P., and Gautier, D. (1994). Nonadiabatic models of Jupiter and Saturn. *Icarus*, 112(2):354–367.

[81] Hanel, R., Conrath, B., Flasar, M., Kunde, V., Lowman, P., Maguire, W., Pearl, J., Pirraglia, J., Samuelson, R., Gautier, D., Gierasch, P., Horn, L., Kumar, S., and

Ponnamperuma, C. (1979b). Infrared observations of the Jovian system from Voyager 2. *Science*, 206:952–956.

[82] Hanel, R., Conrath, B., Flasar, M., Kunde, V., Lowman, P., Maguire, W., Pearl, J., Pirraglia, J., Samuelson, R., Gautier, D., Gierasch, P., Kumar, S., and Ponnamperuma, C. (1979a). Infrared observations of the Jovian system from voyager 1. *Science*, 204:972–976.

[83] Hanel, R., Conrath, B., Herath, L., Kunde, V., and Pirraglia, J. (1981). Albedo, internal heat, and energy balance of Jupiter: preliminary results of the Voyager infrared investigation. *J. Geophys. Res.*, 86(A10):8705–8712.

[84] Hanel, R., Crosby, D., Herath, L., Vanous, D., Collins, D., Creswick, H., Harris, C., and Rhodes, M. (1980). Infrared spectrometer for Voyager. *Appl. Opt.*, 19:1391–1400.

[85] Hansen, J. and Travis, L. (1974). Light scattering in planetary atmospheres. *Space Sci. Rev.*, 16:527–610.

[86] Harrington, J., Dowling, T., and Baron, R. (1996). Jupiter's tropospheric thermal emission. *Icarus*, 124(1):32–44.

[87] Herzberg, G. (1945). *Molecular spectra and molecular structure. II: infrared and Raman spectra of polyatmoic molecules.* Van Nostrand Reinhold Company, USA, 1st edition.

[88] Hubbard, W. (1989). Structure and composition of giant planet interiors. In Atreya, S., Pollack, J., and Matthews, M., editors, *Origin and evolution of planetary and satellite atmospheres*, pages 539–563. Univ. Arizona Press.

[89] Hubbard, W., Nather, R., Evans, D., Tull, R., Wells, D., van Citters, G., Warner, B., and Vanden Bout, P. (1972). The occultation of β Scorpii by Jupiter and Io. i. *Astron. J.*, 77:41–59.

[90] Hubbard, W. and Slattery, W. (1976). Interior structure of Jupiter: theory of gravity sounding. In Gehrels, T., editor, *Jupiter: studies of the interior, atmosphere, magnetosphere and satellites*, number 1 in Space Science, pages 176–194. Univ. Arizona Press.

[91] Hunten, D., Colin, L., and Hansen, J. (1986). Atmospheric science on the Galileo mission. *Space Sci. Rev.*, 44(3-4):191–240.

[92] Ingersoll, A., Münch, G., Neugebauer, G., Diner, D., Orton, G., Schupler, B., Schroeder, M., Chase, S., Ruiz, R., and Trafton, L. (1975). Pioneer 11 infrared radiometer experiment: the global heat balance of Jupiter. *Science*, 188:472–473.

[93] Ingersoll, A., Münch, G., Neugebauer, G., and Orton, G. (1976). Results of the infrared radiometer experiment on pioneers 10 and 11. In Gehrels, T., editor, *Jupiter: Studies of the interior, atmosphere, magnetosphere and satellites*, number 1 in Space Science, pages 197–205. Univ. Arizona Press.

[94] Irwin, P. (2003a). Private communication. CIRS Team Meeting, Venice, Italy.

[95] Irwin, P. (2003b). Private communication. CIRS Team Meeting, Washington, DC USA.

[96] Irwin, P. (2003c). *Giant planets of our solar system: atmospheres, composition and structure.* Springer-Praxis, UK, 1st edition.

[97] Irwin, P., Calcutt, S., Taylor, F., Baugh, A., Webster, S., Nixon, C., and Carlson, R. (2000). Evidence for the existence of a deep water cloud from the Galileo Near Infrared Mapping Spectrometer. In Milkey, R., editor, *Bull. Amer. Astron. Soc.*, 32nd DPS meeting, page 1007, Pasadena, California. American Astronomical Society.

[98] Irwin, P., Weir, A., Smith, S., Taylor, F., Lambert, A., Calcutt, S., Carlson, R., Baines, K., Orton, G., Drossart, P., Encrenaz, T., and Roos-Serote, M. (1998). Cloud structure and atmospheric composition of Jupiter retrieved from Galileo Near-Infrared Mapping Spectrometer real-time spectra. *J. Geophys. Res.*, 103(E10):23,001–23,021.

[99] Irwin, P., Weir, A., Taylor, F., Calcutt, S., and Carlson, R. (2001). The origin of belt/zone contrasts in the atmosphere of Jupiter and their correlation with 5-μm opacity. *Icarus*, 149(2):397–415.

[100] Kaye, J. and Strobel, D. (1983a). HCN formation on Jupiter: the coupled photochemistry of ammonia and acetylene. *Icarus*, 54(3):417–433.

[101] Kessler, M., Steinz, J., Anderegg, M., Clavel, J., Drechsel, G., Estaria, P., Faelker, J., Riedinger, J., Robson, A., Taylor, B., and deFerran, S. (1996). The infrared space observatory (ISO) mission. *Astron. Astrophys. Rev.*, 315(2):L27–L31.

[102] Khurana, K., Kivelson, M., Stevenson, D., Schubert, G., Russell, C., Walker, C., and Polanskey, C. (1998). Induced magnetic fields as evidence for subsurface oceans in Europa and Callisto. *Nature*, 395(6704):777–780.

[103] Kiess, C., Corliss, C., and Kiess, H. (1960). High-dispersion spectra of Jupiter. *Astrophys. J.*, 132:221–231.

[104] Kim, S., Drossart, P., Caldwell, J. Maillard, J.-P., and Herbst, T. (1985). Infrared polar brightness of Jupiter iii: spectrometry from the Voyager 1 IRIS experiment. *Icarus*, 64(2):233–248.

[105] Klaasen, K., Belton, M., Breneman, H., McEwan, A., Davies, M., Sullivan, R., Chapman, C., G., N., Heffernan, C., Harch, A., Kaufman, J., Merline, W., Gaddis, L., Cunningham, W., Helfenstein, P., and Colvin, T. (1997). Inflight performance characteristics, calibration and utilization of the Galileo SSI camera. *Opt. Eng.*, 36(11):3001–3027.

[106] Kliner, I., Tarrago, G., Cottaz, C., Sagui, L., Brown, L., Poynter, R., Pickett, H., Chen, P., Pearson, J., Sams, R., Blake, G., Matsuura, S., Nemtchinov, V., Varanasi, P., Fusina, L., and di Lonardo, G. (2003). NH_3 and PH_3 line parameters: the 2000 HITRAN update and new results. *J. Quant. Spectro. Rad. Trans.*, 82:293–312.

[107] Kliore, A. and Woiceshyn, P. (1976). Structure of the atmosphere of Jupiter from Pioneer 10 and 11 radio occultation measurements. In Gehrels, T., editor, *Jupiter: Studies of the interior, atmosphere, magnetosphere and satellites*, number 1 in Space Science, pages 216–237. Univ. Arizona Press.

[108] Kunde, V., Ade, P., Barney, R., D., B., Bonnal, J., Borelli, R., Boyd, D., Brasunas, J., Brown, G., Calcutt, S., Carrol, F., Courtin, R., Cretolle, J., Cooke, J., Davis, M., Edberg, S., Fettig, R., Flasar, M., Gelnar, D., Graham, S., Hagopian, J., Hakun, C., Hayes, P., Herath, L., Horn, L., Jennings, D., Karpati, G., Kellebenz, C., Lakew, B., Lindsay, J., Lohr, J., Lyons, J., Martineau, R., Marino, A., Matsumura, M., J., M., Melak, T., Michel, G., Morell, A., Mosier, C., Pack, L., Plants, M., Robinson, D., Rodriguez, L., Romani, P., Schaefer, W., Schmidt, S., Trujillo, C., Vellcott, T., Wagner, K., and Yun, D. (1996). Cassini infrared Fourier spectroscopic investigation. In *Cassini/Huygens: A mission to the Saturnian system*, volume 2803, pages 162–177, Denver, Colorado. SPIE Proceedings.

[109] Kunde, V., Flasar, M., Achterberg, R., Conrath, B., Simon-Miller, A., Nixon, C., Gierasch, P., Romani, P., Bézard, B., Irwin, P., Bjoraker, G., Brasunas, J., Jennings, D. Pearl, J., Smith, M., Orton, G., Spilker, L., Edberg, S., Carlson, R., Calcutt, S., Read, P., Taylor, F., Fouchet, T., Parrish, P., Barucci, A., Courtin, R., Coustenis, A., Gautier, D., Lellouch, E., Marten, A., Biraud, Y., Ferrari, C., Prangé, R., Owen, T., Abbas, M., Samuelson, R., Raulin, F., Ade, P., Césarsky, C., Grossman, K., and Coradini, A. (2004). Jupiter's composition from thermal-infrared observations at high spectral and spatial resolution. submitted Science.

[110] Kunde, V., Hanel, R., Maguire, W., Gautier, D., Baluteau, J., Marten, A., Chedin, A., Husson, N., and Scott, N. (1982). The tropospheric gas composition of Jupiter's North Equatorial Belt (NH_3, PH_3, CH_3D, GH_4, H_2O) and the Jovian D/H isotopic ratio. *Astrophys. J.*, 263(1):443–467.

[111] Lacis, A. and Oinas, V. (1991). A description of the correlated-k distribution

method for modeling nongray gaseous absorption, thermal emission, and mulitple scattering in vertically inhomogeneous atmospheres. *J. Geophys. Res.*, 96(D5):9027–9063.

[112] Lara, L.-M., Bézard, B., Griffith, C., Lacy, J., and Owen, T. (1998). High-resolution 10-micronmeter spectroscopy of ammonia and phosphine lines on Jupiter. *Icarus*, 131(2):317–333.

[113] Larson, H., Treffers, R., and Fink, U. (1977). Phosphine in Jupiter's atmosphere: the evidence from high altitude observations at 5 microns. *Astrophys. J.*, 211:972–979.

[114] Lellouch, E., Bézard, B., Fouchet, T., Feuchtgruber, H., Encrenaz, T., and de Graauw, T. (2001). The deuterium abundance in Jupiter and Saturn from ISO-SWS observations. *Astron. Astrophys. Rev.*, 370(2):610–622.

[115] Levenberg, K. (1944). A method of the solution of certain nonlinear problems in least squares. *Quart. Appl. Math.*, 2:164.

[116] Levy, A., Lacome, N., and Tarrago, G. (1993). Hydrogen- and helium-broadening of phosphine lines. *J. Molec. Spectro.*, 157(1):172–181.

[117] Levy, A., Lacome, N., and Tarrago, G. (1994). Temperature-dependence of collision-broadened lines of phosphine. *J. Molec. Spectro.*, 166(1):20–31.

[118] Lewis, J. (1969). The clouds of Jupiter and the NH_3-H_2O and NH_3-H_2S systems. *Icarus*, 10:365–378.

[119] Limaye, S. (1986). Jupiter: new estimates of the mean zonal flow at the cloud level. *Icarus*, 65(1):335–352.

[120] Lindal, G., Wood, G., Anderson, J., Sweetnam, D., Hotz, H., Buckles, B., Holmes, D., Doms, P., Eshleman, V., Tyler, G., and Croft, T. (1981). The atmosphere of Jupiter: An analysis of the Voyager radio occultation measurements. *J. Geophys. Res.*, 86(A10):8721–8727.

[121] Link, D., Anne, J., Beretta, A., Dechezelles, J., Gluitz, K., Jablonski, A., Draper, R., Horttor, R., and Bonnefoy, R. (2000). Huygens communications Link inquiry board: findings, recommendations and conclusions. Technical report, European Space Agency.

[122] Liou, K. (2002). *An introduction to atmospheric radiation*. ap, USA, 2nd edition.

[123] Little, B., Anger, C., Ingersoll, A., Vasavada, A., Senske, D., Breneman, H., Borucki, W., and the Galileo SSI Team (1999). Galileo images of lightning on Jupiter. *Icarus*, 142(2):306–323.

[124] Lodders, K. and Fegley, B. (1998). *The Planetary Scientist's Companion*. Oxford Univ. Press, USA, 1st edition.

[125] Magalhães, J., Weir, A., Conrath, B., Gierasch, P., and Leroy, S. (1990). Zonal motion and structure in Jupiter's upper troposphere from Voyager infrared and imaging observations. *Icarus*, 89(1):39–72.

[126] Mahaffy, P., Niemann, H., Alpert, A., Atreya, S., Demick, J., Donahue, T., Harpold, D., and Owen, T. (2000). Noble gas abundance and isotope ratios in the atmosphere of Jupiter from the Galileo probe mass spectrometer. *J. Geophys. Res.*, 105(E6):15061–15072.

[127] Marley, M. (1999). Interiors of the giant planets. In Weissman, P., McFadden, L.-A., and Johnson, T., editors, *Encyclopedia of the Solar System*, pages 339–355. Academic Press.

[128] Marquardt, D. (1963). An algorithm for least-squares estimation of nonlinear parameters. *SIAM J. Appl. Math.*, 11:431.

[129] Marten, A., Courtin, R., Gautier, D., and Lacombes, A. (1980). Ammonia vertical density profile in the equatorial region of Jupiter from their radioelectric and infrared emissivities. *Icarus*, 41(3):410–422.

[130] Martin, D. and Pulpett, E. (1969). Polarised interferometric spectroscopy of the millimetre and sub-millimetre spectrum. *Infr. Phys.*, 10:105–109.

[131] Matson, D., Spilker, L., and Lebreton, J.-P. (2002). The Cassini/Huygens mission to the Saturnian system. *Space Sci. Rev.*, 104(1-2):1–58.

[132] Melnick, G., Stauffer, J., Ashby, M., Bergin, E., Chin, G., Erickson, N., Goldsmith, P., Harwit, M. Howe, J., Kleiner, S., Koch, D., Neufeld, D., Patten, B., Plume, R., Schieder, R., Snell, R., Tolls, V., Wang, Z., Winnewisser, G., and Zhang, Y. (2000). Submillimeter Wave Astronomy Satellite: objectives and instrument description. *Astrophys. J.*, 539(2):L77–L85.

[133] Moses, J., Bézard, B., Lellouch, E., Gladstone, G., Feuchtgruber, H., and Allen, M. (2000). Photochemistry in Saturn's atmosphere. *Icarus*, 143(2):244–298.

[134] Nellis, W. (2000). Metallization of fluid hydrogen at 140 GPa (1.4 Mbar): implications for Jupiter. *Plan. & Space Sci.*, 48:671–677.

[135] Niemann, H., Atreya, S., Carignan, G., Donahue, T., Haberman, J., Harpold, D., Hartle, R., Hunten, D., Kasprzak, W., Mahaffy, P., Owen, T., and Way, S. (1998). The composition of the Jovian atmosphere as determined by the Galileo probe mass spectrometer. *J. Geophys. Res.*, 103(E10):22,831–22,845.

[136] Niemann, H., Harpold, D., Atreya, S., Carignan, G., Hunten, D., and Owen, T. (1992). Galileo mass spectrometer experiment. *Space Sci. Rev.*, 60(1-2):111–142.

[137] Nixon, C. (1998). *Remote sounding of the atmosphere of Titan.* D.Phil. thesis, Oxford University.

[138] Nixon, C. (2003a). Private communication.

[139] Nixon, C. (2003b). *CIRS FP1 interference.* NASA Goddard Space Flight Center, Code 693.0, Greenbelt, MD USA.

[140] Nixon, C., Achterberg, R., Conrath, B., Irwin, P., Fouchet, T., Parrish, P., Romani, P., Abbas, M., LeClaire, A., Strobel, D., Simon-Miller, A., Jennings, D., Flasar, M., and Kunde, V. (2004). Meridional variations for C_2H_2 and C_2H_6 in Jupiter's atmosphere from cassini/cirs infrared spectra. submitted Icarus.

[141] Nixon, C., Irwin, P., Calcutt, S., Taylor, F., and Carlson, R. (2001). Atmospheric composition and cloud structure in Jovian 5-μm hotspots from analysis of Galileo NIMS measurements. *Icarus*, 150(1):48–68.

[142] Noll, K., Gilmore, D., Knacke, R., Womack, M., Griffith, C., and Orton, G. (1997). Carbon monoxide in Jupiter after comet Shoemaker-Levy 9. *Icarus*, 126(2):324–335.

[143] Ortiz, J., Orton, G., Friedson, A., Stewart, S., Fisher, B., and Spencer, J. (1998). Evolution and persistence of 5-μm hot spots at the Galileo probe entry latitude. *J. Geophys. Res.*, 103(E10):23051–23069.

[144] Orton, G. (1975). Spatially resolved absolute spectral reflectivity of Jupiter: 3390-8400 Angstroms. *Icarus*, 26(1):159–174.

[145] Orton, G. (2001). Private communication. "The extent of the GRS can be determined from its location around Dec. 29, which I'm interpolating among our data [IRTF] as: 45.5 - 62.0 degrees West longitude in System III.".

[146] Orton, G., Appleby, J., and Martonchik, J. (1982). The effect of ammonia ice on the outgoing thermal radiance in the atmosphere of Jupiter. *Icarus*, 52(1):94–116.

[147] Orton, G., Fisher, B., Baines, K., Stewart, S., Friedson, A., Ortiz, J., Marinova, M., Ressler, M., Dayal, A., Hoffmann, W., Hora, J., Hinkley, S., Krishnan, V., Masanovic, M., Tesic, J., Tziolas, A., and Parija, K. (1998). Characteristics of the Galileo probe entry site from Earth-based observations. *J. Geophys. Res.*, 103(E10):22791–22814.

[148] Orton, G., Friedson, A., Caldwell, J., Hammel, H., Baines, K., Bergstralh, J., Martin, T., Malcom, M., West, R., Golisch, W., D., G., Kaminski, C. Tokunaga, A.,

Baron, R., and Shure, M. (1991). Thermal maps of Jupiter: spatial organisation and time dependence of stratospheric temperatures, 1980 to 1990. *Science*, 252(5005):537–542.

[149] Orton, G., Friedson, A., Yanamandra-Fisher, P., Caldwell, J., Hammel, H., Baines, K., Bergstralh, J. Martin, T., West, R., Veeder, G., Lynch, D., Russell, R., Malcom, M., Golisch, W., Griep, D., Kaminski, C., Tokunaga, A., Herbst, T., and Shure, M. (1994). Spatial-organisation and time-dependence of Jupiter's tropospheric temperatures, 1980-1993. *Science*, 265(5172):625–631.

[150] Owen, T., Mahaffy, P., Niemann, H., Atreya, S., Donahue, T., Bar-Nun, A., and de Pater, I. (1999). A low-temperature origin for the planetesimals that formed Jupiter. *Nature*, 402(6759):269–270.

[151] Perraglia, J. (1984). Meridional energy balance of Jupiter. *Icarus*, 59(2):169–176.

[152] Porco, C. (2000). Cassini/ISS Christmas movie. Cassini Imaging: Central Laboratory for Operations website: http://ciclops.lpl.arizona.edu.

[153] Porco, C., West, R., McEwen, A., Del Genio, A., Ingersoll, A., Thomas, P., Squyres, S., Dones, L., Murray, C., Johnson, T., Burns, J., Brahic, A., Neukum, G., Veverka, J., Barbara, J., Denk, T., Evans, M., Ferrier, J., Geissler, P., Helfenstein, P., Roatsch, T., Throop, H., Tiscareno, M., and Vasavada, A. (2003). Cassini imaging of Jupiter's atmosphere, satellites and rings. *Science*, 299(5612):1541–1547.

[154] Prinn, R., Larson, H., Caldwell, J., and Gautier, D. (1984). Composition and chemistry of Saturn's atmosphere. In Gehrels, T. and Matthews, M., editors, *Saturn: studies of the interior, atmosphere, magnetosphere and satellites*, number 1 in Space Science, pages 88–149. Univ. Arizona Press.

[155] Prinn, R. and Lewis, J. (1975). Phosphine on Jupiter and implications for the Great Red Spot. *Science*, 190:274–276.

[156] Prinn, R. and Owen, T. (1976). Chemistry and spectroscopy of the Jovian atmosphere. In Gehrels, T., editor, *Jupiter: studies of the interior, atmosphere, magnetosphere and satellites*, number 1 in Space Science, pages 319–371. Univ. Arizona Press.

[157] Pryor, W. and Hord, C. (1991). A study of photopolarimeter system UV absorption data on Jupiter, Saturn, Uranus and Neptune: implications for auroral haze formation. *Icarus*, 91(1):161–172.

[158] Ragent, B., Colburn, D., Rages, K., Knight, T., Avrin, P., Orton, G., Yanamandra-Fisher, P., and Grams, G. (1998). The clouds of Jupiter: results of the Galileo Jupiter mission probe Nephelometer experiment. *J. Geophys. Res.*, 103(E10):22891–22909.

[159] Rages, K., Beebe, R., and Senske, D. (1999). Jovian stratospheric hazes: the high phase angle view from Galileo. *Icarus*, 139(2):211–226.

[160] Ridgway, S., Wallace, L., and Smith, G. (1976). The 800-1200 inverse centimeter absorption spectrum of Jupiter. *Astrophys. J.*, 207:1002–1006.

[161] Rodgers, C. (2000). *Inverse Methods for Atmospheric Sounding: Theory and Practice.* World Scientific, Singapore, 1st edition.

[162] Rogers, J. (1995). *The Giant Planet Jupiter.* Camb. Univ. Press, UK, 1st edition.

[163] Romani, P. (1996). Recent rate constant and product measurements of the reactions $C_2H_3 + H_2$ and $C_2H_3 + H$ – importance for photochemical modelling of hydrocarbons on Jupiter. *Icarus*, 122(2):233–241.

[164] Romani, P. (1999). Private communication. Photochemical model update: based on 1996 paper, updated to incorporate new rate-reaction data and CH_4 branching ratios.

[165] Roos-Serote, M., Atreya, S., Wong, M., and Drossart, P. (2003). On the water abundance in the atmosphere of Jupiter. accepted Plan. & Space Sci.

[166] Roos-Serote, M., Drossart, P., Encrenaz, T., Carlson, R., and Leader, F. (1999). Constraints on the tropospheric cloud structure of Jupiter from spectroscopy in the 5-μm region: a comparison between voyager/iris, galileo/nims and iso/sws spectra. *Icarus*, 137(2):315–340.

[167] Roos-Serote, M., Vasavada, A., Kamp, L., Irwin, P., Nixon, C., and Carlson, R. (2000). Proximate humid and dry regions in Jupiter's atmosphere indicate complex local meteorology. *Nature*, 405(6783):158–160.

[168] Roulston, M. and Stevenson, D. (1995). Prediction of neon depletion in Jupiter's atmosphere (abstract). *Eos*, 76:F343.

[169] Sada, P., Beebe, R., and Conrath, B. (1996). Comparison of the structure and dynamics of Jupiter's Great Red Spot between Voyager 1 and 2 encounters. *Icarus*, 119(2):311–335.

[170] Sada, P., Bjoraker, G., Jennings, D., McCabe, G., and Romani, P. (1998). Observations of CH_4, $C_2H_6$and C_2H_2 in the stratosphere of Jupiter. *Icarus*, 136(2):192–201.

[171] Schulze-Makuch, D. and Irwin, L. (2002). Energy cycling and hypothetical organisms in Europa's ocean. *Astbio.*, 2(1):105–121.

[172] Seiff, A., Kirk, D., Knight, T., Young, R., Mihalov, J., Young, L., Milos, F., Schubert, G., Blanchard, R., and Atkinson, D. (1998). Thermal structure of Jupiter's atmosphere near the edge of a 5-μm hot spot in the North Equatorial Belt. *J. Geophys. Res.*, 103(E10):22857–22889.

[173] Sheppard, S. and Jewitt, D. (2003). An abundant population of small irregular bodies around Jupiter. *Nature*, 423(6937):261–263.

[174] Showalter, M., Burns, J., Cuzzi, J., and Pollack, J. (1987). Jupiter's ring system: new results on structure and particle properties. *Icarus*, 69(3):458–498.

[175] Showman, A. and Dowling, T. (2000). Nonlinear simulations of Jupiter's 5-micron hot spots. *Nature*, 289(5485):1737–1749.

[176] Showman, A. and Ingersoll, A. (1998). Interpretation of Galileo probe data and implications for Jupiter's dry downdrafts. *Icarus*, 132(2):205–220.

[177] Simon, A. (1999). The structure and temporal stability of Jupiter's zonal winds: a study of the North Tropical region. *Icarus*, 141(1):29–39.

[178] Simon-Miller, A., Banfield, D., and Gierasch, P. (2001). Color and the vertical structure in Jupiter's belts, zones and weather systems. *Icarus*, 154(2):459–474.

[179] Simon-Miller, A., Conrath, B., Gierasch, P., and Beebe, R. (2000). A detection of water ice on Jupiter with Voyager IRIS. *Icarus*, 145(2):454–461.

[180] Simon-Miller, A., Gierasch, P., Beebe, R., Conrath, B., Flasar, M., and Achterberg, R. (2002). New observational results concerning Jupiter's Great Red Spot. *Icarus*, 158(1):249–266.

[181] Smith, B., Soderblom, L., Johnson, T., Ingersoll, A., Collins, S., Shoemaker, E., Hunt, G., Masursky, H., Carr, M., Davies, M., Cook, A., Boyce, J., Danielson, G. Owen, T., Sagan, C., Beebe, R., Veverka, J., Strom, R., McCauley, J., Morrison, D., Briggs, G., and Suomi, V. (1979). The Jupiter system through the eyes of Voyager 1. *Science*, 204:951–972.

[182] Smith, M. (1998). Estimation of a length scale to use with the quench level approximation for obtaining chemical abundances. *Icarus*, 132(1):176–184.

[183] Smith, M. (2003). *CIRS field-of-view overview.* NASA Goddard Space Flight Center, Code 693.0, Greenbelt, MD, USA.

[184] Smith, M. and Gierasch, P. (1995). Convection in the outer planet atmospheres including ortho-para hydrogen conversion. *Icarus*, 116(1):159–179.

[185] Smith, P. and Tomasko, M. (1984). Photometry and polarimetry of jupiter at large phase angles. II: polarimetry of the South Tropical Zone, South Equatorial Belt and the polar-regions from the Pioneer-10 and Pioneer-11 missions. *Icarus*, 58(1):35–73.

[186] spacenews03 (2003). NASA to test Pluto probe during Jupiter fly-by. Space News.

[187] Sromovsky, L., Collard, A., Fry, P., Orton, G., Lemmon, M., Tomasko, M., and Freedman, R. (1998). Galileo probe measurements of thermal and solar radiation fluxes in the Jovian atmosphere. *J. Geophys. Res.*, 103(E10):22929–22977.

[188] Sromovsky, L. and Fry, P. (2002). Jupiter's cloud structure as constrained by Galileo probe and HST observations. *Icarus*, 157(2):373–400.

[189] Stevenson, D. and Salpeter, E. (1976). Interior models of Jupiter. In Gehrels, T., editor, *Jupiter: Studies of the interior, atmosphere, magnetosphere and satellites*, number 1 in Space Science, pages 85–112. Univ. Arizona Press.

[190] Stone, P. (1976). The meteorology of the Jovian atmosphere. In Gehrels, T., editor, *Jupiter: Studies of the interior, atmosphere, magnetosphere and satellites*, number 1 in Space Science, pages 586–618. Univ. Arizona Press.

[191] Strobel, D. (1977). NH_3 and PH_3 photochemistry in the Jovian atmosphere. *Astrophys. J.*, 214:L97–L99.

[192] Tarrago, G., Dang-Nhu, M., and Goldman, A. (1981). Analysis of phosphine absorption in the region 9-10 μm and high-resolution line-by-line simluation of the $\nu 2$ and $\nu 4$ bands. *J. Molec. Spectro.*, 88(2):311–322.

[193] Tokunaga, A., Beck, S., Geballe, T., Lacy, J., and Serabyn, E. (1981). The detection of HCN on Jupiter. *Icarus*, 48(2):283–289.

[194] Tokunaga, A., Knacke, R., and Ridgway, S. (1980). High spatial and spectral resolution 10-μm observations of Jupiter. *Icarus*, 44(1):93–101.

[195] Vapillon, L., Combes, M., and Lecacheux, J. (1973). The β Scorpii occultation of Jupiter. ii. the temperature and density profiles of the Jovian upper atmosphere. *Astron. Astrophys. Rev.*, 29:135–149.

[196] Vasavada, A. (2002). Private communication.

[197] Vasavada, A., Ingersoll, A., Banfield, D., Bell, M. Gierasch, P., Belton, M., Orton, G., Klaasen, K., DeJong, E., Breneman, H., Jones, T., Kaufman, J., Magee, K., and Senske, D. (1998). Galileo imaging of Jupiter's atmosphere: the Great Red Spot, equatorial region and white ovals. *Icarus*, 135(1):265–275.

[198] Vererka, J., Wasserman, L., Elliot, J., Sagan, C., and Liller, W. (1974a). The occultation of β Scorpii by Jupiter. i. the structure of the Jovian upper atmosphere. *Astron. J.*, 79:73–84.

[199] von Zahn, U., Hunten, D., and Lehmacher, G. (1998). Helium in Jupiter's atmosphere: results from the Galileo probe Helium Interferometer experiment. *J. Geophys. Res.*, 103(E10):22815–22829.

[200] Wagener, R., Caldwell, J., and Owen, T. (1986). Constraints on the NH_3 and PH_3 distributions in the GRS. *Icarus*, 66(1):188–191.

[201] Wallace, J. and Hobbs, P. (1977). *Atmospheric Science: an Introductory Survey.* Academic Press, USA, 1st edition.

[202] Weidenschilling, S. and Lewis, J. (1973). Atmospheric and cloud structures of the planet Jupiter. *Icarus*, 20(4):465–476.

[203] West, R., Strobel, D., and Tomasko, M. (1986). Clouds, aerosols and photochemistry in the Jovian atmosphere. *Icarus*, 65(2-3):161–217.

[204] Wong, M., Bjoraker, G., Smith, M., Flasar, M., and Nixon, C. (2003). Identification of the 10-μm ammonia ice feature on Jupiter. accepted Plan. & Space Sci.

[205] Young, R. (1998). The Galileo probe mission to Jupiter: science overview. *J. Geophys. Res.*, 103(E10):22775–22790.

Figure C.1: On the way to Saturn; Io and Jupiter as viewed by Cassini/ISS (15 Jan 2001). [NASA]